UNIVERSITY of BRADFORD Library

University of Bradford eThesis

This thesis is hosted in Bradford Scholars – The University of Bradford Open Access repository. Visit the repository for full metadata or to contact the repository team

© University of Bradford. This work is licenced for reuse under a Creative Commons Licence.

CONTROL STRATEGIES FOR BLENDED BRAKING IN ROAD VEHICLES

ZAINI

PhD

UNIVERSITY OF BRADFORD

2012

CONTROL STRATEGIES FOR BLENDED BRAKING IN ROAD VEHICLES

A study of control strategies for blended friction and regenerative braking in road vehicles based on maximising energy recovery while always meeting the driver demand

ZAINI

Submitted for the Degree of
Doctor of Philosophy

School of
Engineering Design and Technology
University of Bradford

2012

CONTROL STRATEGIES FOR BLENDED BRAKING IN ROAD VEHICLES

Zaini
University of Bradford

Abstract

In HEV and EV, higher fuel economy is achieved by operating the ICE and electric motor in the most efficient region and by using regenerative braking. Such a braking system converts, transfers, stores and reuses kinetic energy which would otherwise be dissipated as heat through friction brakes to the environment. This research investigates the control of braking for a mixed-mode braking system in a these vehicles based on the proportion of braking energy that can be stored.

Achieving mixed-mode braking requires the ‘blending’ of the two systems (regenerative and friction), and in brake blending, the electric motor/generator (M/G) and the hydraulic actuation pressure are controlled together to meet the driver’s braking demand. The research presented here has established a new robust dynamic modelling procedure for the design of combined regenerative and hydraulic braking systems. Direct torque control and pressure control were selected as the control criteria in both brakes.

Two simulation models have been developed in Matlab/Simulink to generate analysis the performance of the control strategy in the blended braking system. Integration of the regenerative braking system with ABS has also been completed, based on two conditions, with and without the deactivation of the regenerative braking. Verification of the models is presented, based on experimental work on two EVs manufactured by TATA Motors; the ACE light commercial vehicle and the VISTA small passenger car. It is concluded that braking demand and vehicle speed determine the operating point of the motor/generator and hence the regenerative braking ratio.

Keyword: braking, vehicle, regenerative, Matlab, control, blending, friction, electric, analysis, modelling

Acknowledgments

I would like to express my gratitude to my supervisors Dr. Khalid Hussain and Professor A. J. Day for their assistance, encouragement, advice, motivation and support throughout this research. I am greatly indebted to my supervisors for the valuable guidance which they have provided me throughout my study.

This thesis is dedicated to my parents Dalimus and Yusmaniar whose support, love and encouragement have always been a constant source of strength in my life.

I wish to extend this dedication to my wife Riska Lilianti in recognition of her untiring encouragement, support, understanding and patience during the period of this study. I also dedicate it to my delightful children, Dzaky Muhammad and Zaskia Ramadani, who have tolerated my absence.

I would like to thank colleagues on the School of Engineering, Design & Technology technical staff especially Chhibubhai Mistry, TMETC who provided two EVs for my experimental work, and Jaguar Land Rover who supplied the data for model validation.

Finally I would like to thank the Ministry of Higher Education of Indonesia for sponsoring my studies at the University of Bradford. I also appreciate the help of all my friends in the School of Engineering, Design and Technology.

List of Contents

Abstract i

Acknowledgments ii

List of Contents iii

List of Figures viii

List of Tables xiv

Nomenclature xvi

Glossary of Terms xxii

CHAPTER 1

INTRODUCTION

1.1 General Background 1

1.2 Project Definition 7

  1.2.1 Overall Aim 7

  1.2.2 Objectives and Methodology 7

1.3 Thesis Structure 10

1.4 Research Findings 12

CHAPTER 2

LITERATURE REVIEW

2.1 Introduction 14

2.2 Implementation of Mixed-mode Braking Systems 16

2.3 Pressure Control of Series Braking Systems 21

2.4 Design Models of Mixed-mode Braking System 25

2.5 Integration of a Mixed-mode Braking System with ABS and ESC 31

2.6 Electric Drive Application 35

2.7 Electrical Energy Storage Systems 47

2.8 Chapter Summary 56

2.9 Research Approach and Methodology 59

CHAPTER 3

THEORY OF MIXED-MODE BRAKING SYSTEMS

3.1 Introduction 61

3.2 Vehicle Modelling 62

3.3 Conventional Braking Systems 72

3.4 Mixed-mode Braking Systems 78

3.5 Torque Distribution Strategy 84

3.6 Chapter Summary 88

CHAPTER 4

DYNAMIC MODEL OF COMBINED REGENERATIVE AND FRICTION BRAKING SYSTEMS

4.1 Introduction 91

4.2 Models of induction Motor / Generators and DC Motor / Generators 92

4.3 Control Systems of Motor / Generators 99

4.4 Pressure Control of Friction Brake Systems 106

4.5 Integration of Mixed-mode Braking with ABS 110

4.6 Chapter Summary 112

CHAPTER 5

SIMULATIONS OF A MIXED-MODE BRAKING SYSTEM

5.1 Introduction 115

5.2 Braking Characteristics of Typical Drive Cycles 116

5.3 Energy Recovery from the FTP Drive Cycle 130

5.4 Operation of a Series Braking System on Different Drive Cycles 135

5.5 Operation of a Parallel Braking System on Different Drive Cycles 145

5.6 Integration of a Regenerative Braking System with ABS 149

5.7 Chapter Summary 157

CHAPTER 6

EXPERIMENTAL WORK

6.1 Introduction 160

6.2 ACE EV Braking System

6.2.1 Objectives 161

6.2.2 Apparatus and Equipment 161

6.2.3 Test Setup and Procedure 164

6.2.4 Results and Discussion 169

6.2.5 Interim Conclusions 176

6.3 VISTA EV Braking System

6.3.1 Objectives 176

6.3.2 Apparatus and Equipment 177

6.3.3 Instrumentation 178

6.3.4 Test Setup and Procedure 179

6.3.5 Results and Discussion 180

6.3.6 Interim Conclusions 193

CHAPTER 7

GENERAL DISCUSSION AND VALIDATION

7.1 General Discussion 195

7.2 Validation 202

CHAPTER 8

SUMMARY, CONCLUSIONS AND RECOMMENDATIONS

8.1 Summary 210

8.2 Conclusions 215

8.3 Recommendations 221

REFERENCES 223

APPENDICES 220

List of Figures

Figure 1.1	Electrical traction/ braking system in HEV	3
Figure 1.2	Summary flowchart of research methodology	10
Figure 2.1	Brake blending in a 4WD hybrid car	17
Figure 2.2	Basic brake versus ECB	18
Figure 2.3	Structure of servo unit in Honda design	19
Figure 2.4	Simulator brake actuation	20
Figure 2.5	Cross-section of the e-ACT braking system	21
Figure 2.6	Pressures and vehicle speed on mixed-mode braking	22
Figure 2.7	Feasibility Test at HILS	23
Figure 2.8	Characteristic of Toyota’s stroke simulator	24
Figure 2.9	Characteristic of Honda’s stroke simulator	25
Figure 2.10	Characteristic of Continental’s stroke simulator	25
Figure 2.11	Braking force requirements and maximum system outputs	26
Figure 2.12	Block diagram of HiLS	27
Figure 2.13	Schematic diagram of the HEV bench tester	28
Figure 2.14	EMB system in a parallel hybrid vehicle	30
Figure 2.15	The configuration of the braking system	31
Figure 2.16	ECB control composition	32
Figure 2.17	Integration of e-ACT with VDC in the Nissan Leaf EV	33
Figure 2.18	The effect of regenerative braking on vehicle stability	34
Figure 2.19	Fuzzy logic controller for the regenerative braking system	35
Figure 2.20	(a) Induction M/G (b) SR M/G (c) PMBL M/G	38
Figure 2.21	Torque and power as functions of motor speed	39
Figure 2.22	Efficiency of Leaf EV electric drive	40
Figure 2.23	Implementation of DTC into PMBL drive	41
Figure 2.24	Torque dynamic responses of PMBL drive with DTCs	42
Figure 2.25	Scheme for the EV sensorless DTC simulation	44
Figure 2.26	Switching characteristics of the SR drive	45
Figure 2.27	Global performance map of SR drive at 9,950 rev/min	46
Figure 2.28	Configuration of EV powertrain	47
Figure 2.29	Trade-offs between fuel economy and vehicle cost for HEV	49
Figure 2.30	Electrochemical model of battery	50

Figure 2.31 Measured and simulated values of cell voltage 50
Figure 2.32 The ESS and buffering in e-CVT equipped HEV 52
Figure 2.33 Operation modes of the ESS; (a) Mode I (b) Mode II (c) Mode III 53
Figure 2.34 Discharge characteristics of a lead–acid battery 54
Figure 2.35 NiMH voltage versus SoC with rate as parameter at 20 ^{0}C cell 55
Figure 3.1 Road load as function of vehicle speed 63
Figure 3.2 Speed-torque curve of a gasoline engine 65
Figure 3.3 Local and global coordinates of a road vehicle 66
Figure 3.4 7-DOF four wheel vehicle dynamic model 67
Figure 3.5 Adhesion coefficient in the *x*-direction as a function of slip ratio for different sideslip 69
Figure 3.6 Adhesion coefficient in the *y*-direction as a function of slip ratio for different sideslip 70
Figure 3.7 Tyre characteristics obtained with Pacejka's model 71
Figure 3.8 Operating principle of a vacuum servo 73
Figure 3.9 Pedal force/travel characteristic of a mid-size passenger car 74
Figure 3.10 Boosted vs. Non-Boosted Brake Output 75
Figure 3.11 Cross sectional diagram of a standard tandem master cylinder 76
Figure 3.12 The friction coefficient as a function of disc temperature 77
Figure 3.13 Characteristics of hydraulic brake actuation (line) pressure and brake pedal travel 78
Figure 3.14 Reproduction of the brake pedal force/pressure curve 80
Figure 3.15 Characteristic curve of PMBL M/G 80
Figure 3.16 Weight factors for regenerative braking 81
Figure 3.17 Efficiency contour of electric M/G on the torque-speed plane 82
Figure 3.18 Performance curve of TM4 electric motor 83
Figure 3.19 Internal resistance battery model electrical schematic 83
Figure 3.20 Flowchart of series braking system 86
Figure 3.21 Algorithm for integrating series braking system with ABS 87
Figure 3.22 Algorithm for integrating parallel braking system with ABS 88

Figure 4.1 3-phase symmetric induction motor 93
Figure 4.2 Induction motor with rotating reference frame 96
Figure 4.3 Structure of DC motor and flux density 97
Figure 4.4 Separately excited DC motor 98
Figure 4.5 DTC scheme of induction motor for induction motor drives 100
Figure 4.6 Sector definition: (a) circular and (b) hexagonal stator flux vector path 101
Figure 4.7 (a) Torque controller (b) flux controller with hysteresis functions 102
Figure 4.8 Proposed traction system of DC drive 104
Figure 4.9 Hysteresis function for current controller 104
Figure 4.10 Proposed braking system of DC drive 105
Figure 4.11 Force balance on solenoid valve 107
Figure 4.12 Hydrokinetic force-plunger position curve 108
Figure 4.13 Friction braking model using pressure control criteria 109
Figure 4.14 AMESim model of brake caliper 110
Figure 4.15 Integrated model of braking system in EV and HEV 112
Figure 5.1 FTP drive cycle 117
Figure 5.2 US06 drive cycle 118
Figure 5.3 EUDC drive cycle 118
Figure 5.4 Forward facing simulation structure 121
Figure 5.5 Backward facing simulation structure 121
Figure 5.6 Simulink vehicle model for traction and braking dynamics 123
Figure 5.7 Pedal travel and pedal force during braking 123
Figure 5.8 Master cylinder pressures during one second of braking 124
Figure 5.9 Vehicle road speed and translational wheel speeds 125
Figure 5.10 Load transfer from rear to front axles in braking 125
Figure 5.11 Longitudinal tyre force as function of σ_x at constant vertical load 126
Figure 5.12 Vehicle decelerations during one second of braking 127
Figure 5.13 Slip ratios during one second of braking 128
Figure 5.14 Regenerative ratio of FTP drive cycle 131
Figure 5.15 M/G efficiency in the regenerative braking period 131
Figure 5.16 Braking and acceleration intervals in FTP drive cycle 132

Figure 5.17 Battery SoC condition in both braking and traction intervals 133
Figure 5.18 Deceleration profiles in the FTP drive cycle 134
Figure 5.19 Operating points of M/G in the FTP drive cycle 134
Figure 5.20 Battery currents during different braking intervals 135
Figure 5.21 Vehicle speed and torque demands on the FTP drive cycle 136
Figure 5.22 Vehicle speed and torque demands on the US06 drive cycle 137
Figure 5.23 Speed-torque curve of the motor on the wheel 138
Figure 5.24 Simulink model of regenerative braking system 139
Figure 5.25 Oscillating regenerative torque caused by the direct torque controller 139
Figure 5.26 Torque and speed of the induction motor in the forward-facing model 140
Figure 5.27 Switch status and motor currents (t=2.001 s) 141
Figure 5.28 Phase currents of the induction motor 141
Figure 5.29 Simulink model of hydraulic brake for one wheel 143
Figure 5.30 Vehicle speed and braking torques on the wheel 144
Figure 5.31 Controlled wheel pressure in the mixed-mode braking system 144
Figure 5.32 Vehicle deceleration in the last 2s of braking 145
Figure 5.33 Regenerative brake using a separately excited DC motor 146
Figure 5.34 Armature voltage and current during braking 147
Figure 5.35 Field current and negative armature current during braking 148
Figure 5.36 Armature currents for different duty cycles of GTO switch 149
Figure 5.37 Field and armature currents generated ($If.\omega$ = constant) 149
Figure 5.38 Wheel pressure responses for different PWM ratios 151
Figure 5.39 Outputs of first and second order systems 152
Figure 5.40 Pacejka’s static model as used in the research 152
Figure 5.41 Adhesion coefficient curves of different road conditions 153
Figure 5.42 Vehicle model including regenerative brake and ABS 154
Figure 5.43 Pedal force and resulting master cylinder pressure 154

Figure 5.44 Regenerative and friction torques during braking 155
Figure 5.45 Rotational wheel speeds and vehicle speed during braking 156
Figure 5.46 Vehicle and wheel translation speeds ($T_{motor} \neq 0$) 157
Figure 6.1 Powertrain of ACE EV 162
Figure 6.2 Rototest dynamometer connected to rear axle 162
Figure 6.3 Instrumentation for measuring current and voltage 163
Figure 6.4 Comparison of Hall Effect sensor with inductive sensor 164
Figure 6.5 Calibrating torque transducer of Rototest dynamometer 167
Figure 6.6 Profile of vehicle speeds and wheel torque 169
Figure 6.7 Battery current and voltage during ECE drive cycle 170
Figure 6.8 Battery power during the ECE drive cycle 171
Figure 6.9 Vehicle speed and battery power of ACE EV 172
Figure 6.10 Electrical power system of ACE EV 173
Figure 6.11 Vehicle speed and powers during acceleration interval 175
Figure 6.12 Open-circuit voltage of battery as the battery discharged 175
Figure 6.13 Under the bonnet of the VISTA 177
Figure 6.14 CAN-log 3 and 4 for data logging application 179
Figure 6.15 Profile of VISTA speed (Vmax=107 km/h) 179
Figure 6.16 Battery current measured by Pico and VMU systems 180
Figure 6.17 Profile of battery current (Ireg,max=61.7 Amps) 181
Figure 6.18 Regenerative current flowing to the battery 181
Figure 6.19 Voltage of battery terminal during regenerative braking 182
Figure 6.20 Vehicle speed and battery power 183
Figure 6.21 Profile of VISTA battery power 184
Figure 6.22 Braking interval whose low regenerative ratio 185
Figure 6.23 Braking interval whose high regenerative ratio 185
Figure 6.24 Effect of depressing accelerator pedal to regenerative power 185
Figure 6.25 Effect of battery losses to regenerative ratio 187
Figure 6.26 Efficiency map and operating point of electric motor 188
Figure 6.27 Retarding powers at low accelerator pedal positions 189
Figure 6.28 Vehicle speed during normal braking 190
Figure 6.29 Phase currents of motor during braking 190
Figure 6.30 Currents flow from the motor to inverter at t= 325.2 s 191
Figure 6.31 Vehicle speed and battery power during ABS 192

	intervention	
Figure 6.32	Vehicle deceleration during hard braking with ABS activated	192
Figure 6.33	Vehicle deceleration during hard braking with ABS not activated	193
Figure 7.1	Brake torques with different approaches	197
Figure 7.2	Field and armature currents of ACE DC motor/generator	203
Figure 7.3	Brake torque demand of VISTA EV	204
Figure 7.4	Reference and generated torques of VISTA M/G	205
Figure 7.5	Vehicle road speed of VISTA during braking	205
Figure 7.6	Reference and generated torques of simulation model	206
Figure 7.7	Pedal travel and front pressure of Auris braking system	207
Figure 7.8	Comparing model output with experimental result	208
Figure 7.9	Reference and actual caliper pressures	209
Figure 7.10	Inlet and outlet valve positions to follow reference pressure.	209

List of Tables

Table 2.1 Applications of electric drive to EVs and HEVs 36

Table 2.2 Torque density of electrical motors 37

Table 2.3 Comparison of electric M/G's of HEV 38

Table 2.4 Type of Batteries in modern EVs and HEVs 48

Table 2.5 Advantages and disadvantages of modern batteries 48

Table 2.6 Battery versus ultracapacitor performance 51

Table 3.1 Pacejka’s parameters for different driving conditions 71

Table 3.2 Selected data from the brake pedal travel/pressure characteristic 79

Table 3.3 NiMH battery data 84

Table 4.1 Optimum switching table of DTC 102

Table 4.2 Generated voltage vectors of DTC 103

Table 5.1 Braking intervals in the FTP drive cycle 120

Table 5.2 Braking intervals in the US06 drive cycle 120

Table 5.3 Braking intervals in the EUDS drive cycle 120

Table 5.4 Pedal force and travel data as inputs 124

Table 6.1 Braking related functions of the GE vehicle controller 165

Table 6.2 ACE EV parameters inputted to Rototest software 166

Table 6.3 Weight positions and calibration results 167

Table 6.4 Braking intervals in the ECE drive cycle 171

Table 6.5 Regenerative ratio of ACE EV on ECE drive cycle 173

Table 6.6 Efficiency of motor/controller during acceleration intervals 175

Table 6.7 Braking intervals in speed profile of VISTA EV 183

Table 6.8 Regenerative ratio of VISTA braking system 184

Table 6.9 Li-Ion battery data 186

Table 6.10 Experimental results for hard braking condition 192

Nomenclature

a	First constant of stroke-force curve (H^{-1})
A	Effective frontal vehicle cross-sectional area (m^2)
A_{cal}	Cross-section area of caliper (m^2)
A_0	Orifice area (m^2)
A_1	Cross-sectional area of power piston (m^2)
B	Stiffness factor of Pacejka’s tyre model
b	Second constant of stroke-force curve (Hm^{-1})
B_m	Viscous friction coefficient ($Nmsrad^{-1}$)
C	Shape factor of Pacejka’s tyre model
C	Damping coefficient ($Nsm-^{1}$)
C_{Fx}	Tyre longitudinal stiffness (Nm^{-1})
C_α	Lateral stiffness (N)
C_d	Aerodynamic drag coefficient ($Ns^2m^{-1}kg^{-1}$)
C_d	Discharge coefficient
C_{ro}	Rolling resistance coefficient
C_s	Longitudinal stiffness (N)
D	Peak value of Pacejka’s tyre model
E	Curvature factor of Pacejka’s tyre model
F_d	Aerodynamic drag force (N)
F_{disk}	reaction force from the disk (N)
F_{EM}	Regenerative brake force (N)
F_{ro}	Rolling resistance force (N)
F_{vis}	Viscous friction (N)

F_{xf}	Longitudinal forces at the ground contact points of front wheels (N)
F_{xr}	Longitudinal forces at the ground contact points of rear wheels (N)
F_{yf}	Lateral tyre forces generated by front wheels (N)
F_{yr}	Lateral tyre forces generated by rear wheels (N)
F_{zf}	Vertical load force at the front wheel ground contact points (N)
F_{zr}	Vertical load force at the rear wheel ground contact points (N)
g	Gravitational acceleration (ms^{-2})
h	Height of vehicle centre gravity above the ground (m)
i	Solenoid current (A)
I	Moment of inertia about its centre of mass (kgm^2)
$\mathbf{i}_{\mathrm{dq0r}}$	dq0 components of rotor current vector
$\mathbf{i}_{\mathrm{dq0s}}$	dq0 components of stator current vector
$\mathbf{i}_{\mathrm{abcr}}$	Rotor current vector
$\mathbf{i}_{\mathrm{abcs}}$	Stator current vector
i_{ar}	Phase *a* current of rotor winding (A)
i_{as}	Phase *a* current of stator winding (A)
I_{br}	Phase *b* current of rotor winding (A)
I_{bs}	Phase *b* current of stator winding (A)
I_{cr}	Phase *c* current of rotor winding (A)
I_{cs}	Phase *c* current of stator winding (A)
I_{w}	Wheel-tyre assembly inertia ($\mathrm{kg.m}^2$)
I_z	Moment of inertia of the vehicle about the z axis (kgm^2)
K	Constant of second-order transfer function
K_a	Motor constant (NmA^{-1})

K_{m}	Rotational inertia coefficient
K_{pad}	Pad stiffness (Nm^{-1})
L	Inductance of magnetic circuit (H)
L_{arar}	Phase *a* self-inductance of rotor (H)
L_{arbr}	Mutual inductance between rotor-rotor windings (H)
L_{asar}	Mutual inductance between stator-roto windings (H)
L_{asas}	Phase *a* self-inductance of stator (H)
L_{asbs}	Mutual inductance between stator-stator windings (H)
L_{brbr}	Phase *b* self-inductance of rotor (H)
L_{bsbs}	Phase *b* self-inductance of stator (H)
L_{crcr}	Phase *c* self-inductance of rotor (H)
L_{cscs}	Phase *c* self-inductance of stator (H)
l_f	Distance from front axle to the centre of gravity (m)
L_{lr}	Rotor leakage inductance (H)
L_{ls}	Stator leakage inductance (H)
L_{mr}	Rotor magnetizing inductance (H)
L_{ms}	Stator magnetizing inductance (H)
L_{p}	Pedal ratio
l_r	Distance from rear axle to the centre of gravity (m)
$\mathbf{L}_{r}$	Matrix of the rotor self-inductances
$\mathbf{L}_{s}$	Matrix of the stator self-inductances
$\mathbf{L}_{sr}$	Stator-rotor mutual inductance mapping
m	Vehicle mass (kg)
M_{zf}	Aligning moment on the tyre for front wheels (kgm^2)

M_{zr}	Aligning moments on the tyre for rear wheels (kgm^2)
M_1	mass of piston (kg)
N	Normal force (N)
$\mathrm{N_r}$	Number of turns of the rotor winding
$\mathrm{N_s}$	Number of turns of the stator winding
$\mathrm{N_0}$	Final drive gear ratio
$\mathrm{N_1}$	Reduction gear ratio
P	Input power to the battery (W)
p	Number of poles
$\mathrm{P_1}$	Upstream pressure (Pa)
$\mathrm{P_1}$	Primary line pressure (Pa)
$\mathrm{P_2}$	Downstream pressure (Pa)
Q	Flow rate (m^3/s^{-1})
$\mathrm{R_e}$	Effective rolling radius (m)
$\mathrm{r_r}$	Resistance of the rotor winding (Ω)
$\mathrm{r_s}$	Resistance of the stator winding (Ω)
s	Wheel slip ratio
S_a	First binary number of inverter switch status
S_b	Second binary number of inverter switch status
S_c	Third binary number of inverter switch status
$\mathrm{t_1}$	Initial time of each braking interval (s)
$\mathrm{t_2}$	Final time of each braking interval (s)
$\mathrm{T_L}$	Load torque (Nm)
$\mathbf{u}_{\mathrm{dq0r}}$	dq0 components of rotor voltage vector

$\mathbf{u}_{dq0s}$	dq0 components of stator voltage vector
$\mathbf{u}_{abcr}$	Rotor voltage vector
$\mathbf{u}_{abcs}$	Stator voltage vector
u_{ar}	Phase voltage supplied to the *a*rotor winding (V)
u_{as}	Phase voltage supplied to the *a* stator winding (V)
u_{br}	Phase voltage supplied to the *b*rotor winding (V)
u_{bs}	Phase voltage supplied to the *b* stator winding (V)
u_{cr}	Phase voltage supplied to the *c*rotor winding (V)
u_{cs}	Phase voltage supplied to the *c* stator winding (V)
U_{DC}	DC link voltage of the inverter (V)
V_1	Initial vehicle speed of each braking interval (kmh^{-1})
V_2	Final vehicle speed of each braking interval ($\mathrm{km/h}^{-1}$)
V_{sx}	Wheel slip velocity (ms^{-2})
V_x	Longitudinal vehicle velocity (ms^{-1})
α_f	Slip angle of front tyre (rad)
α_r	Slip angle of rear tyre (rad)
β	Angle of vehicle speed (rad)
δ_ψ	Angle between the stator flux and the rotor flux (rad)
δ_{fw}	Steering angle (rad)
Φ_P	Flux per pole (Wb)
η_t	Efficiency of transmission
φ	Vehicle yaw angle (rad)
μ_d	Dynamic coefficient of friction
μ_s	Static coefficient of friction

ρ	Fluid mass density (kgm^{-3})
σ	Leakage factor
σ_x'	Contact patch slip
τ_{EM}	Regenerative brake torque (Nm)
ω_{rm}	Mechanical angular velocity (rads^{-1})
ω_r	Electrical angular velocity (rads^{-1})
ψ_{dq0r}	dq0 components of rotor flux linkage vector
ψ_{abcr}	Rotor flux linkage vector
ψ_{abcs}	Stator flux linkage vector
ψ_{ar}	Phase *a* flux linkage of rotor (Wb)
ψ_{as}	Phase *a* flux linkage of stator (Wb)
ψ_{br}	Phase *b* flux linkage of rotor (Wb)
ψ_{bs}	Phase *b* flux linkage of stator (Wb)
ψ_{cr}	Phase *c* flux linkage of rotor (Wb)
ψ_{cs}	Phase *c* flux linkage of stator (Wb)
ψ_{dq0s}	dq0 components of stator flux linkage vector
$\Re_m$	Magnetizing reluctance (H^{-1})
$\dot{x}$	Piston speed (ms^{-1})

Glossary of Terms

4WD	Four-wheel Drive
ABS	Antilock Braking System
AC	Alternating Current
ADVISOR	Advanced Vehicle Simulator
BMS	Battery Management System
CAN	Controller Area Network
CG	Centre of Gravity
CVT	Continuously Variable Transmission
DC	Direct Current
DoF	Degrees of Freedom
DSC	Direct Self Control
DTC	Direct Torque Control
ECB	Electronically Controlled Brake
ECU	Electronic Control Unit
EHB	Electrohydraulic Brake
EMB	Electromechanical Brake
EMF	Electromotive Force
EPA	Environmental Protection Agency
ESC	Electronic Stability Control (includes Vehicle Stability Control - VSC)
ESS	Energy Storage System
EUDC	Extra Urban Driving Cycle

EV	Electric Vehicle
FEV	Full Electric Vehicle
FNN	Fuzzy Neural Network
FTP	Federal Testing Procedure
FUDS	Federal Urban Driving Schedule
GE	General Electric
GTO	Gate Turned Off
HCU	Hydraulic Control Unit
HEV	Hybrid Electric Vehicle
HiLS	Hardware in Loop Simulation
HPPC	Hybrid Pulse Power Characteristic
ICE	Internal Combustion Engine
IEA	International Energy Agency
LED	Light Emitting Diode
Li-Ion	Lithium Ion
M/G	Motor/Generator
MCU	Motor Control Unit
MMF	Magnetic Motive Force
Ni-Cd	Nickel-Cadmium
NiMH	Nickel Metal Hydride
NREL	National Renewable Energy Laboratory
OEM	Original Equipment Manufacturer
PC	Personal Computer
PFI	Port Fuel Injected

PI	Proportional Integral
PID	Proportional Integral Differential
PM	Permanent Magnet
PMBL	Permanent Magnet Brushless
PNGV	Partnership for a New Generation of Vehicle
PWM	Pulse Width Modulation
SMC	Sliding Mode Control
SoC	State of Charge
SPEED	Scottish Power Electronics and Electric Drives
SR	Switched Reluctance
SVM	Space Vector Modulation
VDC	Vehicle Dynamic Control
VMU	Vehicle Management Unit
VSC	Vehicle Stability Control (usually covered by the term ESC)

CHAPTER 1

INTRODUCTION

1.1 General Background

Data from the IEA reveals that energy consumption of the transportation sector increases by 9.3 % annually. Other data from the US EPA also shows that transportation contributed about 40 % of the total CO_2 emission in 2007. Therefore, to conserve energy and reduce the impact on the environment, world governments urge automobile companies to produce low fuel consumption and low emission vehicles. These are achieved by many technical improvements including inventing more advanced internal combustion engines (ICE) and using more lightweight materials. It was predicted that the fuel consumption of ICE's would reduce about 6-15% in 2010 compared to 2000 (Taylor, 2008). Lightweight materials such as polymers and aluminum have been introduced to replace iron and steel.

Energy contained in fuel cannot totally be converted to mechanical work to drive the vehicle; only 12-20 % is available at the drive wheels (Williamson et al., 2006). This is because of the low efficiency of the ICE and losses which occur in the drivetrain. Furthermore, the efficiency of an ICE is affected by its operating region in terms of engine speed and engine torque. For example, for a 67 kW SI engine, highest efficiency is obtained when the engine operates at torques near 150 Nm and speeds in the range of 1500 to 3000 rev/min (Gao and Ehsani, 2010). To help an ICE operate at higher efficiency, the concept of the HEV has been introduced. An HEV is defined as a vehicle in which propulsion energy is available from two or more kinds or types of energy store, source or converter, where at least one of them can deliver electrical energy (Chau et al., 2001). This definition can be narrowed to refer to vehicles which have both an ICE and an electric motor for the drive train.

The most popular HEV worldwide is the Toyota Prius (davebarton.com, 2011) which entered the market in 1997.The operation of the M/G's (there are 2 in this HEV) in the Toyota Prius depends on the driving conditions. First, at low speed, M/G2 provides all the power to drive the wheels. The engine contributes when the battery state of charge (SoC) is low or the vehicle speed is greater than 24 km/h. Secondly, under normal driving, the engine power is distributed to the wheels and to M/G1 which charges the battery. Thirdly, during full acceleration, both the engine and M/G2 are active to meet the large torque demand. Finally, during braking, M/G2 recovers the vehicle's kinetic energy and delivers it to the battery (Ehsani et al., 2010).

A schematic diagram of a regenerative braking system is shown in Figure 1.1. Current flows from the induction motor to the battery in braking mode and vice versa in traction mode. The torque controller uses voltages, currents and rotor position measurements to switch on or off the three-phase inverter. To match the voltage level of the inverter and the battery and generate a smooth battery current, a DC link is needed.

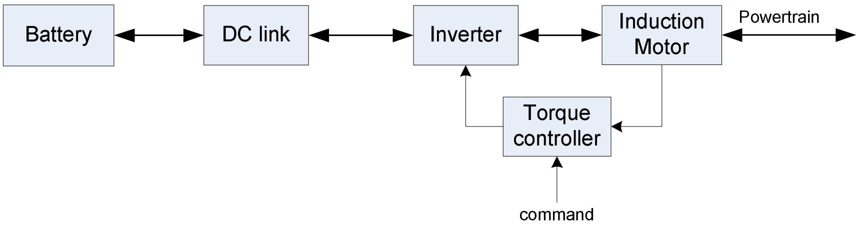

Figure 1.1 Electrical traction/ braking system in an HEV.

In urban driving with frequent start and stop events, more energy is dissipated by braking. The FTP75 vehicle drive cycle includes an urban driving profile where about 40 % of the traction energy is dissipated as heat during the braking cycle (Gao and Ehsani, 2001). They found that a 20 kW electric motor could recover a substantial proportion of the journey braking energy from the front axle which shows the benefit of HEV’s in capturing useful amounts of braking energy. However, the braking power can be higher than the power capacity of the M/G and thus friction braking must be always fitted to HEV’s, even in a Full Electric Vehicle (FEV) or an Electric Vehicle (EV).An FEV is considered to be an EV with full performance like ICE-based vehicle (Tate, 2008).

To capture the braking energy, either parallel or series regenerative braking systems can be used (Albrichsfeld and Karner, 2009). In a parallel system, the brake pedal has a mechanical connection to the friction brakes and the electric motor provides additional braking torque to stop the vehicle.

On the other hand, the brake pedal is decoupled from the friction brakes in a series system. When the driver's braking demand is higher than the M/G power capacity, the friction brakes are then applied. This suggests hat a series system can recover more energy than parallel systems.

However, the series regenerative braking system is more complicated since the wheel pressure must be controlled without causing noise and vibration and must have fast response characteristics (Nakamura et al, 2002). This can be achieved by using an input unit to determine brake demand and provide normal pedal feel to the driver, an hydraulic pressure control unit to modulate the wheel pressure, and an hydraulic pressure supply source to pressurise the brake fluid. In normal driving, the friction brakes provide the difference between the torque demand and the regenerative torque. As the speed reduces, the regenerative torque increases until the speed drops to below the base speed of the motor. But, at low speed, the regenerative brake is not used for two reasons; the energy recovery is small and it is difficult to meet the driver's pedal feel expectations (Yeo and Kim, 2002). They found that the driver behaviour in braking greatly affects the recovered energy. For example, if the brake demand is constantly high deceleration from high speed this causes the friction brakes to be continuously actuated from the start of braking, and a lower proportion of the braking energy can be captured. The Toyota Prius and Honda Insight are examples of modern HEV's employing a series braking system. But the detailed implementation of the braking system is different between these two vehicles as explained later.

Simplicity is the main advantage of a parallel regenerative braking system. A conventional braking system can be directly applied to these vehicles with this braking system and as a result, a lower cost of ownership can result. The TATA ACE is a small electric truck which uses a parallel regenerative braking system. In this system, the electric motor generates regenerative braking force to supplement the friction braking force generated by the pressure in the wheel cylinders of the friction brakes; unlike the series system, this pressure is controlled by the driver. The contribution of the regenerative braking can be controlled at any level based on the electric motor capacity at any given speed. There is a trade-off between the regenerative torque energy and the driver perception of the brake system. The driver would expect for a given pedal force to sense that the vehicle decelerates at a certain rate of braking. If the total braking torque is larger than the driver expects from the pedal effort applied, and thus the vehicle decelerates faster, the driver might feel uncomfortable about the brake system. Besides regenerative braking, modern HEV’s and EV’s are equipped with brake-based safety features such as Anti-lock Braking (ABS) and Electronic Stability Control (ESC). Since passenger safety is critical compared to energy recovery, the regenerative braking is usually deactivated when the ABS unit or the ESC unit are initiated. This requires synchronisation between these systems e.g. if the regenerative braking has been switched off but the ABS has not generated high enough pressure to decelerate the vehicle and thus the brake torque drops significantly for a short period of time.

In a series braking system, both regenerative and friction brakes are controlled to meet the brake demand. Therefore, control systems that accurately generate the motor torque and hydraulic pressure are important, otherwise, the resulting vehicle deceleration is not as intended by the driver. Drive cycle data available in the ADVISOR software can be used to derive the brake demand and then the performance of these control systems. ADVISOR is a simulator in Matlab/Simulink environment developed by National Renewable Energy Laboratory. It is usually used to analyse fuel economy, performance and emission of a newly developed powertrain (Markel et al., 2002).

Possible results include that the developed control system works well on certain drive cycles but has poor performance on others. Furthermore, the complexity of the control system greatly affects the computation time in real applications. If an execution delay between the brake demand received up to the actuator engaged in the ECU is perceived by the driver, an uncomfortable braking feel will result.

1.2 Project Definition

1.2.1 Overall Aim

The overall aim of this research was to make a contribution to extending the driving range of EV's or to increase fuel efficiency in HEV's by improving the design process for mixed-mode braking, i.e. regenerative braking with friction braking, to achieve safe braking under all conditions of vehicle usage while maximizing energy recovery and re-use, and hence fuel economy.

1.2.2 Objectives and Methodology

The main objective of this research was to establish an improved control system design methodology for mixed-mode braking in an EV or HEV. The proposed methodology was based upon the following two aspects of mixed-mode braking control:

- The control system: use information from drivetrain components such as the engine, M/G and wheels, and storage devices including batteries and ultracapacitors as the control parameters to enable the control system to distribute braking force into the friction and regenerative components by taking into account the deceleration required, the state of charge of the battery, the power capacity of the M/G, and the braking stability of the vehicle.

- Modelling: all the associated components and devices which make up the friction brake system were proposed to be modelled in the Matlab/Simulink environment using both static and dynamic modelling. After investigating them, it was proposed to build the control system for regenerative torque and hydraulic pressure using toolboxes available in Matlab/Simulink. Finally, it was proposed to carry out experimental work to validate the designed control system.

The research objectives were as follows:

i. To review and evaluate different configurations of regenerative braking systems applied in EV's and HEV's and the associated technology of energy storage systems.

ii. To generate a more accurate analytical method for obtaining brake torque from a given drive cycle. This involves studying vehicle dynamics during braking to understand braking characteristics.

iii. To develop mathematical models to simulate the main elements of mixed-mode braking systems viz. the motor / generator (M/G) and the solenoid valve. The models could be either 'simple' or 'advanced' depending the aim of the simulation.

iv. To determine the suitable size of the M/G when the vehicle operates under typical driving conditions such as the FTP, US06 and EUDC drive cycles.

v. To design a control system methodology that manages both friction and regenerative braking according to the brake demand from the driver.

vi. To simulate and investigate the performance of the control system, and to validate and verify predicted results from theoretical models with results from experimental work.

vii. To investigate brake blending in EV’s equipped with parallel braking systems through dynamometer and road tests.

viii. To analyse the integration of regenerative braking systems with ABS using both simulation and actual EV road test methods.

ix. To measure recuperation energy in EV’s and to develop battery discharge data experimentally.

The research methodology was determined after an extensive Literature Review (Chapter 2), and is summarized in the flowchart shown in Figure 1.2.This also explains how data were taken from a drive cycle and used in the simulations.

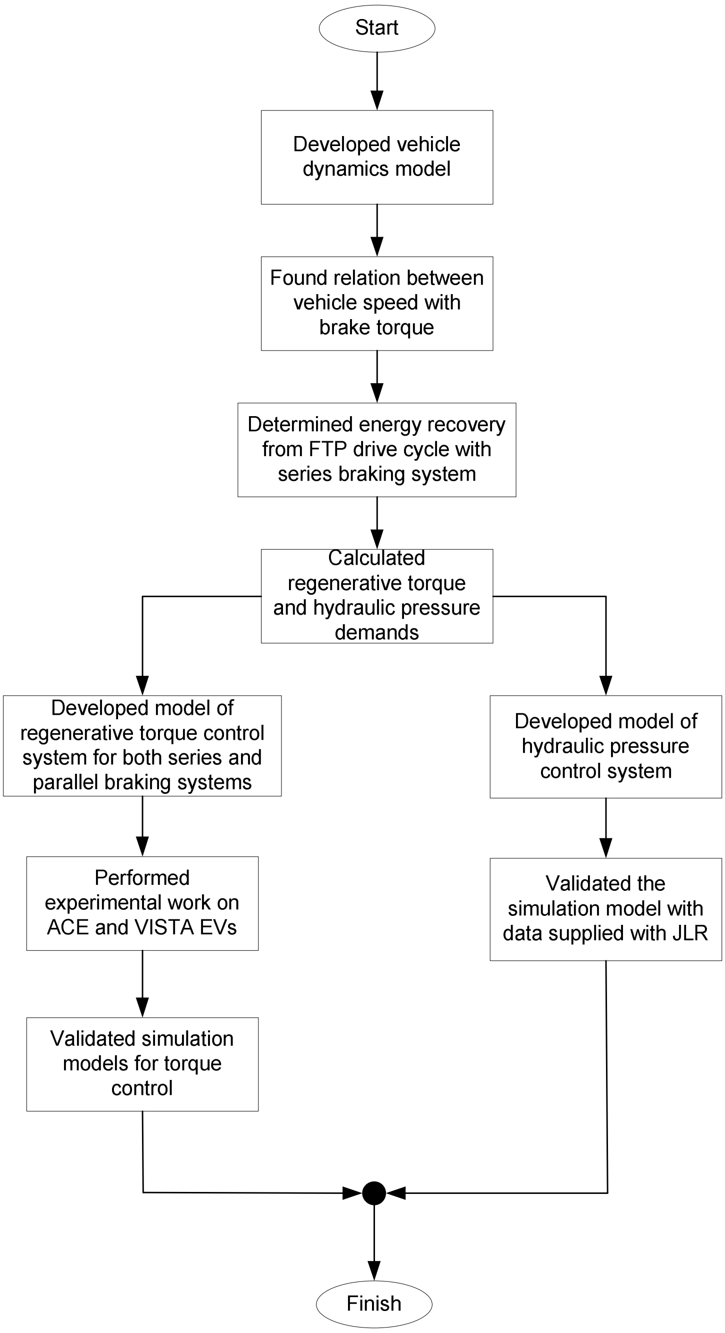
Start
Developed vehicle dynamics model
Found relation between vehicle speed with brake torque
Determined energy recovery from FTP drive cycle with series braking system
Calculated regenerative torque and hydraulic pressure demands
Developed model of regenerative torque control system for both series and parallel braking systems
Developed model of hydraulic pressure control system
Performed experimental work on ACE and VISTA EVs
Validated the simulation model with data supplied with JLR
Validated simulation models for torque control
Finish

Figure 1.2 Summary flowchart of research methodology

1.3 Thesis Structure

The thesis is organized into eight chapters. The first chapter presents a general background of mixed-mode braking systems in EV's and HEV's focussing on the structure of regenerative braking systems and their interaction with friction brake systems. Chapter 2 reviews published research about mixed-mode braking systems, electric (M/G’s, electrical energy storage, and the application of M/G’s to improve the performance of ABS and vehicle stability control (VSC/ESC). There many concepts and implementations that are possible for such braking systems and their selection would be based on complexity and cost. Selection of the M/G and the type and size of energy storage greatly affect the performance and cost of regenerative braking systems, so these are discussed in detailed. Chapter 3 introduces an analysis of a ‘standard’ type of road vehicle to understand its behaviour under braking conditions, the distribution of mixed-mode braking systems and the static characteristics of the M/G and energy storage. Dynamic models of regenerative and friction brakes are described in Chapter 4, where closed-loop control systems of motor torque and hydraulic pressure are proposed. In Chapter 3, hydraulic and electric systems to distribute brake demand were explained in basic terms while in Chapter 4 the detailed models of these systems were derived for the purpose of control system design. Both models i.e. simple and complex were simulated in the research.

Next, Chapter 5 is devoted to simulations using Matlab/Simulink. Many simulation models are presented based on formulations derived in previous chapters. These enable the complete analysis of mixed-mode braking systems, starting from tyre-road interaction and energy recuperation up to control system operation. Chapter 6 describes experimental work which was carried out to measure the currents and voltages of the DC motor and lead-acid batteries of a research vehicle, the TATA Ace EV. Energy recovery, battery discharge characteristics and M/G control operation can be quantified from this work. Additional experimental work is presented from a more advanced passenger car, the TATA Vista EV with a permanent magnet M/G and a Lithium-Ion battery. A general discussion is presented in Chapter 7, and Chapter 8 includes the summary, conclusions and recommendations for future work.

1.4 Research Findings

The research started by studying road vehicle drive cycles and vehicle dynamics. In the literature it was found that brake torque has normally been derived from vehicle deceleration and road loads in which longitudinal force is proportional to braking torque. In the research presented here wheel dynamics and tyre behaviour modelling have been considered together with some more advanced ways of obtaining the brake torque.

The calculation of regenerative braking ratio was presented by Peng et. al. (2008). The research in this thesis addresses the question of how two braking intervals with similar initial speeds and braking times would result in different braking regenerative ratios. This is important in system design because the regenerative braking ratio is affected by the profile of brake demand during braking.

Direct torque control has been widely adapted for permanent magnet brushless motors and induction motor drives as indicated by Khoucha et. al.

(2007) who used the ECE-15 drive cycle to test the control algorithm in an automotive (EV) powertrain context. The limitation is that friction brake and braking torque distribution have not been taken into account in published research, and it is this which represents the main part of the scientific advance presented here.

Most EV / HEV manufacturers use blended braking strategies where the regenerative braking system is disabled when the ABS operates. Several researchers have proposed using the M/G to improve ABS performance, e.g. for the purpose of simulation, Peng et al. (2008) used a simple model to investigate ABS operation in blended (mixed-mode) braking. The research presented in this thesis has developed advanced dynamic vehicle braking system models which include detailed models of motor torque and hydraulic brake pressure controls to study the integration of regenerative braking within the ABS operation.

CHAPTER 2

LITERATURE REVIEW

2.1 Introduction

In a conventional vehicle, the braking to achieve vehicle retardation is performed by friction brakes on each wheel. The vehicle’s kinetic energy is transformed into heat energy through the process of friction between the two surfaces in contact in the brake; the rotor and the stator. On the other hand, an electric Vehicle (EV) or a Hybrid Electric Vehicle (HEV) allows the kinetic energy to be converted into electrical energy using an electric M/G, and stored in a battery or an ultracapacitor (or a combination of the two), and this is known as regenerative braking. The amount of energy that can be recovered is determined by the electric M/G size and the capacity of the energy storage device(s).

This chapter presents a literature review relating to regenerative braking in EV’s and HEV’s. Firstly, the development of mixed-mode braking systems made by brake manufacturers and researchers is reviewed and the ways to obtain brake demand and to generate pressure in the brake caliper are discussed. Since brake blending should be invisible to the driver of an EV or HEV, brake pedal feel must be considered. Secondly, integrating a mixed-mode braking system with ABS and ESC is explained and the advantages and disadvantages of using regenerative braking during ABS and ESC operations are illustrated. The types of electric drives used in EV’s and HEV’s and the associated control systems which are available are indicated, and typical speed-torque characteristics of an electric motor/generator are discussed. Finally, modern batteries used in EV and HEV are discussed including appropriate electrochemical models and a comparison of the performance of battery and ultracapacitor energy storage devices is made. Since the state of charge of both the battery and the ultracapacitor are crucial, some methods to measure or to predict this are explained.

In all modern EV / HEV cars, the main components of electric regenerative braking systems are basically the same, comprising an electric traction system based on a motor/generator (M/G), a motor control unit (MCU), an inverter and a battery. The differences are just the power management, to or from the battery, and the control strategy. A brake system ECU determines the fraction of braking torque generated by the motor/generator and informs what rate of braking energy should be delivered to the battery. The MCU then accepts a torque reference from the ECU and switches the inverter accordingly. Therefore, communication links are needed to establish coordination between these subsystems, usually through the vehicle’s CAN bus. A conventional CAN bus can reach transfer rates up to 125 kb/s and a higher rate of 500 kb/s is possible with advanced CAN technology called Time Triggered CAN (Miller, 2004).

2.2 Implementation of Mixed-mode Braking Systems

Toyota pioneered the development of HEV's;its first hybrid was launched in 1997, and regenerative braking was one of the main features of the vehicle to achieve lower fuel consumption and reduced emissions (Sasaki, 1998). The Toyota Prius was firstly marketed in Japan in 1998, two years before the Honda Insight was launched in North America (Duoba et al., 2001).Braking was performed by maximising the M/G torque, and friction brakes were used to balance the driver's brake demand. To control the brake line pressure at the wheel, pressure control valves were used in which valve opening was modulated by controlling the solenoid current.

In subsequent research by Toyota, Nakamura et al. (2002) presented an Electronically Controlled Brake (ECB) system designed for a 4-wheel drive (4WD) HEV. The ECB system implemented mixed-mode braking with ABS, ESC and traction control using hydraulic pressure control. Brake blending in this series braking system is illustrated in Figure 2.1. From high speed, the driver's demand ramps up and then is constant until the vehicle comes to rest. Beyond the base speed of the M/G, the regenerative torque is reduced as speed increases to maintain power at or below the maximum limit. Thus the regenerative braking force is lower at higher speeds when a larger portion of the demand is covered by the friction brakes. As the speed reduces, the regenerative brake torque increases and reaches the maximum value at some interim speed depending on the design and construction of the M/G. At lower speeds, the regenerative forces decrease to zero and the friction brakes alone retard the vehicle.

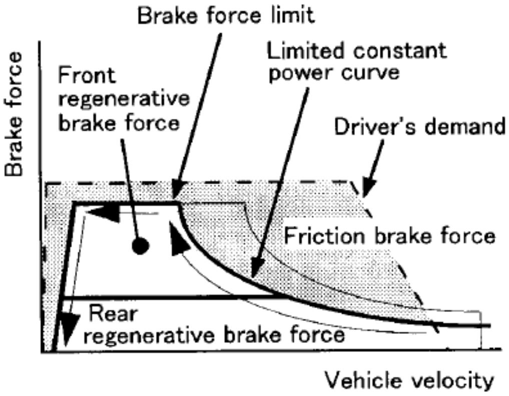

Figure 2.1 Brake blending in a 4WD hybrid car (Nakamura et al, 2002)

As there was no direct hydraulic link from the brake pedal to the brake caliper in the ECB, this system can also be referred to as “brake by wire” (Reuter et al., 2003). Figure 2.2 shows the complexity of the ECB compared to a conventional hydraulically actuated braking system. There are sensors in the pedal unit to measure the driver demand from which signals are sent to the Electronic Control Unit (ECU). These signals are converted into commands e.g. to open or close the related valve in the Hydraulic Control Unit (HCU). Hydraulic pressure is generated by a pump and stored in the accumulator. If the ECB fails, there is still a hydraulic link from the master cylinder to the caliper through a normally open valve and in this condition the basic hydraulically actuated friction braking system comes into play.

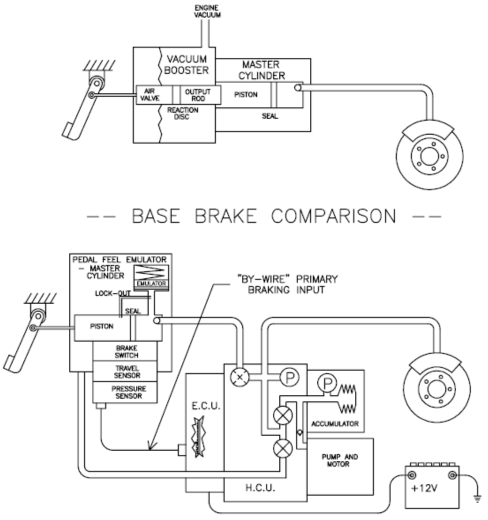
ENGINE VACUUM
VACUUM BOOSTER
MASTER CYLINDER
AIR VALVE
OUTPUT ROD
PISTON
REACTION DISC
SEAL
-- BASE BRAKE COMPARISON --
PEDAL FEEL EMULATOR - MASTER CYLINDER
EMULATOR
LOCK-OUT
SEAL
PISTON
"BY-WIRE" PRIMARY BRAKING INPUT
BRAKE SWITCH
TRAVEL SENSOR
PRESSURE SENSOR
E.C.U.
P
P
ACCUMULATOR
PUMP AND MOTOR
H.C.U.
+12V

Figure 2.2 Basic brake versus ECB (Reuter et al., 2003)

A similar approach was adopted by Honda with a different hardware implementation of a series braking system (Aoki et al, 2007).Toyota and Delphi used two valves at each wheel to increase, hold or decrease the wheel brake actuation pressure and a “stroke simulator” (separate unit) was used to provide force feedback to the driver through the brake pedal (Nakamura et al, 2002; Reuter et al., 2003). As an alternative approach Honda used a regulator valve to regulate the pressure from an accumulator to the master cylinder which then generated brake line pressure (Aoki et al, 2007). Four solenoid valves were used to modulate this line pressure as required by the brake control unit. Unlike the Toyota design, the stroke simulator, valve regulator and master cylinder were enclosed into one unit as shown in Figure 2.3.

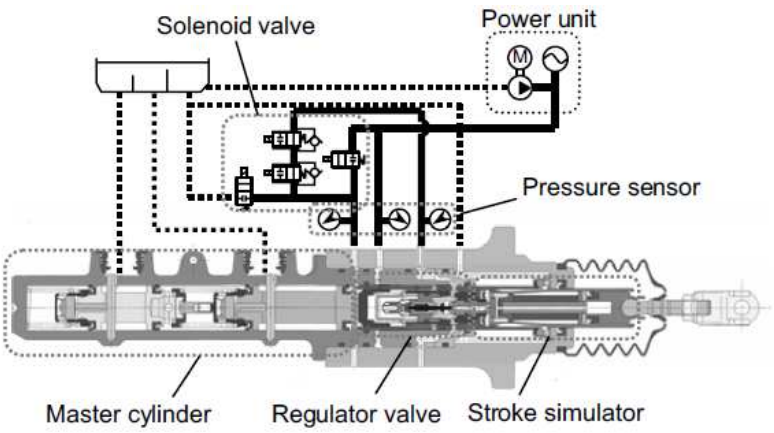

Figure 2.3 Structure of servo unit in the Honda design (Aoki et al., 2007)

A newly developed hydraulic braking system from Continental suggests a different approach to the implementation of brake blending (Albrichsfeld and Karner, 2009). Rather than using solenoid valves to modulate line pressure, a brake booster as in a conventional car brake system is used. The so-called “active booster” is connected to a membrane vacuum pump driven by an electric motor. The controlled booster exerts a force on the master cylinder piston which in turn generates pressure in the wheel cylinders. Figure 2.4 shows the simulator brake actuation similar to a conventional brake servo system, except that more components have been added such as sensors, simulator cut-off and pedal feel simulator. When the booster knee point is reached, the hydraulic pump in the ESC unit is engaged to increase the brake hydraulic pressure.

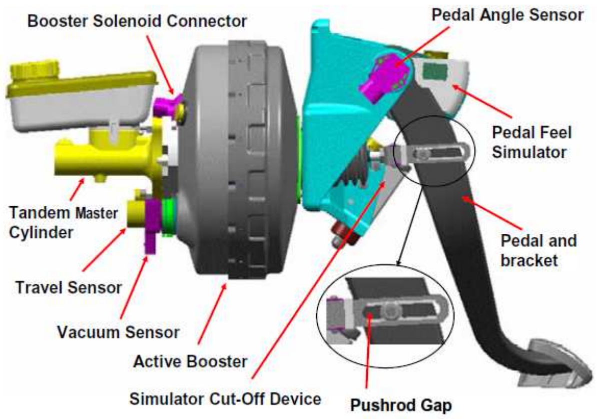
Booster Solenoid Connector
Pedal Angle Sensor
Pedal Feel Simulator
Tandem Master Cylinder
Pedal and bracket
Travel Sensor
Vacuum Sensor
Active Booster
Simulator Cut-Off Device
Pushrod Gap

Figure 2.4 Simulator brake actuation (Albrichsfeld and Karner, 2009)

Ohtani et al. (2011) claimed that brake by wire systems in the market were expensive and less efficient. An electrically-assisted actuation called e-ACT was developed and implemented in the Nissan Leaf car. To generate pressure in the master cylinder, the vacuum booster was replaced by an electric motor. A stroke sensor in the brake pedal measured the driver’s demand (i.e. the force applied by the driver to the brake pedal) and transmitted it to the ECU to distribute into regenerative and friction portions. The motor then actuated a ball screw which acted on the primary piston of the master cylinder as shown in Figure 2.5. In this design, the stroke simulator was replaced by a pedal-force compensator consisting of two springs which eliminated pedal force changes in mixed-mode braking.

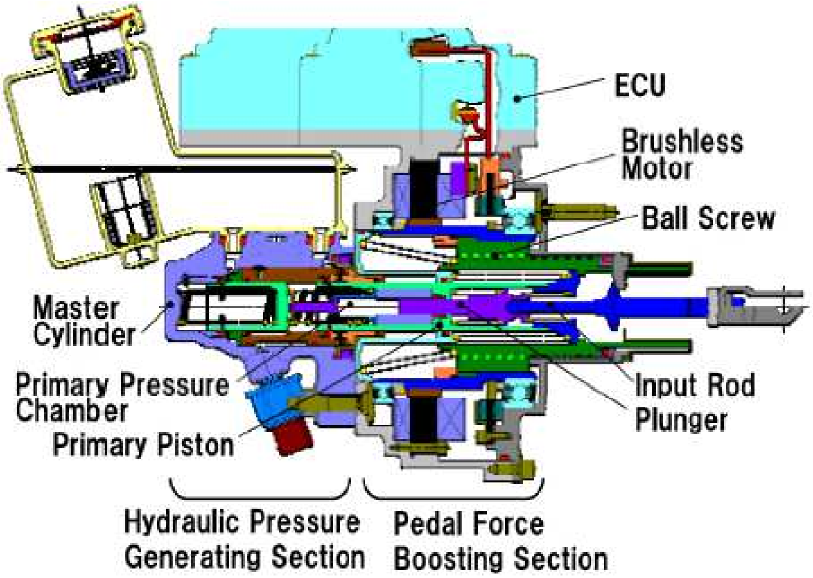
ECU
Brushless Motor
Ball Screw
Master Cylinder
Primary Pressure Chamber
Primary Piston
Input Rod
Plunger
Hydraulic Pressure Generating Section
Pedal Force Boosting Section

Figure 2.5 Cross-section of the e-ACT braking system (Ohtani et al., 2011)

2.3 Pressure Control of Series Braking Systems

The review of published information shows that all mixed-mode series braking systems share the same goal, i.e. to control hydraulic pressure to the friction brakes, for which the brake manufacturers have employed solenoid valves, active boosters and electric motors. In the valves, hydraulic pressure is sensed and the related valve position is adjusted accordingly. For two other actuators, it was established that position sensors were used to measure the membrane position of the booster and the rotor position of the electric motor. Two control methods were found in the literature for modulating the pressure with a solenoid valve viz. sliding mode control (Aoki et al., 2007) and threshold pressure control (Park et al., 2009).The pressure modulation with the position control method was not found in the literature, so only these two control methods are reviewed here.

The robust and effective characteristics of sliding mode control make it suitable for nonlinear systems such as an automotive hydraulic brake actuation system (Aoki et al., 2007). The state variables are the difference between target and control pressures at current and previous time steps. The error is the difference between the target pressure and the control pressure of the master cylinder at time step *n*. The state variables were the error at time step *n* and the error at time step *n-1*. The state variables were kept in the switching line and shifted to the origin by calculating three terms of the control input and applying the result to the solenoid valve that was represented by the discrete-time first-order lag model. At the end, the state variables reached the origin indicating no difference between the target and control pressures. The performance of this control system in mixed- mode braking to decelerate the vehicle from 55 km/h is shown in Figure 2.6. The regulator pressure represents the driver’s demand which is about 12bar during braking. As can be seen, the control pressure generally closely follows the target pressure.

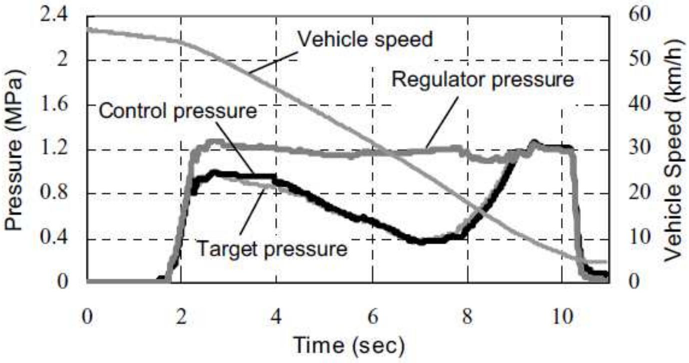

Figure 2.6 Pressures and vehicle speed on mixed-mode braking

(Aoki et al., 2007)

Park et al. (2009) developed threshold pressure control and started with an investigation of valve characteristics. A normally open valve was located between the master cylinder and caliper and a normally closed valve was installed between the caliper and the fluid reservoir. The solenoid current to open or close these valves as a function of pressure difference required were determined and showed a linear relationship. The wheel pressure control error was defined as the difference between desired and measured pressures. The control criterion was to apply the pressure when the error was greater than the upper threshold, to dump the pressure when the error was less than the lower threshold and to hold the pressure when the error was within these boundaries. Results from the Hardware in Loop Simulation (HiLS) indicated that the target pressure in general was followed as shown in Figure 2.7 but more pressure fluctuation was present compared with the result shown in Figure 2.6.

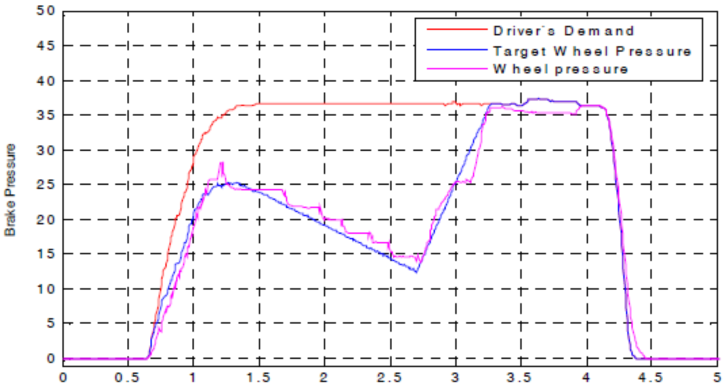

Figure 2.7 Feasibility Test at HiLS (Park et al., 2009)

Mixed-mode braking in EV’s and HEV’s can reduce road vehicle energy consumption and consequent engine emissions, but at the same time the driver’s comfort in brake operation must be satisfied. As mentioned in section 2.2, referring to Figures 2.3, 2.4 and 2.5, a stroke simulator or pedal feel emulator must always be present in any brake-by-wire system to generate the appropriate pedal reaction force and stroke. Components of the stroke simulator include spring coils and rubber to give a natural feel to the driver in operation (Nakamura et el., 2002; Aoki et al., 2007). The relationship between brake pedal force and stroke is usually used to judge the brake pedal feel as shown in Figures 2.8, 2.9 and 2.10 for different manufacturers. It is clear from these graphs that the pedal feel is different from one vehicle to another.

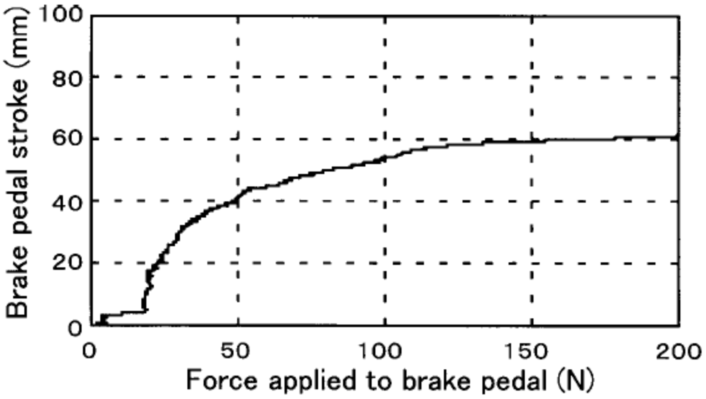

Figure 2.8 Characteristic of Toyota’s stroke simulator (Nakamura et el., 2002)

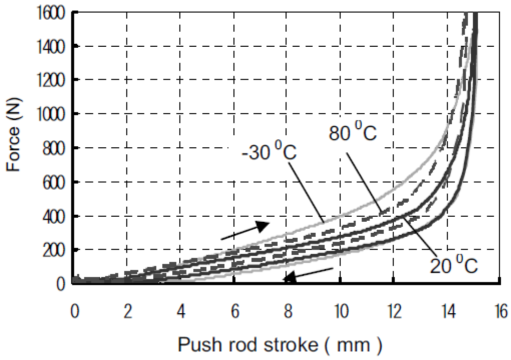

Figure 2.9 Characteristic of Honda’s stroke simulator (Aoki et al., 2007)

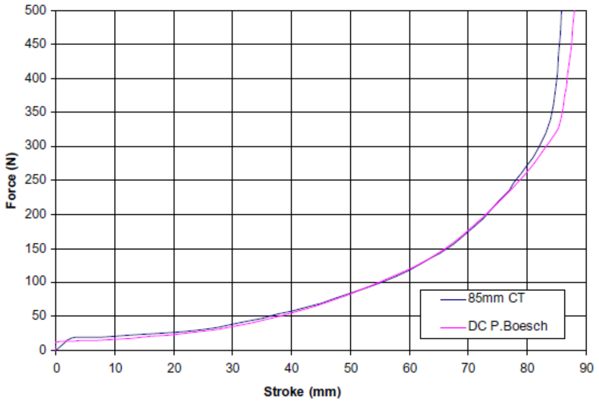

Figure 2.10 Characteristic of Continental’s stroke simulator

(Albrichsfeld and Karner, 2009)

2.4 Design Models of Mixed-Mode Braking Systems

Progress has also been made in the simulation of mixed-mode braking systems. Panagiotidis et al. (2000) developed a Matlab/Simulink model to distribute brake demand into regenerative and friction portions assuming the wheel-lock force is known. Four possible braking states were defined as:

- Electric and hydraulic,
- Only electric,
- Electric and hydraulic limited, and
- Electric limited.

Electric and hydraulic limited and electric limited states mean that the braking force is limited to wheel-lock force though the brake demand may be higher.

The distribution of brake demand into the regenerative and the friction portion for those states is illustrated in Figure 2.11. In each state, the bars from left to right represent generator brake force, demanded force (brake pedal effort), lock-up force and friction brake force. As can be seen, the force demands are less than the lock-up forces in states 1 and 2, and are higher than the lock-up forces in state 3 and state 4. Furthermore, the M/G can provide all the brake force demands in states 2 and 4. Based on simulations using ADVISOR, it was found that a fuel economy improvement of 19% could be achieved on a vehicle combining a 67 kW diesel engine with an 83 kW electrical machine and a 30.8 kWh battery (Panagiotidis et al., 2000).

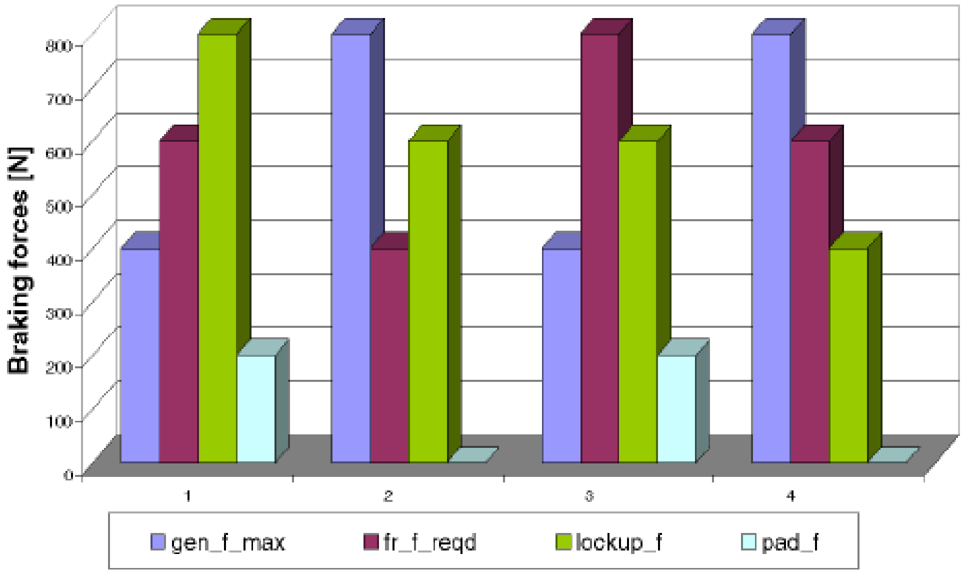

Figure 2.11 Braking force requirements and maximum system outputs (Panagiotidis et al., 2000)

The above brake states approach was improved by Yeo and Kim (2002); the available motor/generator torque was limited by two factors:

- Battery SoC, and
- Vehicle velocity.

In this case, the M/G was not engaged if the battery state of charge was higher than 90% or the vehicle speed was less than 15 km/h. In their research, some components were modelled in the Simulink environment as shown inside the dotted line in Figure 2.12. The hardware part consisted of an hydraulic braking system as shown in the lower part of Figure 2.12, (Hardware in Loop Simulation, the combination of software simulation and hardware parts, is called HiLS). It was found that the desired speed could be followed by the driver while combining regenerative braking with the front friction brakes.

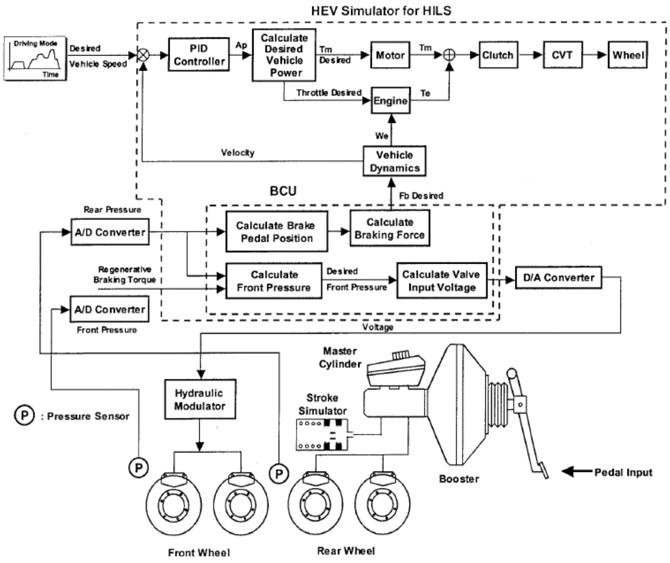
HEV Simulator for HILS
Driving Mode
Time
Desired
Vehicle Speed
PID Controller
Ap
Calculate Desired Vehicle Power
Tm Desired
Motor
Tm
Clutch
CVT
Wheel
Throttle Desired
Engine
Te
We
Velocity
Vehicle Dynamics
BCU
Fb Desired
Rear Pressure
A/D Converter
Calculate Brake Pedal Position
Calculate Braking Force
Regenerative Braking Torque
Calculate Front Pressure
Desired Front Pressure
Calculate Valve Input Voltage
D/A Converter
A/D Converter
Front Pressure
Voltage
Master Cylinder
Hydraulic Modulator
Stroke Simulator
P : Pressure Sensor
P
P
Booster
Pedal Input
Front Wheel
Rear Wheel

Figure 2.12 Block diagram of HiLS (Yeo and Kim, 2002)

Yeo et al. (2006) replaced the HiLS with a bench tester including an engine (ICE), M/G, Continuously Variable Transmission (CVT), clutch, flywheel, regenerative braking module and control system module as shown in Figure 2.13. Both the ICE and the M/G were connected to the flywheel through the CVT which maintained the engine in the optimum operating region regardless of vehicle speed. Therefore, the CVT speed ratio was another parameter that varied the regenerative torque transmitted to the wheel. It was found that the operating region of the motor was closer to the optimum operating line when the CVT regenerative control was utilized than with conventional CVT control. As a result, higher battery state of charge (SoC) was observed during the experiment, and both regenerative and friction brakes successfully combined to decelerate the vehicle from 50 km/h to zero in 15s.

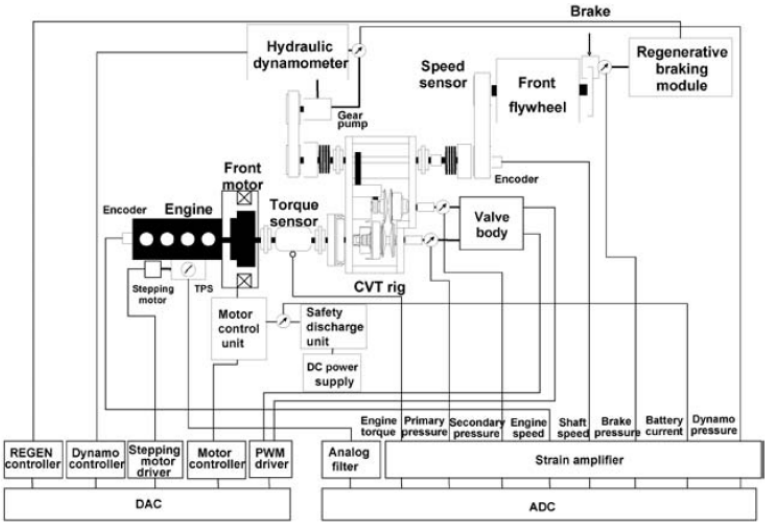
Brake
Hydraulic dynamometer
Speed sensor
Front flywheel
Regenerative braking module
Gear pump
Front motor
Encoder
Encoder
Engine
Torque sensor
Valve body
CVT rig
Stepping motor
TPS
Motor control unit
Safety discharge unit
DC power supply
Engine torque
Primary pressure
Secondary pressure
Engine speed
Shaft speed
Brake pressure
Battery current
Dynamo pressure
REGEN controller
Dynamo controller
Stepping motor driver
Motor controller
PWM driver
Analog filter
Strain amplifier
DAC
ADC

Figure 2.13 Schematic diagram of the HEV bench tester (Yeo et al., 2006)

The work of Panagiotidis et al. was improved by Wang and Zhuo (2008) with a simulation model of an HEV equipped with a CVT, and ultracapacitors as the energy storage system. A regenerative torque optimisation was proposed to maximise regenerative power delivered to the ultracapacitors. The output from the optimisation algorithm was a three-dimensional look-up table relating regenerative power demand, vehicle speed and ultracapacitor voltage to optimum motor torque and desired CVT ratio. From the simulation, it was found that the ultracapacitor voltage improved by 8.2% with torque optimisation because of operating the motor/generator in a more efficient region during braking. Also, brake pressure was modulated to meet the driver demand as the vehicle decelerated from 80km/h to zero speed in 14.8s.

An Electromechanical Brake (EMB) system was proposed to replace the hydraulic system in a hybrid vehicle, with electronic control to each wheel independently (Ahn et al., 2009). The EMB module consisted of electric calipers and electro-mechanical disc brakes. During braking, the vehicle controller distributed braking torque into regenerative torque and EMB torque based on information from many inputs such as driver demand, vehicle velocity, battery SoC, and motor characteristics as illustrated in Figure 2.14. To produce an inexpensive EMB system, clamping force and braking torque were estimated using voltage, current and position of the brushless DC motor, measured by sensors and the applied Proportional Integral Differential (PID) controller. The model was tested by Matlab/Simulink simulation and revealed that the vehicle speed closely followed the Federal Urban Driving Schedule (FUDS) mode and the battery SoC was preserved.

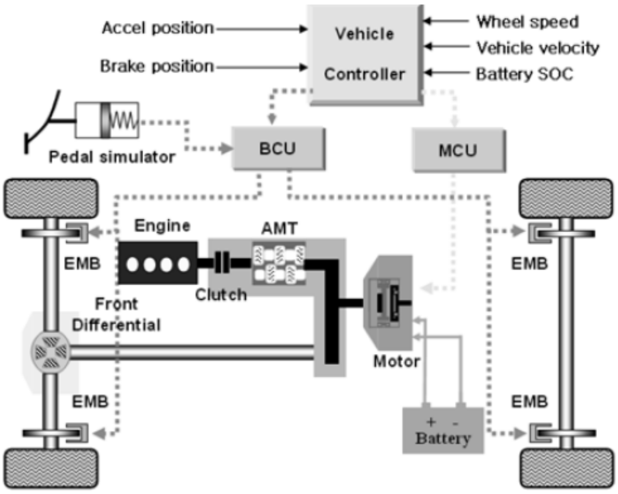
Accel position
Brake position
Vehicle Controller
Wheel speed
Vehicle velocity
Battery SOC
Pedal simulator
BCU
MCU
Engine
AMT
EMB
Clutch
Front Differential
Motor
EMB
EMB
EMB
+ -
Battery

Figure 2.14 EMB system in a parallel hybrid vehicle (Ahn et al., 2009)

The regenerative braking system proposed for electric vehicle applications by Ye et al. (2008) had a different approach; a simple parallel braking system. In this design, master cylinder pressure was supplied directly to each wheel cylinder without any modulation. A brake pedal sensor converted the pedal position into the torque demand on the M/G as shown in Figure 2.15. The electronic controller combined optimal and robust control techniques to address the non-linear characteristics and any unknown environmental parameters. It was claimed through published research in the form of simulation and experiment that the robust hybrid controller in a Direct Current (DC) drive was robust and gave more recovered braking energy compared with a proportional-integral DC drive. A test was conducted on an urban road where the initial terminal voltage was 127V and the test was stopped when the battery voltage dropped to 108V. It was found that driving ranges were 105km and 135km without and with the regenerative braking system respectively.

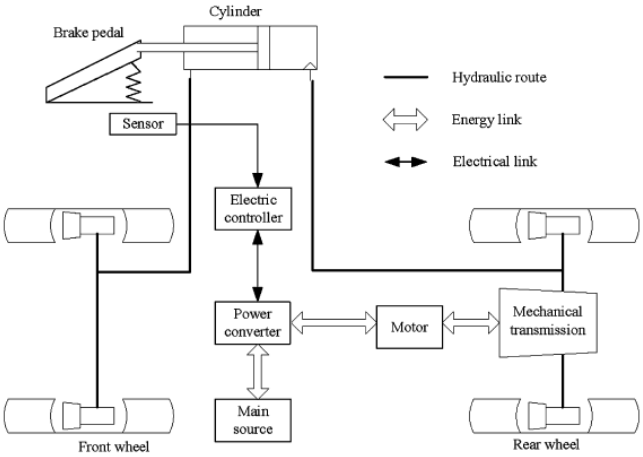
Cylinder
Brake pedal
Sensor
Hydraulic route
Energy link
Electrical link
Electric controller
Power converter
Motor
Mechanical transmission
Main source
Front wheel
Rear wheel

Figure 2.15 The configuration of the braking system (Ye et al., 2008)

2.5 Integration of a Mixed-mode Braking System with ABS and ESC

To improve driving safety, ABS has been applied to road vehicles since the late 1970's (Song et al, 2007). In ABS, the hydraulic brake line pressure is modulated to prevent wheel lock where the driver could lose control of the vehicle. Vehicle Stability Control (VSC, also known as ESC) was first implemented by Mercedes-Benz on a road vehicle in 1995 (Durisek and Granat, 2008), where the brake was engaged at the selected wheel to prevent lateral instability during a steering manoeuvre. Toyota combined all regenerative braking, ABS, and ESC into one brake ECU as shown in Figure 2.16. Beside communication with the hybrid ECU, the brake ECU accepted signals from numerous sensors including wheel speed, acceleration, yaw rate and steering angle. In the designed 4WD hybrid car, the traction and braking torque from the M/G on the front and rear axles was used to improve vehicle stability (Nakamura et al, 2002). An alternative approach which is now more commonly employed was proposed by Albrichsfeld and Karner (2009), to disable regenerative braking when ABS or ESC is active.

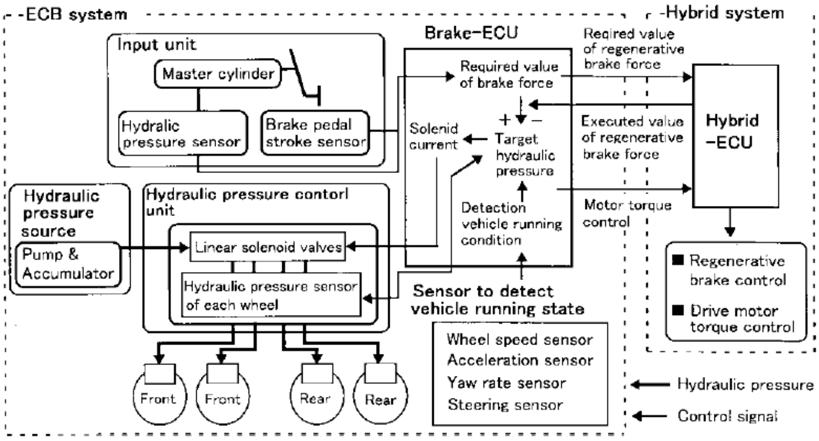
ECB system
Hybrid system
Input unit
Master cylinder
Hydralic pressure sensor
Brake pedal stroke sensor
Brake-ECU
Required value of brake force
Solenid current
Target hydraulic pressure
Detection vehicle running condition
Reqired value of regenerative brake force
Executed value of regenerative brake force
Motor torque control
Hybrid -ECU
■ Regenerative brake control
■ Drive motor torque control
Hydraulic pressure source
Pump & Accumulator
Hydraulic pressure contorl unit
Linear solenoid valves
Hydraulic pressure sensor of each wheel
Sensor to detect vehicle running state
Wheel speed sensor
Acceleration sensor
Yaw rate sensor
Steering sensor
Front
Front
Rear
Rear
Hydraulic pressure
Control signal

Figure 2.16 ECB control composition (Nakamura et al., 2002)

In the Nissan Leaf EV, regeneration and friction braking combination is achieved by an ECU located in the e-ACT unit. The Vehicle Dynamic Control (VDC) unit is a separate unit as shown in Figure 2.17. The brake lines from the master cylinder in the e-ACT were directly connected to the input ports of the VDC unit and from this, separate brake lines were provided to each wheel. Series communication was established between the e-ACT and the VDC to integrate both systems for the purposes of redundancy and fail-safe (Ohtani et al., 2011).

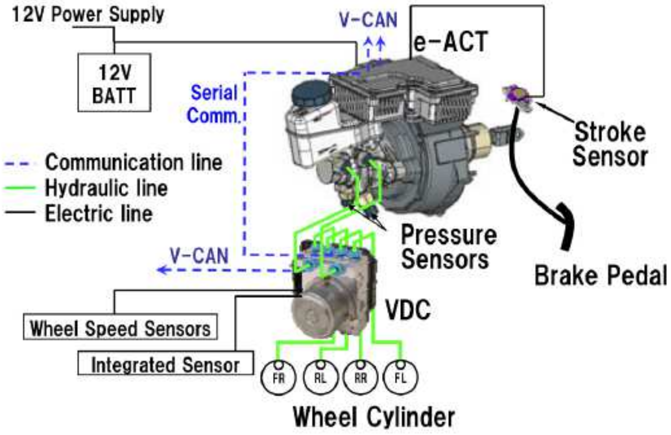
12V Power Supply
12V BATT
V-CAN
e-ACT
Serial Comm.
Stroke Sensor
Communication line
Hydraulic line
Electric line
Pressure Sensors
Brake Pedal
V-CAN
VDC
Wheel Speed Sensors
Integrated Sensor
FR
RL
RR
FL
Wheel Cylinder

Figure 2.17 Integration of e-ACT with VDC in the Nissan Leaf EV

(Ohtani et al., 2011)

A simulation model to investigate the effect of regenerative braking in vehicle stability was developed by Kim et al. (2006) for a hybrid electric vehicle which had electric M/G's on the front and rear axles. Braking forces to stabilize the vehicle came from the rear M/G and the EHB system operated on both the front and rear wheels. Fuzzy logic control was used to calculate the direct yaw moment i.e. the sum of moments generated by longitudinal forces at the centre of gravity. In the simulations, the driver manoeuvres to follow the trajectory shown in Figure 2.18 when the vehicle speed was 80 km/h. It can be seen that a combination of regenerative braking with the Electro-hydraulic braking enabled the vehicle to keep to the required path.

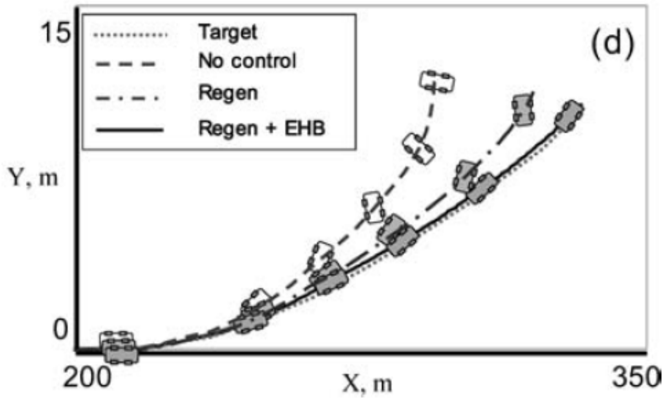

Figure 2.18 The effect of regenerative braking on vehicle stability

(Kim et al., 2006)

Peng et al. (2008) investigated the use of regenerative braking combined with ABS on a road with a low adhesion coefficient. Hydraulic pressure was modulated using logic threshold control to allow increasing, decreasing or holding wheel pressure. When the wheel reached a second slip ratio threshold, regenerative braking was activated. To determine the amount of regenerative torque, a fuzzy logic controller was developed which had two inputs viz. the difference between target and real slip ratios, and battery SoC, as shown in Figure 2.19. In the simulation, the vehicle was decelerated to rest from 90km/h in 9.5s. It was found that the regenerative braking contributed to maintain a slip ratio around 12%, and 9% of the braking energy was stored in the battery. This result was then validated against road test under the same braking conditions. Though the time response of slip ratio, regenerative current, and torque were different, the stored energy was close to the simulation result, within 9%.

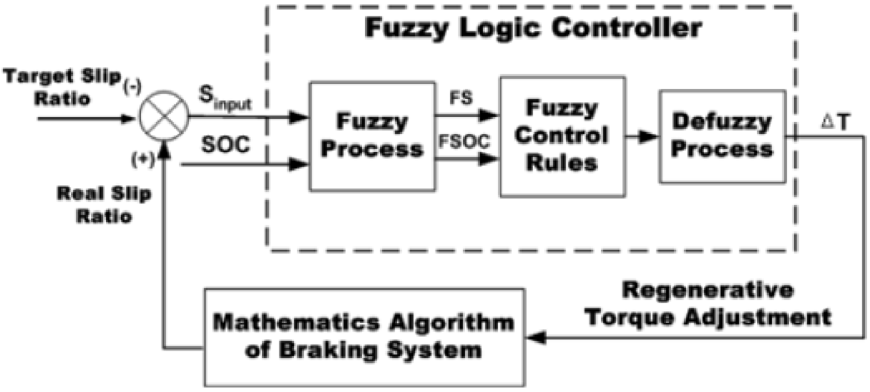
Fuzzy Logic Controller
Target Slip Ratio
(-)
(+)
Real Slip Ratio
S_{input}
SOC
Fuzzy Process
FS
FSOC
Fuzzy Control Rules
Defuzzy Process
ΔT
Regenerative Torque Adjustment
Mathematics Algorithm of Braking System

Figure 2.19 Fuzzy logic controller for the regenerative braking system

(Peng et al., 2008)

2.6 Electric Drive Application

Electric drive plays an important role during the traction and braking of EV's and HEV's. In the discussion in section 2.6 of regenerative braking, it is usually an M/G which functions to provide brake torque and at same time to convert kinetic energy into electric energy. The speed-torque characteristic of an M/G is considered to perform brake blending in a series braking system. Since there are many types of M/G that have been proposed for EV and HEV applications, a comparison of their performance in terms of torque density, efficiency and control system complexity is important.

Electric drive comprises four main components: electric motor, sensor, controller, and power processing unit. The controller accepts a command signal and a feedback signal from the sensors and turns electronic switches in the power processing unit on or off to allow the current to flow to or from the M/G. The electric drive is classified according to the type of M/G used, for example, series DC drive, induction drive or Permanent Magnet (PM) brushless drive. These drives have been used in EV’s and HEV’s as listed in Table 2.1. Among these drives, the Permanent Magnet Brushless (PMBL) drive is most popular and has been adopted in many production cars e.g. Toyota Prius, Honda Insight and Nissan Leaf (Aoki et al., 2000; Sato et al., 2011).

EV/HEV	Electric drive
Fiat Panda Elettra	Series DC drive
Mazda Bongo	Shunt DC drive
Conceptor G-Van	Separately excited DC drive
Suzuki Senior Tricycle	PM DC drive
GM EV1	Induction drive
Toyota Prius	PMBL drive
Chloride Lucas	Switched-reluctance (SR) drive

Table 2.1 Applications of electric drive to EV’s and HEV’s (Chau et al., 2008)

The requirements of electric drive for EV and HEV applications include high torque and power densities, wide speed range, high efficiency, transient overload capability, high reliability and affordable cost (Zhu and Howe, 2007). Table 2.2 compares the torque density of three types of brushless motors. A higher torque / volume (T/V) value means higher torque is generated for the same volume of motor and higher torque / mass (T/mass) value indicates less copper wire is needed to generate the same torque. The PMBL M/G type can be seen to be superior in terms of torque density, power density and efficiency. The Induction M/G type is a better choice if the requirements of lower material and manufacturing costs, and higher durability are considered (Dorrel et al., 2010). The main benefits of the Switched Reluctance (SR) type of M/G are high speed operation, low cost, rugged construction and high fault-tolerance (Rahman and Schulz, 2002).

Type	T/$V_{envelope}$ (Nm/m3)	T/Cu mass (Nm/kg)
PMBL motor	28860	28.7 - 48
Induction motor	4170	6.6
SR motor	6780	6.1

Table 2.2 Torque density of electrical motors (Ehsani et al., 2003)

The principles of torque generation are different for these M/G's. In a 3 phase induction motor, symmetrical currents with ω_s frequency in the stator windings produce a resultant stator Magnetic Motive Force (MMF) which rotates at ω_s frequency. This rotating MMF induces voltage in the rotor conductor, and rotor current is generated. The torque is generated from the interaction between the stator MMF and the rotor current. The torque vanishes when the stator MMF speed is equal to the rotor speed. In the SR M/G, torque is generated as a result of minimising the reluctance of the stator flux path. To achieve this, both the stator and the rotor have silent poles, and stator currents are electronically switched. As the name implies, the permanent magnets are positioned in the rotor of a PMBL M/G. The stator currents are electronically commutated to change their direction. To enable torque generation, the directions of rotor flux density and stator current must be different. Figure 2.2 shows the different topologies of the induction M/G, switched reluctance M/G and PM brushless M/G. It is can be seen that stator structures of the induction and PMBL M/G's are similar; both have distributed windings. The configuration of the SR motor is called 8/6 indicating the number of poles in the stator and the rotor respectively.

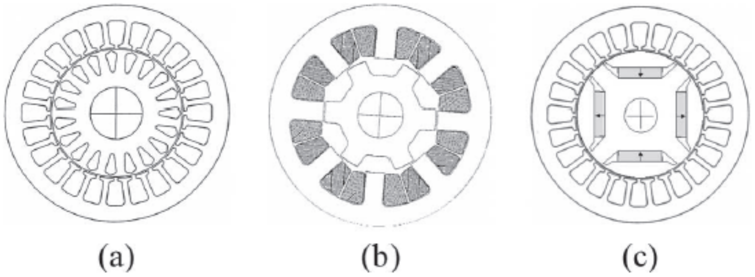

Figure 2.20 (a) Induction M/G (b) SR M/G (c) PMBL M/G

(Zhu and Howe, 2007)

Software called SPEED was used to make further comparisons between these M/G's. Using that software, Dorrell et al. (2010) developed a model PMBL M/G of the 2004 Toyota Prius and designed induction and switched-reluctance M/Gs that met the Prius specifications. Three important characteristics of the M/G's were considered *viz*. torque over a wide speed range, efficiency and thermal stability. The simulation results are summarised in Table 2.3 for two operating points of 1,500rev/min (base speed) and 6,000rev/min (maximum speed) together with total weight and approximate material cost. Based on this data, it was suggested that the induction motor and the SR M/G's were also feasible solutions for HEV applications.

Motor	**Speed = 1,500 rev/min**			**Speed = 6,000 rev/min**			**Weight (kg)**	**Material Cost (US$)**
	Torque (Nm)	Current (A)	Eff (%)	Torque (Nm)	Current (A)	Eff (%)		
PMBL	303	141.1	91.3	45.6	31.8	96.1	31.16	242.17
Induction	297	168.8	83.1	50.8	47.1	95.2	26.71	143.8
SR	294	300	85.2	52.1	60	88.2	36.25	74.16

Table 2.3 Comparison of electric M/G's of HEV (Dorrell et al., 2010)

The M/G operates in either the constant torque region at low speed or in the constant power region at high speed. Transition from one region to another occurs at a base speed as shown in Figure 2.21, and the power is gradually reduced at critical speed. An electric drive efficiency map is usually superimposed on the speed-torque curve of the M/G as shown in Figure 2.22 for the Nissan Leaf EV. The M/G specifications of the Leaf EV can be obtained from this figure; maximum torque is 280Nm and maximum power is 80kW. The base and maximum speeds are 2,728rev/min and 10,390rev/min respectively. This maximum motor speed corresponded to a maximum vehicle speed of 145km/h. Also shown in Figure 2.22 is that a higher efficiency of 95% was achieved when the M/G operated in the constant power region. The lowest efficiency was 85% which occurred at low speed or low torque operation. The key technologies to improve this efficiency were magnetic circuit design, materials and manufacturing processes (Sato et al., 2011).

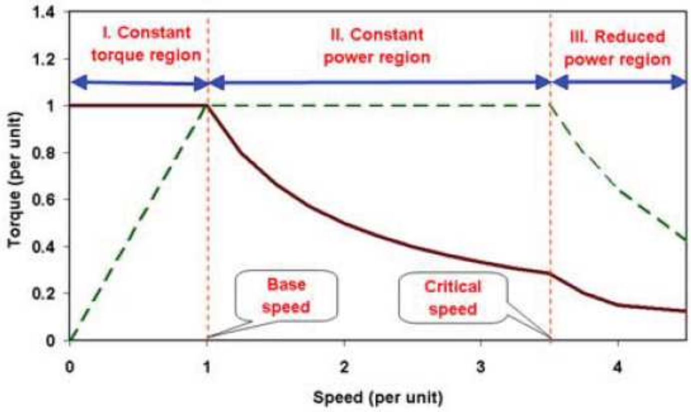

Figure 2.21 Torque and power as functions of motor speed

(Zhu and Howe, 2007)

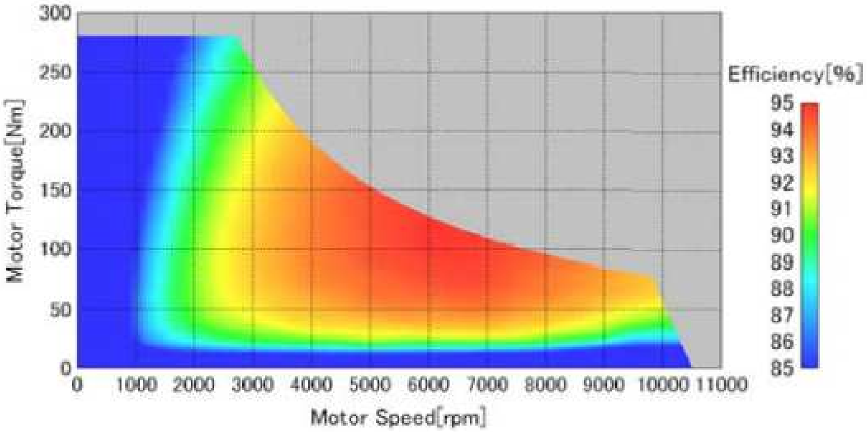

Figure 2.22 Efficiency of Leaf EV electric drive (Sato et al., 2011)

In comparison, the Electrodynamic System Company manufactures a PMBL motor (MΦ120) in which power and torque ratings are 77kW and 170Nm. Though these ratings are lower, its base speed of 4,300rev/min was higher than that of the Nissan Leaf M/G. The advantage was that accelerating torque was available for a wider speed range. The efficiency at nominal operation was 93%, but the efficiency map was not available. An interesting feature is that the mass is low at 28kg, compared with the Nissan Leaf M/G mass of about 58kg.

Control techniques applied in PMBL drives include efficiency optimizing, direct torque, artificial intelligence and position-sensorless controls. All these controllers calculate outputs to adjust the firing angle of a PWM-based inverter and the phase currents are shaped accordingly. The advantages of DTC are fast torque response, no current controller and fewer parameters involved (Chau et al., 2008).

The permanent magnet positioned inside the rotor of a PMBL M/G as shown in Figure 2.20 causes the reluctance torque to be more significant.

The DTC solves the problem faced by the rotor flux oriented torque control in that motor and makes it more attractive for EV and HEV applications (Meyer et al, 2007). The DTC works on the principle that the electromagnetic torque can be controlled by changing the load angle for a constant stator flux linkage (Vyncke et al., 2006). The load angle is the angle between the stator flux linkage vector and the permanent magnet flux linkage vector. Reference values of the torque and the stator flux linkage are compared with measurement values that are estimated from stator voltages and currents and rotor position as shown in Figure 2.23. From the errors of torque and flux, and the angle of flux, an entry in the switching table is selected to switch the inverter. Experimental results proved that the torque reference of 150Nm was followed in less than 2 milliseconds and flux weakening at high speed was achieved, but torque ripple was present.

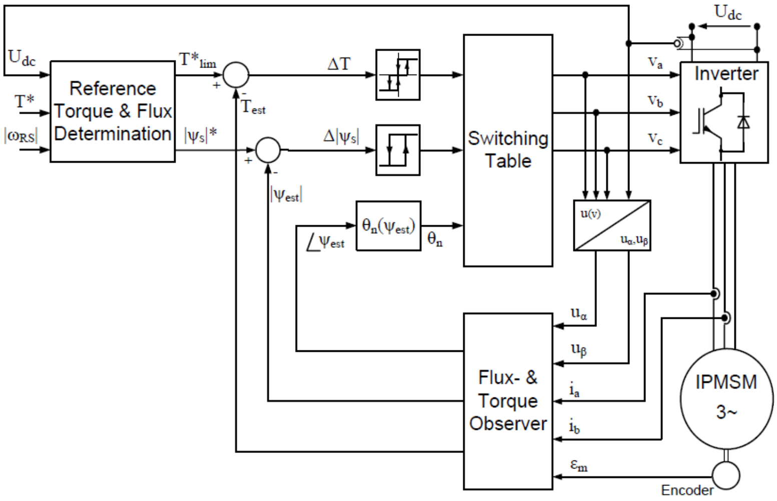
U_{dc}
T^*
$|\omega_{RS}|$
Reference Torque & Flux Determination
T^*_{lim}
T_{est}
ΔT
$|\psi_s|^*$
$\Delta|\psi_s|$
$|\psi_{est}|$
$\angle\psi_{est}$
$\theta_n(\psi_{est})$
θ_n
Switching Table
U_{dc}
V_a
V_b
V_c
Inverter
u(v)
u_α, u_β
u_α
u_β
i_a
i_b
ε_m
Flux- & Torque Observer
IPMSM 3~
Encoder

Figure 2.23 Implementation of DTC into PMBL drive (Meyer et al, 2007)

To reduce the torque ripple, maintain fast response, and improve robustness against load variations, measurement error and parameter uncertainty, a Direct Torque Control (DTC) technique with Space Vector Modulation (SVM) was proposed by Fu et al. (2009); SVM replaced the switching table in classic DTC. A sliding mode controller was developed which used the errors of torque and flux to calculate the magnitude of the voltage vector needed by the SVC to switch the inverter. As shown in Figure 2.24, the DTC-SVM significantly reduced the torque ripple.

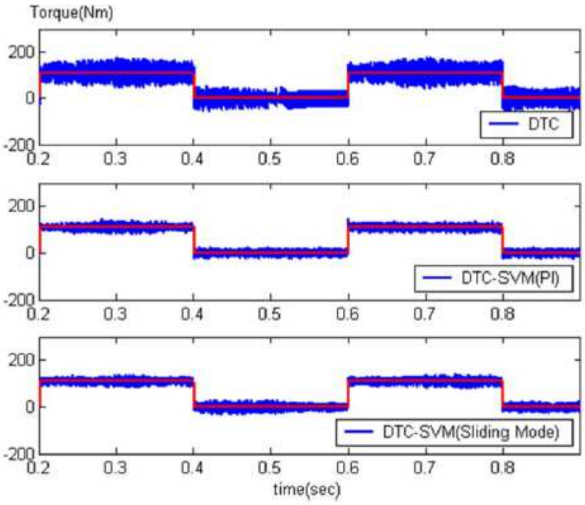

Figure 2.24 Torque dynamic responses of PMBL drive with DTCs

(Fu et al., 2009)

Buja and Kazmierkowski (2004) classified variable frequency control of an induction M/G as scalar control or vector control. The DTC, field oriented, feedback linearization, and passive based controls fall into the category of vector control. It was concluded that DTC did not need an accurate estimation of the motor flux as required by field oriented control. The DTC method was then divided into ‘switching table DTC’, DSC, and

SVM-DTC. The ‘switching table DTC’ was preferred for very fast torque-controlled drives due to its simplicity but torque ripple was found to be present. The benefits of SVM-DTC included reduced torque and flux pulsations, reliable start up and low-speed operation, well-defined harmonic spectrum, and radiated noise. DSC was considered to be suitable for high-power low-switching-frequency drives and was very effective in the square-wave operation region.

Sliding Mode Control (SMC) was included to add robustness in the SVM-DTC of an induction drive for HEV applications (Fu and Xie, 2006). In this case, the flux and torque observer, and hysteresis controllers in Figure 2.23 were replaced by a sliding mode observer and controller. A Simulink model was developed to observe the torque response to different reference signals viz. step, sinusoidal and piecewise wave and white-noise external load. It was found that the reference signals were closely followed and the proposed control system was insensitive to disturbance.

For EV applications with an induction drive, Khoucha et al. (2007) designed and implemented a sensorless DTC technique in which rotor flux and motor speed were adaptively estimated using measured currents and voltages. A hysteresis controller and a switching table were used to switch the inverter. A complete EV model with a 37 kW induction motor as shown in Figure 2.25 was developed and tested based on the ECE-15 drive cycle. The results demonstrated that the vehicle speed and demanded torque were closely followed, but torque ripple was present. To validate the sensorless scheme, a test rig was set up to compare estimated speed with reference speed. Again, the reference speed was followed effectively, though speed ripple was still apparent. When compared with results from Mayer et. al (2007) for the PMBL M/G, the torque ripple in this induction M/G was greater.

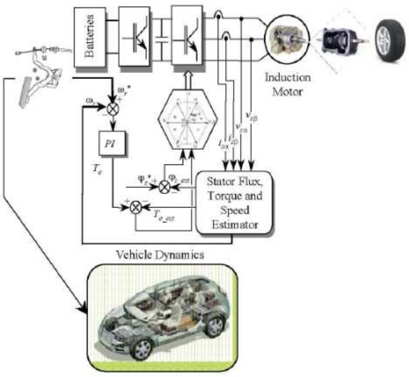
Batteries
Induction
Motor
ω_r^*
ω_r
PI
T_e
φ_s^*
φ_{s_est}
T_{e_est}
$i_{s\alpha}$
$i_{s\beta}$
$v_{s\alpha}$
$v_{s\beta}$
Stator Flux,
Torque and
Speed
Estimator
Vehicle Dynamics

Figure 2.25 Scheme for the EV sensorless DTC simulation

(Khoucha et al., 2007)

Unlike the PMBL and induction drives, the phase windings in the SR drive were not concurrently switched; the principle was to excite the phase when its inductance increased (Gao et al., 2001). Figure 2.26 illustrates the varying phase inductance and the corresponding phase voltage and current. As seen in that graph, the current was controlled by adjusting the firing angle and switching frequency of inverter. The current increased or decreased as the $+V_{bus}$ or $-V_{bus}$ was applied to the winding. PWM or Hysteresis controllers could be used to actuate the inverter. Constant torque and constant power operations used different angles and frequency values.

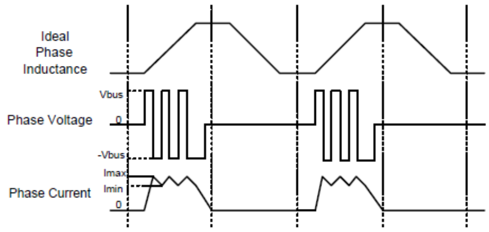
Ideal
Phase
Inductance
Vbus
Phase Voltage
0
-Vbus
Imax
Imin
Phase Current
0

Operation of SRM below base speed.

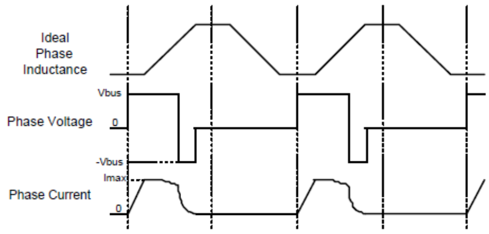
Ideal
Phase
Inductance
Vbus
Phase Voltage
0
-Vbus
Imax
Phase Current
0

Operation of SRM above base speed.

Figure 2.26 Switching characteristics of the SR drive (Gao et al., 2001)

Omekanda (2003) suggested using a search technique for optimum turn-on and turn-off angles, current set level, etc., of an SR drive. Phase flux linkage as functions of rotor position and phase current was developed using the Finite Element method and then was used to determine the M/G torque generated. Next, three dimensional maps for torque, efficiency, and torque ripple coefficient were produced from the turn-on and turn-off angle data using a computer program. The operation point was found by plotting these two-dimensional contours in the angle plane as shown in Figure 2.27 for a motor speed of 9,950rev/min. The predicted efficiency was compared with the results of dynamometer tests for all possible speed-torque points and showed good agreement. It was found that the highest efficiency of the 102kW SR motor was 93%.

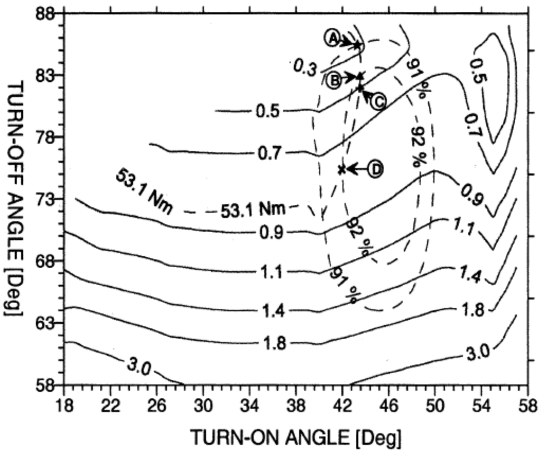

Figure 2.27 Global performance map of SR drive at 9,950 rev/min (Omekanda, 2003)

The turn-on angle affected the accelerating performance and maximum speed of an EV driven by a 40kW SR motor (Aida et al., 2008). The motor configuration used was 12/8 poles with aligned pole positions at 22.5° angular separation. The powertrain of the developed EV is shown in Figure 2.28. The driver command was first converted into torque demand and then current demand. To generate the control signal to the Pulse Width Modulation (PWM) inverter, a Proportional Integral (PI) controller was applied; current and position were measured as feedback to the controller. The main drawback of this proposed Switched Reluctance (SR) drive was a high noise level of 97dB measured 1m from the M/G.

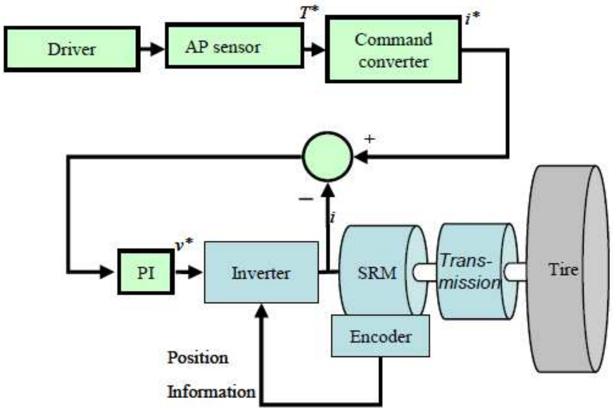
Driver
AP sensor
T*
Command converter
i*
+
−
i
PI
v*
Inverter
SRM
Trans-mission
Tire
Encoder
Position Information

Figure 2.28 Configuration of EV powertrain (Aida et al., 2008)

2.7 Electrical Energy Storage Systems

Electrical energy storage units are required to store sufficient energy for the desired all-electric range, to provide adequate power for acceleration and braking, and to meet the required cycle life [Burke, 2007]. The size of the storage units required varies with the type of driveline, whether battery powered, engine hybrid-electric or fuel cell powered. The battery specifications used in mass-produced EV's and HEV's are listed in Table 2.4 and a summary of the advantages and disadvantages of these batteries (including lead-acid) is listed in Table 2.5. Compared to HEV's, EV's require higher energy and power, and thus have adopted more advanced battery technology. But higher battery technology and high energy capacity makes EV's more expensive.

Vehicle	Battery	Energy (kWh)	Power (kW)	Weight (kg)
Toyota Prius	Nickel Metal Hydride (NiMH)	1.8	21	40
Honda Insight	NiMH	0.9	10	20
Nissan Leaf	Lithium Ion (Li-Ion)	24	90	300

Table 2.4 Type of Batteries in modern EV's and HEV's

(Duoba et al., 2001; Kawamura et al., 2011)

Lead-acid	NiMH	Li-ion
Low cost	Twice energy density of lead-acid	Twice energy density of NiMH
Mature technology	Recyclable	Recyclable
Limited life cycle at deep rate of SoC	Storing volumetric energy and power	Long cycle life
Low deep of discharge	Long cycle life	Wide temperature range
Low energy and power densities	Wide temperature range	Low memory effect
	Life cycle affected by high discharge current	Lower price/kWh than NiMH
	Memory effect	

Table 2.5 Advantages and disadvantages of modern batteries

(Khaligh et al., 2010)

Burke (2007) performed simulations to determine the energy use and driving range of a 1133kg EV powered by a 25kWh/50kW Lithium Ion (Li-ion) battery. Using the FUDS and other highway drive cycles, the energy uses were 175Wh/minute and 166Wh/minute respectively. The driving range on the FUDS drive cycle was 152miles, while on highway it was lower at 146miles. For HEV applications, the effect on fuel economy was investigated. Figure 2.29 shows the fuel economy factors for conventional, mild hybrid and full hybrid vehicles with different types of engines. In this case, the full hybrid employed higher M/G and Nickel Metal Hydride (NiMH) battery capacity. Figure 2.29 compares the fuel economy of HEV's with conventional vehicles using three different engine technologies i.e. Port Fuel Injected (PFI), lean burn and turbo diesel. The baseline vehicle was a conventional vehicle powered by a PFI gasoline engine. The full hybrid powered turbo diesel engine gave the highest factor. The best option would appear to be to use lean burn engine technology in HEV’s since this would yield good factors at lower cost.

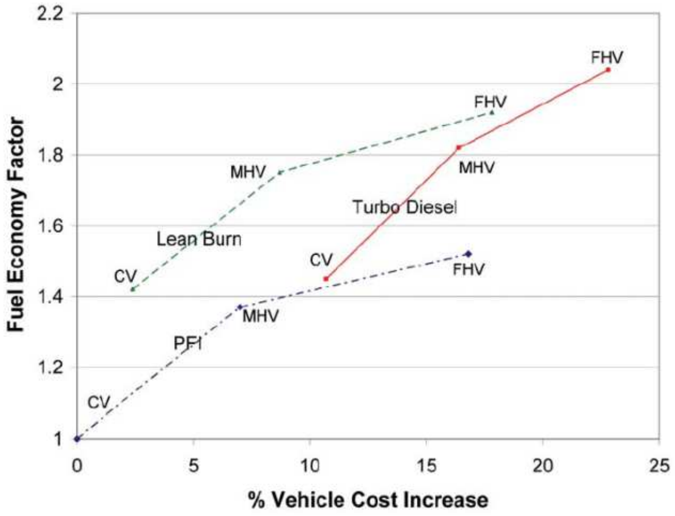

Figure 2.29 Trade-offs between fuel economy and vehicle cost for HEV (Burke, 2007)

A battery can be modelled as a controlled voltage source in series with an internal resistance as shown in Figure 2.30 (Tremblay and Dessaint, 2009). Different types of batteries have different parameters of B, A and K, and the function $u(t)$ is either 1 or 0 to indicate charge or discharge conditions. Steady state validation was performed by reproducing the given discharge curve and showed good agreement within 90%. The voltages, currents and SoC of batteries from simulation and experiment were compared in a “dynamic” validation. It was found that the voltage error was ±5% for $20\% \leq \text{SoC} \leq 100\%$ and the voltage error was ±10% for $\text{SoC} < 20\%$.

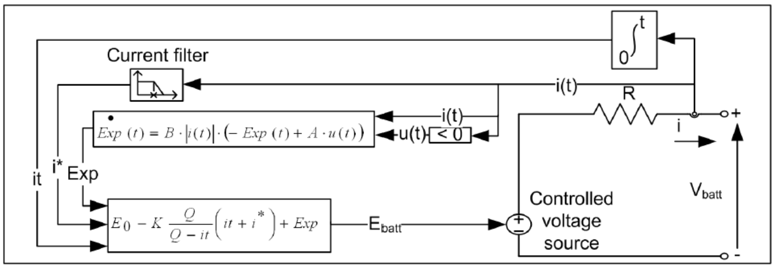

Current filter
i(t)
R
$\dot{Exp}(t) = B \cdot |i(t)| \cdot (-Exp(t) + A \cdot u(t))$
i(t)
u(t)
< 0
i
+
it
i*
Exp
$E_0 - K \frac{Q}{Q - it}\left(it + i^*\right) + Exp$
E_{batt}
Controlled voltage source
V_{batt}
-
t
0

Figure 2.30 Electrochemical model of battery (Tremblay and Dessaint, 2009)

Benger et al. (2009) proposed a different model for the Li-ion battery where the internal voltage was in series with inductance, resistance and two RC couples. Battery SoC affects the internal voltage and resistance and the temperature also affects the resistance. These parameters were investigated using electrochemical impedance spectroscopy and current pulse measurement. Validation was successfully achieved by discharging the battery at rated currents of 1C, 2C and 5C, and the battery voltages are shown below. ‘C’ is defined as battery capacity in Ampere-hour (Ah). For a 110Ah battery, 1C means the battery is discharged for one hour at the rated current of 110Ampere.

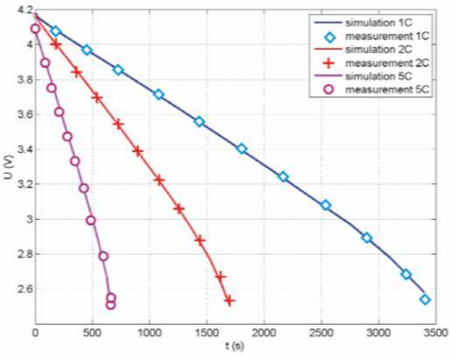

Figure 2.31 Measured and simulated values of cell voltage

(Benger et al., 2009)

In the case of an ultracapacitor substituting the battery, energy storage (Wh) is used instead of energy density due to its low value. Depending on the driving conditions, the ultracapacitor may suffer from deep discharges because of low energy storage size. Fortunately, its cycle life is higher than 500,000 (Burke, 2007). A comparison between the battery and the ultracapacitor in terms of energy density, power density, efficiency and life expectancy are summarised in Table 2.6. This indicates that a battery is better suited to store braking energy and an ultracapacitor is better suited to providing peak power during acceleration.

Performance	Battery	Ultracapacitor
Specific energy	10-100 Wh/kg	5-10 Wh/kg
Specific power	< 1000 W/kg	< 10,000 W/kg
Charge/discharge efficiency	50-80 %	85-98 %
Life expectancy	3 years	10 years

Table 2.6 Battery versus ultracapacitor performance (Baisden et al., 2004)

Miller et al. (2005) studied the benefits of combining a battery and an ultracapacitor in a hybrid vehicle equipped with an electronic CVT such as the Toyota Prius. The US-06 drive cycle was used to determine the accelerating and braking power and it was found that the braking powers of 30.9kW and 37.9kW respectively were higher than the power capacity of the 20kW NiMH battery. To accommodate the difference, a 21.8kW Maxwell ultracapacitor was incorporated connected to the battery through a

300V/200V DC-DC converter, and the power capacity of the battery was reduced. Figure 2.32 shows the proposed Energy Storage System (ESS) for the Prius HEV.

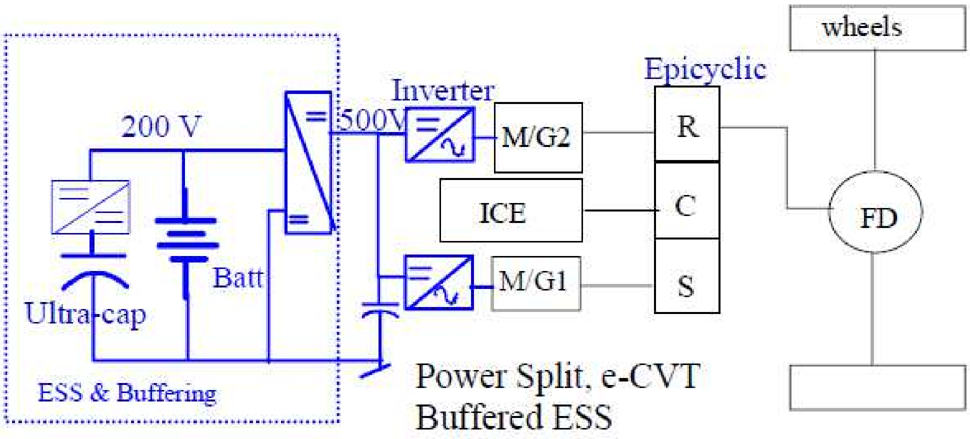

Figure 2.32 The ESS and buffering in e-CVT equipped HEV

(Miller et al., 2005)

Higher efficiency and lower cost of an ESS were obtained by connecting the ultracapacitor directly to the inverter, rather than using a conventional connection in which the ultracapacitor and the inverter were linked with a DC/DC converter (Lu et al., 2007). Three operating modes of the ESS were developed. In mode I, high efficiency, the ultracapacitor could deliver or absorb the power in the urban speed range. In mode II, both the ultracapacitor and the battery could deliver or absorb the power when the vehicle was driven between urban speed and highway speed. In this condition the full power capacity of the ultracapacitor was used and the rest of the demand was met by the battery. During mode III, the battery charged the ultracapacitor when the vehicle was cruising. The power flow in each mode is illustrated in Figure 2.33 in which mode I and II represent the acceleration condition. For braking, these power directions are reversed. The switching states of transistors T_1 and T_2 are also shown in these circuits.

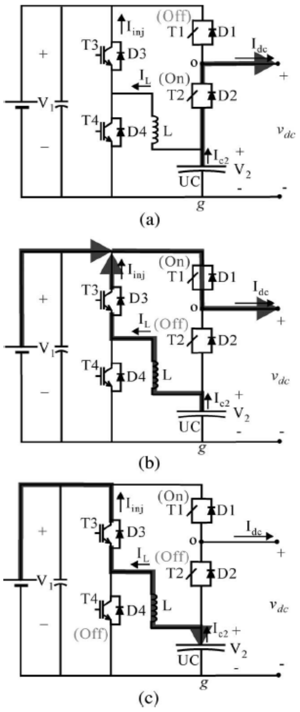

Figure 2.33 Operation modes of the ESS; (a) Mode I (b) Mode II (c) Mode III (Lu et al., 2007)

Charge/discharge rates are specified in terms of the current flow while the battery is being charged or discharged. The unit is Q/h, where Q is the rated battery capacity in Ah, and h is the charge/discharge time in hours. The battery is modelled with a discharge curve which relates state of discharge to cell voltage. As shown in Figure 2.34, the discharge rate has a great effect on the actual battery capacity. With an increase of discharge current, the battery capacity is decreased.

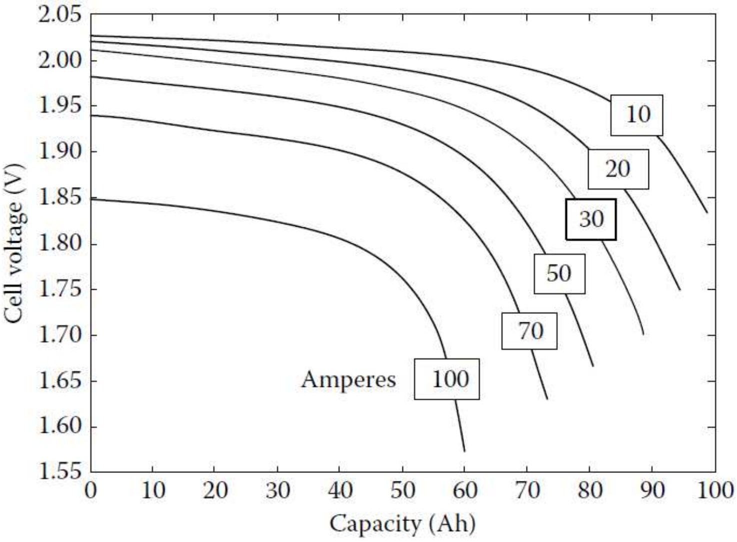

Figure 2.34 Discharge characteristics of a lead–acid battery

(Ehsani et al., 2010)

Due to the asymmetrical reaction rate process in discharging and charging, the charging rate is lower than the discharging rate. For example, $I_{chg} \leq 0.2Q$ and $I_{dischg} \leq 2.5Q$ for a Nickel-Cadmium (Ni-Cd) battery (Miller, 2004). The charging rate affects the capability of a battery to attain the nominal cell voltage as illustrated in Figure 2.35 for a NiMH battery. A ‘1C’ rate leads to greater than nominal cell voltage while a ‘C/3’ rate produces a lower cell voltage. A ‘C/2’ rate produces a voltage closer to the nominal cell voltage.

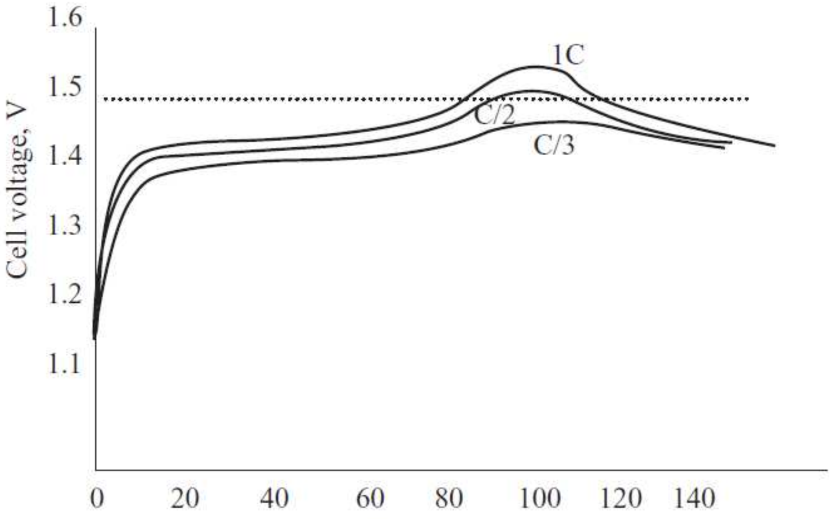

Figure 2.35 NiMH voltage versus SOC with rate as parameter at 20°C Cell (Miller, 2004)

Recently, high level energy management control strategies have been introduced to optimize available energy and increase the system reliability (Karden, 2007). These strategies control the on-board electric generation and allocate power and energy to loads at a subsystem or component level. A prioritization is set up to deliver power to the loads, so temporary functional degradation is allowed. As for the battery, the energy management performs two functions; monitoring and active control. Monitoring quantities such as voltage and current is used to calculate battery state. Controlling battery SoC, maintaining upper and lower temperature, and limiting the temperature gradients of battery are examples of active control.

As an example, work was done by Wang et al.(2009) to develop a Fuzzy Neural Network (FNN) model to monitor battery condition during charge and discharge on noisy input and output data. 3500 pairs of training data were generated by the AV-900 power processing system connected to an 80Ah Nickel Metal Hydride (Ni-MH) battery pack. The current, temperature and state of charge were chosen as the inputs to the FNN model and the model output was the load voltage of the battery. The learning algorithm used these training data to generate the FNN parameters. The model was then tested with 3000 pairs of data obtained from a vehicle driven on the FUDS drive cycle. For comparison, a conventional back-propagation network was developed using the same training and testing data. It was found that the FNN produced more accurate results than the conventional network.

2.8 Chapter Summary

In EV's and HEV's, the mixed-mode braking system can be either series or parallel. A mixed mode braking system is required because the regenerative braking cannot meet all braking demands especially during hard braking at high speed. The series system recovers more braking energy than the parallel system because it can maximise regenerative brake usage. But it adds complexity such as the need for a pressure source, control devices, sensors, stroke simulator and brake controller. There are two ways to generate the pressure; an accumulator fed by an hydraulic pump, and a master cylinder pressurised from an active booster or an electric motor. The brake controller actuates solenoid valves, a vacuum pump or an electric motor in order to control the pressure using information from the sensor. The driver demand is detected by a pressure sensor in the master cylinder or a stroke sensor on the brake pedal. Since there is no direct connection from the pedal to the calliper, a stroke simulator is used to provide pedal feel for the driver.

A parallel braking system is simpler, being like a conventional braking system supplemented by regenerative braking. The performance of these braking systems has been analysed using simulation modelling and experimental work.

In addition to the mixed-mode braking system, modern EV's and HEV's are also required to be equipped with braking safety features such as ABS and ESC. One approach taken by brake system designers in blended braking is to deactivate the regenerative braking when these systems operate. The reason is that safety is crucial and recovering energy is no longer important. The second approach leaves the regenerative braking operational and argues that regenerative braking can improve the performance of ABS and ESC.

In the future electric drives for EV's and HEV's are likely to employ PMBL motors, induction motors or SR motors, each with their own particular advantages. However, manufacturers of mass-produced EV and HEV will most likely continue to choose to use a PMBL M/G due to its high torque and power density characteristics, and the associated high efficiency. The speed-torque characteristic of the electric M/G affects the amount of braking energy that it is possible to be recovered. Various control methods have been proposed for the electric drive of these vehicles, and a front runner seems to be the DTC which is relatively simple in structure and robust against uncertainties.

Among electric energy storage, Li-ion is the best candidate for future EV’s and HEV’s as this technology overcomes the problems of encountered in lead-acid and NiMH batteries such as low depth of discharge and memory effects. Furthermore, it has higher energy density and lower price per kWh compared with NiMH battery technology. For applications with power surges such as acceleration and braking, combining a battery with ultracapacitors is recommended to make use of the high power capacity of the ultracapacitor and to preserve the life of the battery. A battery monitoring system is essential to inform voltage, current and SoC to the brake controller in performing mixed-mode braking.

From the review of literature it has been found that mixed-mode braking systems have already been implemented by many car manufacturers, but performance tests on real driving have not been reported yet to justify the quality of their design. Therefore research to collect and analyse braking related data from existing EV’s or HEV’s is necessary.

Laboratory and simulation research has reached the point where the stored energy in a battery can be quantified from the driver’s brake demand or drive cycle. However, the steps to obtain regenerative and friction torques from the drive cycle have not been published. The torque values stated are the desired braking torques, not the actual braking torque at the wheels. Therefore, a dynamic model of mixed-mode braking systems is important as part of a general braking system design procedure for vehicles with regenerative braking. The control strategies for both regenerative torque and hydraulic brake pressure reviewed in this chapter will be applied in a dynamic model as part of the research presented in this thesis.

2.9 Research Approach and Methodology

Having completed the review of published and available work in the field of RB system control, it was decided that the approach taken in this research would be to use analytical and simulation techniques to design a mixed-mode braking system for an EV or HEV including its control system and to validate with experimental data obtained from testing a prototype EV on a chassis dynamometer and also on road test. A summary flowchart of the research methodology was shown in Figure 1.2.

The methodology adopted was thus based on computer simulation and experimental work to develop a mixed-mode braking system. A full vehicle model incorporating longitudinal dynamic, lateral dynamic and tyre models would be applied to investigate the operation of mixed-mode braking systems. Several drive cycles as have been used in previous research would be used to determine the amount of braking energy that it is possible to recover from the designed braking system. A comparison between a series design of braking system and a parallel design of braking system would be made in terms of performance, energy recuperation and cost. Control systems for both regenerative and friction brakes would be designed, evaluated, and verified. All these simulations would be performed in Matlab.

Two prototype EV’s with different powertrain topology and rating would be studied to determine their brake system control and performance during braking. For the dynamometer test, the EUDC would be used as the standard test cycle, enabling data including vehicle speed, wheel torque, battery current and battery voltage to be logged for further analysis. Road tests would also be performed to log real-life information relating to the operation of the designed blended brake control system e.g. by measuring motor currents and voltages.

CHAPTER 3

THEORY OF MIXED-MODE BRAKING SYSTEMS

3.1 Introduction

In this chapter the theory of mixed-mode braking systems is studied, starting with a vehicle model in the longitudinal and lateral directions. In normal braking, a longitudinal model is sufficient for mixed-mode braking with ABS. But combining the longitudinal model with a lateral model is necessary to investigate braking during steering manoeuvres. This results in a 7-degree of freedom of vehicle model. The “bicycle” model of a road vehicle is also considered as it is used as a reference model in the design of a controller for lateral stability. The operating principles of conventional (friction) braking systems are discussed; the friction braking comes into play when partial system failure occurs in a series braking system and always operates in a parallel braking system. Formulae are derived to quantify force, pressure and brake torque.

In a series braking system, brake demand is derived from pedal travel/pressure or pedal force/pressure characteristics. Two algorithms to control the operation of this brake system are proposed, one assumes the adhesion coefficient is known and another incorporates the ABS system. The latter algorithm is slightly modified to be used in a parallel braking system. Static characteristics are used to model both the M/G and the battery as the main elements of a regenerative braking system. Since the ABS operation is included in the algorithm, control techniques for them are derived in Appendix A which was adapted from work of Kienhöfer et al (2004) with modification that the caliper pressure was controlled in both acceleration and deceleration phases.

3.2 Vehicle modelling

The vehicle model used in this study had two axles, one front and one rear, with two wheels fitted to each axle (one at each end). Longitudinal forces acting at the front and rear wheel tyre / road contact points were used to accelerate or decelerate the vehicle. These forces are originally generated by the vehicle's tractive power source such as the engine and the electric M/G, or by the brakes. The longitudinal vehicle speed is determined from Newton's second law of motion and can be written as:

$$m \cdot \dot{V}_x = F_{xf} + F_{xr} - F_d - F_{ro} - m \cdot g \cdot \sin\beta \tag{3.1}$$

$$F_d = \frac{1}{2} C_d \cdot \rho \cdot A \cdot V_x^2 \tag{3.2}$$

$$F_{ro} = C_{ro} \cdot m \cdot g \tag{3.3}$$

Rolling resistance is dominant over aerodynamic drag at lower speeds as shown in Figure 3.1. These two forces are equal at vehicle speed of

53.3km/h. The graph represents the road load of the research test vehicle, the TATA ACE EV.

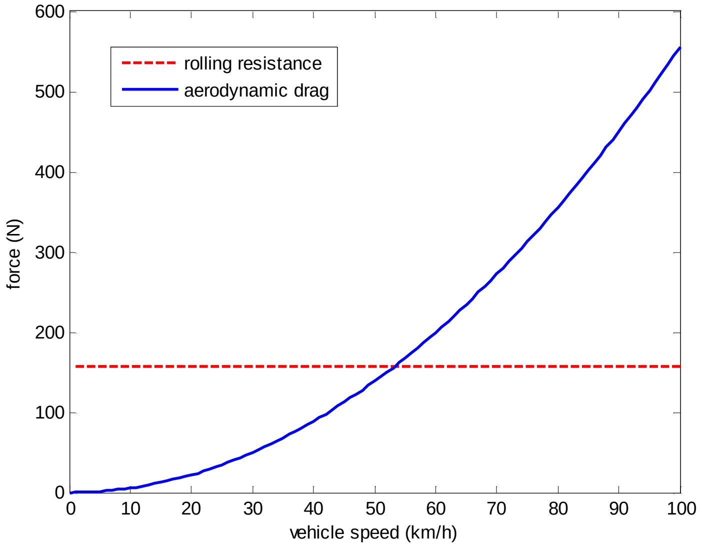

Figure 3.1 Road load as function of vehicle speed

In the case of zero vertical acceleration and zero pitch torque, vertical load forces are given by the following equations:

$$F_{zf} = \frac{h(F_d - m \cdot g \cdot \sin\beta - m \cdot \dot{V}_x) + l_r \cdot m \cdot g \cdot \cos\beta}{l_f + l_r} \tag{3.4}$$

$$F_{zr} = \frac{-h(F_d - m \cdot g \cdot \sin\beta - m \cdot \dot{V}_x) + l_f \cdot m \cdot g \cdot \cos\beta}{l_f + l_r} \tag{3.5}$$

Wheel angular velocity is calculated from the following differential equation:

$$I_w \frac{d\omega_w}{dt} = \tau_{drive} - R_e \cdot F_x \tag{3.6}$$

The effect of rotational inertia on vehicle acceleration was included by Husain and Islam (1999) as follows:

$$k_m \cdot m \frac{dV_x}{dt} = F_{accel} \tag{3.7}$$

The range of k_m is between 1.08 and 1.1. The vehicle global inertia moment is included so that the total inertia is:

$$I = I_w + \frac{1}{2} m \cdot R_e^2 (1 - s) \tag{3.8}$$

$$s = 1 - \frac{R_e \cdot \omega}{V_x} \tag{3.9}$$

The value of *s* is usually low (10 – 20%) for a road with high adhesion coefficient.

Instead of using a detailed model of an ICE, the Matlab/Simulink built-in model was adapted which provides a lookup table that relates the engine speed and the maximum torque available at that speed. For this study, a given maximum power of 40kW, speed at maximum power of 5000rev/min and maximum speed of 6000rev/min were used. As shown in Figure 3.2, at zero speed, the engine could generate torque up to 76.4Nm and as the speed increases the torque also increases. A maximum of 95.49Nm is generated at 2640rev/min. A throttle input signal from zero to one is multiplied with the available torque to get the actual torque delivered by the engine.

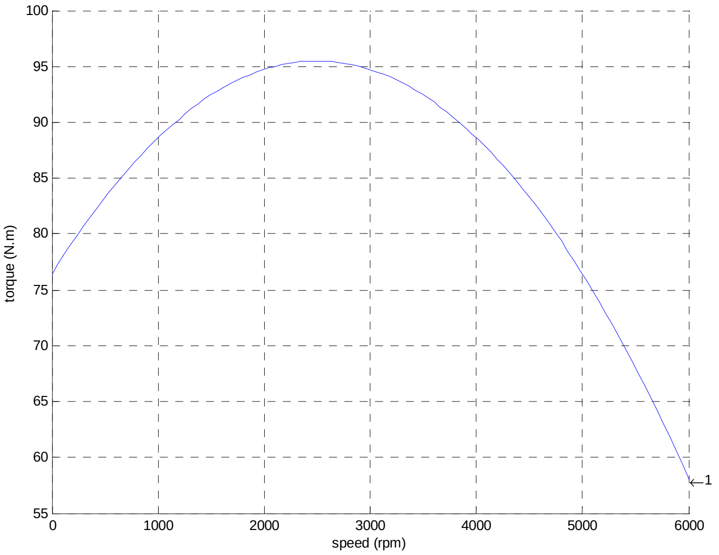

Figure 3.2 Speed-torque curve of a gasoline engine (Mathworks, 2011)

The 7-DoF model was considered in developing the simulation model proposed in Chapter 4 section 5, though its Simulink model was not generated in this thesis. The wheel slip model wasused in the forward simulation of the vehicle longitudinal dynamics to analyse the braking characteristics and also to analyse the integration of the regenerative braking system with ABS. In designing a controller for lateral stability, the bicycle mode was used as the reference vehicle model (Hancock et al., 2005; Li and Yu, 2009). The bicycle model has two degrees of freedom *viz.* the vehicle lateral position y and the vehicle yaw angle ψ. The lateral position is measured from the CG towards the centre of rotation and the yaw angle is the angle between the longitudinal axis and the global x axis as illustrated in Figure 3.3.

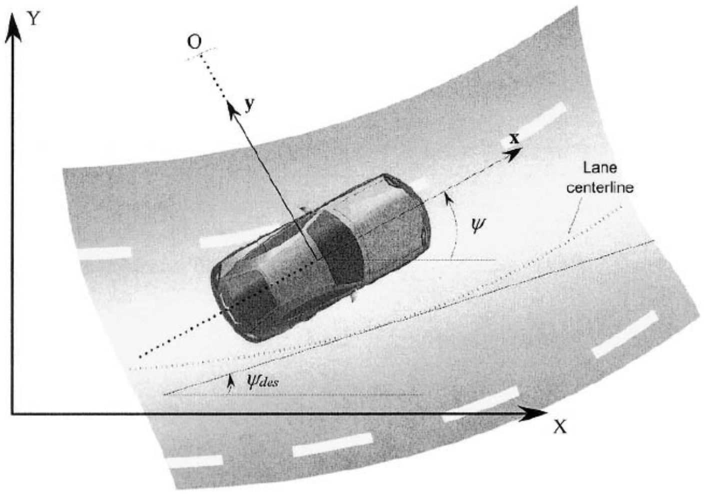

Figure 3.3 Local and global coordinates of a road vehicle

(Rajamani, 2006)

Lateral motion of a vehicle is governed by Newton's second law as follows:

$$m \cdot a_y = F_{yf} + F_{yr} \tag{3.10}$$

Lateral acceleration a_y is affected by motion along the lateral axis and centripetal acceleration:

$$a_y = \dot{V}_y + V_x \cdot \dot{\psi} \tag{3.11}$$

Taking the moment balance about the *z* axis, the yaw torque is given by:

$$I_z \ddot{\psi} = l_f \cdot F_{yf} - l_r \cdot F_{yr} + M_{zf} + M_{zr} \tag{3.12}$$

The lateral tyre forces and the aligning moments are function of slip angle and from the geometry is found that:

$$\tan(\alpha_f + \delta_{fw}) = \frac{V_y + l_f \cdot \psi}{V_x} \tag{3.13}$$

$$\tan \alpha_r = \frac{V_y - l_r \cdot \psi}{V_x} \tag{3.14}$$

To investigate braking during cornering, seven degrees of freedom are required: longitudinal, lateral, and yaw motions, and rotations of four wheels as illustrated in Figure 3.4. The model inputs are steering angle and traction or braking torque on each wheel.

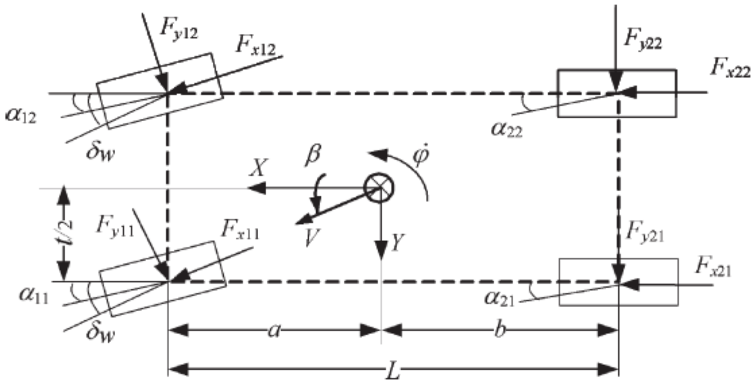
F_{y12}
F_{x12}
F_{y22}
F_{x22}
α_{12}
δ_W
α_{22}
X
β
$\dot{\varphi}$
$t/2$
F_{y11}
F_{x11}
V
Y
F_{y21}
F_{x21}
α_{11}
α_{21}
δ_W
a
b
L

Figure 3.4 7-DoF four wheel vehicle dynamic model (Li et al., 2009)

Applying Newton's second law on the longitudinal axis of the vehicle, the equations of motion are derived as:

$$m \cdot a_x = F_{xf} \cdot \cos \delta_w - F_{yf} \cdot \sin \delta_w + F_{xr} \tag{3.15}$$

$$a_x = \dot{V}_x - V_y \dot{\varphi} \tag{3.16}$$

$$F_{xf} = F_{x11} + F_{x12} \tag{3.17}$$

$$F_{yf} = F_{y11} + F_{y12} \tag{3.18}$$

In the same way, the equations of lateral motion are given by:

$$m \cdot a_y = F_{xf} \cdot \sin \delta_w + F_{yf} \cdot \cos \delta_w + F_{yr} \tag{3.19}$$

$$a_y = \dot{V}_y + V_x \dot{\varphi} \tag{3.20}$$

By taking moments with respect to the vehicle's centre of gravity, the equation of yaw motion is:

$$I_z \ddot{\varphi} = F_{yf} a \cos\delta_w - (F_{y11} - F_{y12})\frac{t}{2}\sin\delta_w - F_{yr} b - F_{xf} a \sin\delta_w - (F_{x11} - F_{x12})\frac{t}{2}\cos\delta_w$$
$$-(F_{x21} - F_{x22})\frac{t}{2}$$

(3.21)

And the equation of four-wheel rotation is:

$$J_{ij}\frac{d\omega_{ij}}{dt} = T_{ij} - F_{xij} R_e \tag{3.22}$$

where *i* = 1 for the front and 2 for the rear axles, *j* = 1 for the left and 2 for the right wheels. The global X-Y coordinates of the vehicle are:

$$X = \int V \cdot \cos(\varphi + \beta) \cdot dt \tag{3.23}$$

$$Y = \int V \cdot \sin(\varphi + \beta) \cdot dt \tag{3.24}$$

When cornering and braking is performed, vehicle load is transferred from rear axle to the front axle due to longitudinal acceleration and from the inner wheels to the outer wheels due to lateral acceleration (Kim and Kim, 2006). Dynamic loads at all wheels are given as:

$$F_{z11} = \frac{bmg}{2(a+b)} - \frac{ma_x h}{2(a+b)} + \frac{ma_y hb}{t(a+b)} \tag{3.25}$$

$$F_{z12} = \frac{bmg}{2(a+b)} - \frac{ma_x h}{2(a+b)} - \frac{ma_y hb}{t(a+b)} \tag{3.26}$$

$$F_{z21} = \frac{amg}{2(a+b)} + \frac{ma_x h}{2(a+b)} + \frac{ma_y ha}{t(a+b)} \tag{3.27}$$

$$F_{z22} = \frac{amg}{2(a+b)} + \frac{ma_x h}{2(a+b)} - \frac{ma_y ha}{t(a+b)} \tag{3.28}$$

The longitudinal slip of the front and rear wheels is calculated from:

$$s_{1j} = \frac{r_e \cdot \omega_{1j}}{V_x \pm t \cdot \dot{\varphi}/2} - 1 \tag{3.29}$$

$$s_{2j} = \frac{r_e \cdot \omega_{2j}}{V_x \pm t \cdot \dot{\varphi}/2} - 1 \qquad (3.30)$$

The tyre slip angles are expressed as:

$$\alpha_{1j} = \delta_w - tg^{-1}\left(\frac{V_y + a\dot{\varphi}}{V_x \pm t\dot{\varphi}/2}\right) \qquad (3.31)$$

$$\alpha_{2j} = -tg^{-1}\left(\frac{V_y + b\dot{\varphi}}{V_x \pm t\dot{\varphi}/2}\right) \qquad (3.32)$$

A wheel slip model is used in the forward simulation of the vehicle's longitudinal dynamics to analyse braking characteristics and also to analyse the integration of the regenerative braking system with ABS. Tyre forces are affected by both longitudinal slip and slip angle as shown in Figures 3.5 and 3.6. The peak adhesion decreases as the slip angle increases but the sideways adhesion coefficient increases with slip angle. This indicates that during cornering, the wheel would lock sooner when braking and the stopping distance would be longer. Also the lateral force would decrease as the slip ratio increases, and at higher slip ratio, the driver would lose control due to oversteer.

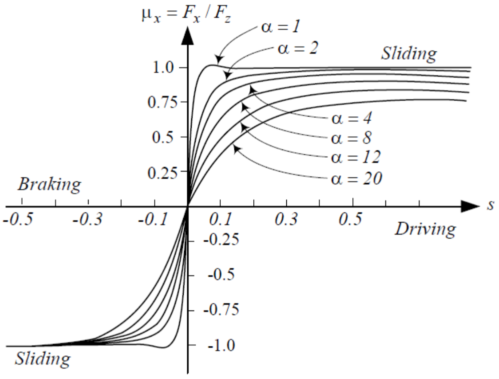

Figure 3.5 Adhesion coefficient in the *x*-direction as a function of slip ratio for different sideslip (Janar, 2008)

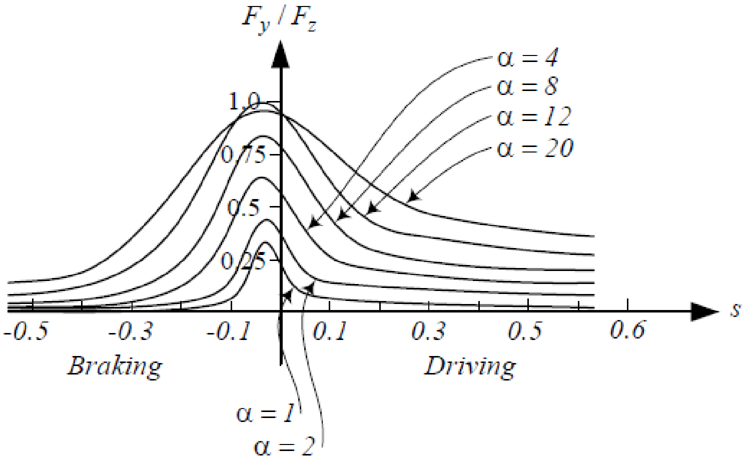

Figure 3.6 Adhesion coefficient in the *y*-direction as a function of slip ratio for different sideslip (Janar, 2008)

Longitudinal and lateral forces generated by each tyre can be formulated as:

$$F_{xij} = F_{zij}(a_x, a_y) \cdot \mu_{xij}(s_{ij}, \alpha_{ij}) \tag{3.33}$$

$$F_{yij} = F_{zij}(a_x, a_y) \cdot \mu_{yij}(s_{ij}, \alpha_{ij}) \tag{3.34}$$

Pacejka's model is used later in Chapter 5 when the vehicle longitudinal dynamics model is simulated with Matlab/Simulink. Pacejka's "magic formula" approximates these empirical adhesion coefficients using nonlinear equations as follows:

$$\mu_x = D_x \cdot \sin\left\{C_x \cdot \tan^{-1}\left[B_x(1-E_x)s + E_x \cdot \tan^{-1}(B_x \cdot s)\right]\right\} \tag{3.35}$$

$$\mu_y = D_y \cdot \sin\left\{C_y \cdot \tan^{-1}\left[B_y(1-E_y)s + E_y \cdot \tan^{-1}(B_y \cdot s)\right]\right\} \tag{3.36}$$

Pacejka's model is parameterised by choosing suitable parameters D, C, E and B to relate wheel slip to the adhesion coefficient of tyre. Different parameters are selected to produce different curves to follow experimentally generated curves and these are listed in Table 3.1. Figure 3.7 shows tyre characteristics for each set of Pacejka's parameters.

Parameter	I	II	III	IV	V
D	0.980	0.900	0.910	0.910	0.905
C	1.300	1.100	0.900	0.900	0.940
B	11.275	11.275	11.275	8.000	4.000
E	-1.999	-1.999	-1.999	-1.999	-1.999

Table 3.1 Pacejka's parameters for different driving conditions

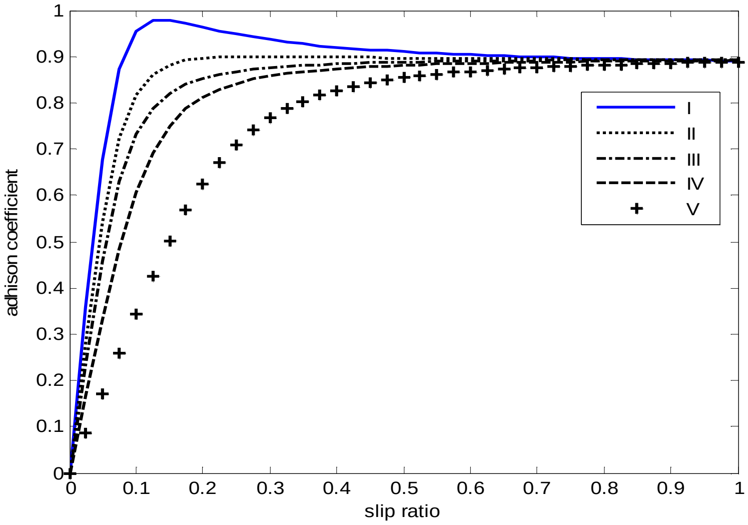

Figure 3.7 Tyre characteristics obtained with Pacejka's model

Pacejka's model is used later in Chapter 5 when the vehicle longitudinal dynamics model is simulated with Matlab/Simulink.

Beside Pacejka's tyre model, there is another model named "Dugoff's" tyre model which assumes uniform normal pressure distribution on the tyre contact patch; in comparison Pacejka used a more realistic parabolic pressure distribution in his model (Rajamani, 2006). In Dugoff's model the longitudinal and lateral tyre forces are simpler than in the Pacejka model, and are given by:

$$F_{xij} = C_{sij} \frac{s_{ij}}{1+s_{ij}} f\left(\lambda_{ij}\right) \tag{3.37}$$

$$F_{yij} = C_{\alpha ij} \frac{\tan \alpha_{ij}}{1+\alpha_{ij}} f\left(\lambda_{ij}\right) \tag{3.38}$$

$$\lambda = \frac{\mu_x \cdot F_z (1+s)}{2\left[(C_s \cdot s)^2 + (C_\alpha \cdot \tan \alpha)^2\right]^{1/2}} \tag{3.39}$$

$$f(\lambda) = \begin{cases} (2-\lambda)\lambda, \lambda < 1 \\ 1, \lambda \geq 1 \end{cases} \tag{3.40}$$

Finally, knowing the braking force from the tyre model enables the braking efficiency to be calculated:

$$\eta_{brake} = \frac{F_{brake}}{m \cdot g} \times 100\% \tag{3.41}$$

3.3 Conventional braking systems

The basic brake system components in a conventional passenger car are the brake pedal and linkage, master cylinder, vacuum booster, pipes, disc or drum brake assembly including slave cylinder(s), brake pads or shoes, and rotor (disc or drum). The brake pedal is a lever that amplifies the foot force F generated by the driver (the 'driver effort') as shown in Figure 3.7. The force on the pushrod F_1 is:

$$F_1 = L_P \cdot F \tag{3.42}$$

The L_p value is 4 for the brake pedal illustrated in Figure 3.8. The force on the pushrod is amplified by the action of the brake servo or booster; for a "vacuum" servo atmospheric air at pressure P_1 enters the rear chamber of the servo while the front chamber is held at lower pressure P_2 either by engine inlet depression or a "vacuum" pump (e.g. on diesel engines). This pressure difference generates a force F_2 on the master cylinder piston given by:

$$F_2 = (P_1 - P_2) \cdot A_1 \tag{3.43}$$

and the brake boost ratio is defined as:

$$B = \frac{F_2}{F_1} \tag{3.44}$$

The boost ratio of modern passenger cars is typically between 4 and 9.

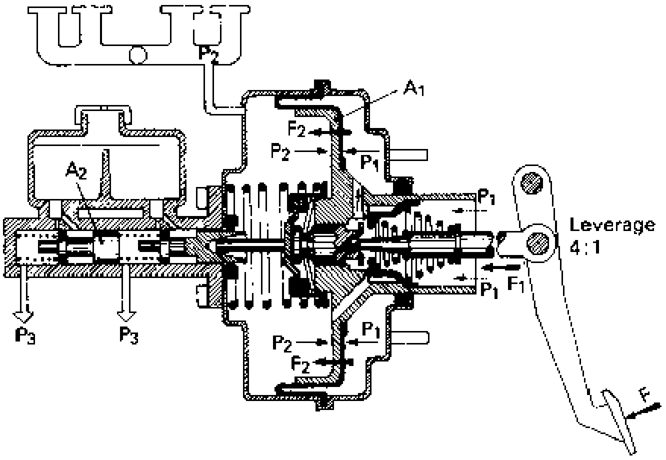

Figure 3.8 Operating principle of a vacuum servo (Heisler, 2002)

In vacuum booster operation, the pedal force/travel characteristic curve has three distinct regions (Zehnder et al., 1999). First, the pedal moves under constant applied force from the origin to a point called “Jump-in”. Second, the pedal moves further as the applied force increases up to a point called the “Knee point”; beyond this point no additional boost force is available. These two points are shown as “A” point and “B” point in Figure 3.9 and are typically about 25 and 300 N. Third, the applied force generates any additional brake actuation hydraulic pressure only based on the non-boosted state. This third state is dangerous if reached in practice since the driver will not be able to make any significant increase in hydraulic brake line actuation pressure and thus braking force. Additionally, he/she will sense the absence of servo assistance and will interpret this as brake failure, leading to a loss of confidence and panic.

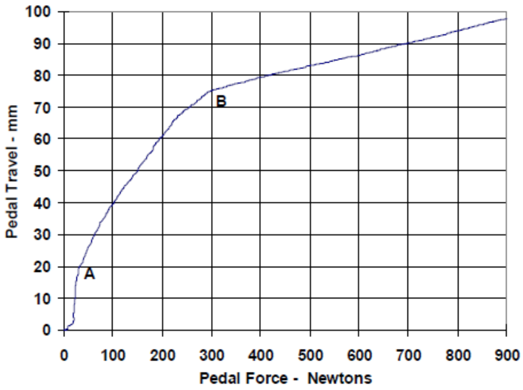

Figure 3.9 Pedal force/travel characteristic of a mid-size passenger car

(Zehnder et al., 1999)

Legislation requires that the vehicle meets a defined braking performance in the event of booster fail. The base braking system in the Toyota Prius and the Honda Insight did not include a brake booster as in conventional cars. But, their brake-by-wire system incorporates a pedal simulator with a similar pedal characteristic to the conventional ones. This means that Figure 3.9 can be used to show what the drivers of these two cars experience in failure modes. In this case, all brake line pressure is generated by the driver.

Figure 3.10 illustrates the actuation pressure reduction in the booster fail condition. At the legal pedal force limit (500N for 0.25g deceleration in the booster fail condition), the generated actuation line pressure is reduced from e.g. 85bar to 25bar which translates to a reduction in vehicle deceleration from 0.9*g* to 0.3*g* (Reuter et al., 2003). Figure 3.10 also indicates that no actuation line pressure is generated when the pedal force is less than 90N in the booster fail condition and less than about 30 N in the boosted condition. This represents the effect of "threshold pressure" in the brake actuation system to overcome pull-off spring and seal friction forces.

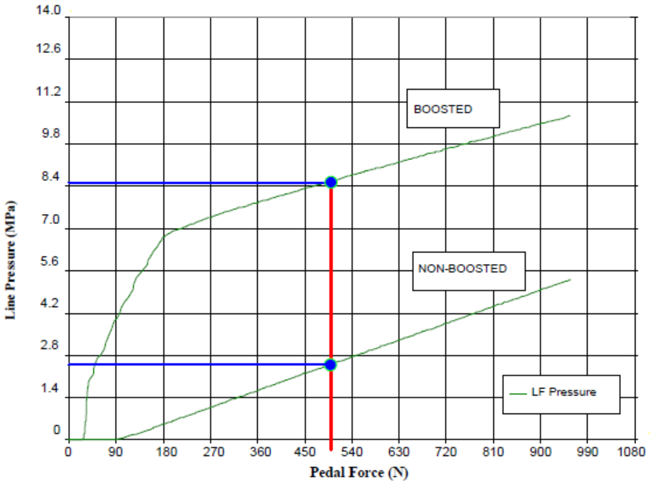

Figure 3.10 Boosted vs. Non-Boosted Brake Output (Reuter et al., 2003)

The force on the master cylinder primary piston F_1 + F_2 and the generated pressure P_3 is:

$$P_3 = \frac{F_1 + F_2}{A_2} \tag{3.45}$$

This equation does not include spring forces and seal friction forces in the master cylinder. Using the simplified cross-section of the master cylinder shown in Figure 3.11, the generated hydraulic actuation line pressures are:

$$P_1 = \frac{F_{mc} - F_{k1} - F_{f1}}{A_{mc}} \tag{3.46}$$

$$P_2 = P_1 - \frac{F_{k2} + F_{f2}}{A_{mc}} \tag{3.47}$$

Therefore, the pressure in cylinder 2 is less than the pressure in cylinder 1 because of the reaction forces. Seal friction includes both static and dynamic friction and can be estimated from:

$$F_f = \mu_s \cdot N(\dot{x}) + \mu_d \cdot N \cdot sign(\dot{x}) \tag{3.48}$$

Static friction force is the force required to move the piston hydraulic seal from the stationary state, and dynamic friction occurs between the seal and the cylinder bore when the seal is sliding.

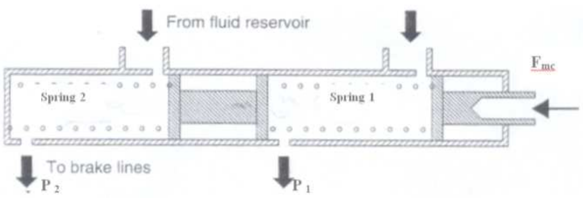

Figure 3.11Cross-sectional diagram of a standard tandem master cylinder (Vlacic et al, 2001)

In friction brakes, kinetic energy conversion into heat occurs when the friction material is forced (by the actuation mechanism e.g. hydraulic pressure on the slave piston) against the rotating brake rotor (brake disc or drum). The relationship between the hydraulic actuation pressure in a typical passenger car braking system and the brake torque generated by the brake at each wheel is explained elsewhere e.g. Heisler, (2002). The friction coefficient (μ) of the friction material (pad or lining) is not constant but is affected by factors including the rotor temperature (Day et al, 2011).

Figure 3.12 shows that μ decreases noticeably when the temperature rises over 200 °C, resulting in a reduction in generated brake torque and hence increased stopping distance. But this result was obtained from a small scale friction tester in which the disc specimen was rotated by the electric motor and friction pads were actuated with a hydraulic pressure of 80bar. The initial brake temperature was 100°C and the test lasted for 10minutes. In practice, the air flow in the vehicle providing brake cooling was not present in this test, therefore the temperature rise was greater.

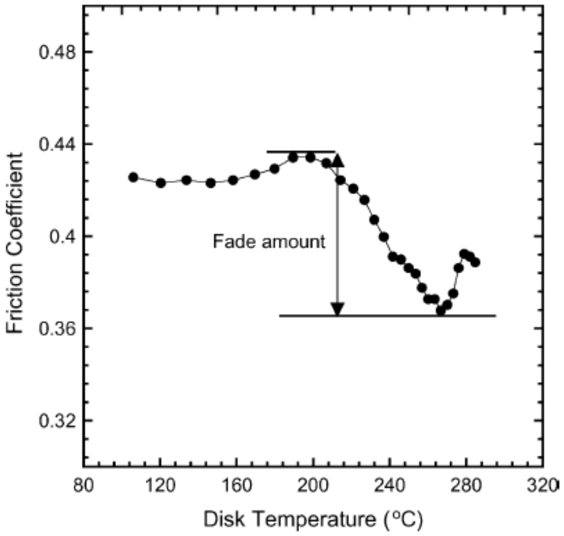

Figure 3.12 The friction coefficient as a function of disc temperature

(Cho et al., 2005)

3.4 Mixed-mode braking systems

For a given pedal force/travel characteristic, the braking system fitted to an EV or HEV should produce the same braking force as in a conventionally-braked vehicle. Therefore, calculating the braking torque required from each brake (i.e. the friction brake torque and the regenerative braking torque at each wheel) for a given driver demand in order to achieve the desired deceleration or rate of braking of a hybrid vehicle should start from the braking parameters of the basic vehicle.

The hydraulic actuation pressure generated by an example master cylinder was measured on a test rig and is plotted as a function of pedal travel in Figure 3.13. This characteristic is similar to the on-car characteristic, see Ho (2009) for more information.

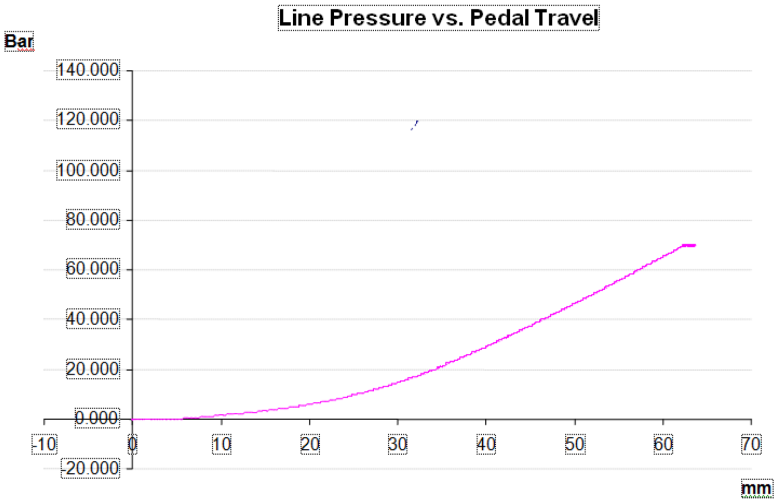

Figure 3.13 Characteristics of hydraulic brake actuation (line) pressure and brake pedal travel (Ho, 2009)

Using the test rig data from Figure 3.13, the relationship between hydraulic brake actuation (line) pressure and brake pedal travel can be approximated by a quadratic function as:

$$P_{MC} = 0.018 \cdot 10^5 \cdot u^2 \tag{3.49}$$

As well as the pedal travel/line pressure relationship, the relationship between pedal force and line pressure can also be used to determine the brake demand from the driver. The pedal force/pressure characteristic of a boosted system is shown in Figure 3.9 above, and this was converted to a “lookup table” which was used later in the simulation part of this research. Table 3.2 lists data taken from that curve for pedal forces less than 500 N. This data has been redrawn in Figure 3.14 and shows a good match with the initial curve. The advantage of the lookup table compared to the approximation function is that a more realistic model is obtained.

Pedal force (N)	Pressure (bar)
0	0
15	0
30	0
90	41
135	56
180	68
270	74
360	78
450	82
500	85

Table 3.2 Selected data from the brake pedal force/pressure characteristic

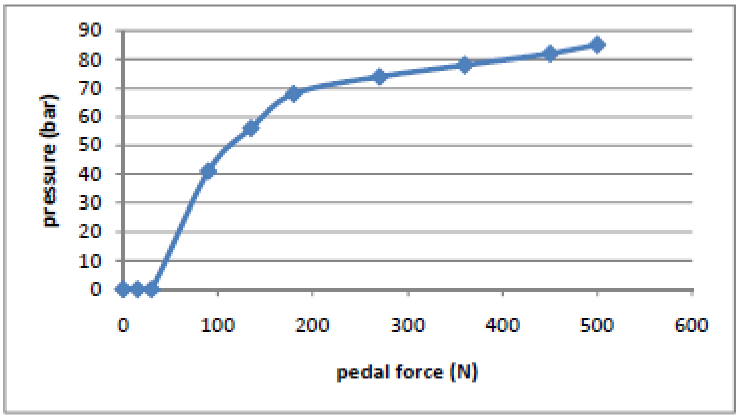

Figure 3.14 Reproduction of the brake pedal force/pressure curve

The next step was to model a regenerative braking system which comprises an M/G and a battery. The M/G was represented by a speed/torque characteristic as discussed in section 2.6, and is shown in Figure 3.15 for a PMBL M/G. Negative M/G torque means that the M/G is acting as a generator. When the M/G speed is less than 1500rev/min, it can generate braking torques up to 76.4Nm, but in practice, no such high braking torque is generated at such a very low speed. As the M/G speed increases the torque decreases and reaches zero at a speed of 6,000rev/min.

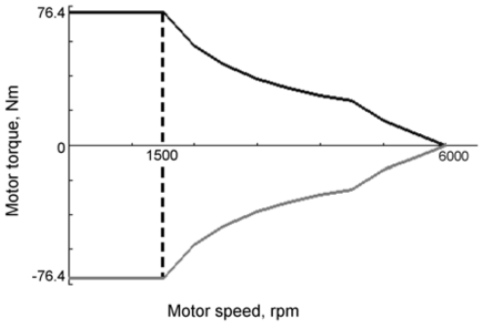

Figure 3.15 Characteristic curve of PMBL M/G (An, 2009).

If the M/G were connected to the wheel through a transmission and reduction gear, the regenerative brake force available at the tyre/road interface would be:

$$F_{EM} = \frac{\tau_{EM} \cdot N \cdot N_0}{\eta_t \cdot r_{eff}} \tag{3.50}$$

Considering the battery SoC and the vehicle speed, this force is limited by introducing two weighting factors as follows:

$$F_{reg} = W_1 \cdot W_2 \cdot F_{EM} \tag{3.51}$$

The weighting factor values were between 0 and 1 depending on the SoC and the speed as shown in Figure 3.16. This indicated that the full capacity of the M/G was used when the SoC was less than 80% and vehicle speed was greater than V_2. Both V_2 and V_1 values are indicated in the literature; e.g. Albrichsfeld and Karner (2009) used V_2 about 10km/h and V_1 about 7km/h in their series braking system.

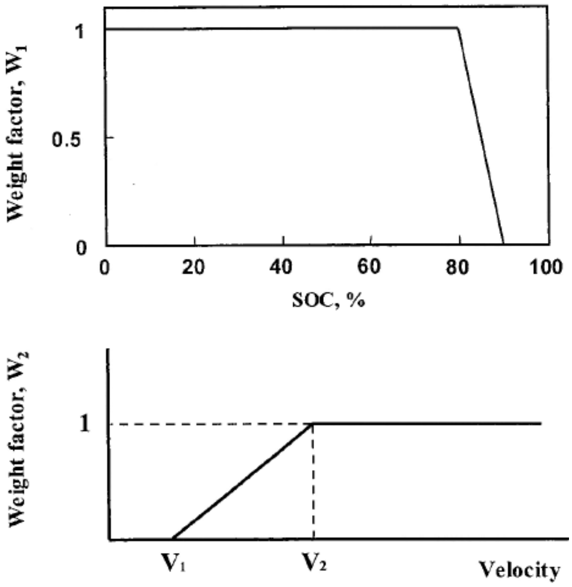

Figure 3.16 Weight factors for regenerative braking (Yeo and Kim, 2002)

The generated electric power of the M/G during braking is determined from:

$$P_{EM} = \tau_{EM} \cdot \omega_m \cdot \eta(\tau_{EM}, \omega_m) \tag{3.52}$$

In this equation, the efficiency curve is 3-dimensional as functions of torque and speed, and is usually modelled as efficiency contours as shown in Figure 3.17. This represents a 30kW PMBL M/G; the data was taken from the ADVISOR software, based on testing conducted by the NREL, and the electric M/G was manufactured by Unique Mobility (AVL, 2010). The efficiency ranges from 65% in the high-torque and low-speed region to 90% in the low-torque and high-speed region. Figure 3.18 illustrates how the continuous power of 37 kW is significantly smaller than the transient power of 77kW in acceleration or braking periods of driving. However, the ADVISOR data did not contain information about that transient power.

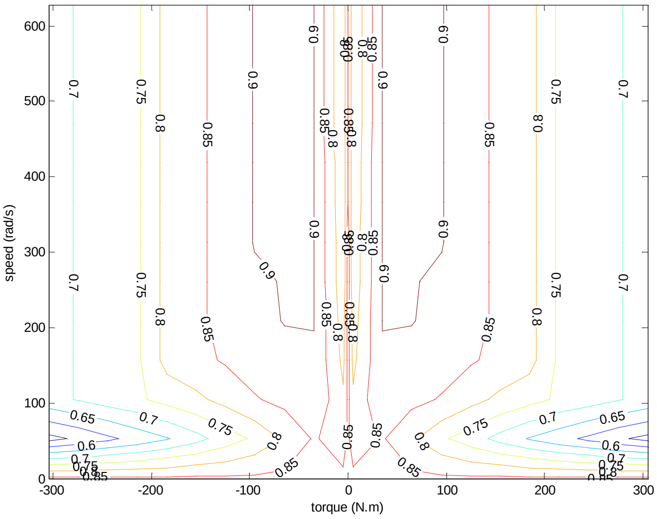

Figure 3.17 Efficiency contour of electric M/G on the torque-speed plane

(AVL, 2010)

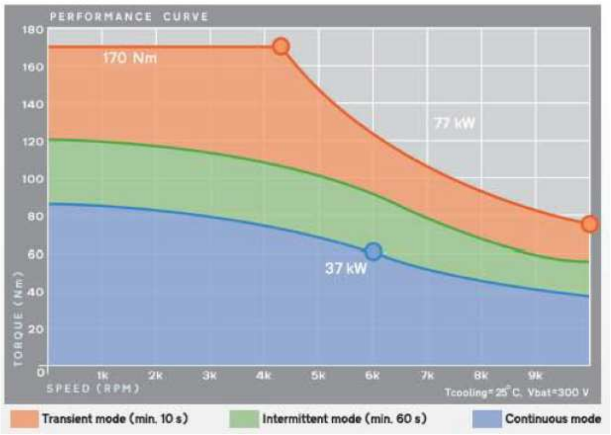

Figure 3.18 Performance curve of TM4 electric motor (TM4, 2012)

The battery was modelled as a voltage source in series with a resistor adopted from ADVISOR model where their values are functions of battery SoC and temperature. In Figure 3.19, V_{oc} is the open-circuit voltage which is the terminal voltage at zero current flowing in or out of the battery. The internal resistance value (R) also depends on the state of the battery, either charged or discharged. In this research, the data were taken from the ADVISOR software as listed in Table 3.3, which was derived from the experimental results of tests conducted by NREL on NiMH batteries at a temperature of 25°C. The test complied with the PNGV-HPPC procedure (AVL, 2010).

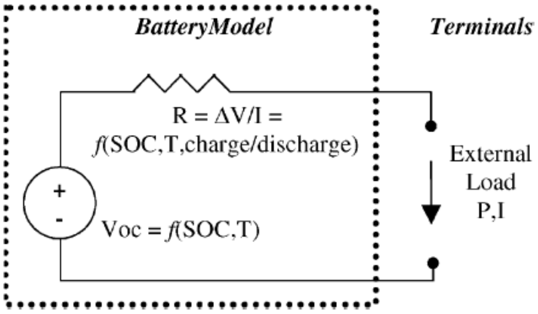

Figure 3.19 Internal resistance battery model electrical schematic

(Markel, 2002)

SoC	0.0	0.1	0.2	0.3	0.4	0.5	0.6	0.7	0.8	0.9	1.0
V_{oc}	7.2370	7.4047	7.5106	7.5873	7.6459	7.6909	7.7294	7.7666	7.8076	7.9143	8.3645
R_{chg}	0.0235	0.0220	0.0250	0.0198	0.0198	0.0196	0.0198	0.0197	0.0203	0.0204	0.0204

Table 3.3 NiMH battery data (AVL, 2010)

For this battery model, V_{oc} and R are known from Table 3.2. The charging current and the updated SoC are calculated as follows:

$$R \cdot I^2 + V_{oc} \cdot I + P = 0 \tag{3.53}$$

$$I = \frac{-V_{oc} + \sqrt{V_{oc}^2 - 4P \cdot R}}{2 \cdot R} \tag{3.54}$$

$$SoC(t) = SoC(0) + \frac{1}{3600 \cdot C_{batt}} \int_0^t I(t)dt \tag{3.55}$$

Since the charging current is positive, the SoC increases as regenerative power is stored in the battery. The next section (3.5) discusses the algorithms used to distribute the brake demand from the driver.

3.5 Torque distribution strategy

After determining the braking demand in terms of pressure for a given pedal travel or pedal force (or combination), the braking force on the vehicle is generated by both the friction brakes and the regenerative brakes on the front wheels and the friction brakes only on the rear wheels. The amount of braking force that the friction brakes generate when they are used is:

$$F_i = 2 \cdot P_{demand} \cdot A_c \cdot \mu_{pad} \cdot \frac{R_{disk}}{R_e} \tag{3.56}$$

for a disc brake, and for a drum brake:

$$F_i = P_l \cdot A_c \cdot (S_{leading} + S_{trail}) \cdot \frac{R_{drum}}{R_e} \tag{3.57}$$

These forces are the braking force generated at 1 wheel, thus for one axle these are multiplied by 2.

The strategy would be to maximise the regenerative braking force, which is generated by the electric M/G, in order to recover more braking energy. But the amount of regenerative braking is limited by the capacity of the M/G. The algorithm to distribute braking demand to friction and regenerative brakes is presented in Figure 3.20. To avoid wheel lock, the brake force at the tyre/road interface must not be higher than the maximum grip, which is equal to the product of the vertical load and the adhesion coefficient *k*.

$$T_i \leq k \cdot N_i \tag{3.58}$$

Braking performance is measured by the adhesion utilisation that determines how close the braking force is to the point of wheel lock and is defined as:

$$f = \frac{z}{k} \tag{3.59}$$

It is apparent that the braking force at the front axleT_{1_demand} is limited by the locking force (kN_1). After this point the braking force on the wheel (with the wheel locked and not rotating). The sliding friction force $F = \mu_t N_i$ applies only when the braking demand is higher than the braking force available. In real applications, ABS is used to prevent the wheel from locking and an algorithm was proposed by Wang et al (Wang 2008) in which the regenerative brake was disengaged when the ABS system was activated as shown in Figure 3.21.

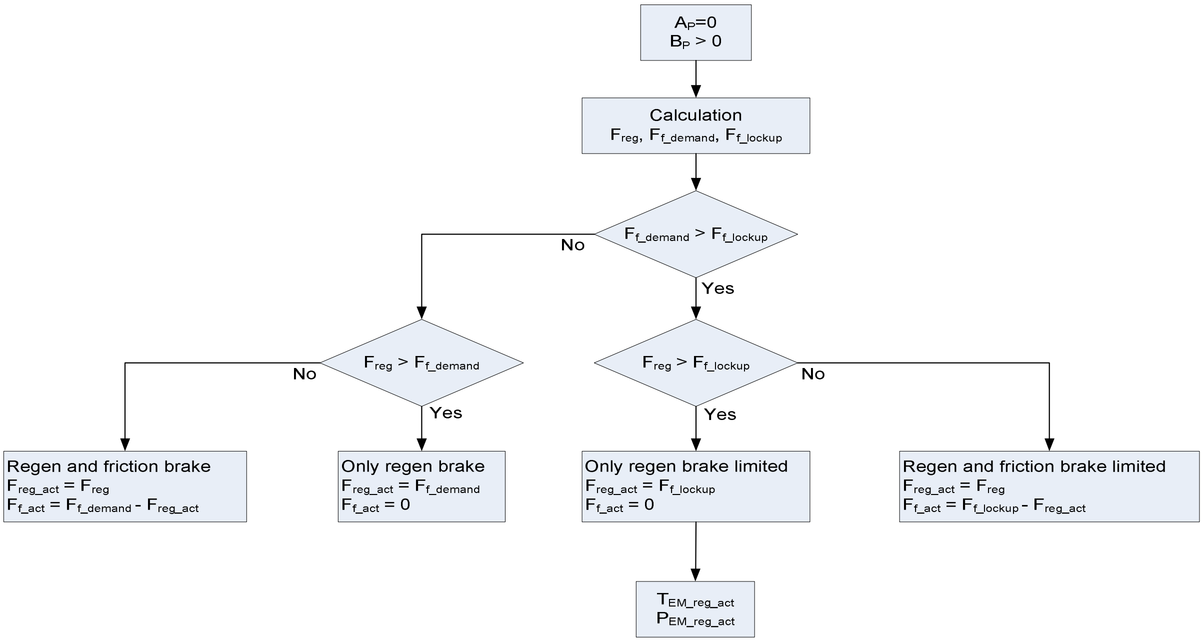
$A_P=0$
$B_P > 0$
Calculation
F_{reg}, F_{f_demand}, F_{f_lockup}
$F_{f\_demand} > F_{f\_lockup}$
No
Yes
$F_{reg} > F_{f\_demand}$
No
Yes
$F_{reg} > F_{f\_lockup}$
No
Yes
Regen and friction brake
$F_{reg\_act} = F_{reg}$
$F_{f\_act} = F_{f\_demand} - F_{reg\_act}$
Only regen brake
$F_{reg\_act} = F_{f\_demand}$
$F_{f\_act} = 0$
Only regen brake limited
$F_{reg\_act} = F_{f\_lockup}$
$F_{f\_act} = 0$
Regen and friction brake limited
$F_{reg\_act} = F_{reg}$
$F_{f\_act} = F_{f\_lockup} - F_{reg\_act}$
$T_{EM\_reg\_act}$
$P_{EM\_reg\_act}$

Figure 3.20 Flowchart of series braking system (Wang, 2008)

Here, a modified algorithm for series braking system is proposed, in which wheel speed and yaw rate act as indicators of whether the vehicle is tending to become instable. Based on control techniques used in the ABS, the decision was made to activate the associated programs. If the program was not activated, mixed-mode braking was used only where the maximum regenerative braking force available was applied. In this research, only the friction brake was used when ABS or any other stability control programs were operational, even though the literature review (Chapter 2) indicated that the regenerative brake could actually improve the performance of such systems.

As shown in Figure 3.22, a parallel mixed-mode braking system does not compare the driver braking demand with the regenerative force available. The demanded braking force is delivered by the friction brakes and a set amount of regenerative force which is added. This is the reason why a parallel braking system recovers less braking energy than a series system.

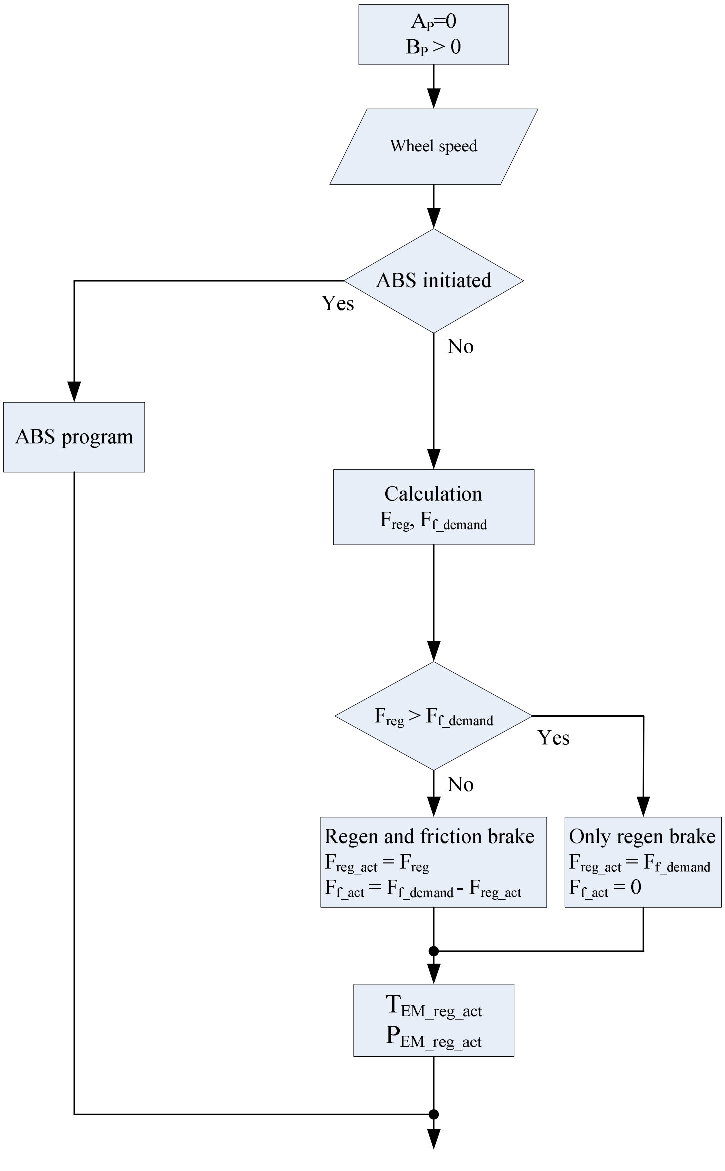
$A_P=0$
$B_P > 0$
Wheel speed
ABS initiated
Yes
No
ABS program
Calculation
F_{reg}, F_{f_demand}
$F_{reg} > F_{f\_demand}$
Yes
No
Regen and friction brake
$F_{reg\_act} = F_{reg}$
$F_{f\_act} = F_{f\_demand} - F_{reg\_act}$
Only regen brake
$F_{reg\_act} = F_{f\_demand}$
$F_{f\_act} = 0$
$T_{EM\_reg\_act}$
$P_{EM\_reg\_act}$

Figure 3.21 Algorithm for integrating series braking system with ABS

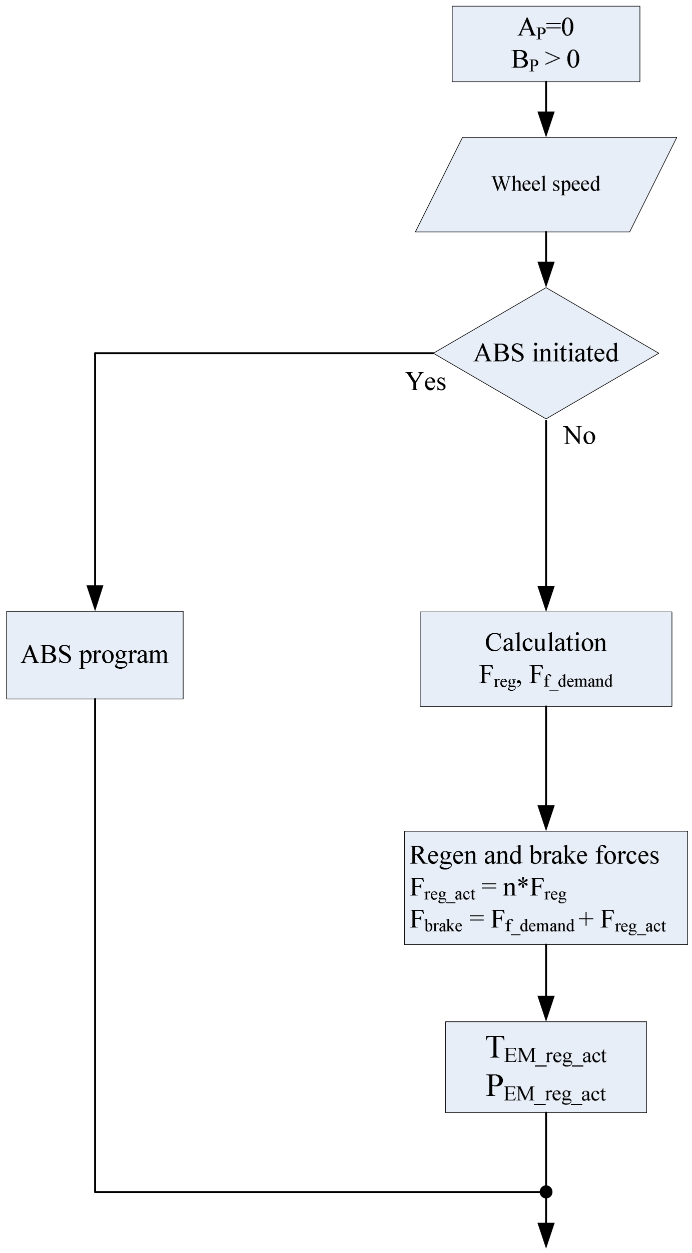
AP=0
BP > 0
Wheel speed
ABS initiated
Yes
No
ABS program
Calculation
Freg, Ff_demand
Regen and brake forces
Freg_act = n*Freg
Fbrake = Ff_demand + Freg_act
TEM_reg_act
PEM_reg_act

Figure 3.22 Algorithm for integrating parallel braking system with ABS

3.6 Chapter summary

During the motion of a road vehicle, traction and/or braking torques are generated at the wheels. The tyre generates opposing forces that depend on their interaction with the road, which can be represented by “Pacejka’s” or “Dugoff’s” tyre models, and as a result, longitudinal acceleration /

deceleration is developed. Lateral acceleration appears when the vehicle is manoeuvring, for example, cornering and turning.

When the driver exerts a force on the brake pedal in a conventional braking system, the force on the master cylinder piston is increased by the amplification provided by the brake pedal lever and the vacuum booster. The brake pedal characteristic represented by the pedal force/travel relationship changes significantly with the operation of the vacuum booster. The opposing forces acting on the master cylinder piston includes spring force and seal friction forces. Actuation of the friction brakes causes kinetic energy to be converted into heat energy and temperature rise causes the friction coefficient of pad or lining to vary.

For simulation purpose, the pedal travel and/or the pedal force applied by the driver are converted into brake line pressure using an approximation function or a lookup table. The regenerative torque delivered by the M/G is initially determined from its speed-torque characteristic, and battery SoC and vehicle speed affect the actual torque that the M/G can generate. The regenerative power generated is a function of speed, torque and efficiency of M/G, and substituting that power into battery model equations, the battery current and SoC can be found.

If the lockup force on the wheels is known, the series braking system has four possible operating modes. But in a real application, the ABS is used to prevent wheel lock. The algorithms to integrate mixed-mode braking system with these safety systems have been introduced based on the principle of disabling the regenerative braking system when one or both of them are engaged.

CHAPTER 4

DYNAMIC MODEL OF COMBINED REGENERATIVE AND FRICTION BRAKING SYSTEMS

4.1 Introduction

This chapter starts by presenting detailed models of a 3-phase AC electric induction motor to derive equations for stator and rotor voltages. Since the DC motor is still used in lower power EV's, a mathematical model for this type of electrical machine is also discussed. These machines are controlled through power electronic devices which include inverters and "buck-boost" converters, and the operating principles and circuits of such devices are explained in Appendix B. They are effectively a set of switches using semiconductor devices that turn on or turn off the current to the motor, and the controller uses the requested torque to control the switching time of the inverter or converter and aims to generate the M/G torque that follows that requested from the vehicle controller. For an AC induction motor drive, DTC is the control method which is generally (and widely) used to achieve this aim, while less sophisticated current control is adopted for DC drive systems.

An hydraulic system model for the friction braking is presented which has been derived from the study of the pressure response to valves' opening and closing. Pressure control can be achieved by controlling solenoid current and thus the stroke of an actuation valve. In the hydraulic controller, the demanded wheel pressure can be compared with measured pressure to determine which valve must be opened or closed based on pressure threshold.

Finally, integration of a mixed-mode braking system with ABS is proposed. These systems are modular and have been developed separately and then included in the 3 DoF vehicle model. Using the complete vehicle braking system simulation allows that integration to be analysed.

4.2 Models of Induction Motor / Generators and DC Motor / Generators

The electromagnetic torque produced by an electric induction motor is a result of the interaction between the electromagnetic fields of the stator and those of the rotor. In the stator, 3-phase currents generate a rotating magnetic field in the radial direction. Because there is a relative movement between the stator and the rotor, a phase voltage is induced in the rotor. The rotor, whether solid iron or having a winding, is effectively short-circuited but with a finite resistance so that current flowing in this path produces a magnetic field. The stator is modelled as three Alternating Current (AC) voltage sources in series with resistances and reactances as shown in Figure 4.1.

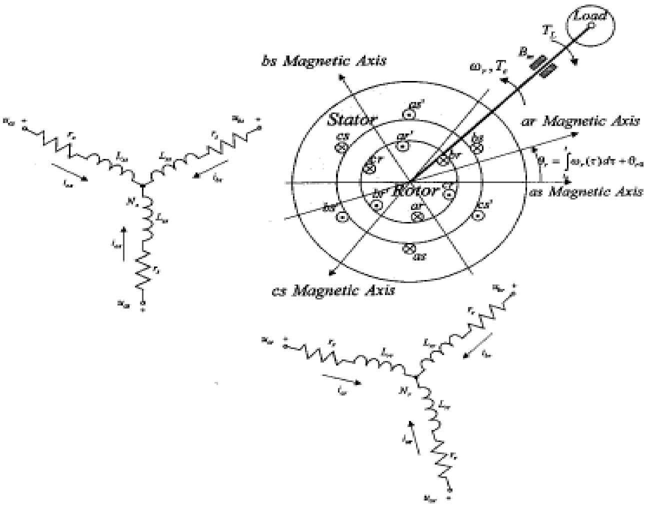
Load
T_L
B_m
ω_r, T_e
bs Magnetic Axis
Stator
as'
cs
ar'
cr
bs
br
ar Magnetic Axis
$\theta_r = \int \omega_r(\tau)d\tau + \theta_{r0}$
Rotor
br'
bs'
ar
cs'
as Magnetic Axis
as
cs Magnetic Axis
r_s
N_s
N_r
r_r

Figure 4.1 3-phase symmetric induction motor (Lyshevski, 1999)

Each phase of the stator winding is connected to the neutral point and, according to Kirchoff's current law; the sum of all stator currents is zero. Kirchoff's voltage law is applied to the stator and rotor windings as follows.

$$u_{as} = r_s i_{as} + \frac{d\psi_{as}}{dt} \tag{4.1}$$

$$u_{bs} = r_s i_{bs} + \frac{d\psi_{bs}}{dt} \tag{4.2}$$

$$u_{cs} = r_s i_{cs} + \frac{d\psi_{cs}}{dt} \tag{4.3}$$

$$u_{ar} = r_r i_{ar} + \frac{d\psi_{ar}}{dt} \tag{4.4}$$

$$u_{br} = r_r i_{br} + \frac{d\psi_{br}}{dt} \tag{4.5}$$

$$u_{cr} = r_r i_{cr} + \frac{d\psi_{cr}}{dt} \tag{4.6}$$

Flux linkage in the windings is defined as the sum of the flux generated by its own current and that of other currents, mathematically:

$$\begin{bmatrix} \psi_{as} \\ \psi_{bs} \\ \psi_{cs} \\ \psi_{ar} \\ \psi_{br} \\ \psi_{cr} \end{bmatrix} = \begin{bmatrix} L_{asas} & L_{asbs} & L_{ascs} & L_{ascar} & L_{asbr} & L_{ascr} \\ L_{bsas} & L_{bsbs} & L_{bscs} & L_{bsar} & L_{bsbr} & L_{bscr} \\ L_{csas} & L_{csbs} & L_{cscs} & L_{csar} & L_{csbr} & L_{cscr} \\ L_{aras} & L_{arbs} & L_{arcs} & L_{arar} & L_{arbr} & L_{arcr} \\ L_{bras} & L_{brbs} & L_{brcs} & L_{brar} & L_{brbr} & L_{brcr} \\ L_{cras} & L_{crbs} & L_{crcs} & L_{crar} & L_{crbr} & L_{crcr} \end{bmatrix} \begin{bmatrix} i_{as} \\ i_{bs} \\ i_{cs} \\ i_{ar} \\ i_{br} \\ i_{cr} \end{bmatrix} \tag{4.7}$$

Since the stator and rotor windings are similarly configured and apart by a rotation of 2π/3 magnetically:

$$\mathbf{L}_s = \begin{bmatrix} L_{ls} + L_{ms} & -L_{ms}/2 & -L_{ms}/2 \\ -L_{ms}/2 & L_{ls} + L_{ms} & -L_{ms}/2 \\ -L_{ms}/2 & -L_{ms}/2 & L_{ls} + L_{ms} \end{bmatrix} \tag{4.8}$$

$$\mathbf{L}_r = \begin{bmatrix} L_{lr} + L_{mr} & -L_{mr}/2 & -L_{mr}/2 \\ -L_{mr}/2 & L_{lr} + L_{mr} & -L_{mr}/2 \\ -L_{mr}/2 & -L_{mr}/2 & L_{lr} + L_{mr} \end{bmatrix} \tag{4.9}$$

These matrices are constant, but the mutual inductances between the stator and rotor circuits are time-varying functions and, depending on the electric angular displacement θ_r of the rotor, for a sinusoidal function:

$$\mathbf{L}_{sr} = L_{sr} \begin{bmatrix} \cos\theta_r & \cos(\theta_r + 2\pi/3) & \cos(\theta_r - 2\pi/3) \\ \cos(\theta_r - 2\pi/3) & \cos\theta_r & \cos(\theta_r + 2\pi/3) \\ \cos(\theta_r + 2\pi/3) & \cos(\theta_r - 2\pi/3) & \cos\theta_r \end{bmatrix} \tag{4.10}$$

It is defined that

$$L_{ms} = \frac{N_s^2}{\Re_m} \tag{4.11}$$

$$L_{mr} = \frac{N_r^2}{\Re_m} \tag{4.12}$$

$$L_{sr} = \frac{N_s N_r}{\Re_m} \tag{4.13}$$

Equation (4.7) can be rewritten in compact form as follows:

$$\begin{bmatrix} \boldsymbol{\psi}_{abcs} \\ \boldsymbol{\psi}_{abcr} \end{bmatrix} = \begin{bmatrix} \mathbf{L}_s & \mathbf{L}_{sr} \\ \mathbf{L}_{sr}^T & \mathbf{L}_r \end{bmatrix} \begin{bmatrix} \mathbf{i}_{abcs} \\ \mathbf{i}_{abcr} \end{bmatrix} \tag{4.14}$$

Flux linkage derivatives in equation (4.1) up to equation (4.6) are given by:

$$\frac{d\boldsymbol{\psi}_{abcs}}{dt} = \mathbf{L}_s \frac{d\mathbf{i}_{abcs}}{dt} + \mathbf{i}_{abcr} \frac{d\mathbf{L}_{sr}}{dt} + \mathbf{L}_{sr} \frac{d\mathbf{i}_{abcr}}{dt} \tag{4.15}$$

$$\frac{d\boldsymbol{\psi}_{abcr}}{dt} = \mathbf{L}_r \frac{d\mathbf{i}_{abcr}}{dt} + \mathbf{i}_{abcs} \frac{d\mathbf{L}_{sr}}{dt} + \mathbf{L}_{sr} \frac{d\mathbf{i}_{abcs}}{dt} \tag{4.16}$$

The electromagnetic torque is derived by taking the partial differential of coenergy with respect to angular displacement:

$$T_e = \frac{p}{2}\frac{\partial W_c(i_{abcs}, i'_{abcr}, \theta_r)}{\partial \theta_r} \tag{4.17}$$

Where the coenergy is mathematically defined as:

$$W_c = \frac{1}{2}\mathbf{i}_{abcs}^T(\mathbf{L}_s - L_{ls}\mathbf{I})\mathbf{i}_{abcs} + \mathbf{i}_{abcs}^T\mathbf{L}'_{sr}\,\mathbf{i}'_{abcr} + \frac{1}{2}\mathbf{i}'^{T}_{abcr}\,(\mathbf{L}_r - L_{lr}\mathbf{I})\mathbf{i}'_{abcr} \tag{4.18}$$

Substituting equation (4.18) into equation (4.17) results in:

$$T_e = \frac{p}{2}\mathbf{i}_{abcs}^T\frac{\partial \mathbf{L}'_{sr}}{\partial \theta_r}\mathbf{i}'_{abcr} \tag{4.19}$$

$$\frac{\partial \mathbf{L}'_{sr}}{\partial \theta_r} = -L_{sr}\begin{bmatrix} \sin\theta_r & \sin(\theta_r + 2\pi/3) & \sin(\theta_r - 2\pi/3) \\ \sin(\theta_r - 2\pi/3) & \sin\theta_r & \sin(\theta_r + 2\pi/3) \\ \sin(\theta_r + 2\pi/3) & \sin(\theta_r - 2\pi/3) & \sin\theta_r \end{bmatrix} \tag{4.20}$$

The mechanical angular velocity of the rotor is determined using Newton's second law:

$$\frac{d\omega_{rm}}{dt} = \frac{1}{I}\left(T_e - B_m\omega_{rm} - T_L\right) \tag{4.21}$$

The electrical angular velocity is related to the mechanical angular velocity according to equation 4.22:

$$\omega_{rm} = \frac{2}{p}\omega_r \tag{4.22}$$

It is difficult to solve equations (4.15) and (4.16), even using Laplace transformation because the phase voltages are non-linearly dependent on the angular displacement θ_r. To reduce this complexity, machine variables (stator and rotor voltages, currents and flux linkages) are transformed to the corresponding quadrature, direct and zero (*qd0*) components using the Park transformation or any other suitable device. The axes of these components (relative to the reference frame) can be static or rotating at certain velocities as illustrated in Figure 4.2.

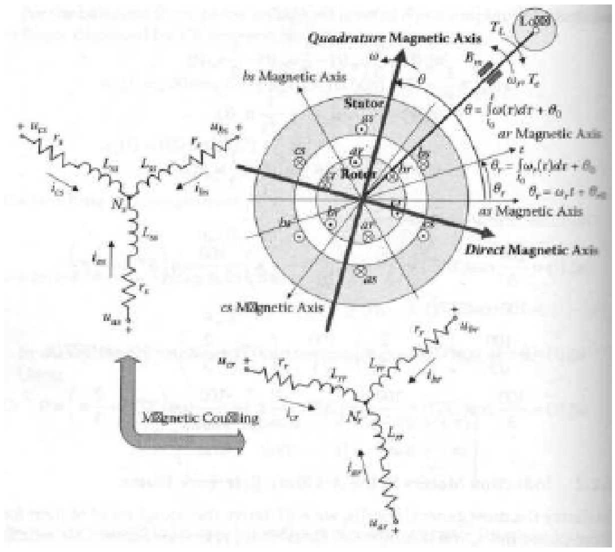
Quadrature Magnetic Axis
T_L
Load
ω
B_m
bs Magnetic Axis
θ
ω_r, T_e
Stator
$\theta = \int_{t_0}^{t} \omega(\tau)d\tau + \theta_0$
ar Magnetic Axis
$\theta_r = \int_{t_0}^{t} \omega_r(\tau)d\tau + \theta_{r0}$
θ_r
$\theta_r = \omega_r t + \theta_{r0}$
as Magnetic Axis
Rotor
Direct Magnetic Axis
cs Magnetic Axis
u_{cs}
u_{bs}
r_s
L_{ss}
i_{cs}
i_{bs}
N_s
i_{as}
u_{as}
u_{br}
u_{cr}
r_r
L_{rr}
i_{br}
i_{cr}
N_r
i_{ar}
u_{ar}
Magnetic Coupling

Figure 4.2 Induction motor with rotating reference frame (Lyshevski, 2008)

The detail can be found in Lyshevski (2008), the stator and rotor voltages in reference frame are:

$$u_{qs} = r_s i_{qs} + \omega(L_{ls} i_{ds} + L_m i_{ds} + L_m i'_{dr}) + \frac{d(L_{ls} i_{qs} + L_m i_{qs} + L_m i'_{qr})}{dt} \tag{4.23}$$

$$u_{ds} = r_s i_{ds} + \omega(L_{ls} i_{qs} + L_m i_{qs} + L_m i'_{qr}) + \frac{d(L_{ls} i_{ds} + L_m i_{ds} + L_m i'_{dr})}{dt} \tag{4.24}$$

$$u_{0s} = r_s i_{0s} + \frac{d(L_{ls} i_{0s})}{dt} \tag{4.25}$$

$$u'_{qr} = r'_r i'_{qr} - (\omega - \omega_r)(L'_{lr} i'_{dr} + L_m i_{ds} + L_m i'_{dr}) + \frac{d(L'_{lr} i'_{qr} + L_m i_{qs} + L_m i'_{qr})}{dt} \tag{4.26}$$

$$u'_{dr} = r'_r i'_{dr} - (\omega - \omega_r)(L'_{lr} i'_{qr} + L_m i_{qs} + L_m i'_{qr}) + \frac{d(L'_{lr} i'_{dr} + L_m i_{ds} + L_m i'_{dr})}{dt} \tag{4.27}$$

$$u'_{0r} = r'_r i'_{0r} + \frac{d(L'_{lr} i'_{0r})}{dt} \tag{4.28}$$

$$L_m = \frac{3}{2} L_{ms} \tag{4.29}$$

By replacing stator and rotor currents in equation (4.19) with *dq0* currents and some matrix manipulations, the electromagnetic torque is found as:

$$T_e = \frac{9PL_{ms}}{8}\left(i_{qs}i'_{dr} - i_{ds}i'_{qr}\right) \qquad (4.30)$$

In practice, the rotor is short-circuited and thus the rotor voltages in equations (4.26) and (4.27) are equal to zero. The rotor currents are generated as a result of induced EMF from the stator circuits and appear in terms containing i_{ds} and i_{qs} in these equations. Equations (4.23) up to (4.30) are used later in Chapter 5section 4 when the regenerative braking system is developed with Simulink software.

Unlike the AC induction motor, the field flux of a DC motor is produced by the stator circuit and the armature current flows to the rotor circuit through fixed brushes and the rotating commutator as shown in Figure 4.3. The field flux crosses the air gap to the rotor from the North pole and comes back to the South pole of the stator. The Rotor position is measured with respect to the South pole. Air gap flux density B_f is constant under the poles. While under the neutral zone, the flux density changes its polarity.

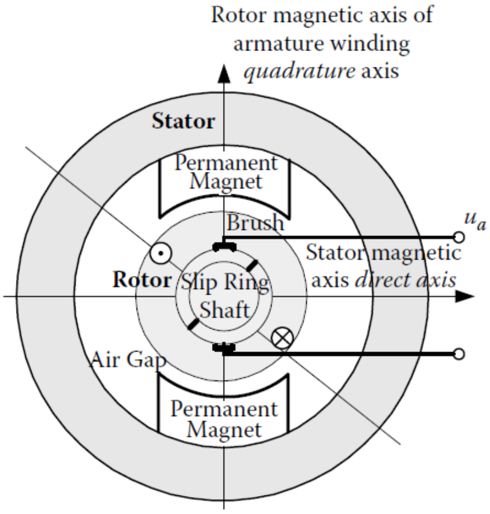
Rotor magnetic axis of armature winding *quadrature* axis
Stator
Permanent Magnet
Brush
u_a
Stator magnetic axis *direct axis*
Rotor
Slip Ring
Shaft
Air Gap
Permanent Magnet

Figure 4.3 Structure of DC motor and flux density (Lyshevski, 2008)

The field magnet is excited either by a permanent magnet or the current in the field winding. In this research separately excited DC motor is adopted as presented in Figure 4.4.

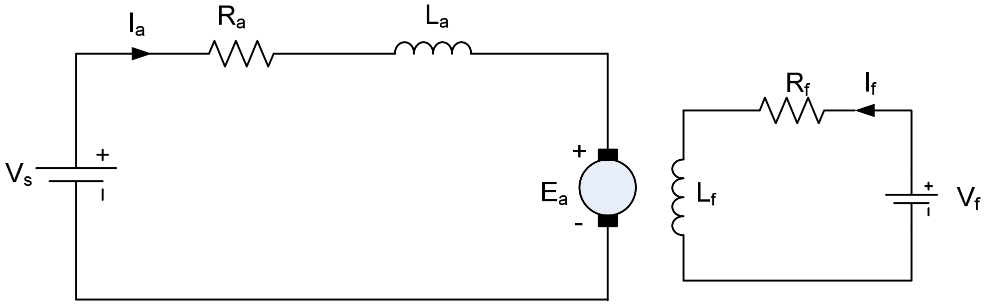

Figure 4.4 Separately excited DC motor

Applying Kirchoff’s voltage law to both armature and field circuits gives:

$$V_s = I_a R_a + L_a \frac{dI_a}{dt} + E_a \tag{4.31}$$

$$V_f = R_f I_f + L_f \frac{dI_f}{dt} \tag{4.32}$$

The induced EMF in the armature winding is formulated as:

$$E_a = K_a \Phi_P \omega_{rm} \tag{4.33}$$

If magnetic saturation is ignored, the flux is proportional to field current.

$$\Phi_P = K_f I_f \tag{4.34}$$

And the developed torque is:

$$T_e = K_a K_f I_f I_a \tag{4.35}$$

It can be seen that the DC motor model is much simpler than the induction motor model. This model of the DC motor is used in Chapter 5 section 5 with the help of Simulink software.

4.3 Control Systems of Motor / Generators

Buja and Kazmierkowski (2004) modified equation (4.30) to show the dependency of electromagnetic torque on the stator and rotor fluxes as follows:

$$T_e = \frac{L_M}{L_r}\psi_r \frac{1}{\sigma L_s}\psi_s \sin\delta_\psi \tag{4.36}$$

$$\psi_s = \sqrt{\psi_{sd}^2 + \psi_{sq}^2} \tag{4.37}$$

$$\psi_r = \sqrt{\psi_{rd}^2 + \psi_{rq}^2} \tag{4.38}$$

The principle of DTC is the modification of the stator flux and torque angle in order to control the torque. The stator flux is an integral of the back Electromotive Force (EMF), i.e.:

$$\psi_s = \psi_s(0) + \int (U_s - r_s I_s)dt \tag{4.39}$$

$$U_s = \sqrt{u_{ds}^2 + u_{qs}^2}$$

(4.40)

$$I_s = \sqrt{i_{ds}^2 + i_{qs}^2} \tag{4.41}$$

And the rotor flux is given by:

$$\psi_r = \frac{L_r}{L_m}\left(\psi_s - \sigma L_s I_s\right) \tag{4.42}$$

It has been shown (Fu et al., 2009) that by applying the selected voltage across motor terminals, the magnitude or angle of stator flux can be increased or decreased. A switching table DTC with circular stator flux path has been used in this research as shown in Figure 4.5. The idea was to select an entry in the optimal switching table of the inverter based on the estimation of electromagnetic torque and stator flux linkage. The stator flux reference is derived from motor speed considering constant torque and constant power operation and the torque reference is obtained from the vehicle controller.

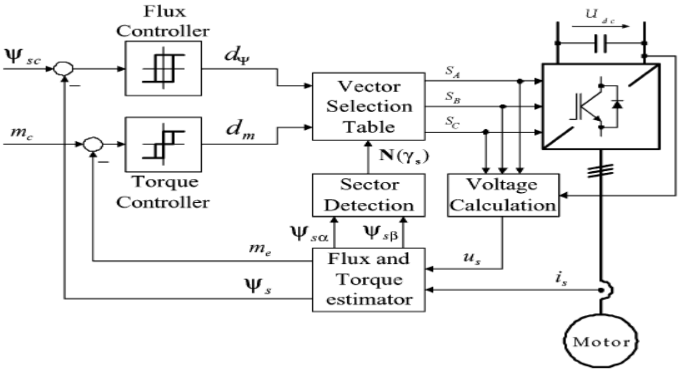
Flux Controller
Ψ_{sc}
d_Ψ
m_c
d_m
Torque Controller
Vector Selection Table
S_A
S_B
S_C
U_{dc}
$N(\gamma_s)$
Sector Detection
Voltage Calculation
$\Psi_{s\alpha}$
$\Psi_{s\beta}$
m_e
Ψ_s
Flux and Torque estimator
u_s
i_s
Motor

Figure 4.5 DTC scheme of induction motor for induction motor drives

(Buja, 2004)

The first block is voltage calculation which calculates the voltage vector by:

$$\overrightarrow{U_s} = U_{s\alpha} + jU_{s\beta} = \sqrt{2/3}U_{DC}\left(S_a + S_b e^{j2\pi/3} + S_c e^{j4\pi/3}\right) \tag{4.43}$$

For example, at phase a S_a = 0 will turn switch S_1 off and turn switch S_4 on, S_a = 1 will turn switch S_1 on and turn switch S_4 off. Switches of phases b and c operate in the same way using numbers S_b and S_c. Stator currents are also transformed into current vectors by:

$$\overrightarrow{I_s} = I_{s\alpha} + jI_{s\beta} = \sqrt{2/3}\left(i_a + i_b e^{j2\pi/3} + i_c e^{j4\pi/3}\right) \tag{4.44}$$

From the stator voltage and current vectors, the estimations of stator and rotor flux vectors can be found. Next, the torque estimation is determined using equation (4.36). The $\alpha\beta$-plane is divided into 6stors using either a circular or a hexagonal stator flux vector path as shown in Figure 4.6. The stator flux vector position in the plane can be obtained from:

$$\overrightarrow{\psi_s} = \psi_{s\alpha} + j\psi_{s\beta} \tag{4.45}$$

$$\theta_{\psi} = tg^{-1}\frac{\psi_{s\alpha}}{\psi_{s\beta}} \tag{4.46}$$

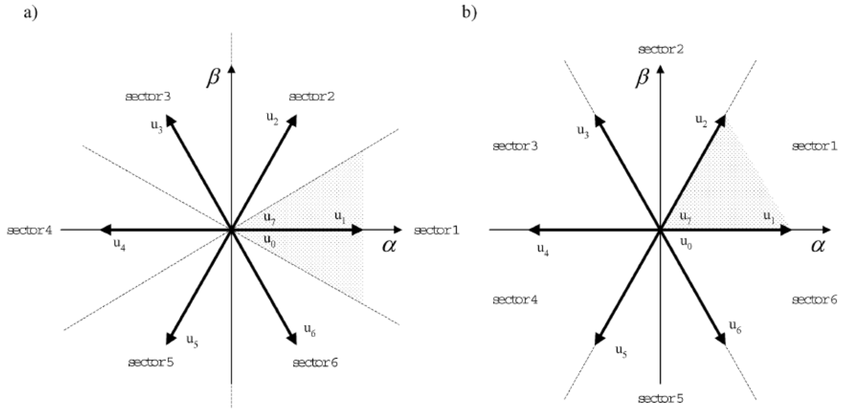

Figure 4.6 Sector definition: (a) circular and (b) hexagonal stator flux vector path (Buja and Kazmierkowski,2004)

The torque and stator flux errors are fed into the associated hysteresis controllers. The magnitude and direction of the errors determine the controller output as illustrated in Figure 4.7. The output of the flux controller has two possible values, 0 and 1, while the output of the torque controller can be -1, 0 or 1. To give an example, d_T remains 1 when the torque error decreases to zero and instantly changes to 0 after that. Then, d_T remains 0 when the torque error is less than ΔT or bigger than $-\Delta T$. Outside the interval, d_T can be either -1 or 1 depending on ΔT.

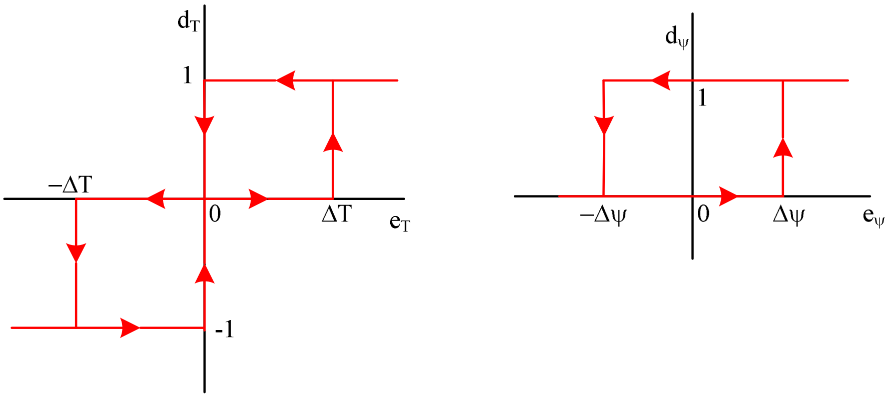

(a) (b)

Figure 4.7 (a) Torque controller (b) flux controller with hysteresis functions

The final step is to use the controller outputs d_T, $d_\psi$and sector number N(ψ) where the flux vector is located in choosing the switching table entry as shown in Table 4.1. This optimum switching table was initially proposed by Takahashi and Noguchi (1986), and the table entry is actually values of S_a, S_b and S_c numbers. Substituting these numbers into equation (4.43), 6 possible voltage vectors are obtained as listed in Table 4.2. The magnitude of each vector equals $0.8165U_{DC}$ and their angles are equally separated by 60°. When all these numbers equal 0 and 1, no vector is produced and as the result, the stator flux vector is nearly constant.

		Flux vector location N(ψ)					
		1	2	3	4	5	6
d_ψ=1	d_m=1	(1, 1, 0)	(0, 1, 0)	(0, 1, 1)	(0, 0, 1)	(1, 0, 1)	(1, 0, 0)
	d_m=0	(1, 1, 1)	(0, 0, 0)	(1, 0, 0)	(0, 0, 0)	(1, 1, 1)	(0, 0, 0)
	d_m=-1	(1, 0, 1)	(1, 0, 0)	(1, 1, 0)	(0, 1, 0)	(0, 1, 1)	(0, 0, 1)
d_ψ=0	d_m=1	(0, 1, 0)	(0, 1, 1)	(0, 0, 1)	(1, 0, 1)	(1, 0, 0)	(1, 1, 0)
	d_m=0	(0, 0, 0)	(1, 1, 1)	(0, 0, 0)	(1, 1, 1)	(0, 0, 0)	(1, 1, 1)
	d_m=-1	(0, 0, 1)	(1, 0, 1)	(1, 0, 0)	(1, 1, 0)	(0, 1, 0)	(0, 1, 1)

Table 4.1 Optimum switching table of DTC (Takahashi and Noguchi, 1986)

Vector	S_A	S_B	S_C	|V|	∠V
1	1	0	0	$0.8165U_{DC}$	0^0
2	1	1	0	$0.8165U_{DC}$	60^0
3	0	1	0	$0.8165U_{DC}$	120^0
4	0	1	1	$0.8165U_{DC}$	180^0
5	0	0	1	$0.8165U_{DC}$	240^0
6	1	0	1	$0.8165U_{DC}$	300^0

Table 4.2 Generated voltage vectors of DTC

Compared to the induction motor, a DC motor has a much simpler relationship between electromagnetic torque and motor current as indicated in Equation (4.35). Torque control can be obtained by modulating armature current, field current or both. In this research, both currents were modulated to achieve higher generated torque and the proposed traction control system is shown in Figure 4.8. First, the armature current reference is derived from the torque reference and the measured field current as follows:

$$I_{a,ref} = \frac{T_e}{K_a K_f I_f} \tag{4.47}$$

At the same time, the measured armature current is used to determine the field current reference:

$$I_{f,ref} = a + bI_a \tag{4.48}$$

Therefore, the field current is a linear function of the armature current. Next, the armature and field controllers generate the switch status S_1 and S_2 by applying hysteresis functions as illustrated in Figure 4.9. The hysteresis function allows the current to fluctuate around the current reference and thus the developed torque contains ripple. Finally, the input voltage of the buck converters is chopped according to the status of switches S_1 and S_2. As a result, the motor voltages are no longer continuous, but are square voltages with varying duty cycles.

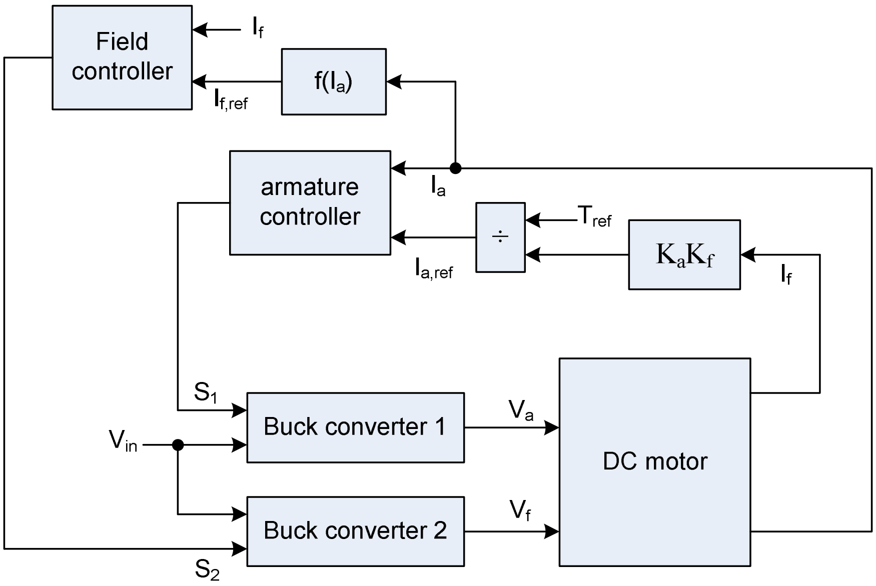
Field controller
I_f
$f(I_a)$
$I_{f,ref}$
armature controller
I_a
T_{ref}
÷
K_aK_f
$I_{a,ref}$
I_f
S_1
Buck converter 1
V_a
V_{in}
DC motor
Buck converter 2
V_f
S_2

Figure 4.8 Proposed traction system of DC drive

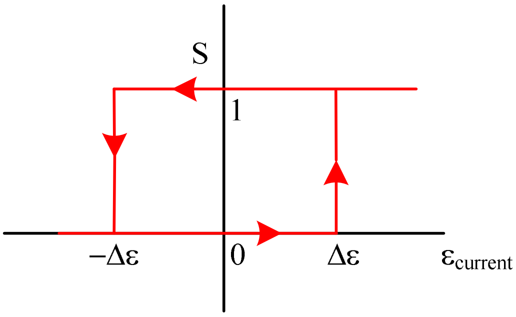
S
1
−Δε
0
Δε
$\varepsilon_{current}$

Figure 4.9 Hysteresis function for current controller

During vehicle traction, a torque reference is obtained based on accelerator pedal position and vehicle speed. Torque reference is not measured during vehicle braking when a parallel braking system is applied because the regenerative brake supplements the friction brakes to decelerate the vehicle. Equation (4.33) shows that the back EMF is affected by the motor speed and field current. Therefore, field current needs to increase while the vehicle (and M/G) speed decreases during braking. The field current reference can be derived from the motor speed or set as a ramp function of elapsed time as follows:

$$I_{f,ref} = a\frac{1}{\omega} \tag{4.49}$$

$$I_{f,ref} = a + bt \tag{4.50}$$

The proposed DC drive during braking is shown in Figure 4.10. Here, a boost converter has been used to direct the armature current to the battery. The armature current reference can be set to maximise energy recovery. A hysteresis function was still adopted for the basic logic in the armature and field controllers. The armature current direction opposes the field current direction during braking.

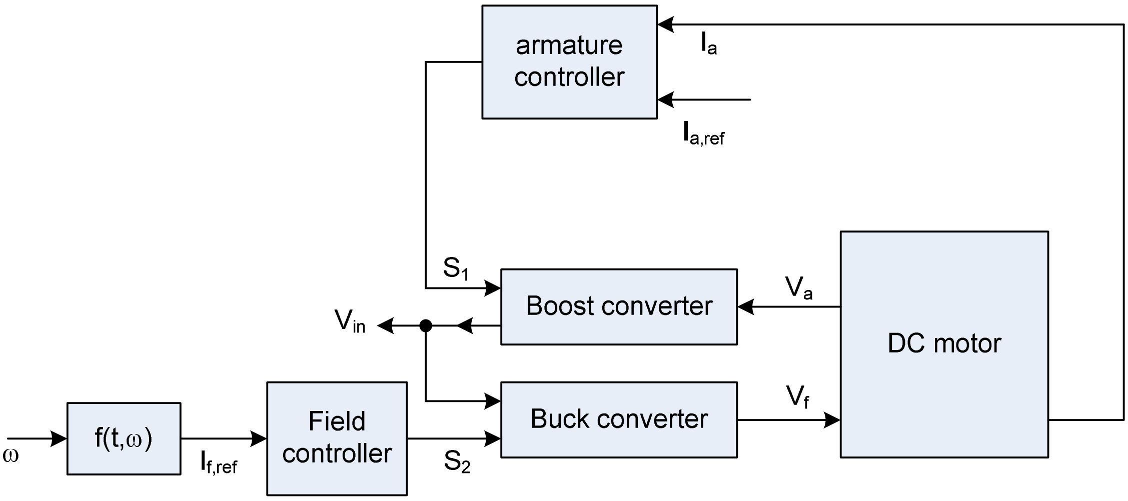
armature controller
Ia
Ia,ref
S1
Boost converter
Va
DC motor
Vin
Vf
Buck converter
ω
f(t,ω)
If,ref
Field controller
S2

Figure 4.10 Proposed braking system of DC drive

4.4 Pressure Control of Friction Brake Systems

A solenoid is used to move the valve. When a voltage is applied, the current flows to the coil from the battery and establishes a magnetic field in the air and the core. The magnetic energy stored depends on the current and magnetic circuit created, i.e:

$$W_e = \frac{1}{2} L i^2 \tag{4.51}$$

The asymmetric magnetic field pushes the iron core to the centre of coil to balance the field and the magnetic force is generated as follows:

$$F_e = -\frac{dW_e}{dx} = -\frac{1}{2}\left(i^2 \frac{\partial L}{\partial x} + 2Li\frac{\partial i}{dx} \right) \tag{4.52}$$

Assuming the second term of Equation 4.52 is much smaller than the first one, the force equation is then simplified into:

$$F_m = -\frac{1}{2} i^2 \frac{dL}{dx} \tag{4.53}$$

The relation of inductance to core displacement is given by:

$$\frac{dL}{dx} = -\frac{b}{(a+bx)^2} \tag{4.54}$$

Thus:

$$F_m = \frac{1}{2} i^2 \frac{b}{(a+bx)^2} \tag{4.55}$$

There are 3 equations governing the dynamics of the solenoid valve as follows:

$$\frac{di}{dt} = \frac{1}{L + i\dfrac{\partial L}{\partial i}} \left(U - Ri - iv\frac{\partial L}{\partial x} \right) \tag{4.56}$$

$$\frac{dv}{dt}=\frac{1}{m}\left(F_m(x,i)-K(x+G_0)-F_p(x)-bv-F_f\right) \tag{4.57}$$

$$\frac{dx}{dt}=v \tag{4.58}$$

The first equation is derived from Kirchoff’s voltage law while the second comes from Newton’s law. The relation between force and inductance to current and position is nonlinear. In this research, it has been assumed that the magnetic saturation is ignored and thus the inductance does not depend on the solenoid current.

Figure 4.11 shows the forces acting on the armature of the solenoid valve. Magnetic force must overcome the hydrokinetic and spring forces to allow the armature to move which changes the orifice area. According to the following equation, the fluid flow is determined by the upper and lower pressures, and the valve parameters.

$$Q=C_d A_0 \frac{\sqrt{2(P_1-P_2)}}{\sqrt{\rho}} \tag{4.59}$$

Both the discharge coefficient and the orifice size are determined by the structural configuration of the solenoid valve.

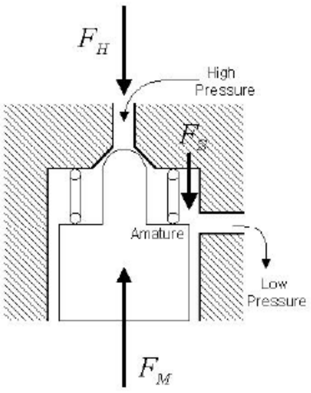

Figure 4.11 Force balance on solenoid valve(Choi et al., 2003)

Qi *et al*. (2004) used ANSYS software to determine the hydrokinetic force on the body valve and the result is depicted in Figure 4.12. Hydrokinetic force is the surface integral of the force acting on the rod of the solenoid valve caused by fluid pressure. The equation is used later in Chapter 5 when the solenoid valve model is developed in Simulink environment. From this figure, a plunger position of 0 mm means the valve is opened, while a position of 0.2 mm means the valve is closed. It can be observed that much higher hydrokinetic force is found at higher valve position. It was also found in the simulation of the solenoid valve that the time taken to open and close the valve after the step voltage was applied or removed from the coil, was 2.9 ms and 3.1 ms, respectively.

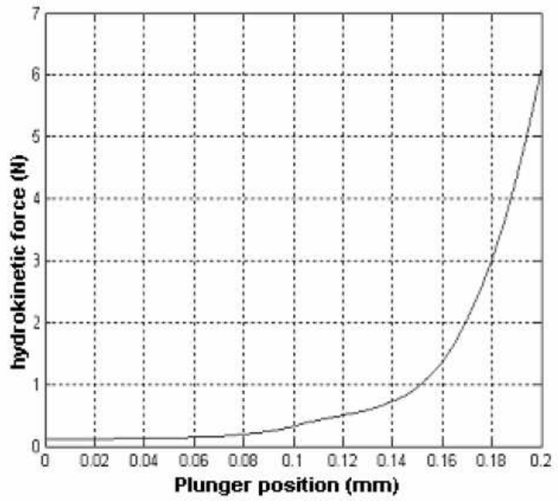

Figure 4.12 Hydrokinetic force-plunger position curve (Qi, 2004)

The control variable is the solenoid voltage which is switched on or off at high frequency to generate controlled current in the electric circuit and thus control the magnetic force in the valve movement. In this simulation, one inlet valve to increase slave cylinder pressure and one outlet valve to decrease slave cylinder pressure have been used in the friction braking system as shown in Figure 4.13. The opening and closing operations of these valves were determined from pressure measurement, and the control criteria were:

$error > \theta_{upper}$: pressure apply control

$\theta_{lower} \leq error \leq \theta_{upper}$: pressure hold control

$error < \theta_{lower}$: pressure dump control

where *error* is difference between the desired pressure and measured pressure. Firstly, “pressure apply” control means the inlet valve is directed to open and the outlet valve is directed to close. Secondly, both valves are directed to close in pressure hold control. Finally, the controller commands the inlet valve to close and the outlet valve to open in pressure dump control.

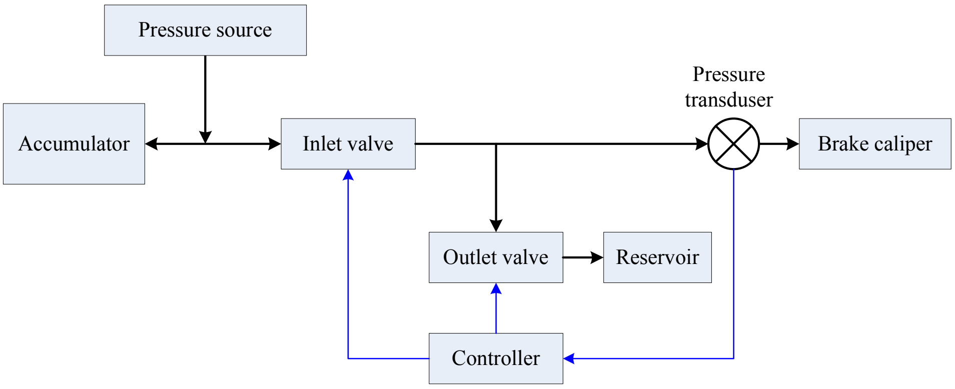
Pressure source
Pressure transduser
Accumulator
Inlet valve
Brake caliper
Outlet valve
Reservoir
Controller

Figure 4.13 Friction braking model using pressure control criteria

Fluid power is converted into mechanical power using a single-acting piston actuator. The fluid flowing into the wheel cylinder follows the law of conservation of mass, that is:

$$Q_{in} - Q_{out} = \frac{dV}{dt} + \frac{V}{\beta}\frac{dP}{dt} \tag{4.60}$$

Bulk modulus β that shows the degree of fluid compressibility and is expressed by:

$$\beta = \frac{-\Delta P}{\Delta V / V} \tag{4.61}$$

The formula describes how relative change in volume is proportional to pressure change. The final actuator in a hydraulic braking system is the brake caliper that converts fluid pressure into caliper piston movement. A caliper model in AMESim software (Ho, 2009) was used in this study which consisted of mechanical and hydraulic components as shown in Figure 4.14.

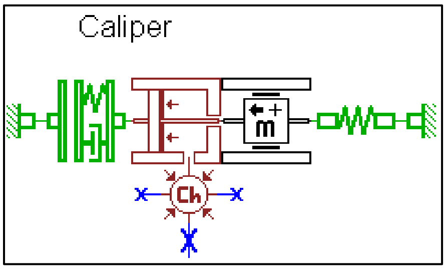

Figure 4.14 AMESim model of brake caliper (Ho,2009)

The caliper piston movement is given by the following equation:

$$M_1 \cdot \ddot{x} = F_{disc} + \left[\frac{P_1 \cdot A_{cal}}{2} - \left(F_{fric} \cdot \dot{x} + F_{vis} \cdot \dot{x}\right)\right] \tag{4.62}$$

$$F_{disc} = K_{pad} \cdot x + C \cdot \dot{x} \tag{4.63}$$

4.5 Integration of Mixed-Mode Braking with ABS

In Chapter 3 and previous sections of this Chapter, all aspects of the braking vehicle related to mixed-mode braking have been studied and modelled. An integrated model of the vehicle during braking is now introduced in which the mixed-mode braking system has been combined with the ABS system. The Integrated model of the braking system in an EV and HEV shown in Figure 4.15 was developed from an algorithm shown in Figure 3.21 (Wang 2008). As shown in Figure 4.15, the driver controls the vehicle through the steering wheel and the accelerator and brake pedals. The 3~~7~~-DoF vehicle model is used to determine the vehicle dynamics during braking on a straight road. The brake controller utilises wheel speed sensor to determine the vehicle state. Normally, a mixed-mode braking system is used to slow or stop the vehicle, but when the vehicle state indicates imminent loss of stability, the mixed-mode braking system is deactivated, and the ABS is activated. ABS apply friction braking torque on the wheels in performing their function.

The complexity of the control system for combined regenerative and a friction mode of braking has been reduced into a single transfer function. For the motor/generator model, the input is motor torque reference and the output is actual motor torque. Wheel pressure reference and friction braking torque are the input and output of the hydraulic brake model. By observing the time responses of the regenerative and the friction braking systems, these can be approximated by first-order or second-order transfer functions as follows:

$$T_m(s) = G_1(s)T_{m,ref}(s) \tag{4.64}$$

$$G_1(s) = \frac{K_1}{\tau_1 s + 1} \tag{4.65}$$

$$G_1(s) = \frac{\omega_{n,1}^2}{s^2 + 2\xi_1\omega_{n,1} + \omega_{n,1}^2} \qquad (4.66)$$

In the same way, the transfer functions for the hydraulically actuated friction brake model are:

$$T_{friction}(s) = G_2(s)P_{w,ref}(s) \qquad (4.67)$$

$$G_2(s) = \frac{K_2}{\tau_2 s + 1} \qquad (4.68)$$

$$G_2(s) = \frac{\omega_{n,2}^2}{s^2 + 2\xi_2\omega_{n,2} + \omega_{n,2}^2} \qquad (4.69)$$

Transfer function parameters *K*, τ, ξ and ω are determined and presented in Chapter 5 to simulate the mixed-mode braking system.

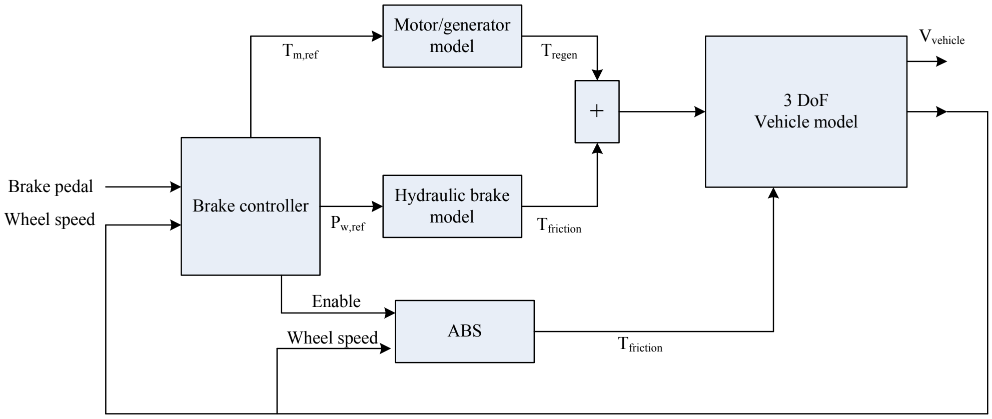
Motor/generator model
$T_{m,ref}$
T_{regen}
$V_{vehicle}$
+
3 DoF Vehicle model
Brake pedal
Wheel speed
Brake controller
Hydraulic brake model
$P_{w,ref}$
$T_{friction}$
Enable
ABS
Wheel speed
$T_{friction}$

Figure 4.15 Integrated model of braking system in EV and HEV

4.6 Chapter Summary

The induction motor has three-phase circuits in the stator and rotor. Using the Park transformation, a complex model of the induction motor has been reduced to linear equations. Stator and rotor currents are then neatly related to motor fluxes and voltages in the dq0 reference frame. The electromagnetic torque equation is also simplified with this transformation.

Voltage equations of the DC motor have been found applying Kirchoff’s voltage law to the armature and field circuits. The torque of DC motor is linearly proportional to the armature and field currents.

The control strategy chosen for the induction motor is switching-based DTC. Each switch of the inverter is turned on or off according to a vector selection table. A table entry is selected to keep flux and torque lower than the predetermined limits. Location ofthe flux vector also contributes to the vector selection. Both flux and torque are estimated from current measurement and voltage vector value. Due to the torque-current relation in the DC motor, torque control is obtained by controlling the field current. After the reference of field current is set, the hysteresis controller will maintain the field current around reference value by switching the buck-boost converter.

The solenoid valve for controlling the wheel pressure is represented by one electrical equation and one mechanical equation. The magnetic force generated by the current allows the valve to open or close. This makes the hydraulic pressure to rise, fall or hold. When the current is removed, the valve returns to the initial position by spring force. The control strategy maintains the pressure error remaining less than the specified threshold. In the wheel cylinder, the controlled pressure exerts a force on caliper piston according to the law of conservation of mass.

Detailed models of both regenerative and friction braking systems have been derived. Based on torque and pressure response to reference values, these systems are reduced into first-order or second-order linear differential equations. Combining them with models of the vehicle, brake controller, ABS allows their cooperation in any driving condition to be analysed.

CHAPTER 5

SIMULATIONS OF A MIXED-MODE BRAKING SYSTEM

5.1 Introduction

This Chapter presents all the simulations completed in this research. First, three drive cycles viz. FTP, US06 and EUDC, have been investigated to determine their braking-related characteristics in terms of braking time, average deceleration and braking energy. These drive cycles were chosen because they have been used extensively in the literature to study HEV's and EV's (e.g. Gao and Ehsani, 2001; Khoucha et. al., 2007; Peng et. al., 2008).

To understand braking dynamics, two Simulink models were developed, one used pedal force as input while the other employed pedal travel as input. Pedal force was considered since it is generated by the driver. Also, during the fail-safe condition, how hard the pedal must be pressed to give the same pressure as in the normal condition can be quantified. On the other hand, the brake system designed by one manufacturer (Ohtani et al., 2011) employed a pedal travel sensor to measure the driver demand. Therefore, the relationship between pedal travel and the master cylinder pressure is needed to enable the conversion of pedal effort to torque demand. From these models, wheel speeds, slip ratio and weight transfer could be analysed during braking. This was necessary to determine the regenerative braking ratio more accurately from the FTP drive cycle.

Knowing the static characteristics of the electric motor and battery and applying the torque distribution strategy, the power flow from the wheels to the battery can be quantified and the corresponding regenerative braking ratio given by Equation (5.13) can be found. Also, the torque demand on both regenerative and friction brakes could be derived that subsequently were used as the input to the dynamic models. Direct torque control and a pressure threshold technique were used to control the brakes. Beside the series braking system, the application of a DC motor in a parallel braking system has also been modelled within Simulink to highlight the differences in behaviour compared to an AC induction motor. A reference of field current during braking was either derived from the motor speed or time and its effect on regenerative current has been evaluated. Finally, the integration of the regenerative braking system with ABS has been completed. Two possible conditions have been simulated, with and without the deactivation of the regenerative brake. To facilitate the simulation, complex electrical and hydraulic systems were reduced into first or second order systems.

5.2 Braking Characteristics of Typical Drive Cycles

A “Drive cycle” is a time-speed profile representing a particular vehicle driving behaviour such as urban and highway driving. Each city in every country could claim to have its own characteristic drive cycle and these would differ from country to country. The purpose of drive cycles however is to provide some standard vehicle usage input in order to provide comparative experimental data e.g. for fuel consumption measurement or emissions measurement of a newly developed powertrain. Drive cycles are also useful to evaluate the energy recovery from regenerative braking systems in EV's and HEV's. There are about 45 drive cycles available worldwide and some of these are available in the ADVISOR software that can be used to test and analyse conventional, EV, HEV and fuel cell powered vehicles through computer simulation. 3 drive cycles were used in this research, viz. the FTP, US06 and the EUDC as shown in Figures 5.1, 5.2 and 5.3. The FTP and US06 cycles are used in the USA for passenger cars and the EUDC cycle is used in Europe for light duty vehicles (AVL, 2010).

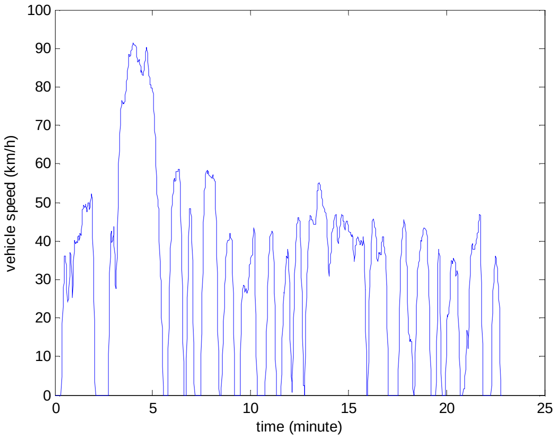

Figure 5.1 FTP drive cycle (AVL, 2010)

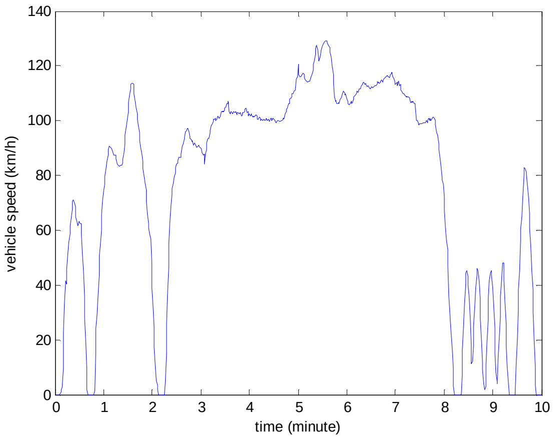

Figure 5.2 US06 drive cycle (AVL, 2010)

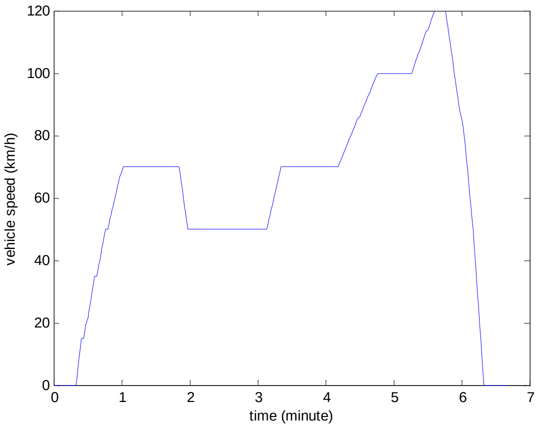

Figure 5.3 EUDC drive cycle (AVL, 2010)

Comparing the FTP and the US06 cycles in Figures 5.1 – 5.3, it is clear that the FTP represents urban driving where most speeds are less than 60km/h and the US06 represents highway driving with a cruising speed averaging about 100km/h and high braking energy. The speed is gradually increased in the EUDC up to 120km/h and then braking is performed in less than 30seconds. Since the FTP drive cycle lasts about 23minutes, it has more braking intervals than the US06 and EUDC cycles in which the driving is about 10minutes and 6.4minutes respectively.

A Matlab program was written to calculate braking time, initial speed, final speed, average deceleration and braking energy for each of these drive cycles as presented in Appendix C.1. ADVISOR stores these drive cycle data in Matlab files (.mat) named CYC_UDDS, CYC_US06 and CYC_EUDC, respectively. The program was then executed for each dataset and the results are listed in Tables 5.1, 5.2 and 5.3 which are sorted for braking energy higher than 100kJ. t_1 and t_2 were the initial and final times of each braking interval, V_1 and V_2 were the corresponding vehicle speeds, and the vehicle mass was 1500kg. Braking time, average deceleration and braking energy were calculated by:

$$t_{braking} = t_2 - t_1 \tag{5.1}$$

$$z_{average} = \frac{-1}{9.8}\frac{10}{36}\frac{V_2 - V_1}{t_2 - t_1} \tag{5.2}$$

$$E_{braking} = \frac{10^2}{36^2}\frac{1}{2}m(V_1^2 - V_2^2) \tag{5.3}$$

Among these drive cycles, the highest braking energy of 833kJ was obtained in the EUDC, however the braking time was quite long at 34seconds, while the highest deceleration of 0.2*g* occurred in the US06 drive cycle where the braking time was 9seconds.

No	t1 (sec)	t2 (sec)	t braking (sec)	V1 (km/h)	V2 (km/h)	E braking (kJ)	deceleration (g)
1	299	333	34	79.66	0.00	367.25	0.07
2	380	397	17	58.74	0.00	199.68	0.10
3	488	505	17	56.33	0.00	183.61	0.09
4	113	125	12	52.14	0.00	157.34	0.12
5	415	429	14	48.44	0.00	135.80	0.10
6	1302	1313	11	46.83	0.00	126.92	0.12
7	747	763	16	46.03	2.41	122.26	0.08
8	611	620	9	43.45	0.00	109.27	0.14
9	1137	1153	16	43.13	0.00	107.65	0.08
10	667	680	13	42.65	0.00	105.26	0.09

Table 5.1 Braking intervals in the FTP drive cycle

No	t1 (sec)	t2 (sec)	t braking (sec)	V1 (km/h)	V2 (km/h)	E braking (kJ)	deceleration (g)
1	96	128	32	113.78	0.00	749.19	0.10
2	467	493	26	101.39	0.00	594.89	0.11
3	579	594	15	83.04	0.00	399.07	0.16
4	337	346	9	127.94	106.86	286.47	0.07
5	32	41	9	62.44	0.00	225.64	0.20
6	552	560	8	48.28	0.00	134.90	0.17
7	521	530	9	45.87	1.93	121.53	0.14
8	538	546	8	45.06	3.86	116.65	0.15
9	508	514	6	45.38	11.10	112.06	0.16

Table 5.2 Braking intervals in the US06 drive cycle

No	t1 (sec)	t2 (sec)	t braking (sec)	V1 (km/h)	V2 (km/h)	E braking (kJ)	deceleration (g)
1	346	380	34	120.00	0.00	833.33	0.10
2	111	119	8	70.00	50.00	138.89	0.07

Table 5.3 Braking intervals in the EUDS drive cycle

Using a time-speed profile and Equation (3.1), the combination of front and rear longitudinal forces can be found. By relating these forces to each other and using Equation (3.6), the brake force can be determined if the wheel acceleration is known. To facilitate this, forward facing simulation is needed as shown in Figure 5.4. The inputs are throttle command and brake pedal force from the driver. The engine provides the traction torque to vehicle while the brake calipers give retarding torques. From the simulation results, the relation between the front and rear longitudinal forces was approximated, together with the vehicle deceleration relationship with wheel deceleration.

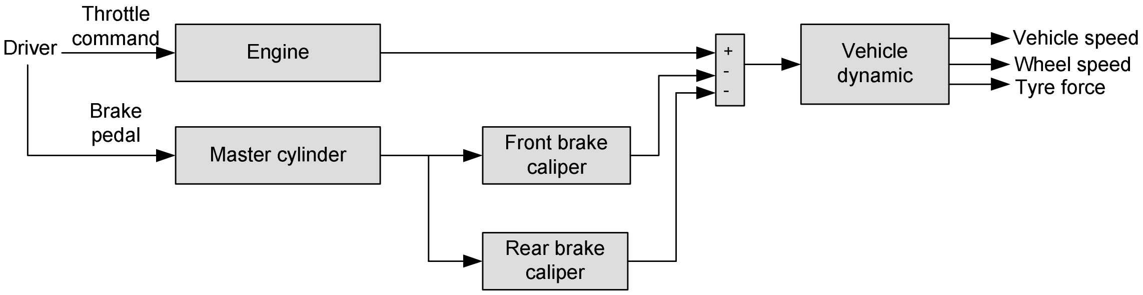
Throttle command
Driver
Engine
Brake pedal
Master cylinder
Front brake caliper
Rear brake caliper
+
-
-
Vehicle dynamic
Vehicle speed
Wheel speed
Tyre force

Figure 5.4 Forward facing simulation structure.

Figure 5.5 shows that the input to the backward facing simulation model is a time-speed profile known as the drive cycle. The vehicle model block contains assumptions made in the forward facing simulation. Using the M/G efficiency map, the electric power generated can be found and later the battery current and SoC will be known. Both the M/G and the battery models have been explained in Chapter 3 section 4 and Figure 5.17 shown that the SoC increased during braking. Equation 3.51 indicated that the SoC affected the available regenerative torque

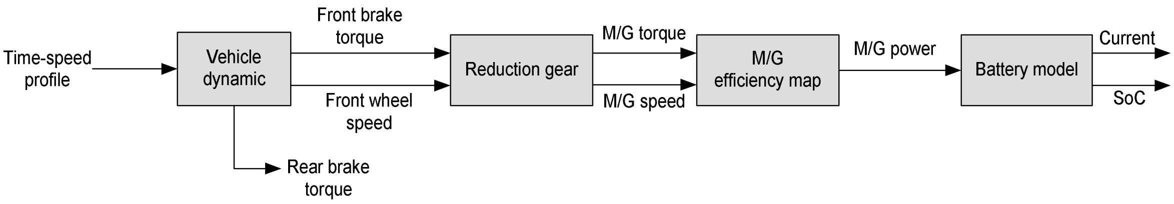
Time-speed profile
Vehicle dynamic
Front brake torque
Front wheel speed
Rear brake torque
Reduction gear
M/G torque
M/G speed
M/G efficiency map
M/G power
Battery model
Current
SoC

Figure 5.5 Backward facing simulation structure

A Simulink model was then developed to predict the braking dynamics in terms of vehicle speed, wheel speeds, slip and weight transfer as shown in

Figure 5.6; the program parameters are listed in Appendix C.2. The ‘Engine’ model is shown in Figure 3.2. The master cylinder is modelled via static functions relating pedal travel or pedal force with hydraulic pressure generated as shown in Figure 3.13 and Figure 3.14. Equation (3.56) and Equation (3.57) are used to model the front and rear brake calipers. The Vehicle dynamics block contains longitudinal vehicle and tyre models derived in section 3.2. Equation (3.50) was used to convert the force available at the tyre/road interface into regenerative brake torque at the M/G shaft. Both the M/G and the battery models have been explained in Chapter 3 section 4.

As indicated in Figure 5.6, the tyre force is multiplied by 2 because both front tyres and rear tyres have the same braking response. The model input was either brake pedal travel or pedal force as plotted in Figure 5.7. These brake demands were adjusted to generate an average deceleration around 0.17*g* and later around 0.14*g*. These values were chosen to show how the slip ratio of the front wheels relates to that of the rear wheels under different brake conditions. If the slip ratio was similar in these conditions, a constant could be used to represent the ratio. Both pedal travel and pedal force reached steady values of 31 mm and 56 N in 0.5s.

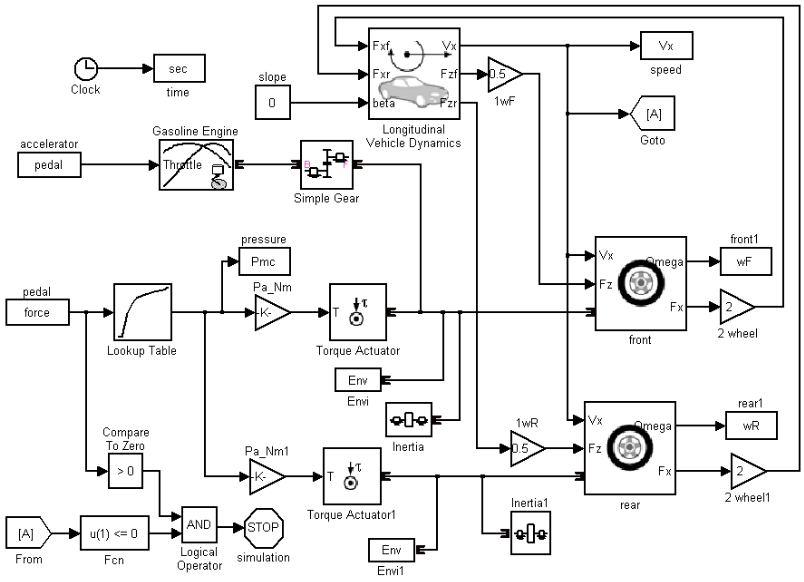

Clock
sec
time
slope
0
Fxf
Vx
Fxr
Fzf
beta
Fzr
Longitudinal Vehicle Dynamics
0.5
1wF
Vx
speed
[A]
Goto
accelerator
pedal
Gasoline Engine
Throttle
Simple Gear
pressure
Pmc
Pa_Nm
-K-
T
Torque Actuator
pedal
force
Lookup Table
Env
Envi
Inertia
Vx
Fz
Omega
Fx
front
front1
wF
2
2 wheel
Compare To Zero
> 0
Pa_Nm1
-K-
T
Torque Actuator1
1wR
0.5
Vx
Fz
Omega
Fx
rear
rear1
wR
2
2 wheel1
Inertia1
[A]
From
u(1) <= 0
Fcn
AND
Logical Operator
STOP
simulation
Env
Envi1

Figure 5.6 Simulink vehicle model for traction and braking dynamics

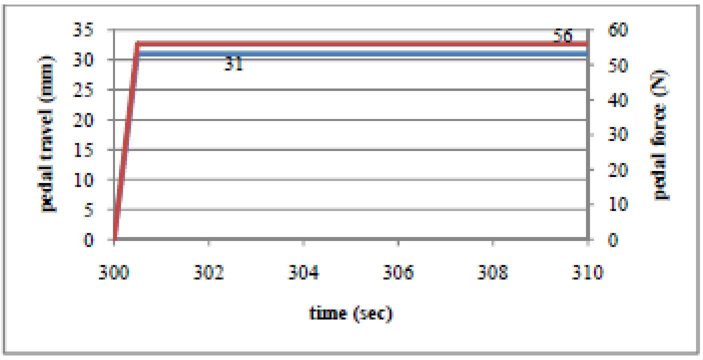

Figure 5.7 Pedal travel and pedal force during braking

Since the master cylinder pressure was modelled differently as discussed in Chapter 3section 4, the pressures generated were also different as shown in Figure 5.8.In Simulink, both the pedal force and travel inputs were time-dependent series as shown in the Table 5.4. It was assumed that these inputs changed linearly with time. With pedal force as input, the pressure rose after 0.25seconds. In contrast, the pressure increased as the pedal travel rose, following a quadratic function.

Time (s)	0	300	300.5	310
Force (N)	0	0	56	56
Travel (mm)	0	0	31	31

Table 5.4 Pedal force and travel data as inputs

Though the initial vehicle speeds of both models were the same at 60.4km/h, different pressure profiles resulted from the different braking times. It was found that the braking system with pedal travel as input had a braking time of 9.9seconds, while with the pedal force as input the braking time was 9.7seconds. The Simulink model with pedal force as input was subsequently used only to evaluate the braking dynamics because it is an actual demand and is sensed by the driver. On the other hand, the pedal travel is the feedback from brake system to the applied pedal force by the driver. The vehicle speed and its wheel translational speeds are shown in Figure 5.9. These speeds exhibited low slip since they were close each other. Compared to the front wheels, the slip of the rear wheels was smaller. Deceleration caused weight transfer of 446N from the rear axle to the front axle as shown in Figure 5.10.

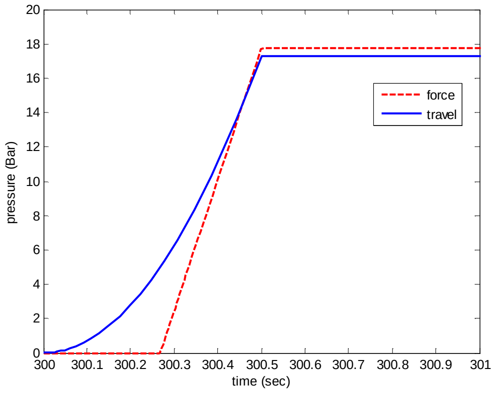

Figure 5.8 Master cylinder pressures during one second of braking

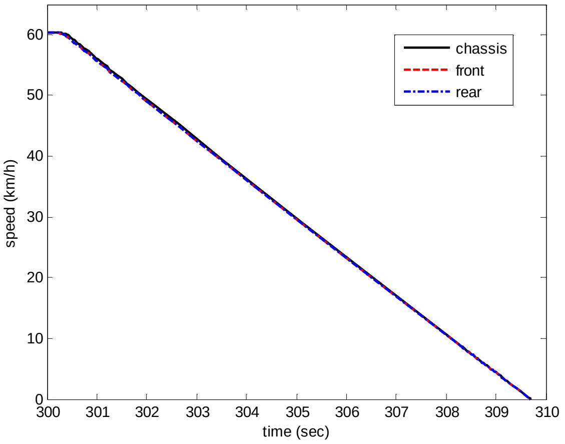

Figure 5.9 Vehicle road speed and translational wheel speeds

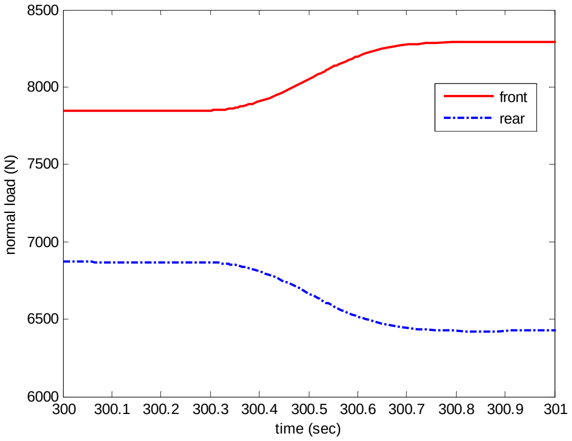

Figure 5.10 Load transfer from rear to front axles in braking

Equation (3.4) and equation (3.5) show that the weight transfer between the rear and the front wheels of a 2-axle rigid vehicle such as a car is affected by vehicle acceleration. During braking, the acceleration is negative, thus the vehicle weight on the front wheels increases and the vehicle weight on the rear wheel decreases with deceleration. The built-in Simulink models included longitudinal vehicle dynamics and tyre models. The former was similar to the model discussed in Chapter 3 section 2 given by

Equations (3.1) to (3.5). The latter was also based on Pacejka's model but the dynamic behaviour is included. The contact patch slip ratio is not constant and is modelled by the following equation:

$$\frac{1}{C_{Fx}}\frac{\partial F_x}{\partial \sigma_x^{'}}\frac{d\sigma_x^{'}}{dt} = -|V_x|\sigma_x^{'} - V_{sx} - \frac{1}{C_{Fx}}\frac{\partial F_x}{\partial F_z}\frac{dF_z}{dt} \tag{5.4}$$

Terms $\partial F_x / \partial \sigma_x^{'}$ and $\partial F_x / \partial F_z$ are determined from lookup tables indexed by the normal load and the contact patch slip ratio. Calculation of the longitudinal tyre force at the contact point used a lookup table indexed by the normal load and the contact patch slip ratio. At the rated vertical load of 3500N, the relation between the slip ratio and the longitudinal tyre force is shown in Figure 5.11.

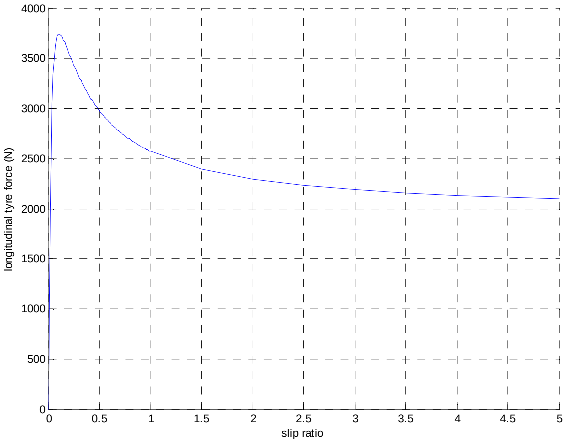

Figure 5.11 Longitudinal tyre force as function of σ_x at constant vertical load (Mathworks, 2010).

In section 5.3 the ratio of regenerative braking to friction braking in the drive cycles is calculated, and in this, two braking parameters were important *viz*. translational (vehicle) deceleration and the ratio of front to rear slip.

These parameters were used to find braking torque from the vehicle road speed change with time. Vehicle deceleration and the translational deceleration of the wheel are shown in Figure 5.12. From 300seconds to 300.3seconds, the pedal force did not generate hydraulic actuation pressure and thus wheel decelerations were zero. During the braking transient, vehicle deceleration increased linearly with time but the wheel decelerations experienced a second-order response in which oscillations occurred. After the pedal force was returned constant at 56N, the chassis and wheel decelerations were also constant at about 1.8m/s^2. It can be seen from Figure 5.13 that the slip ratios of the front and rear wheels were relatively small; at steady state they were 0.68% and 0.22% respectively.

The tyre model discussed in Chapter 3 is valid for the steady state condition. The results in Figure 5.12 were obtained from the built-in model in Simulink which is valid for both transient and steady state conditions. Further information about this complex tyre model can be sourced in Pacejka (2012).

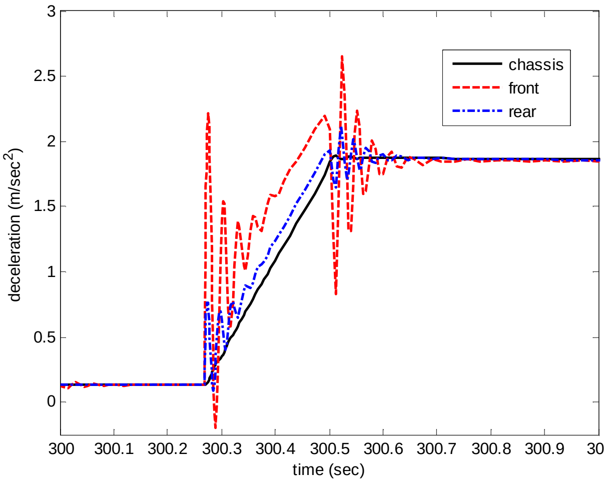

Figure 5.12 Vehicle decelerations during one second of braking

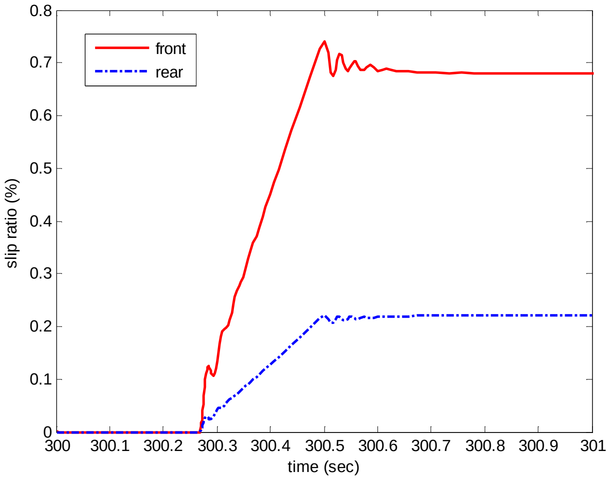

Figure 5.13 Slip ratios during one second of braking

Because the input to the backward-facing model was the vehicle speed profile, two assumptions were made in the calculation of braking torque. First, the slip ratio of the front wheel was 3 times the slip ratio of the rear wheel as calculated from the steady state values in Figure 5.13 whereas in this simulation a front to rear brake ratio of 74/26 was used. To confirm this result, the Simulink model was re-run for another initial speed of 72.9km/h and braking time of 14seconds. This was achieved by increasing the pedal force from 0 to 51 N in 0.5seconds and holding this value during braking. It was found that:

$$\frac{s_f}{s_r} = 3.18 \tag{5.5}$$

Also, assuming the adhesion coefficient is linear with at low slip ratio:

$$\mu_f = \alpha s_f \tag{5.6}$$

$$\mu_r = \alpha s_r \tag{5.7}$$

The relation between the longitudinal forces generated on the front and rear tyreis calculated as:

$$\frac{F_{xf}}{F_{xr}} = \frac{F_{zf}\mu_f}{F_{zr}\mu_r} \approx \frac{F_{zf}}{F_{zr}}\frac{3\alpha s_r}{\alpha s_r} \qquad (5.8)$$

$$\frac{F_{xf}}{F_{xr}} \approx 3\frac{F_{zf}}{F_{zr}} \qquad (5.9)$$

In the case of zero vertical acceleration and zero pitch torque, the vertical load forces are given by the following equations:

$$F_{zf} = \frac{h(F_d - m.\dot{V}_x) + l_2.m.g}{l_1 + l_2} \qquad (5.10)$$

$$F_{zr} = \frac{-h(F_d - m.\dot{V}_x) + l_1.m.g}{l_1 + l_2} \qquad (5.11)$$

These equations assume that the aerodynamic drag acts at the centre of gravity for simplicity (Mathworks, 2012). However, in practice the aerodynamic drag acts on the equivalent frontal area of the vehicle, and there may be a difference between the position of the centre of gravity and the centre of pressure arising from aerodynamic drag. The second assumption is that the vehicle deceleration and the translational deceleration of the wheels are similar as confirmed in Figure 5.12; the consequence is:

$$\frac{dV_x}{dt} \approx R_e\frac{d\omega}{dt} \qquad (5.12)$$

Under these assumptions, the vehicle motion is given by:

$$m\frac{dV_x}{dt} = F_{xf} + \frac{F_{zr}}{3F_{zf}}F_{xf} - F_d \qquad (5.13)$$

And, the brake torque at the front wheel is found by solving equation (5.14):

$$\frac{I_w}{R_e}\frac{dV_x}{dt} = \tau_{brake} - R_e F_{xf} \qquad (5.14)$$

5.3 Energy Recovery from the FTP Drive Cycle

Equation (5.14) to find braking torque for a given drive cycle was derived in section 5.2. Using a flowchart for a series braking system to distribute brake torque demand in Figure 3.18, a Matlab program was developed to calculate the regenerative braking ratio as presented in Appendix C.3. The regenerative braking ratio is mathematically defined as:

$$\varepsilon = 2\frac{\int P_{batt}dt}{m\left(V_1^2 - V_2^2\right)} \tag{5.15}$$

During braking, energy flows from the wheel to the M/G and then to the battery. Therefore, both the M/G and the battery were represented by the models in Figure 3.17 and 3.19 respectively. The data to generate the efficiency contour of the M/G is available in Appendix C4. From the FTP drive cycle and Equation (5.14), the regenerative ratio for braking energy greater than 75kJ is plotted in Figure 5.14. The average value of regenerative ratio based on this data is 56.2%. The number of braking events (11) indicated a large range about the average value. Figure 5.15 shows the efficiency of the M/G during the braking interval 746sec ≤ t ≤ 763sec and its average is 79% The charging efficiency of the battery is 97% on average. Therefore, 76.6% of the braking energy on the front wheels could theoretically be recovered.

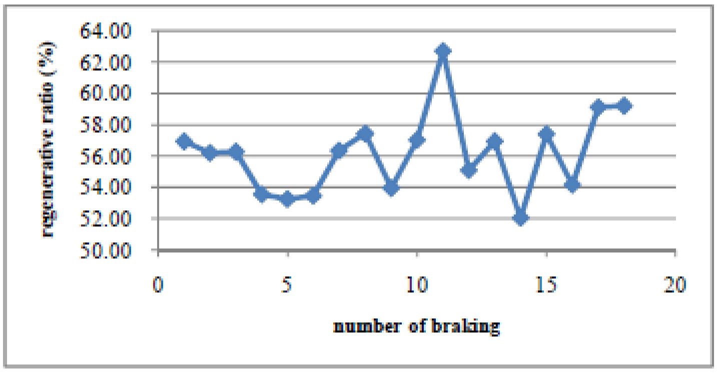

Figure 5.14 Regenerative ratio of FTP drive cycle

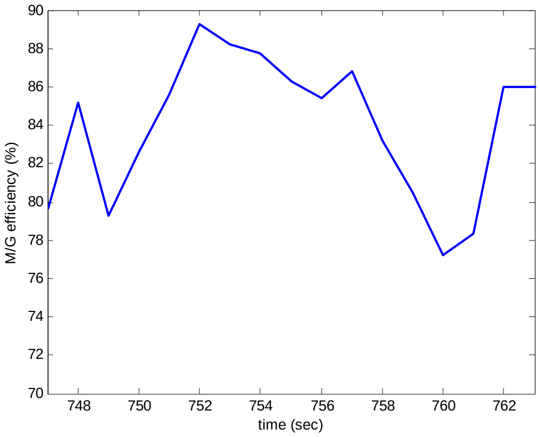

Figure 5.15 M/G efficiency in the regenerative braking period

It was assumed that the battery SoC was 50% when the braking event was started. The consequence was that all stored braking energy was used during the subsequent acceleration interval where the M/G assisted the ICE. For example, after the vehicle stopped at *t*=333seconds and stood still for 13seconds, the vehicle was accelerated from zero speed to 55km/h in 19seconds as plotted in Figure 5.16.

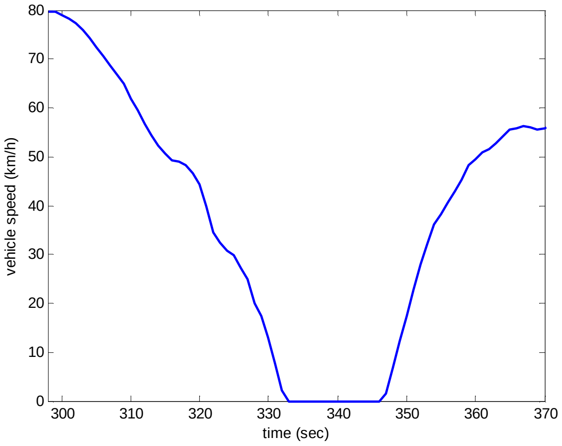

Figure 5.16 Braking and acceleration intervals in FTP drive cycle

For more realistic results, this assumption was then omitted. In the EV, the battery alone provided the traction power and thus the SoC at the beginning of a braking event was not 50% but 82.4% as shown in Figure 5.17. After braking the SoC increased to 82.7% and was followed by the traction interval which further reduced the SoC to 80.7% at t = 369seconds.The vehicle speed for 299sec ≤ t ≤ 370sec was plotted in Figure 5.16 where the braking event is followed by a short time at rest (zero speed)and then by acceleration. From Figure 5.17 it was found that at t = 350sec the SoC was 82.4% and using the speed profile it was deduced that the stored braking energy was used to accelerate the vehicle from 0km/h to 18km/h.

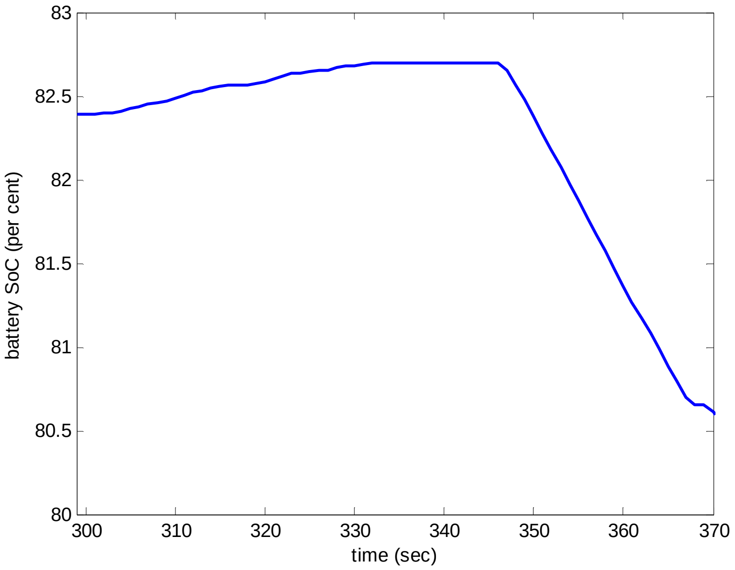

Figure 5.17 Battery SoC condition in both braking and traction intervals

Next, the effect of deceleration on the operating point of the M/G and the battery current was analysed. The two distinct deceleration profiles with similar initial speeds and the same braking times are shown in Figure 5.18. These decelerations were only approximations for the actual definition of deceleration since the time step of the drive cycle is large, $\Delta t = 1s$. Generally, the deceleration increased as the speed decreased and achieved around 0.14*g* in 10s. According to equation (5.13), the braking torque is proportional to the deceleration. Figure 5.19 shows the efficiency map of the M/G superimposed with the operating points of the M/G during braking due to the acceleration profiles in Figure 5.18. It can be observed that the M/G operates at speeds under 500rad/s and in the efficiency range from 80% to 90%. Also, a different deceleration profile results in a different operating point and this affects the M/G efficiency. During braking, the torque demand increased to about 65.2Nm while the maximum torque of the M/G was 191Nm.

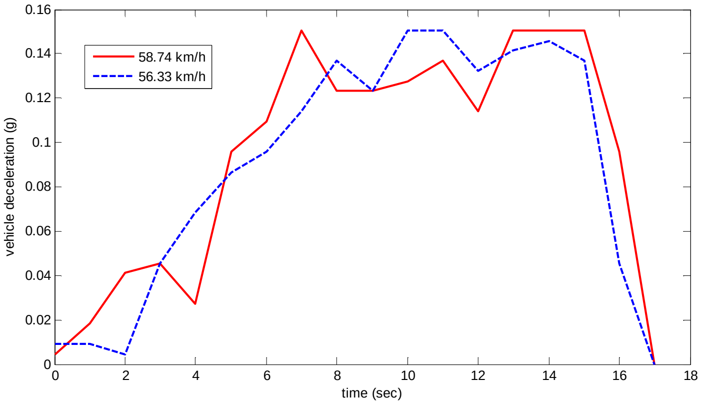

Figure 5.18 Deceleration profiles in the FTP drive cycle

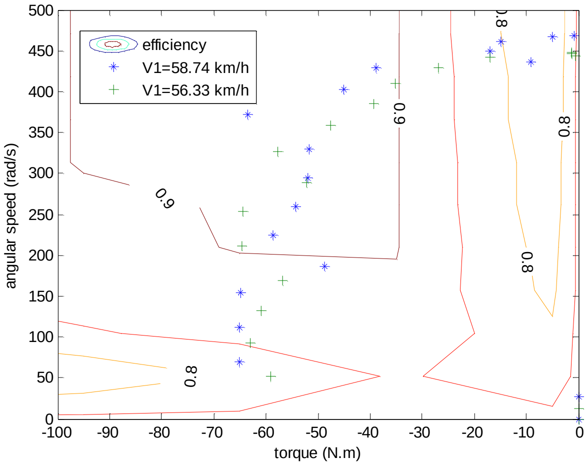

Figure 5.19 Operating points of the M/G in the FTP drive cycle

Following from equation (3.52) and equation (3.54), the battery current was affected by the operating point of the M/G. The battery current generated during braking for two braking intervals is shown in Figure 5.20. Firstly, the current increased as the deceleration increased, up to 109Amps at *t*= 7sec in the solid line and to 90.7Amps at t= 8sec in the dotted line, respectively. After that, the current decreased to zero as the vehicle speed reduced. It is observed that different deceleration profiles generated different current profiles and different peak currents.

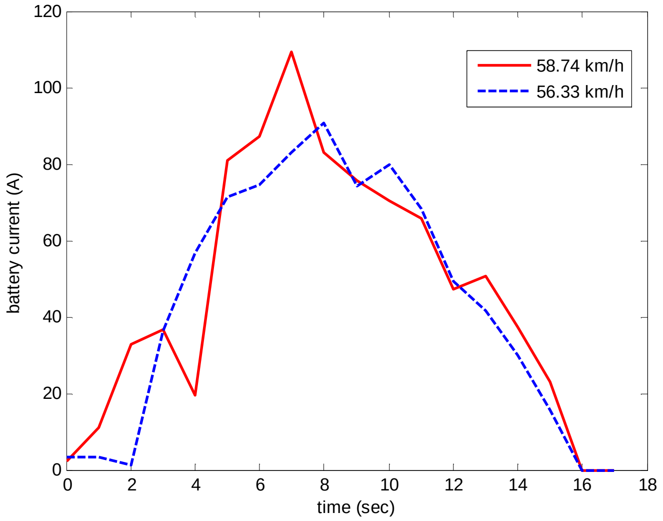

Figure 5.20 Battery currents during different braking intervals

5.4 Operation of a Series Braking System on Different Drive Cycles

In section 5.3, the amount of recovered braking energy and the operating points of the M/G were determined for each drive cycle. The Matlab program also output the brake torque demands that the regenerative and friction brakes should generate using the control systems discussed in Chapter 4 sections 3 and 4. Among many braking intervals in the drive cycle, the one with the highest deceleration was chosen to investigate the operation of both brakes because it demands the highest torque. Figures 5.21 and 5.22 show the vehicle speeds and torque demands of such braking intervals in the FTP and the US06 drive cycles. These figures were produced from the drive cycle using the flowchart of the `series braking system in Chapter 3 section 5 in the backward facing simulation. For the 15kW 1500rev/min induction motor, the maximum torque is 95.5Nm. With a reduction gear of 8, the maximum torque on the wheel is 764Nm. Therefore, the 15kW induction motor did not have sufficient torque to meet the demand on the US02 drive cycle, however it could provide the torque needed on the FTP drive cycle. As seen in Figure 5.21, the friction brake was applied when the braking commenced at high speed. After 4seconds, that brake was disengaged as the motor torque increased. The friction brake was initiated again at very low speed to stop the vehicle completely. The control strategy dictated that at very low speeds, the friction brake delivered all the torque needed.

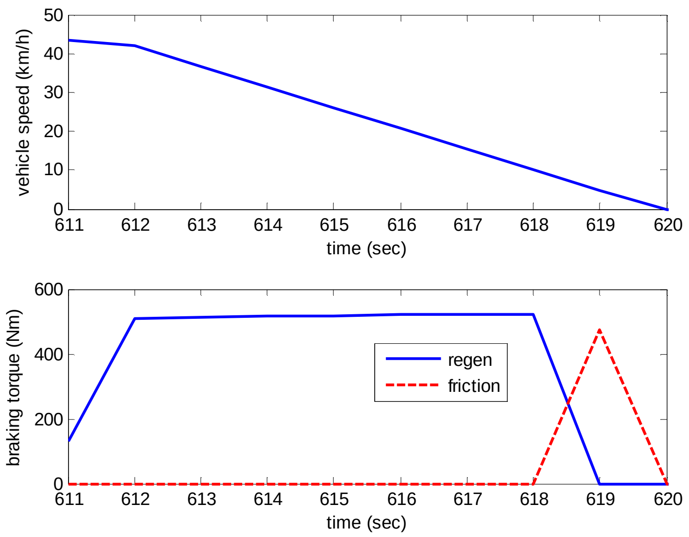

Figure 5.21 Vehicle speed and torque demands on the FTP drive cycle

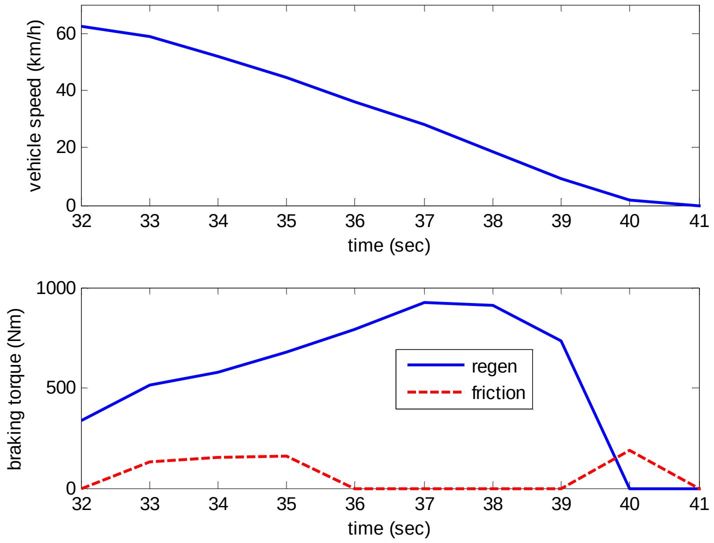

Figure 5.22 Vehicle speed and torque demands on the US06 drive cycle

For the 15kW induction motor with a nominal speed of 1500rev/min connected to the front axle via the reduction gear (*N*=4), the regenerative torque on the wheel was 382Nm for vehicle speeds less than 39.5km/h. Mostly, torque demands are lower at higher speeds, and the induction motor can provide the braking torque required for these braking events. Fortunately, the available torque was smaller in the constant power region (motor speed > 1500rev/min) as shown in Figure 5.23. Changing the gear ratio caused the nominal speed on the wheel to reduce but the maximum torque to rise as indicated by the dotted line in the graph. Changing the gear ratio from 4 to 8 causes the maximum motor torque to double and maximum vehicle speed to reduce to half. It was assumed that the maximum speed of the motor was three times the nominal speed. Therefore, increasing the ratio meant the maximum vehicle speed was reduced according to:

$$\omega_{\max} = \frac{V_{\max}}{R_e} \cdot N \tag{5.16}$$

To operate at the same maximum speed of the motor, a higher gear ratio results in a lower maximum vehicle speed.

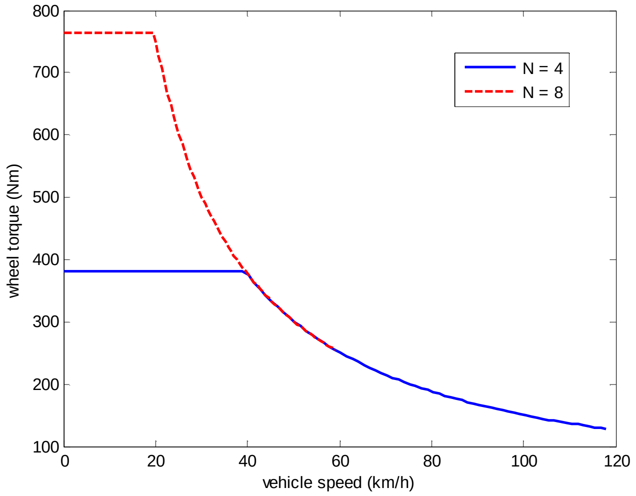

Figure 5.23 Speed-torque curve of the motor on the wheel

The Simulink model of the regenerative braking system using DTC as the control technique for the induction motor is shown in Figure 5.24, and its parameters are listed in Appendix C5. The power electronic device used in the simulation was the IGBT and its physical model was available in the Simulink software that includes efficiency in terms of switching resistance. The simulation model inputs are motor speed and negative motor torque. The negative demanded torque means that the induction motor acts as a generator. Feedback from the motor to the controller included current, voltage and speed. The direct torque controller then generates gate signals to switch the inverter and the torque generated to follow the torque demand is shown in Figure 5.25. The actual torque closely follows the desired torque though it contains a high frequency ripple (> 2 kHz) oscillating around the desired torque. As shown in the next paragraph, this torque oscillation does not affect the wheel speed. Figure 5.26 indicated that after the torque load was removed the oscillation in traction torque didnot cause a change in motor speed.

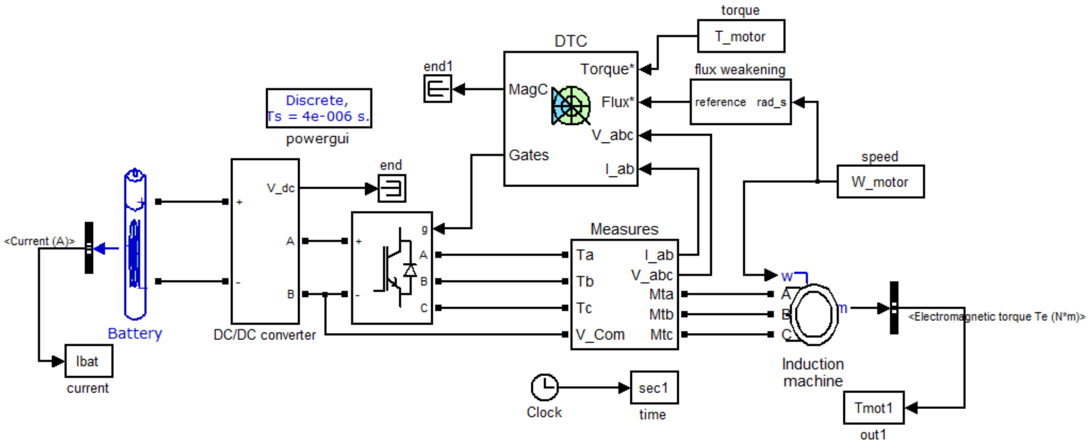
torque
T_motor
DTC
Torque*
MagC
Flux*
V_abc
Gates
I_ab
flux weakening
reference rad_s
end1
Discrete,
Ts = 4e-006 s.
powergui
end
V_dc
speed
W_motor
<Current (A)>
Battery
DC/DC converter
Ibat
current
Measures
Ta
Tb
Tc
V_Com
I_ab
V_abc
Mta
Mtb
Mtc
w
A
B
C
m
<Electromagnetic torque Te (N*m)>
Induction machine
Tmot1
out1
Clock
sec1
time

Figure 5.24 Simulink model of regenerative braking system

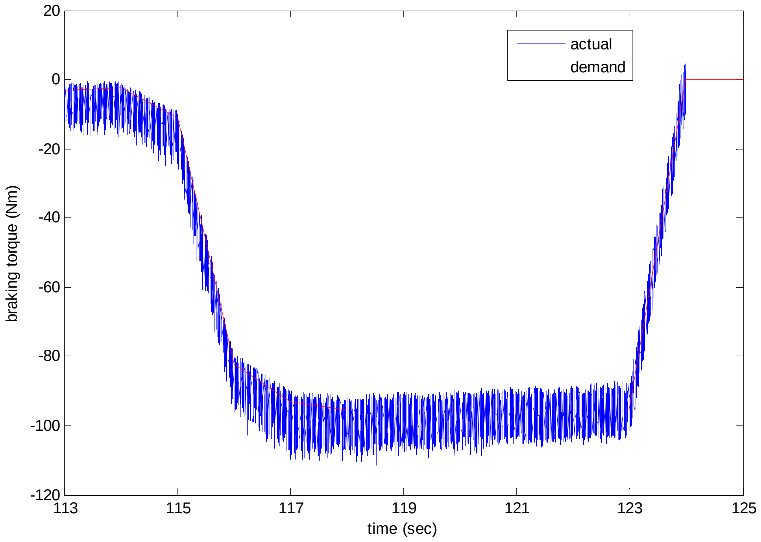

Figure 5.25 Oscillating regenerative torque caused by the direct torque controller

The above torque response can be generalised to observe all braking events in a drive cycle. However, the effect of torque ripple on the wheel speed could not be analysed since it was a backward-facing simulation where the wheel speed was the input to the model. Figure 5.26 shows the result from a forward-facing model where the inputs were load torque and target torque. It is observed that the motor speed was not affected by the oscillation of the traction torque. At *t* = 5sec, the motor was directed to decrease the traction torque from 93Nm to 0Nm and 90Nm torque was also removed in 10ms. After that, the motor torque oscillated around 0Nm while the speed remained constant close to 150rad/s.

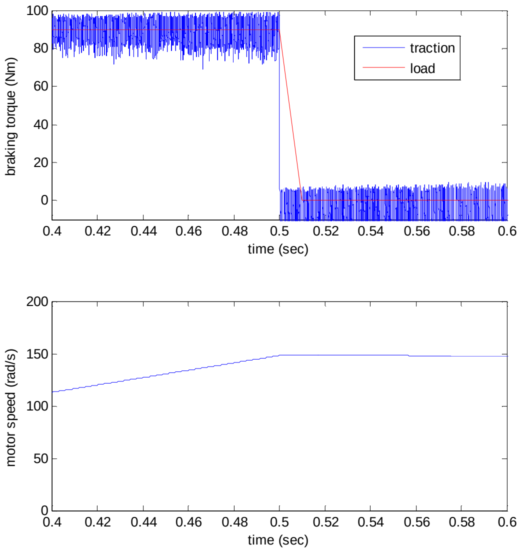

Figure 5.26 Torque and speed of the induction motor in the forward-facing model

As shown in the Simulink model, the controller output gate signals to the inverter which control the currents flowing to and from the induction motor. At *t* = 2.001s, the switch status of the inverter and the phase currents of the motor are shown in Figure 5.27. The controller directs phase *a* to connect to the positive terminal of the DC side while phase *b* and phase *c* connect to the negative terminal. This arrangement generated a regenerative current of 86.3 A flowing from phase *a* to the DC side and coming back to the motor through phase *b* and phase *c*. During the simulation, the controller updates the gate signals every 20 microseconds. The profiles of the motor currents due to the switching operation of the inverter are shown in Figure 5.28. They are not sinusoidal and their shapes are not similar.

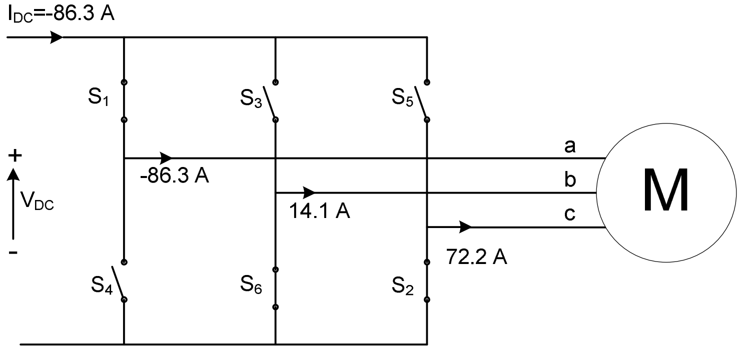

Figure 5.27 Switch status and motor currents (*t*=2.001s)

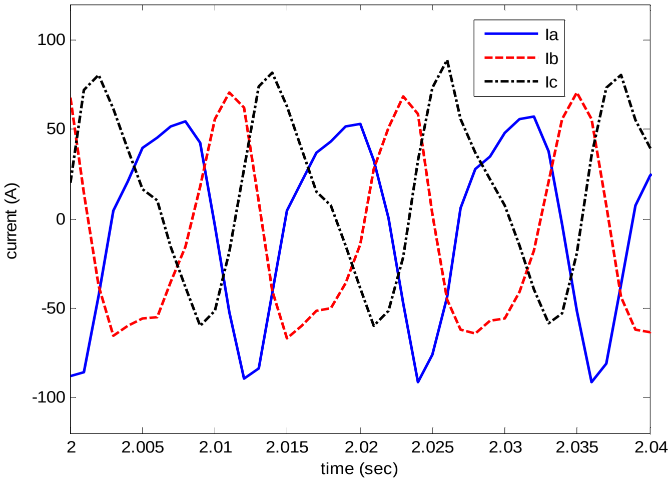

Figure 5.28 Phase currents of the induction motor

As well as the regenerative brake model, an hydraulic brake model was also developed using Simulink as shown in Figure 5.29. The model implemented pressure control in the brake caliper. The error input to the controller was defined as the difference between reference pressure and measured pressure. The control criteria discussed in Chapter 4 section 4 determined which valve must be opened, inlet or outlet valves. The controller output is a PWM signal to generate solenoid voltage. Using both electrical and mechanical equations of the solenoid, valve position was obtained. This was then used as input to the valve models which increased or decreased the pressure in the brake caliper. The simulation parameters of this brake are listed in Appendix C.6.One brake caliper was modelled by mass, spring and damper elements together with a hydraulic cylinder which converted hydraulic pressure into piston movement. Also, pad stiffness was modelled by a linear spring, while viscous friction and damping forces in the disc brake were represented by damping elements. The hydraulic fluid in the accumulator was initially pressurised with a pressure of 30bar. The controller compared the pressure demand with the pressure measured in the downstream side of the inlet valve to determine which valve was opened or closed using the pressure threshold criteria.

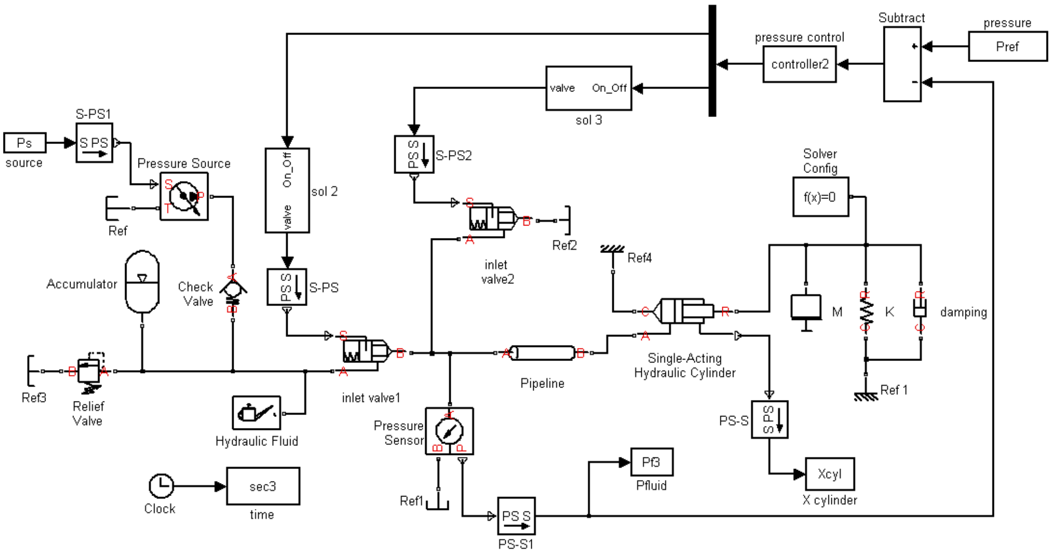
Subtract
pressure
pressure control
controller2
Pref
valve
On_Off
sol 3
S-PS1
Ps
S PS
source
Pressure Source
S
P
T
Ref
On_Off
valve
sol 2
PS S
S-PS2
S
A
B
inlet valve2
Ref2
Solver Config
f(x)=0
Ref4
Accumulator
Check Valve
A
B
PS S
S-PS
C
R
M
K
damping
Single-Acting Hydraulic Cylinder
Ref3
B
A
Relief Valve
inlet valve1
Pipeline
A
B
Ref 1
Hydraulic Fluid
Pressure Sensor
PS-S
S PS
Pf3
Pfluid
Xcyl
X cylinder
Clock
sec3
time
Ref1
PS S
PS-S1

Figure 5.29 Simulink model of hydraulic brake for one wheel

The available regenerative braking is limited by the vehicle speed by introducing a weighting factor in the torque equation. Since that factor is a linear function of vehicle speed, the transition rate from regenerative to friction braking is determined by the vehicle deceleration. The dotted line in Figure 5.30 is the friction brake demand generated by the mixed-mode braking system which rose steadily from *t*=618s. The friction demand reached its maximum value when the regenerative braking was totally disengaged at *t*=619s. The interval between *t*=617s and *t*= 620s is reproduced in Figure 5.31 to highlight the wheel pressure response to the brake demand. The pressure is controlled accurately although a small pressure fluctuation can be seen.

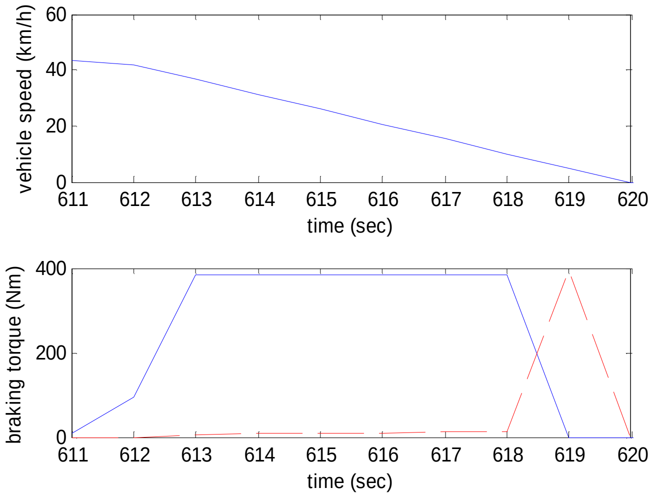

Figure 5.30 Vehicle speed and braking torques on the wheel

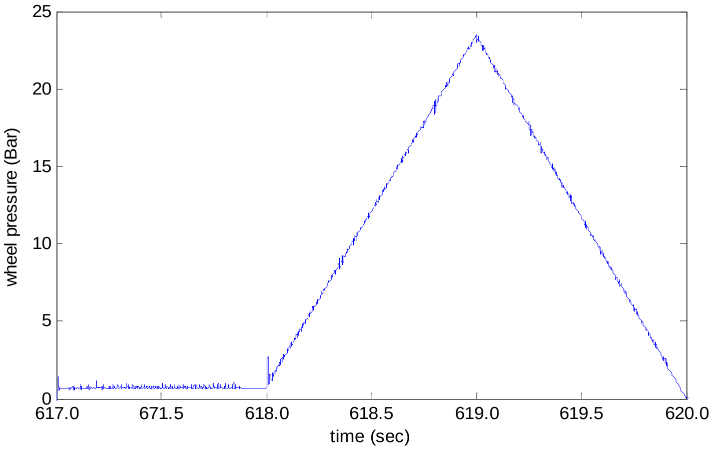

Figure 5.31 Controlled wheel pressure in the mixed-mode braking system

According to Equation (5.12), the braking force and hence the braking pressure is proportional to the vehicle deceleration. In the backward facing simulation, the braking pressure was obtained from vehicle deceleration. It is clear that the vehicle speed plot in Figure 5.25 did not show the change of vehicle deceleration. When the vehicle deceleration was plotted as shown in Figure 5.32, the reduction of vehicle deceleration can be seen.

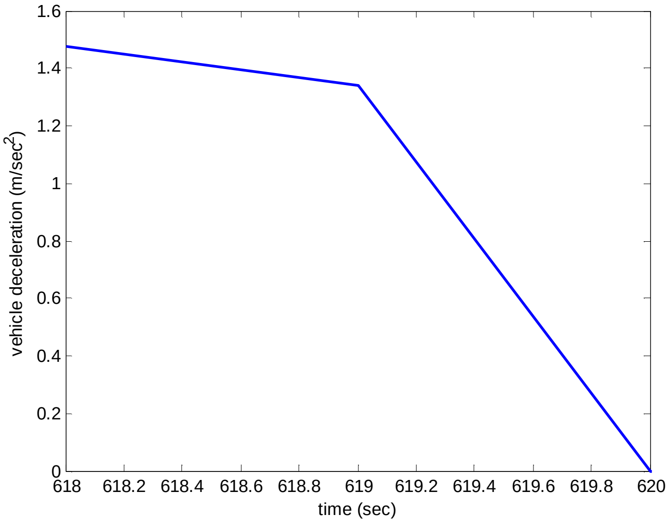

Figure 5.32 Vehicle deceleration in the last 2seconds of braking

5.5 Operation of a Parallel Braking System on Different Drive Cycles

The research aims clearly indicated that although the series braking system appears to be the best option to maximise energy recovery, it is expensive. Therefore, it was worth considering a parallel braking system as an option when the vehicle costs need to be reduced. It was explained in section 2.4 that a parallel braking system is less complicated than a series braking system but the energy recovered is less. The level of energy recovery has an effect on vehicle deceleration as the regenerative brake acts as a supplement to the friction brake. The control strategy proposed in Chapter 4 was simulated with the DC drive model during braking as shown in Figure 5.33. The field current was controlled to maintain the EMF as the speed reduced during braking. The friction brake always operates on the motor shaft during braking with brake torque rise from zero to 15Nm in 1.5s.

Road load was also simulated to exert torque on the motor shaft. A boost converter was installed between the motor armature and the voltage source and controller by a PWM modulator, while the buck converter in the field circuit was switched by the current controller.

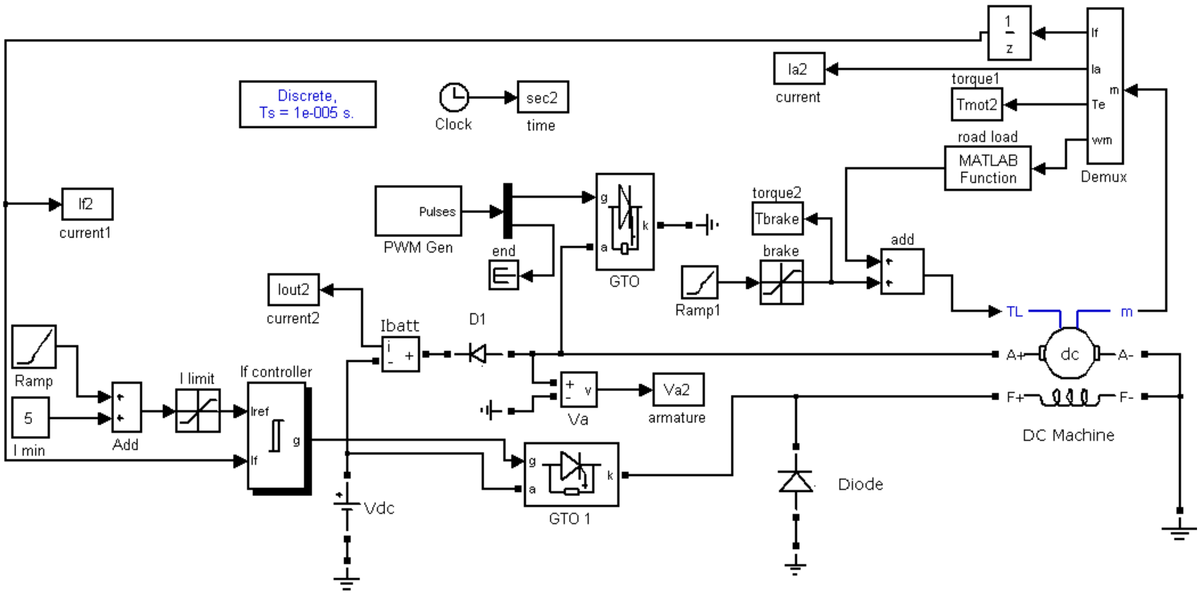
Discrete,
Ts = 1e-005 s.
Clock
sec2
time
Ia2
current
1
z
If
Ia
m
Te
wm
Demux
torque1
Tmot2
road load
MATLAB
Function
If2
current1
Pulses
PWM Gen
end
g
a
k
GTO
torque2
Tbrake
brake
add
Ramp1
Iout2
current2
Ibatt
D1
TL
m
A+
dc
A-
F+
F-
DC Machine
Ramp
5
I min
Add
I limit
If controller
Iref
If
g
+
v
-
Va
Va2
armature
Vdc
GTO 1
Diode

Figure 5.33 Regenerative brake using a separately excited DC motor

The model inputs were friction torque and the reference field current as a function of time, and the model parameters are listed in Appendix C7. During the simulation, the field current was controlled to change from 5A to 15A in 2s and the friction torque increased from 0 to 15N in 1.5s. The road load consisted of rolling resistance and aerodynamic drag which was combined with the friction torque to produce a load torque in the DC motor model. The initial speed of the motor was set at 300rad/s which corresponded to a vehicle speed of 76.3km/h.

Because of the boost converter operation, the armature voltage was no longer constant but took the form of a pulsation waveform as shown in Figure 5.34. At a maximum value of 82V, the armature current flowed to the source which had a lower voltage of 80V. At minimum armature voltage, this charging current reduced to zero while the armature current continued flowing through the Gate Turned Off (GTO) switch. In Figure 5.34, the solid line was the charging current and the dotted line is the armature current. As indicated in the graph, the armature current was a smooth waveform though the armature voltage was a pulsation waveform. In the regenerative braking, the direction of the field and armature currents was different as shown in Figure 5.35. As the motor speed decreases, the field current was increased to maintain the EMF in the armature circuit. As a result, the armature current rose to 65 A in 0.8s and reduced to zero after that.

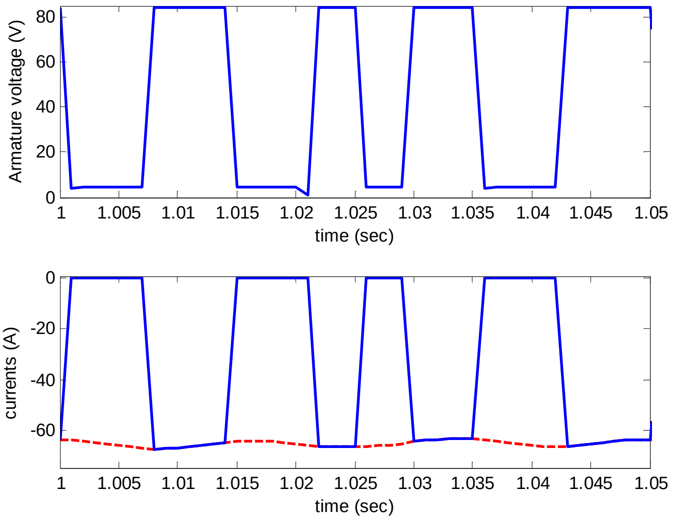

Figure 5.34 Armature voltage and current during braking

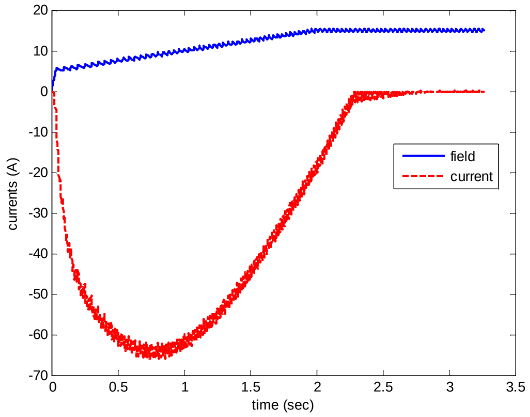

Figure 5.35 Field current and negative armature current during braking

As mentioned in equation (4.63), the higher duty cycle *k* of the GTO switch made the armature voltage increase. The Simulink model was then rerun with *k* = 0.8 to observe this increase in armature current. Figure 5.36 indicates that changing the duty cycle from 0.7 to 0.8 had no effect on the oscillation frequency of the armature current but caused a small increase in the oscillation magnitude. The reference armature current was derived from the motor speed as indicated in equation (4.77) where the constant was equal to 1500Arad/s; multiplication field current with motor speed was always 1500. Different patterns of field and armature currents were obtained with this technique as shown in Figure 5.37. Field current was found to be inversely proportional to motor speed until the upper limit of 15A was reached. The magnitude of the armature current rapidly increased to about 40A and was kept constant for 2s before decreasing to zero in 0.5s.

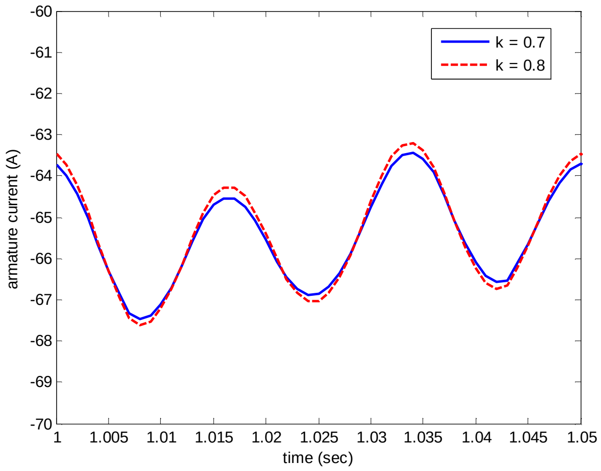

Figure 5.36 Armature currents for different duty cycles of GTO switch

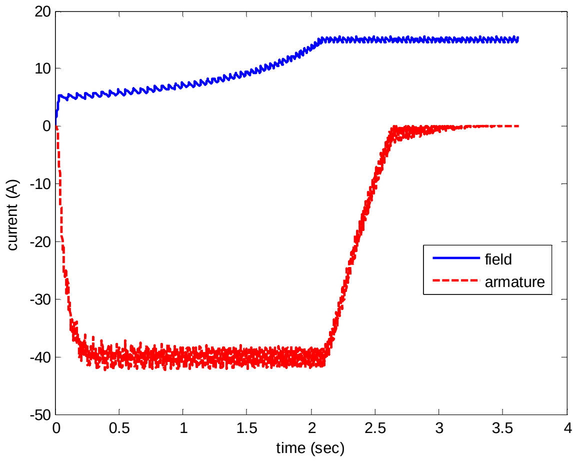

Figure 5.37 Field and armature currents generated ($I_f.\omega$ = constant)

5.6 Integration of a Regenerative Braking System with ABS

When the ABS is initiated, the options are for the regenerative brake to continue to operate or to be deactivated. Therefore, it was important to investigate the effect of the regenerative braking on ABS operation. Using the simulation result in Figure 5.25, the sophisticated control system of the regenerative brake was approximated by a first order system. It has already been shown in section 5.4 that high frequency torque ripple has no effect on wheel deceleration. The transfer function is:

$$\frac{T_m(s)}{T_{ref}(s)} = G(s) = \frac{1}{10^{-3}s+1} \tag{5.16}$$

With this model, the time constant was 1ms and the time needed by the motor to generate the reference torque was about 6ms. From the literature, Sakai and Hori (2000) used the same time constant to model the electric motor.

For the hydraulic braking system, the control input was the reference wheel pressure and then the solenoid valves were opened or closed to generate accurate wheel cylinder pressure. Figure 5.38 shows the pressure response for a step reference of 10 bar with different pulse widths of solenoid voltage. The pressure control was achieved by controlling the voltage supplied to both solenoid circuits. The valves’ status, either ON or OFF, was determined from the control criteria as discussed in Chapter 4 section 4. Choi et al. (2003) explained that a conventional On-Off valve exhibits a pressure pulse-up which was confirmed with this research result. The average solenoid voltage was controlled using PWM where a higher average voltage was obtained with a higher PWM ratio. As a result, higher magnetic force was applied to the valve. As the PWM ratio was increased more overshoot appeared in the pressure. However, their pressure responses were close to each other after one cycle oscillation. In order to simplify the hydraulic system into the second order system, its response to different PWM ratios in the solenoid circuit is important. The results in Figure 5.38 show that the responses were similar for three different ratios, so Equation (5.17) can be used to describe the hydraulic system. This result suggested it would be better to approximate the hydraulic brake with a second order system as follows:

$$\frac{P(s)}{P_{ref}(s)} = G(s) = \frac{4 \cdot 10^4}{s^2 + 4 \cdot 10^2 \cdot 0.2 \cdot s + 4 \cdot 10^4} \tag{5.17}$$

The model parameters were natural frequency ω_n and damping coefficient ξ, the values used were 200rad/s and 0.15 respectively. To highlight the different responses, the brake models represented by equations (5.15) and (5.16) were plotted for a unit step of reference as shown in Figure 5.39. This indicates that the regenerative brake response was much faster than that of the hydraulic brake.

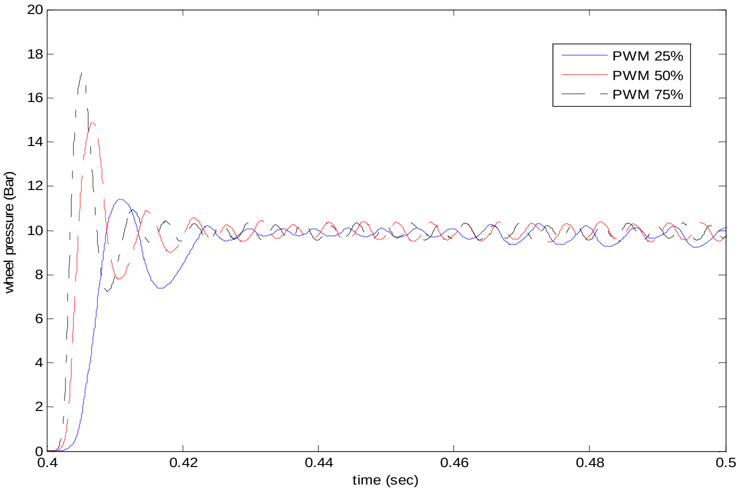

Figure 5.38 Wheel pressure responses for different PWM ratios

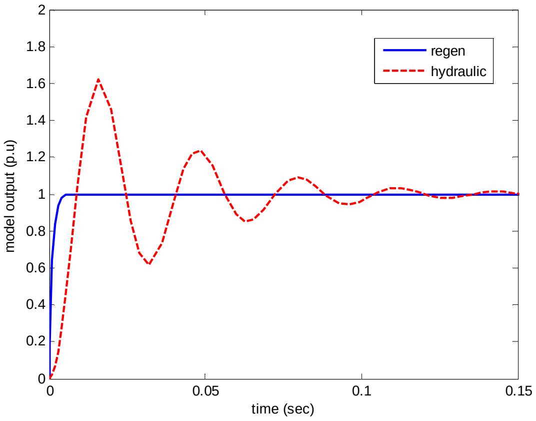

Figure 5.39 Outputs of first and second order systems

In the next simulations, the following figure shows the Pacejka static model (Pacejka, 2012) to simulate braking condition on the front wheels. Compared to Pacejka's static model found in the literature as shown in Figure 5.41, model used in this research was somewhere between dry and wet asphalts.

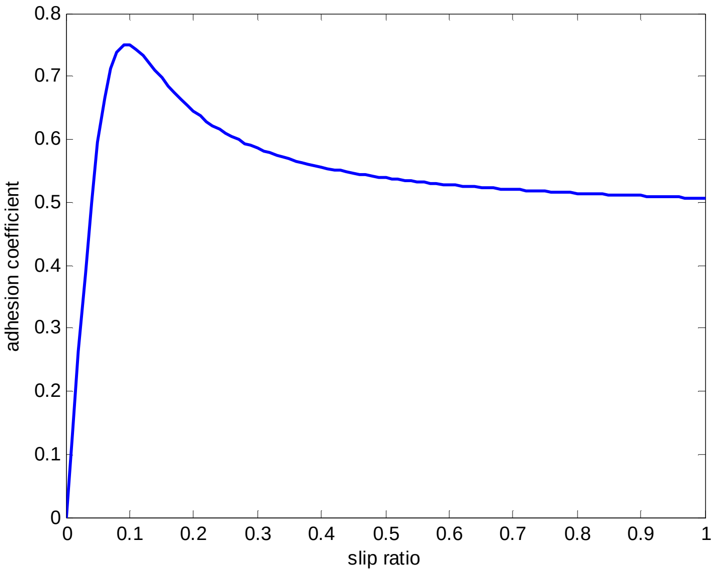

Figure 5.40 Pacejka's static model as used in the research(Pacejka, 2012)

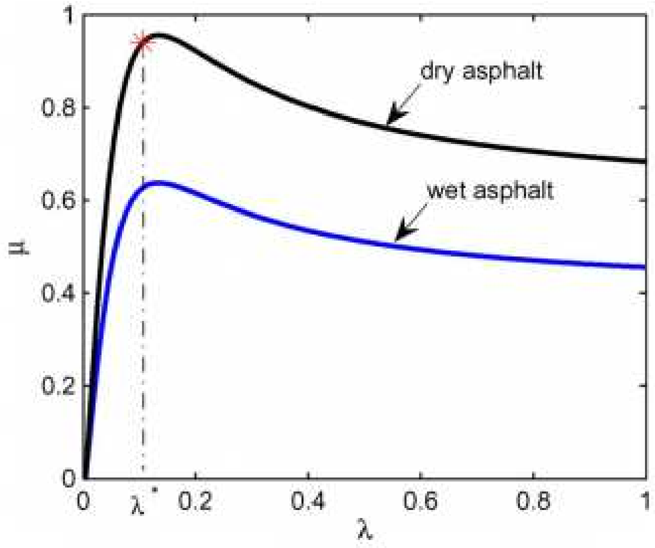

Figure 5.41 Adhesion coefficient curves of different road conditions

(Jing at al., 2011)

The Simulink model was then developed to investigate the deactivation of the regenerative brake at the beginning of ABS operation. As shown in Figure 5.42, the regenerative braking was fitted to the front wheels and the ABS operated at the front and rear wheels. The simulation is for the de-activation of the regenerative brake, not the ABS. Figure 5.43 shows the brake pedal force applied by the driver and the resulting pressure obtained from the force/pressure curve in Figure 3.13. It was found that the master cylinder pressure started to rise after 0.4secs according to the characteristic force/pressure curve and reached a constant value of 27.3bar after 1sec. The ABS was initiated when the wheel acceleration was greater than -32.34m/s^2. The brake controller applied or released the pressure to maintain the wheel acceleration between -32.34m/s^2 and 0.98m/s^2. The controller operation was based on flowchart 3.18 in Chapter 3 Section 5. The wheel speed was measured and wheel acceleration was determined in order to decide whether to initiate the ABS or not. In the case that ABS was not active, the energy recovery was maximised by applying regenerative braking to meet the driver demand.

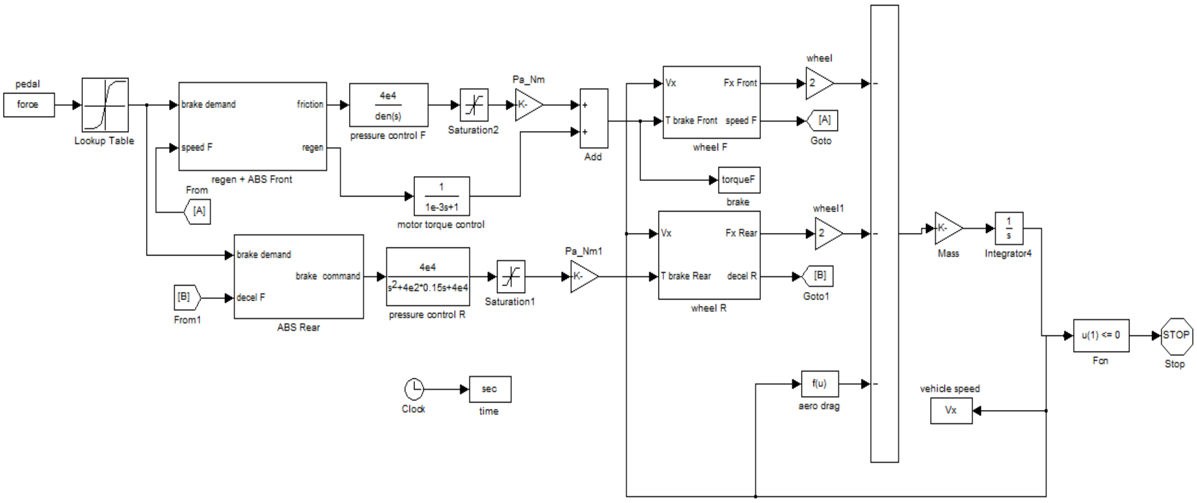
pedal
force
Lookup Table
brake demand
friction
speed F
regen
regen + ABS Front
From
[A]
4e4
den(s)
pressure control F
Saturation2
Pa_Nm
-K-
Add
1
1e-3s+1
motor torque control
brake demand
brake command
decel F
ABS Rear
[B]
From1
4e4
s^2+4e2*0.15s+4e4
pressure control R
Saturation1
Pa_Nm1
-K-
Vx
Fx Front
T brake Front
speed F
wheel F
torqueF
brake
Vx
Fx Rear
T brake Rear
decel R
wheel R
wheel
2
[A]
Goto
wheel1
2
[B]
Goto1
f(u)
aero drag
-K-
Mass
1/s
Integrator4
u(1) <= 0
Fcn
STOP
Stop
vehicle speed
Vx
Clock
sec
time

Figure 5.42 Vehicle model including regenerative brake and ABS

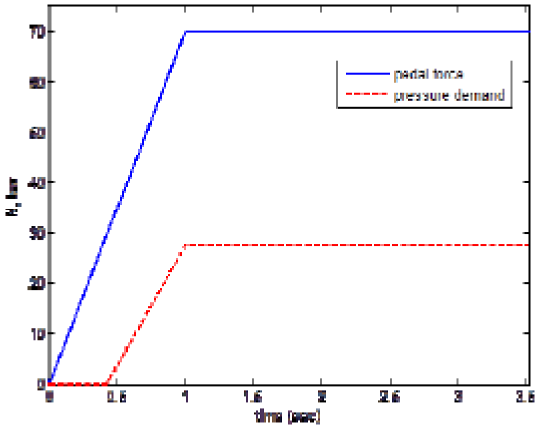

Figure 5.43 Pedal force and resulting master cylinder pressure

Figure 5.44 shows the torque generated by both regenerative and friction brakes at the front wheels. Initially, the regenerative brake was able to meet the demand. After 0.6secs, the friction brake was engaged to assist the regenerative brake. And, at t = 1.02secs the ABS was initiated and after short interval the regenerative brake was de-activated. Since the friction brake was equipped with a pressure sensor, pressure control was included in the ABS operation. During the deceleration phase the pressure was set at 5bar, and was set at 30bar during the acceleration phase. But, at very low speed, this rule was modified to 1bar and 2bar, respectively. It is agreed that further investigation is needed to select the optimum pressure settings. The front and rear wheel rotational speeds, and the vehicle speed are all shown in Figure 5.45. It can be seen that the ABS was not engaged on the rear wheels and the front wheels were prevented from being locked.

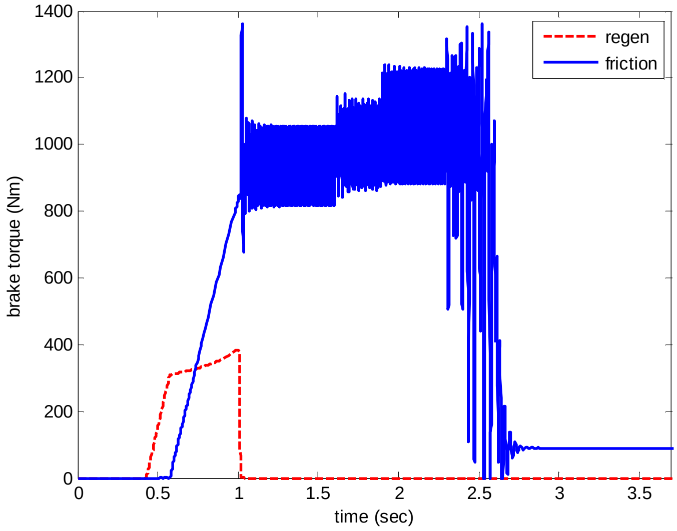

Figure 5.44 Regenerative and friction torques during braking

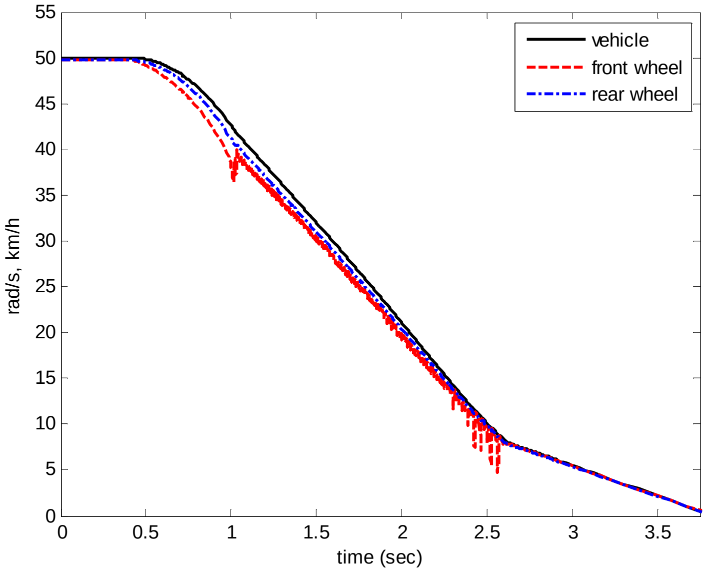

Figure 5.45 Rotational wheel speeds and vehicle speed during braking

The model was rerun for the case where the regenerative braking continued operating with the ABS activated. The regenerative torque of 382N was applied at the front wheels and the ABS tried to avoid wheel lock. Figure 5.46 shows the translational speed of the wheels for this case and it was found that the front wheels locked soon after the ABS was activated, at *t* = 1.05s. One solution to prevent wheel lock while maintaining energy recovery via the RB was to reduce the regenerative torque by one-fifth (76.4N), but this value was found by trial and error using the model thus it is not applicable in practice.

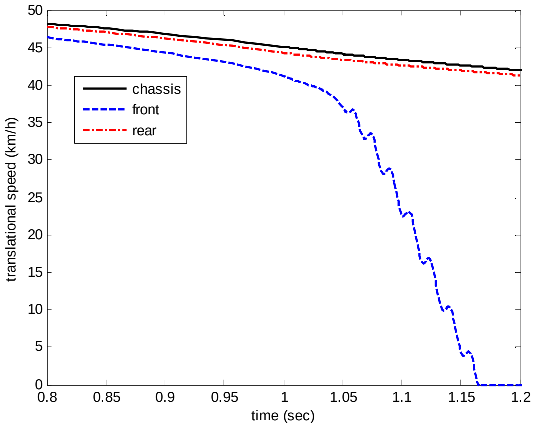

Figure 5.46 Vehicle and wheel translation speeds ($T_{motor} \neq 0$)

5.7 Chapter Summary

Three drive cycles i.e FTP, US06 and EUDC were investigated to represent different driving conditions. Braking characteristics were extracted from these and tabulated to compare braking energy, rate of braking and braking time. From the Simulink model, the slip ratio of the front wheel was assumed to be 3 times the slip ratio of the rear wheel and the vehicle deceleration and the translational deceleration of the wheels were assumed to be similar. Thus, braking torque could be determined from the vehicle speed profile using vehicle and wheel equations of motion.

Knowing the braking torque on the front axle in the FTP drive cycle, for example, the amount of regenerative braking torque could be derived by using the speed-torque characteristic of the M/G. Next, the efficiency map of the M/G was used to calculate the regenerative power delivered to the battery. The stored braking energy was found by taking into account the charging losses represented by the internal resistance of battery. The regenerative braking ratio was the amount of that stored energy divided by the total braking energy. The operating points of the M/G and battery current during braking were analysed to relate them to the rate of braking.

The brake torque distribution in a series braking system resulted in the desired values of both regenerative torque and wheel brake pressure. A control system model of the regenerative brake simulated the DTC for the induction M/G to generate motor torque. On the other hand, the pressure control system switched the solenoid valves to adjust the wheel pressure. The performance of these control systems was evaluated.

Unlike the series braking system, only the regenerative brake was electronically controlled in a parallel braking system. The Simulink model consisted of a DC M/G buck-boost converter, current controller and battery. Here, the field current of DC M/G was modulated to enable the generation of the desired armature current and thus the regenerative braking torque. The boost converter was connected to the armature circuit that allowed the current to flow into the battery during braking.

Predicted responses of regenerative braking torque and wheel pressure showed similar responses of first-order and second-order transfer functions, respectively. They were used to investigate the integration of the regenerative braking system with ABS using the full vehicle simulation model. At the time that the ABS was initiated, situations that might have happened when the regenerative braking torque was still applied or removed were analysed.

In the last section, it was demonstrated that the response of the regenerative braking was not the limiting factor in ABS operation. It was done by predicting the regenerative braking response, and the friction braking response as explained in the section, and this included the effect of PWM on the hydraulic actuation system response for the friction brakes as shown in Figure 5.38. Figure 5.44 shows that despite the fast response of the regenerative braking, when both regenerative and friction braking were operational and ABS was invoked because the tyre/road contact was approaching the limit of adhesion, the wheels were predicted to lock. Various options to avoid wheel lock were tried and one which worked was to reduce the regenerative braking torque; a 20% reduction was found to avoid wheel lock with ABS while at the same time maintaining a reasonable amount of regenerative braking (80%). The approach took for this was ‘trial and error’ and it is not suggesting there is a “magic” 20%, but it is suggested that there is the possibility of maintain some regenerative braking with friction braking during ABS intervention rather than cutting it out altogether, and this needs further investigation. It have not been found much about this in the literature and interestingly JLR has picked this up so it was suspected it is of interest to at least one major vehicle manufacturer.

CHAPTER 6

EXPERIMENTAL WORK

6.1 Introduction

In the experimental work presented in this chapter, the braking systems of two EV's manufactured by TATA Motors Ltd. were evaluated with no modifications to their standard setup; the ACE light commercial vehicle and the VISTA small passenger car. The purpose was to gather data from known regenerative braking set-ups to compare with predictions found in this research. Both employed a parallel braking system where the hydraulic pressure generated in the master cylinder by depressing the brake pedal is applied to the front and the rear brakes. In the VISTA, a vacuum brake booster is provided to supplement the pedal force supplied by the driver while the ACE has no booster in the system. The ACE was tested using the "Rototest" chassis dynamometer in the University laboratory while the VISTA was driven on the public roads in Coventry.

The VISTA is an advanced EV, with a 37kW permanent magnet motor, a 26.5kWh Lithium-Ion battery and a sophisticated Vehicle Management Unit (VMU). The VMU enables the recording of a substantial range of data related to the motor, battery, charger and chassis electronics. Among these data, vehicle speed, battery current, battery voltage were used to evaluate its energy recovery capability in real driving.

The experimental work gave the actual energy recovery from two EV's *viz*. the TATA ACE and the TATA VISTA and the corresponding regenerative braking ratios. Control system models for DC and induction drives developed in Chapter 5 were also validated from the experimental results.

6.2 ACE EV Braking system

6.2.1 Objectives

1. To determine the regenerative ratio of the ACE EV on the ECE drive cycle.
2. To investigate power flow from and to the battery during braking.
3. To calculate the average energy efficiency of the ACE powertrain.
4. To develop the battery characteristic curve on the ECE drive cycle.

6.2.2 Apparatus and Equipment

The TATA full electric vehicle ACE EV is a small rear-wheel drive truck powered by a 7.5hp DC motor as shown in Figure 6.1. There is a reduction gear of ratio 14.7:1 connecting the motor to the rear axle. Ten packs of 110Ah/ 8V lead-acid batteries connected in series are used to store electrical energy onboard. The motor and batteries are supplied by the General Electric Company together with the vehicle controller. The batteries are charged from the mains supply (240V) using an 84V/10A charger from the Delta-Q Company, and the battery charger can be configured with PC-based configuration software. A DC-DC converter is provided to supply 12V electric ancillaries such as lights, horn, LED display, etc.

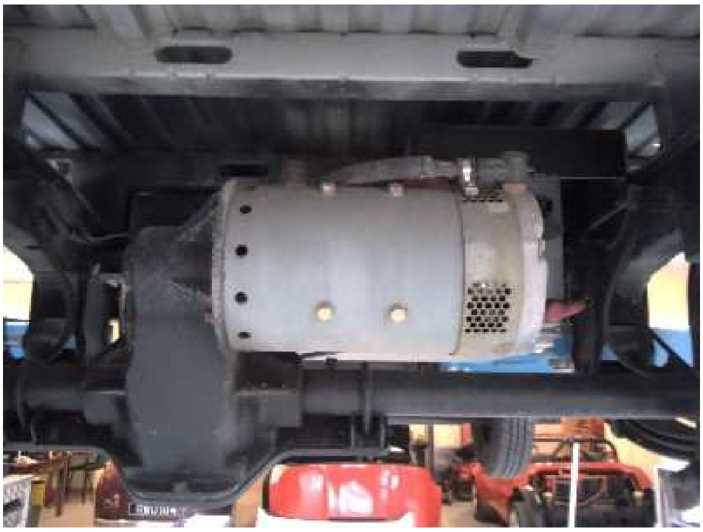

Figure 6.1 Powertrain of ACE EV

Using the chassis dynamometer, the rear axle was connected to the two Rototest dynamometer wheel units to provide simulated road loading as shown in Figure 6.2. The maximum absorbed/generator power and torque for continuous operation are 100kW and 1180Nm, respectively (Rototest, 2011).

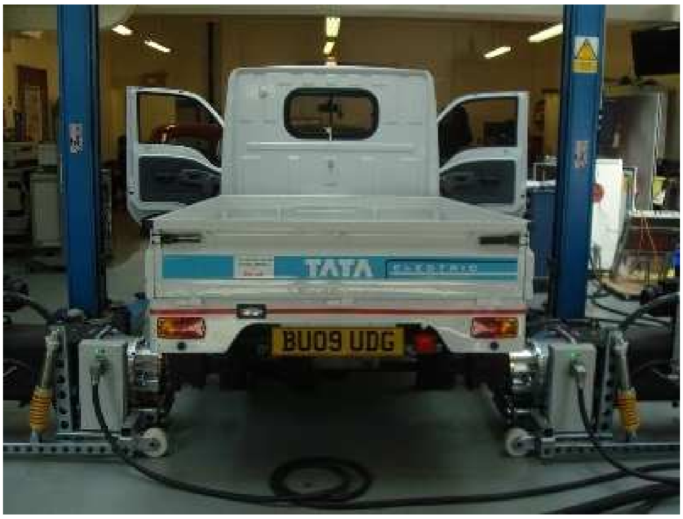

Figure 6.2 Rototest dynamometer connected to rear axle

The instrumentation needed to measure the current and voltage of the battery included a 600A current clamp, voltage divider and Pico oscilloscope as shown in Figure 6.3. The current clamp employed a Hall Effect sensor to generate small voltages as illustrated in Figure 6.3. Magnetic flux is generated by the direct current being measured and a constant current source was supplied with the unit. For the current clamp shown in Figure 6.3, an output voltage of 1mV corresponded to 1Amp current flowing in the cable.

The voltage divider used power resistors to reduce battery voltage to the operating range of the Pico oscilloscope (< 20V). This was connected to a laptop computer through the USB port and software was used to plot and save the data into picture, text or Excel files.

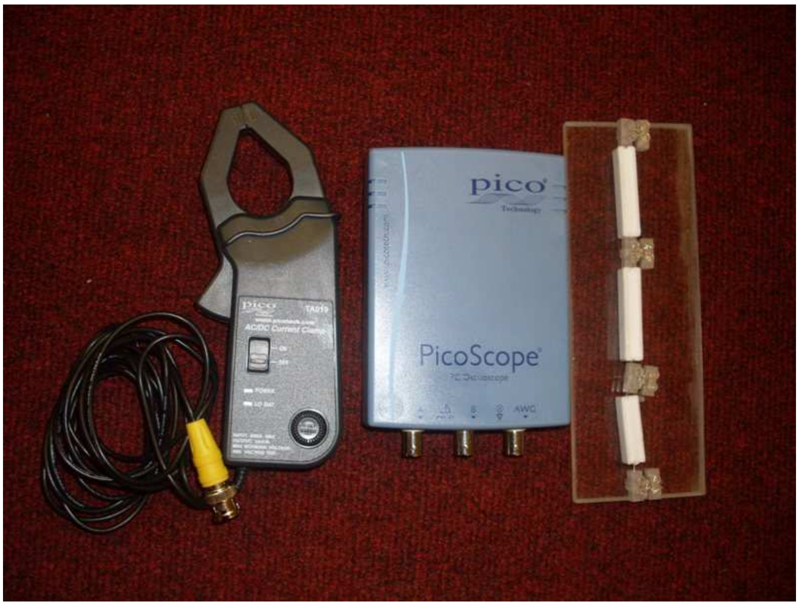

Figure 6.3 Instrumentation for measuring current and voltage

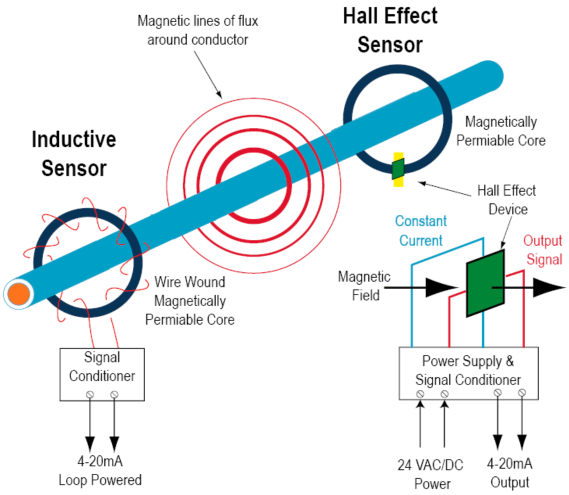
Magnetic lines of flux around conductor
Hall Effect Sensor
Inductive Sensor
Magnetically Permiable Core
Hall Effect Device
Constant Current
Output Signal
Magnetic Field
Wire Wound Magnetically Permiable Core
Signal Conditioner
Power Supply & Signal Conditioner
4-20mA Loop Powered
24 VAC/DC Power
4-20mA Output

Figure 6.4 Comparison of Hall Effect sensor with inductive sensor

(www.nktechnologies.com)

6.2.3 Test Setup and Procedure

The ACE EV used a conventional braking system with disc brakes fitted on the front axle and drum brakes fitted at the rear axle. A brake booster was not provided so the force to develop fluid pressure in the brake slave cylinders originated only from the muscular effort applied to the brake pedal by the driver. The rear axle braking torque was supplemented by regenerative braking delivered by the DC motor. Theoretically, the speed-torque characteristics of the motor were similar for traction and braking conditions as depicted in Figure 3.14. Since the locking force of rear wheels was lower than that of the front wheels, reduced braking torque had to be applied at the rear wheels to avoid premature rear wheel lock and vehicle instability. For this reason, the full capacity of the regenerative braking torque could not always be utilised.

The vehicle controller was provided with configuration, monitoring and troubleshooting software named “GE Sentry”. There were 128 control functions available to be configured; but some were restricted for the OEM. Functions that relate to control of the field and armature currents during braking are listed in Table 6.1

Function	Description	Value	Resolution (per set unit)
5	The braking/armature current level regulated with the accelerator pedal up and the brake switch open.	0-255	1.5 A
8	The adjustment of the maximum field current in order to obtain the maximum torque of the motor.	51-255	0.269 A
9	The adjustment of the Regenerative braking current limit. Higher current correlates to shorter stopping distance.	0-255	1.5 A
10	The adjustment of the field current to be used during the regenerative braking mode.	51-255	0.269 A
19	The adjustment of the rate at which speed is reduced during regenerative braking under speed regulation.	0-255	0.086s
20	To adjust the rate at which speed is reduced during regenerative braking when the accelerator pedal is released and start switch opens or the control receives a directional change signal.	1-255	-

Table 6.1 Braking related functions of the GE vehicle controller

(TATA Motors, 2011)

The vehicle parameters needed for the test as listed in Table 6.2 were entered into the software of the Rototest dynamometer. These included vehicle mass, wheel radius and road load coefficients.

Parameter	Unit	Value
Vehicle type	-	2WD
Wheel circumference	mm	1775
Mass left	kg	575
Mass right	kg	575
Total vehicle mass	kg	1150
Frontal area	m^2	2.4
Drag coefficient		0.5
Rolling resistance coefficient		0.014

Table 6.2 ACE EV parameters input to Rototest software

Before the tests were performed, the dynamometer was calibrated as follows. To calibrate the wheel torque transducer a bar was mounted on the axle drive shaft as shown in Figure 6.5. A calibration program was run in which weights were then placed at points along the bar to generate a torque on the shaft. The location of weights on the bar, measured torque and measurement deviation are listed in Table 6.3. Numbers 1, 2 and 3 inside the table represent three different weights with masses of 19.248kg, 19.214kg and 19.204kg respectively. In the first test, the load torque of 132.57Nm was only generated by the bar since no other weight was loaded on it. The root mean square deviation of the torque measurement was 0.01Nm which indicated the torque transducer was very accurate.

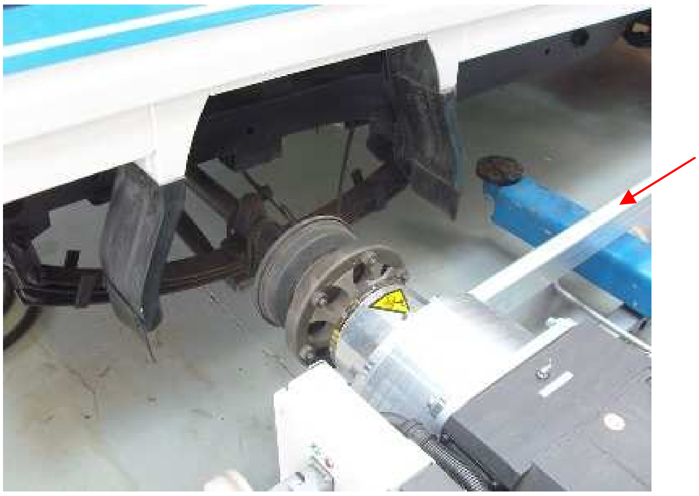

Figure 6.5 Calibrating torque transducer of Rototest dynamometer

Test	Weight position configuration										Nominal torque [Nm]	Deviation [Nm]
	1	2	3	4	5	6	7	8	9	10		
1											132.57	0.01
2		1									272.41	0.08
3		1	2								457.28	-0.08
4		1	2	3							687.31	-0.37
5		1	2							3	834.37	0.08
6		1							2	3	1007.92	0.13
7								1	2	3	1208.24	0.15

Table 6.3 Weight positions and calibration results

The test work involved driving the vehicles on prescribed drive cycles. Battery voltage and current were recorded, and from these results, wheel power, regenerative power and the corresponding energy could be determined. The power flow from and to the battery during braking could also be observed. The ACE was then driven against the dynamometer to follow the ECE drive cycle using the vehicle’s accelerator pedal and brake pedal. The dynamometer software recorded and stored speeds and torques of both rear wheels. In the report generated by the software, average wheel speed, total wheel torque, wheel power, vehicle speed and distance were also included.

In the experimental work, the ACE was driven to follow the ECE drive cycle using the Rototest dynamometer. The aim was to generate as accurately as possible that drive cycle where the acceleration and brake pedals were controlled by the driver. Since the dynamometer was fitted to the rear axle, the front brakes did not contribute to retarding the vehicle under regenerative braking which acted on the rear brakes alone, therefore the Rototest dynamometer was programmed with the total vehicle mass on the rear brakes. The left and right mass values indicate any lateral difference in the braking duty for the dynamometer; the ACE vehicle was found to be symmetrical about the longitudinal centre line.

The maximum permitted speed of this vehicle was 40km/h, which was less than the 50km/h in the actual ECE drive cycle, so in this work, the vehicle was accelerating, cruising, braking and stopping three times with different patterns as shown in Figure 6.6. Since it was difficult to manually control the vehicle speed the profile produced did not match perfectly with the actual ECE cycle.

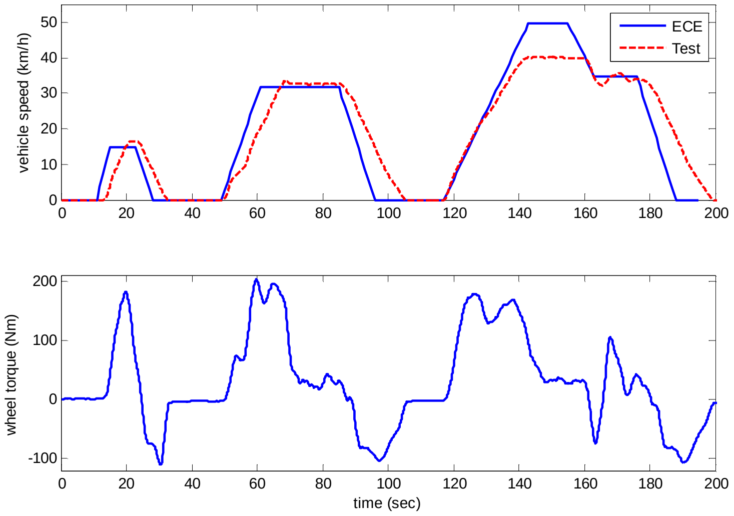

Figure 6.6 Profile of vehicle speeds and wheel torque

6.2.4 Results and discussion

The lower graph in Figure 6.6 shows the wheel torque needed to drive that cycle. It can be seen that the maximum torque in one braking event was different to that in other braking events. By observing the graph of wheel torque at braking intervals, the braking torque was seen to increase and then decrease back to zero.

The battery current and voltage generated for the ECE drive cycle are plotted in Figure 6.7. Large currents up to 124A were needed to accelerate the vehicle from rest until the maximum speed of 40km/h was reached, which caused the battery voltage to reduce to 79.6V. Initially, the battery voltage at zero current was 88.7V.

When the current flowed into the battery during regenerative braking, the battery voltage was higher than that during acceleration or cruising. A maximum regenerative current of 26A was obtained when the vehicle was stopped from 34km/h in 22.8s. At a lower initial speed of 16.5km/h, a smaller regenerative current of 4A was generated.

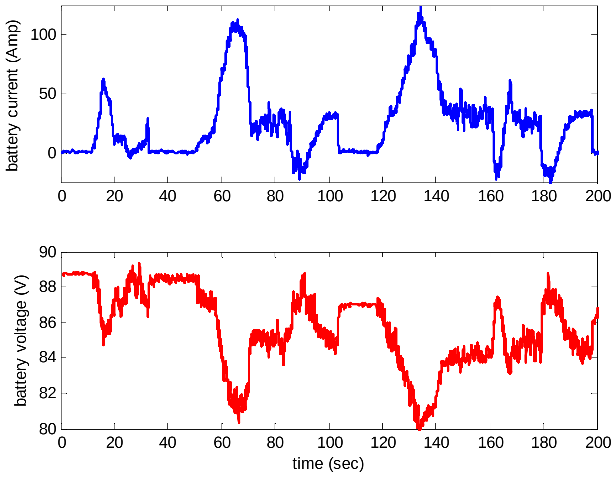

Figure 6.7 Battery current and voltage during the ECE drive cycle

Since the ACE EV employed a parallel braking system, only a fraction of the kinetic energy could be recovered. The battery power delivered and stored during the drive cycle is shown in Figure 6.8. The maximum power flowing from the battery to the electric motor was 9.95kW, to accelerate the vehicle up to 40km/h in 26s. During braking, the maximum regenerative power generated by the electric motor was only 2.27kW.

There are four braking intervals in the ECE drive cycle as listed in Table 6.4. They are characterised by a low deceleration rate, on average 4.4%*g*.The highest braking energy of 51.68 kJ was obtained when braking from an initial speed of 34.1km/h.

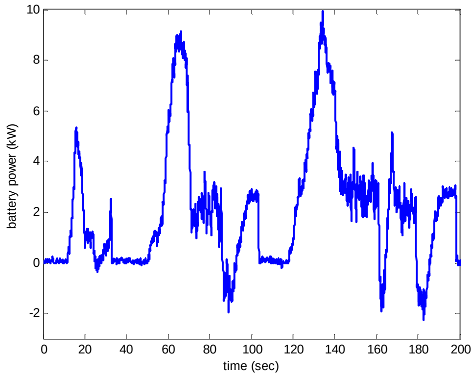

Figure 6.8 Battery power during the ECE drive cycle

No	t1 (sec)	t2 (sec)	t braking (sec)	v1 (km/h)	v2 (km/h)	deceleration (g)	E braking (kJ)
1	176.60	199.40	22.80	34.13	0.00	0.04	51.68
2	84.90	105.50	20.60	32.67	0.00	0.04	47.35
3	159.50	165.50	6.00	40.00	32.11	0.04	25.25
4	23.50	32.70	9.20	16.46	0.00	0.05	12.01

Table 6.4 Braking intervals in the ECE drive cycle

Regenerative braking on the ACE EV was found to be unusual because both directions of power flow were observed during the braking interval 1 (176.6s<t< 199.4s) as shown in Figure 6.9. When the vehicle started to decelerate, the power direction was reversed from positive to negative indicating that the regenerative brake was about to be applied. However, at t = 187s, the power was reversed back to positive which meant that the DC motor or its controller were consuming battery power. This condition always occurred in every braking application.

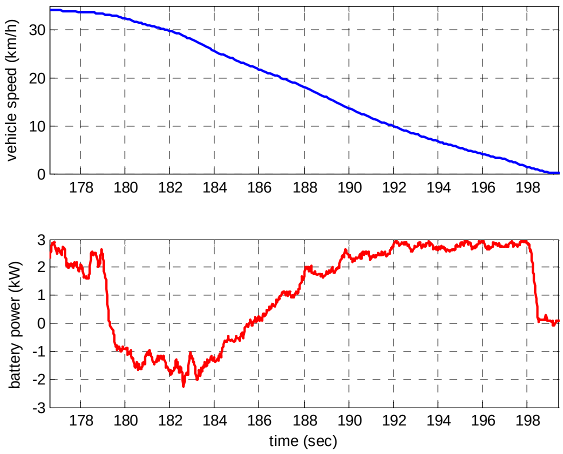

Figure 6.9 Vehicle speed and battery power of ACE EV

To investigate this condition, a circuit diagram of the ACE EV including the current flow from the battery to the DC motor is shown in Figure 6.10. The motor controller bridges the battery and the motor by providing three pairs of terminals, POS-NEG, A1-A2 and F1-F2. Inside the controller, transistors Q1 and Q2 control current flow in the armature winding while transistors Q3, Q4, Q5 and Q6 switch the field winding. The controller also contains a capacitor to assist the battery during traction and braking. The current equation of this circuit is:

$$I_{battery} = I_{capacitor} + I_{armature} + I_{field} \tag{6.1}$$

The field current functions to produce magnetic flux in the DC motor, and torque are generated as a result of the interaction between the magnetic flux and the armature current. For zero torque, the current from the battery to the capacitor and field circuit can continue to flow. The reason for doing this is to fully charge the capacitor and maintain the magnetic field before the next acceleration starts. Therefore, fast acceleration response can be achieved with this technique. However the battery power was dissipated in the field winding according to:

$$P_{loss} = R_{field} \cdot I_{field}^2 \tag{6.2}$$

The power loss is a square function of the field current.

By defining the regenerative ratio as energy flowing into the battery during a certain braking interval divided by the braking energy, the regenerative ratio of the ACE EV on ECE drive cycle was calculated as shown in Table 6.5. This result shows that regenerative braking was not effective at low speed (V < 16km/h). The average regenerative ratio for the first three braking intervals was 12.4% while for all braking intervals it was 9.7%.

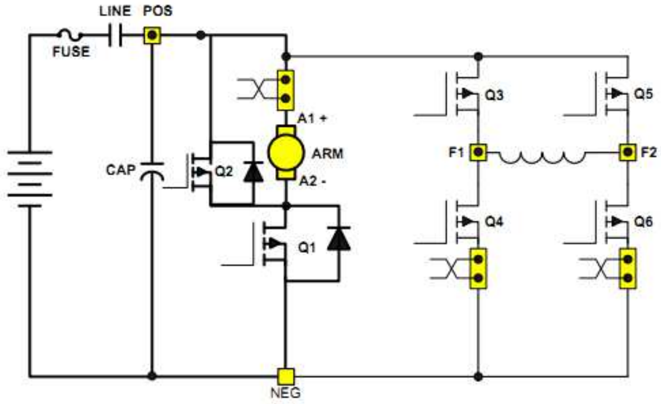

Figure 6.10 Electrical power system of ACE EV (TMETC, 2011)

No	E braking (kJ)	E regen (kJ)	regen ratio (%)
1	51.68	7.34	14.19
2	47.35	5.48	11.58
3	25.25	2.89	11.44
4	12.01	0.21	1.76

Table 6.5 Regenerative ratio of ACE EV on ECE drive cycle

To determine the average efficiency of the DC motor and its controller, the wheel power and battery power during each traction interval were used.

Figure 6.11 shows the vehicle speed, power flowing from the battery to the motor/controller, and wheel power for 117.1s<*t*< 143s. The vehicle was accelerated from rest to 40km/h in 25.9s. The difference between the battery and wheel power was the result of losses in the motor and controller. To find the average efficiency of the motor / controller, these were integrated over the acceleration interval to yield the energy as listed in Table 6.6 for four acceleration intervals. The efficiency of the motor / controller was found to vary from 51% to 89% which increased as the motor operated at higher speeds. On average, the efficiency of the motor/controller was 69%.

The ECE drive cycle was repeated to measure the reduction of the battery open-circuit voltage as the battery was discharged from full capacity and the result is shown in Figure 6.12. The graph indicates that the voltage decreased nonlinearly with the ampere-hours of the battery. A significant drop of voltage was found at the lower discharge (Ah < 15) and after that the voltage changed slowly. On average, the voltage drop was 3.5V when the battery was discharged to 25.2Ah.

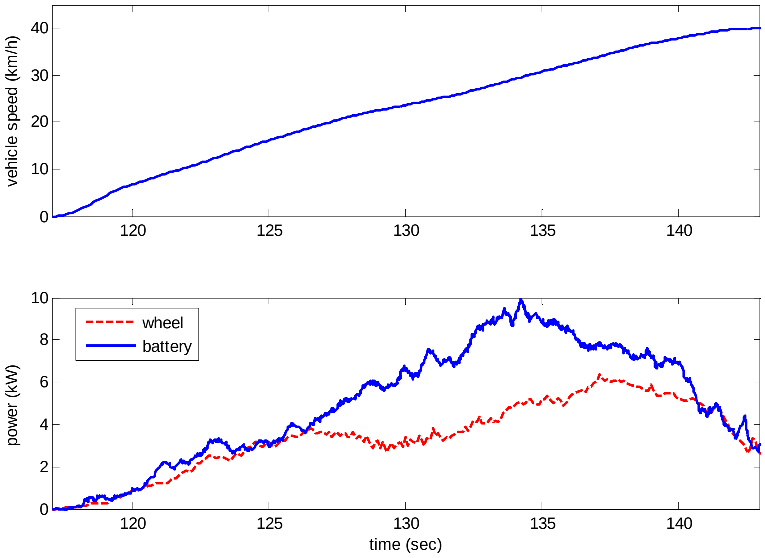

Figure 6.11 Vehicle speed and powers during acceleration interval

No	t1 (sec)	t2 (sec)	V1 (km/h)	V2 (km/h)	E wheel (kJ)	Ebat (kJ)	Efficiency (%)
1	13.10	21.20	0.00	16.44	12.24	24.05	50.90
2	49.60	68.70	0.00	33.49	56.01	85.33	65.64
3	117.10	143.00	0.00	40.03	88.30	129.01	68.44
4	165.50	170.80	32.11	35.61	14.49	16.21	89.38

Table 6.6 Efficiency of motor/controller during acceleration intervals

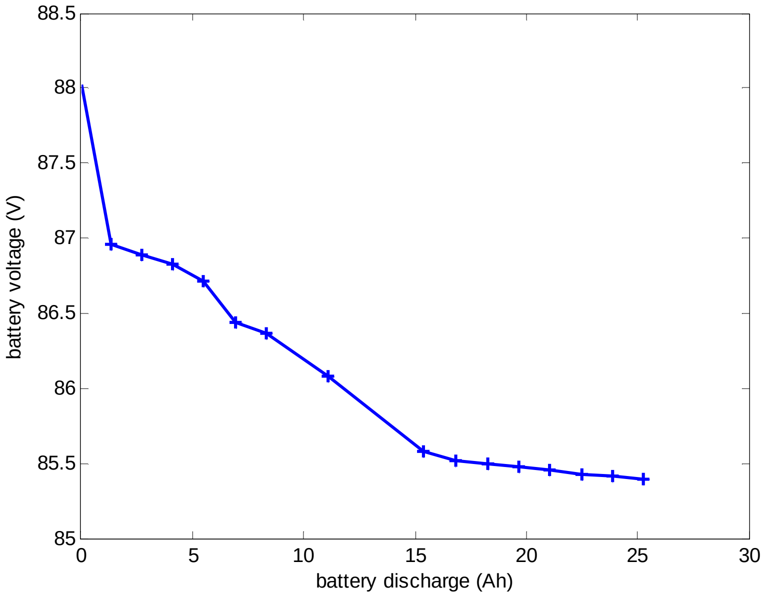

Figure 6.12 Open-circuit voltage of battery as the battery discharged

6.2.5 Interim Conclusions

In the ECE drive cycle, the current flowing from the ACE battery during the acceleration period was much higher than that flowing to the battery during the braking period. This indicated that only a small fraction of kinetic energy gained during acceleration was recovered. The regenerative power was not available at all vehicle speeds, and only a very small proportion of the braking energy was recovered at initial vehicle speeds below 16km/h. The efficiency of the DC M/G was related to the vehicle speed; operating at higher vehicle speeds made the M/G more efficient. The controller feature which maintained the field current after regenerative braking was finished had both advantages and disadvantages. A fast response for next acceleration period was obtained but electric power was dissipated at the field winding.

6.3 VISTA EV Braking System

6.3.1 Objectives

1. To observe the transition from driving mode to braking mode.
2. To analyse the braking characteristics of the VISTA under real-life driving conditions
3. To determine the regenerative ratio of the VISTA parallel braking system.
4. To calculate the average efficiency of the VISTA powertrain.
5. To estimate the energy loss in charging the VISTA during braking.

6. To estimate the road load ofthe VISTA from collected data.
7. To analyse the interaction of the regenerative braking system with the ABS.

6.3.2 Apparatus and Equipment

Figure 6.13 shows the layout under the bonnet of the VISTA including many major systems such as drive, braking, charging, and cooling. For the braking system, the VISTA adopted a parallel system where friction and regenerative brakes worked together to decelerate the vehicle. Therefore, it was able only to recover less braking energy compared with series systems e.g. the Toyota Prius for similar braking conditions. Since there was no ICE in the car, the depression in the brake booster was generated by a vacuum pump. As marked in Figure 6.13, the brake lines from the master cylinder were connected to the ABS modulator to prevent wheel lock.

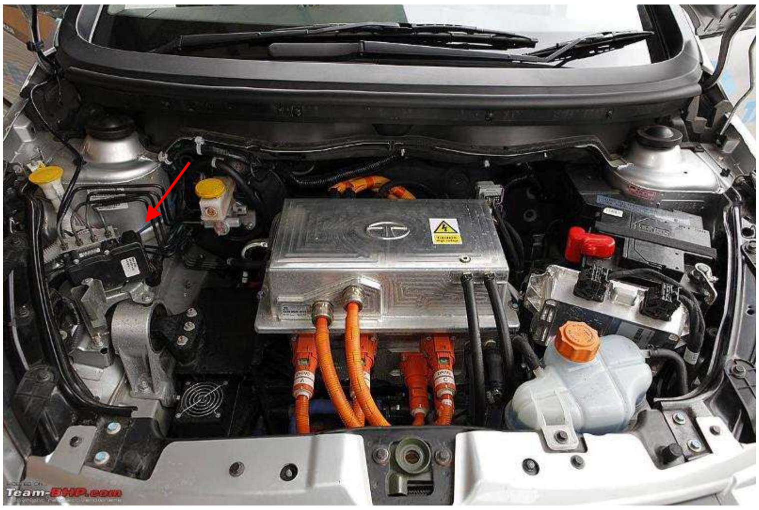

Figure 6.13 Under bonnet view of the VISTA EV

The vehicle was powered by a 37kW permanent magnet motor manufactured by TM4. During transient operation (30s) the motor could deliver a maximum power of 43kW. Continuous torque for speeds less than 3000rev/min was 60Nm and maximum acceleration torque (in 30s) was 157Nm. The motor was connected to the front axle through a single reduction gear of ratio 10:1. For the motor maximum speed of 10,000rev/min, the corresponding maximum vehicle speed was 109km/h. The electrical energy was stored in 26.4kWh Li-Ion batteries operating at a nominal voltage of 215V. The peak power and continuous capacities of the battery were 37.5kW and 25kW respectively.

6.3.3 Instrumentation

The VISTA used a CAN architecture which allowed the VMU to communicate with other controllers such the Motor Control Unit, the battery charger and the BMS as well as an external device to log the traffic in the CAN bus. In this testing, CANalyser software and CANlog 4 hardware as shown in Figure 6.14 from the Vector Company were used to interrogate that bus traffic.

Besides the data collected from the CAN bus, other external data logging was installed using the Pico automotive kit consisting of the Pico oscilloscope and current clamps. These clamps were used to measure battery current as well as motor current. It enabled the visualisation of alternating currents flowing in the motor and inverter operation.

CAN-log 3
CANlog 4
vector
CAN/Supply
USB
AUX
RS232 / I/O

Figure 6.14 CAN-log 3 and 4 for data logging application (vector.com, 2011)

6.3.4 Test Setup and Procedure

The VISTA was driven on a set route around Coventry (in the UK where it was based) to observe and record energy recovery during braking. Figure 6.15 shows the profile of vehicle speed while driving. The car was accelerated once up to its maximum speed of 107km/h and then decelerated to enable regenerative current levels to be observed from a high initial speed. Braking applications from other initial speeds were also performed, so that the regenerative braking ratios could be determined at different braking conditions.

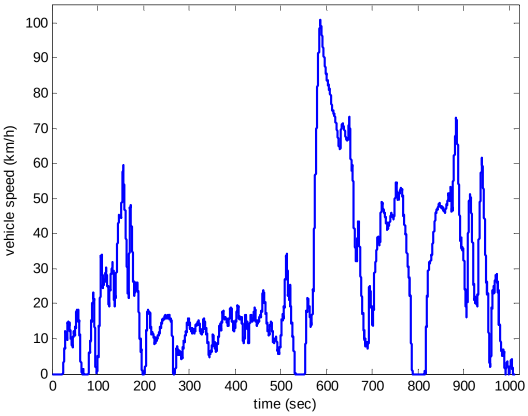

Figure 6.15 Profile of VISTA speed (V_{max}=107 km/h)

6.3.5 Results and Discussion

To determine the accuracy of the measurement made by the current clamp, a comparison with the VMU result was made as shown in Figure 6.16. In general, the clamp indicated good accuracy except that it was found to be susceptible to external noise interference.

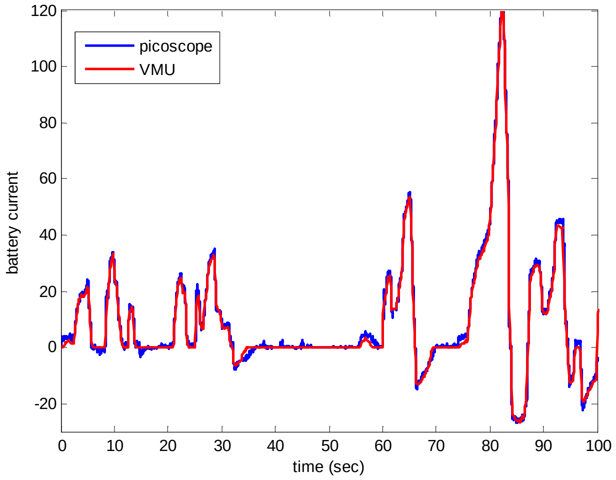

Figure 6.16 Battery current measured by Pico and VMU systems

The current flowing from and to the battery is shown in Figure 6.17. Up to 194.2A of current flowed from the battery to the permanent magnet motor during vehicle acceleration. The maximum regenerative current generated by the motor was 61.7A. By taking closer look from *t* = 862s to t = 874s, profiles of vehicle speed and battery current are shown in Figure 6.18. As braking was initiated, the motor took 1s to reverse the current from 180A to -61.7A.

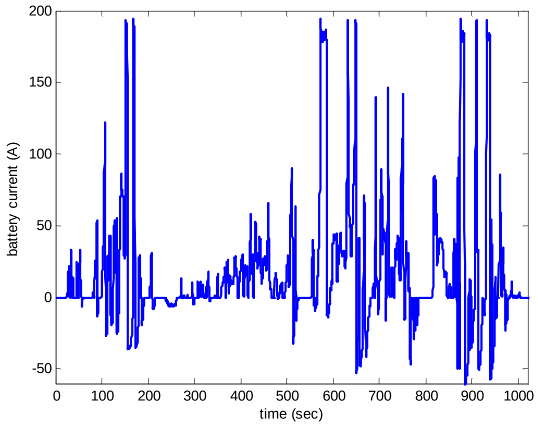

Figure 6.17 Profile of battery current ($I_{reg,max}$=61.7A)

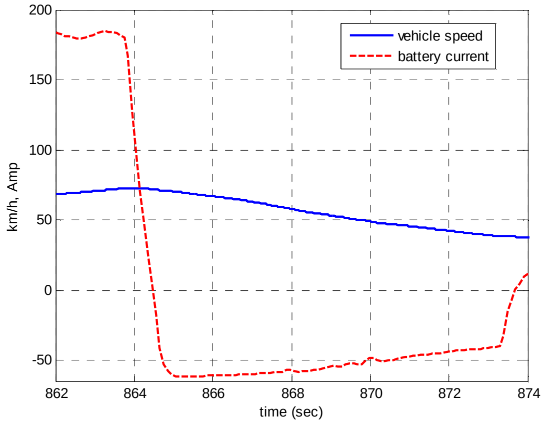

Figure 6.18 Regenerative current flowing to the battery

When the battery current was reversed from positive to negative (which meant from discharging to charging), the voltage across the battery terminals was increasing. For current reversing as in Figure 6.18, the voltage at the battery terminals increased from about 230V to 236.4V in one second as shown in Figure 6.19. As the battery was charging, the voltage further increased to around 237.2V. After the charging current reduced to zero, the voltage reduced to 235.9V. At the limit of battery voltage of 243.6V, the maximum regenerative current allowed was 100A. This corresponded to a maximum regenerative power of 24.4kW delivered to the battery.

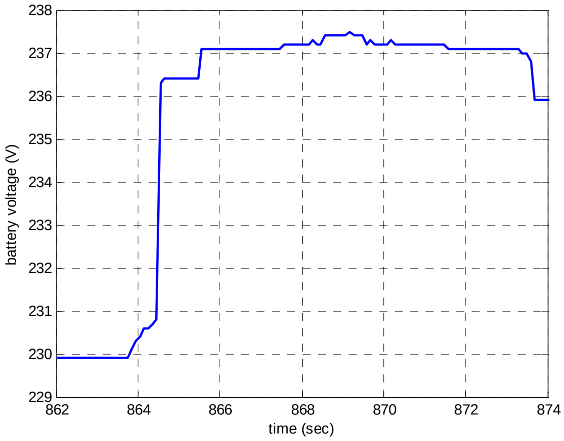

Figure 6.19 Voltage of battery terminal during regenerative braking

To determine the regenerative braking ratio, the total braking energy was calculated from the kinetic energy of the vehicle. Using the values from Figure 6.20, the initial vehicle speed at *t* = 864s was 72km/h and the final vehicle speed at *t* = 873s was 38km/h. If the vehicle weight was 1500kg, the braking energy was 216.43kJ. By integrating the regenerative power, it was found that the regenerative energy was 105kJ. Thus, the regenerative braking ratio for this interval was 48.5%. The Matlab program in Appendix C.1 was applied to determine the braking characteristics of the speed profile in Figure 6.15. The results included braking time, deceleration and braking energy as listed in Table 6.7. Only braking intervals for which the braking energy was higher than 90kJ are tabulated here.

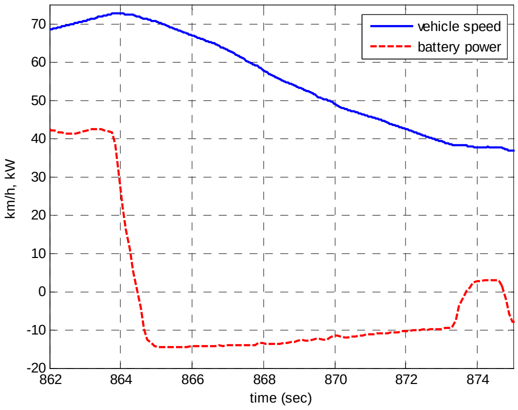

Figure 6.20 Vehicle speed and battery power

No	t1 (sec)	t2 (sec)	t braking (sec)	v1 (km/h)	v2 (km/h)	deceleration (g)	E braking (kJ)
1	864.30	873.44	9.14	72.48	38.27	0.11	219.25
2	136.87	147.69	10.82	58.05	22.16	0.09	166.56
3	746.24	768.47	22.23	51.61	0.05	0.07	154.15
4	637.46	645.13	7.67	57.97	32.48	0.09	133.42
5	922.71	929.86	7.15	53.30	26.17	0.11	124.81
6	894.03	903.82	9.79	50.78	21.32	0.09	122.90
7	650.72	665.07	14.35	43.01	9.27	0.07	102.06
8	631.07	635.20	4.13	71.36	58.43	0.09	97.14
9	153.02	160.38	7.36	46.02	23.25	0.09	91.27

Table 6.7 Braking intervals in speed profile of the VISTA EV

Initial and final times of these braking intervals were used as inputs to a second Matlab program which searched the corresponding intervals in the profile of battery power plotted in Figure 6.21. From the graph, maximum power in accelerating the vehicle was 45.7kW and the battery received regenerative power up to 14.6kW. The program output is summarised in Table 6.8 and indicates that the regenerative ratio varied from 36% to 66% with an average of 49%.

It is worth analysing why braking intervals 3 and 6 had similar initial speeds but a large difference in regenerative ratio. To answer this, profiles of vehicle speed and battery power of both intervals are plotted as shown in

Figure 6.22 and Figure 6.23 respectively. During interval 3, there were times where the regenerative power was reduced to zero caused by depressing the accelerator pedal as indicated in Figure 6.24. Also, the regenerative braking was deactivated when the vehicle speed was less than 10km/h. On the other hand, regenerative power was increased up to 12kW in 2s in interval 3 and after that it reduced slowly to zero.

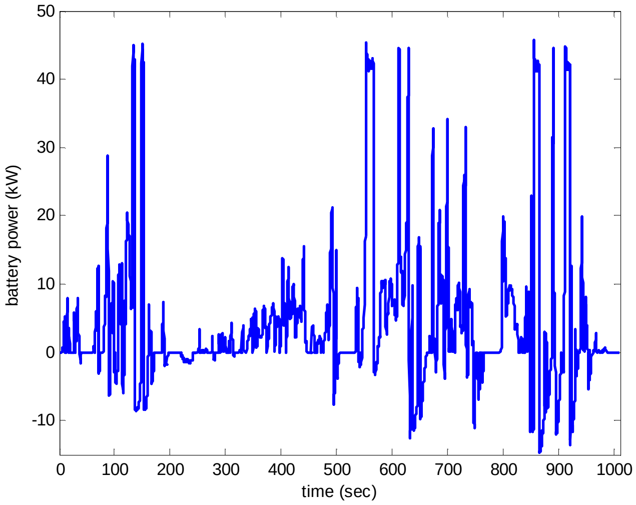

Figure 6.21 Profile of VISTA battery power

No	E braking (kJ)	E regen (kJ)	Regen ratio (%)
1	219.25	109.16	49.79
2	166.56	79.83	47.93
3	154.15	55.42	35.95
4	133.42	77.07	57.77
5	124.81	47.24	37.85
6	122.90	81.04	65.94
7	102.06	54.12	53.03
8	97.14	37.94	39.06
9	91.27	52.44	57.45

Table 6.8 Regenerative ratio of VISTA braking system

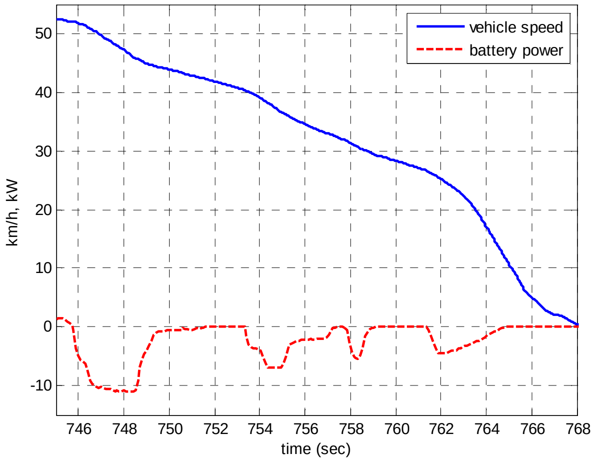

Figure 6.22 Braking interval with a low regenerative ratio

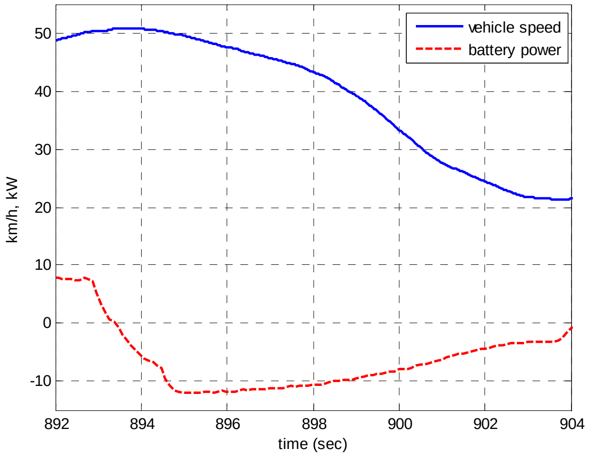

Figure 6.23 Braking interval with a high regenerative ratio

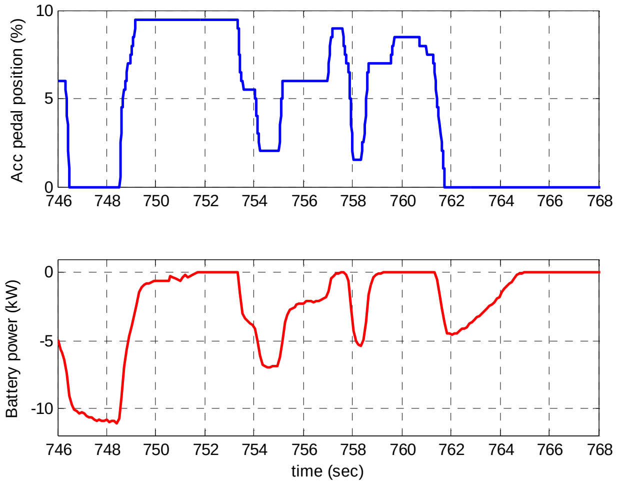

Figure 6.24 Effect of depressing accelerator pedal on regenerative power

Actually, there was energy loss when the regenerated energy was being stored in the battery. Using the battery model in Figure 3.17, the loss was represented by an internal resistance and the power loss:

$$P_{loss} = RI_{regen}^2 \tag{6.3}$$

Therefore, the regenerative ratio listed in Table 6.8 was not valid for stored energy in the battery. Since the battery data of the VISTA EV in terms of open-circuit voltage and internal resistance were not available, the battery data were taken from ADVISOR for a 7Ah Li-Ion battery at 25°C as shown in Table 6.9. This was done to determine how the regenerative ratio found should be corrected by including the charging loss. To get close to the operating voltage range of the VISTA EV, the modelled battery pack consisted of 21 modules. It is clearly shown in Figure 6.25 that battery losses are different between these intervals depending on the charging current and the battery SoC. On average, battery charging during regenerative braking constituted 3% of the energy losses.

SoC (%)	0	10	20	40	60	80	100
R_{charge} (Ohm)	0.0372	0.0204	0.016278	0.01326	0.01389	0.01749	0.01749
V_{oc} (V)	9.372	10.047	10.299	10.554	10.848	11.256	11.694

Table 6.9 Li-Ion battery data (AVL, 2010)

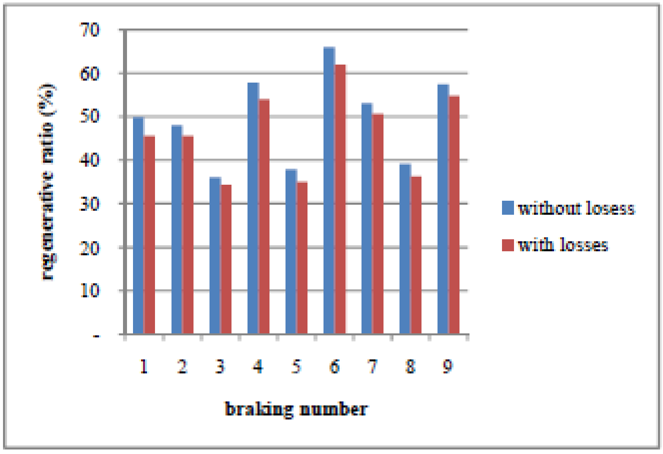

Figure 6.25 Effect of battery losses to regenerative ratio

The regenerative power delivered to the battery was generated by the electric motor. Due to losses in conversion from kinetic energy to electrical energy and in the motor control unit, the mechanical power at the shaft of the electric motor was greater than that power according to equation (3.60). Since the efficiency map of the VISTA electric motor was not available, data from ADVISOR was again used to show the operating points of the electric motor. The efficiency map of the 32kW permanent magnet motor/controller manufactured by Unique Mobility was superimposed with the predicted operating points of the VISTA electric motor as shown in Figure 6.26. As the motor speed was reduced, the regenerative torque was rapidly increased up to about 30 Nm. Under ω= 250rad/s, the torque was then gradually reduced to 10Nm. Mostly, the motor was operating in the high efficiency region (>80%).

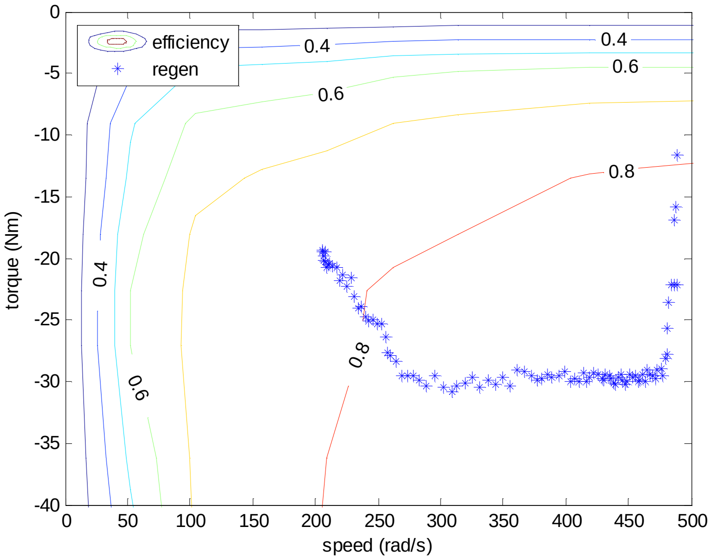

Figure 6.26 Efficiency map and operating point of electric motor

It was also necessary to estimate the road load of the VISTA EV using the collected data. The road load could be found when the accelerator pedal position was less than 20% in which the retarding forces came from regenerative braking and road load. The braking power equation is:

$$m \cdot V \cdot \frac{dV}{dt} = P_{regen} + P_{load} \tag{6.4}$$

Figure 6.27 shows the road load and regenerative power during low accelerator pedal positions. The significant fluctuation in road load was because the vehicle deceleration was obtained from the wheel speed. Using this result, the road load was estimated as 4kW. The contribution of road load to vehicle deceleration is:

$$z = \frac{P_{load}}{m \cdot V} \tag{6.5}$$

For a vehicle speed of 45km/h, the rate of deceleration *z* was 0.2m/s^2 (2.2%*g*).

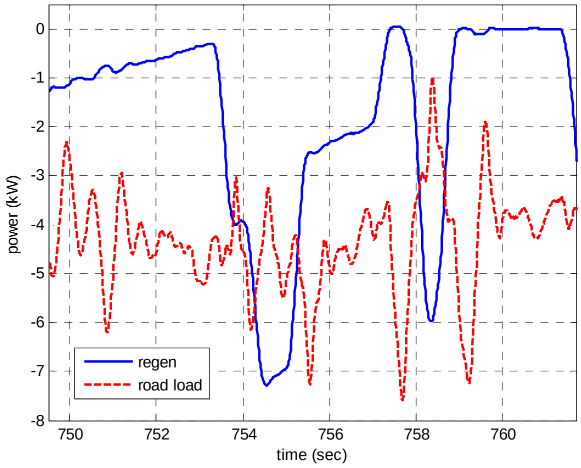

Figure 6.27 Retarding powers at low accelerator pedal positions

It has been shown that the external current sensor to measure battery current had good accuracy. Next, the two current clamps and the Pico oscilloscope were used to measure the phase currents of the permanent magnet motor. The positive current direction was toward the motor. The current of phase *c* could be found from the winding connection of the motor:

$$I_a + I_b + I_c = 0 \tag{6.6}$$

Figure 6.28 shows the vehicle speed during braking between *t* = 324s and *t* = 330s logged using the VMU. In this interval, the speed was reduced from 49.1 km/h to 7.25km/h in 6s. The corresponding phase currents of the motor are plotted in Figure 6.29. These currents contain high frequency components that were caused by the switching operation of the inverter and induced noises.

Most of the time, negative current flowed in phase *c* which indicated that the electric motor was supplying regenerative current to the inverter through that phase. Using the simplified circuit of the inverter and terminal connections of the electric motor, the conversion from AC to DC is illustrated in Figure 6.30 for t = 325.2s. At this instant, the regenerative current of 31.2A was generated at the DC side of the inverter. This current was subsequently shaped by the DC-DC converter circuit before being delivered to the battery. For t> 329.3s where the vehicle speed was less than 10km/h, the magnitudes of the phase currents reduced below 5A.

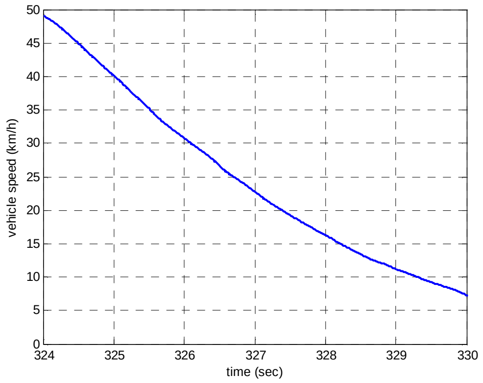

Figure 6.28 Vehicle speed during normal braking

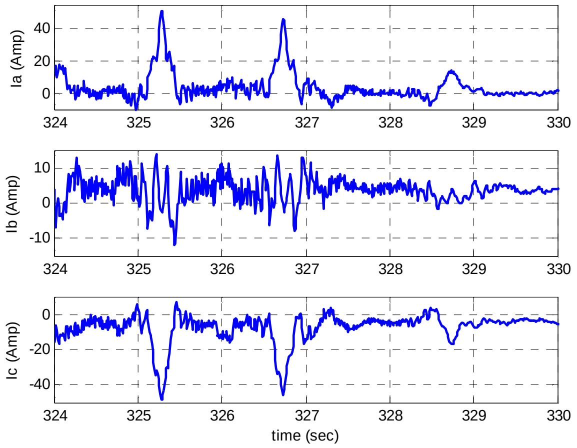

Figure 6.29 Phase currents of motor during braking

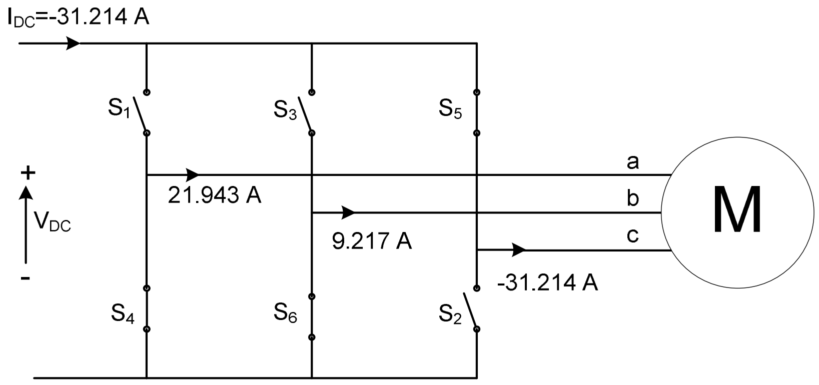

Figure 6.30 Current flow from the motor to inverter at t= 325.2s

To understand how the regenerative brake cooperated with the ABS, the vehicle was stopped under “hard” braking characterised by a short braking duration and high deceleration. Table 6.10 summarizes the braking characteristics for such hard braking classified by average deceleration. During the test it was found that when the vehicle was decelerated at 0.71*g*, the ABS intervened. Figure 6.31 shows that regenerative power was still generated even though the ABS was active. After the accelerator pedal was released, the power was reversed from 40kW to -10kW in about 1s. Then, the regenerative power was held for 0.5s before it reduced to zero at *t* = 193.9s.

In normal braking of the VISTA, the regenerative power was zero below 10km/h. But when the ABS was active, it was zero under 25km/h. Deactivating the regenerative braking would be predicted from the actual deceleration of the vehicle as shown in Figure 6.32. At *t* = 193.3s, the deceleration was greater than 1*g*. By looking carefully in Figure 6.31, from that time the regenerative power had started to reduce. Vehicle decelerations for the other two braking intervals are plotted in Figure 6.33 showing lower peaks of deceleration.

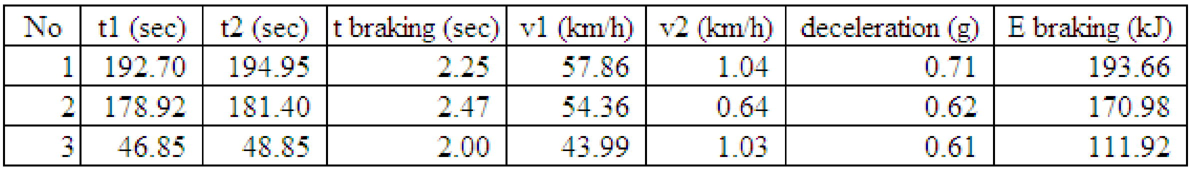

No	t1 (sec)	t2 (sec)	t braking (sec)	v1 (km/h)	v2 (km/h)	deceleration (g)	E braking (kJ)
1	192.70	194.95	2.25	57.86	1.04	0.71	193.66
2	178.92	181.40	2.47	54.36	0.64	0.62	170.98
3	46.85	48.85	2.00	43.99	1.03	0.61	111.92

Table 6.10 Experimental results for hard braking condition

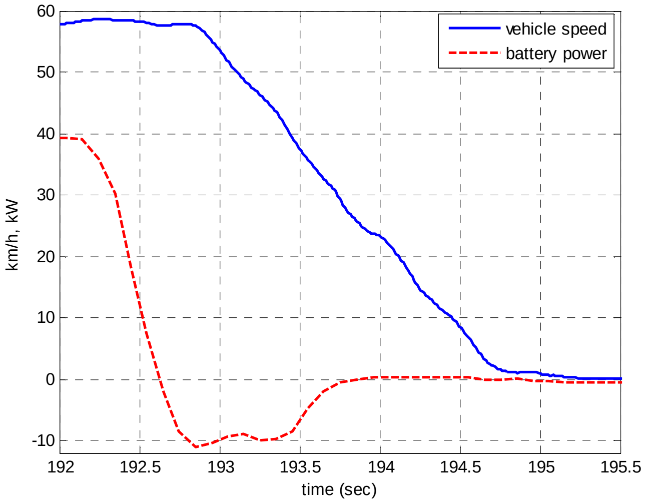

Figure 6.31 Vehicle speed and battery power during ABS intervention

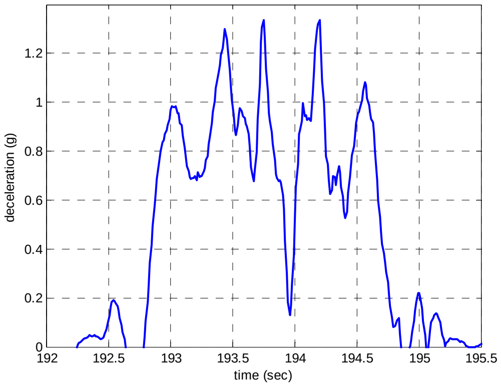

Figure 6.32 Vehicle deceleration during hard braking with ABS activated

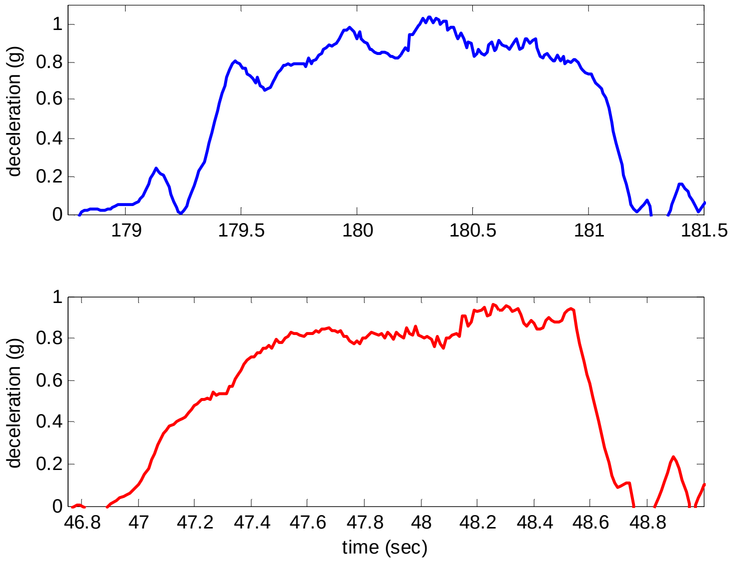

Figure 6.33 Vehicle deceleration during hard braking with ABS not activated

6.3.6 Interim Conclusions

During the test, the full capacity of regenerative current was not utilised. The highest regenerative current was 61.7 A which was lower than the current limit of 100 A. The voltage across the battery terminals was affected by the battery state, discharging or charging. In the charging state, the voltage across the battery terminals must be higher than the internal voltage of the battery to allow current to flow into the battery. For similar initial speeds, a longer braking time resulted in lower recovered braking energy. This was because the M/G efficiency was low when the generated torque was low at higher speed. The profile of regenerative current had a contribution to the stored braking energy. The areas under the square current represented energy losses in the regenerative braking. The regenerative braking system was effectively integrated with the ABS since at the same time the braking energy was recovered and wheel lock was prevented. It was investigated which scenario was adopted by the VISTA EV and found that the regenerative brake was de-activated after the ABS was engaged and the deceleration was greater than 1g.

CHAPTER 7

GENERAL DISCUSSION AND VALIDATION

7.1 General Discussion

The main difference between series and parallel braking systems is in controlling the brake pressure. As shown in Figure 5.29, the series braking system employs a pressure source, accumulator, solenoid valves and controller to achieve electronic pressure control. Since the regenerative braking system is fitted to the front axle and the actuation pressure at both front wheels is the same, that system can provide controlled brake torque on the front wheels. However this is not a complete system because failsafe and brake pedal simulation were not included. A failsafe system would allow the pressure generated in the master cylinder by the driver to reach brake caliper as in the parallel system.

In a series braking system, an algorithm to distribute braking demand into the regenerative and friction portions is needed. The regenerative braking torque available was calculated from the speed-torque characteristic of the M/G. The friction torque matched the difference between these two values. By doing this, the recovered braking energy was maximised and the duty level of the friction brake was reduced. The disadvantages were, in real application, that a sensor to measure brake torque demand and a processing unit to execute the strategy are needed. In this research, the braking torque at the front axle was determined as shown in Figure 5.21 for the FTP drive cycle and Figure 5.22 for the US06 drive cycle.

Two approaches are available to derive the braking demand from a time-speed profile. In previous approaches by other researchers, braking torque was usually found from the total braking force on the vehicle (mass*z). Tyre forces and wheel deceleration were not considered. However, tyre forces on the front wheels and the rear wheels are related and the wheel deceleration must be taken into account. The old method assumed that the brake torque could be directly obtained from the total braking force, whereas the new method proposed here considered the effect of tyre and wheel dynamics in calculating brake torque from total braking force. This has not previously been published in the open literature. The old method assumed that the brake torque could be directly obtained from the total braking force (Panagiotidis et al., 2000; Yeo and Kim, 2002), whereas the new method proposed here considers the effect of tyre and wheel dynamics in calculating brake torque from the total braking force as given by Equations (5.13) and (5.14).

Figure 7.1 shows that previous approaches generated lower braking torque on the front wheels and higher on the rear wheels compared to the approach proposed here. Since the regenerative brake is fitted on the front wheels, less braking energy is recovered when the previous approach was used, thus yielding a lower regenerative braking ratio. With the approach proposed here, the effect of vehicle configurations and road conditions on the assumptions made to derive equations (5.13) and (5.14) can be included.

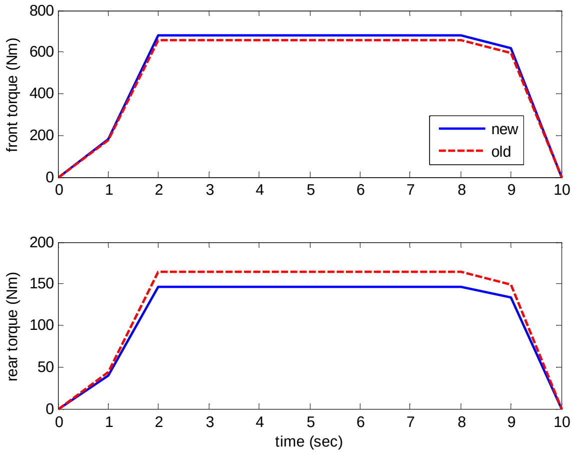

Figure 7.1 Brake torques with different approaches

In the blended braking modeling and design methodology proposed here, a forward-facing simulation was made which required a brake pedal model to accept demand from the driver. The brake pedal was represented by a function relating pedal force or pedal travel to master cylinder pressure. Experimental results from Ho (2009) suggested using a quadratic function to relate pedal travel and pressure. For a braking system with a vacuum booster fitted as Reuter et al. (2003) employed, it was convenient to use a lookup table to relate the pedal force with the pressure. The table entries can be replaced to represent a different brake pedal and accuracy of model can be increased by adding more data to that lookup table. But, each model is only valid for a specified vehicle. Comparison of the first and second models in generating pressure is shown in Figure 5.8. During the simulation, pedal force was used as the input since it represented a common brake pedal in a conventional vehicle with a vacuum booster. Ho (2009) employed a test rig to derive a pedal travel-pressure relationship for his particular system.

When the regenerative power on the wheels is known, models of the M/G and the battery in the powertrain are required to calculate the regenerative braking ratio. ADVISOR was used as the source of the characteristics of M/G and battery since it is well-known in computer simulation of HEV's and EV's. NREL (AVL, 2010) conducted a test to develop efficiency maps of popular M/G's. The battery data included open circuit voltage of the battery module and charging resistance which were generated in NREL's Battery Thermal Management Lab. These data were stored in Matlab files and thus were easily used in this research. However, these data are specific for a certain motor/controller pair and should not be used to simulate a HEV or EV with a different type of motor/controller because their characteristics would be different.

The average value of the regenerative ratio based on the FTP drive cycle was found to be 56.2% based on the assumption that the battery SoC at the beginning of braking was 50%. That average value would be lower if the initial battery SoC were higher because the regenerative force was weighted with the battery SoC and vehicle speed as indicated by equation (3.51) and Figure 3.16. Regenerative power is reduced as the battery SoC reaches 80% and no regenerative power was permitted above 90% of SoC.

Therefore, the regenerative braking ratio was reduced if the current battery SoC reached 80% before the braking event ended. The battery was not allowed to charge at SoC higher than 90% to prevent the overcharge condition that might occur and the vehicle would be safely slowed or stopped using friction brakes alone.

When both regenerative and friction braking demands are known, a knowledge of how the control system works is important to investigate the operation of a series braking system. In a brake-by-wire system, the time which elapses between the start of the brake demand from the driver and the application of both regenerative and friction brakes on the wheels should be minimised. This requires a fast control system to operate, otherwise the driver would notice the delay and feel uncomfortable. The logic and structure of existing control strategies are relatively unsophisticated and thus have small computational delays. Such strategies have drawbacks *viz*. torque ripple and pressure oscillation as shown in Figure 5.25 and Figure 5.31, and for real application these need further consideration of performance.

To control the braking torque of an induction M/G, a direct torque control was chosen because of its simplicity and fast response. DTC employs hysteresis controllers for both torque and flux as shown in Figure 4.7. The controller inputs are torque error and flux error and the controller outputs determine which entry of the vector selection table is used. Errors which are greater than the hysteresis band will cause the selected voltage vector to change in order to minimise these errors. This will switch the motor currents rapidly and generate ripple in the motor torque. As a result, the shape of the motor currents would no longer be sinusoidal as indicated in Figure 5.28. Fortunately, this torque ripple did not affect the motor speed as shown in Figure 5.26.

Each control strategy generates a particular shape of motor currents as indicated in Figure 5.28 from the simulation results and Figure 6.29 from the experimental work. For an induction M/G powered by a battery through an inverter, the voltage at the motor terminals only has two possible values *viz*. battery terminal voltage (U_{bat}) and zero voltage. The selected entry of the voltage vector in the DTC determines which phases connecting to U_{bat} and which to zero voltage. Equations (4.1) to (4.3) describe the circuit in each phase of the induction M/G and equation (4.15) shows the stator currents which are affected by stator inductances, variation of mutual inductances and variation of rotor currents. The shape of the motor currents has an effect on the efficiency of M/G. When the current is not sinusoidal, it contains higher frequency components called harmonics and the iron losses will be higher when these harmonics exist in the motor currents.

Since the DC M/G is still used in low power and low cost EV’s, its operation and control system have been considered in this research. The power source of both induction and DC M/Gs is the same, the battery but the power electronic devices connecting them to the battery are different. The induction M/G needs an inverter in the operation while the DC M/G employs a buck-boost converter to control its operation. A current controller is sufficient to control the torque of a DC M/G, but an induction M/G requires a more advanced technique such as direct torque control. Due to the brush and commutator mechanism in DC M/G, its power rating is lower than an induction M/G.

Two techniques were proposed to determine the reference of field current of a DC M/G. One was a linear function of time and the other was inversely proportional to the motor speed. The advantages of the first technique were that no sensor was needed to obtain the reference current and a higher armature current was generated as shown in Figure 5.35. But if the requirement was to generate a constant armature current, the second technique was a better option though a speed sensor would be needed in the real application.

Beside the regenerative braking system, HEV’s and EV’s are also equipped with safety features such as ABS and ESC which rely on friction brakes in their operation. The purpose of a regenerative braking system is to capture braking energy as much as possible. This indicates that its torque level should be high and thus the ABS could fail to prevent wheel lock if the regenerative braking torque is not removed or lowered as demonstrated in section 5.6. In the case of brake torque reduction, it is difficult to determine its value is real applications. Therefore, the regenerative braking system is normally disabled as the ABS is engaged.

7.2 Validation

In Chapter 5, a Simulink model was developed to investigate braking dynamics on a conventional vehicle. Furthermore, in experimental work with two EV's as detailed in Chapter 6, parallel braking systems were used. Therefore, with the knowledge of the ACE and VISTA braking systems, that model can be improved for application in parallel braking systems.

As explained in Table 6.1, the ACE EV controls the field current to obtain maximum M/G braking torque. Using the ACE circuit diagram in Figure 6.10, the controlling field current was conducted by switching transistors Q3, Q4, Q5 and Q6. In the armature circuit, transistor Q1 was always in the ON state and Q2 acted as a boost converter during braking. No further information about the motor/controller of the ACE was available, such as motor parameters and control techniques applied. Two current clamps were used to measure the field and armature currents as shown in Figure 7.2. The field current was gradually increased during braking at an approximate rate of 4 Amp/sec. The regenerative current rose rapidly from zero to 30 Amp in about 0.5s and was maintained at this level for about one second before returning to zero.

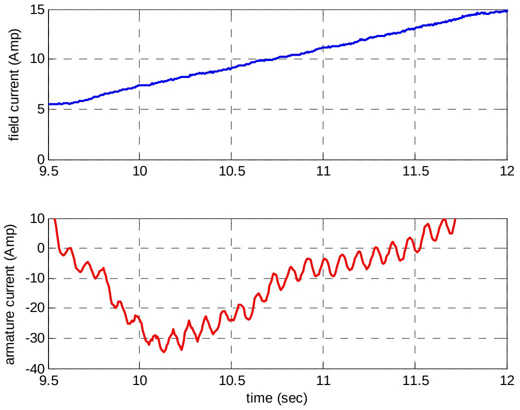

Figure 7.2 Field and armature currents of ACE DC motor/generator.

In Chapter 5, two current control techniques were proposed based on reference current generation. Firstly, field current is directed to increase linearly with time as shown in Figure 5.35. Secondly, the motor speed is used to derive the reference current where the field current is inversely proportional to the motor speed ($I_f\omega$=constant), as shown in Figure 5.37. In comparison, the first control technique showed similar response to measured currents and therefore could be used to simulate the braking system of the ACE EV.

The regenerative torque generated by the VISTA M/G was approximated using the battery power and the efficiency map. Information from TATA was used to find how the regenerative braking torque was generated. This indicated that the demanded regenerative torque was sent from the VMU to the MCU upon detection of the brake pedal status. The torque was raised to the maximum when the pedal was pressed and was reduced when the pedal was released as illustrated in Figure 7.3. The rate of torque rise and fall, and maximum braking torque were configurable to suit the drivers need. As the vehicle speed was decreased to very low values, the availability of regenerative torque was limited. In VISTA, that torque was linearly reduced from maximum value at the time the vehicle speed reached 10 km/h.

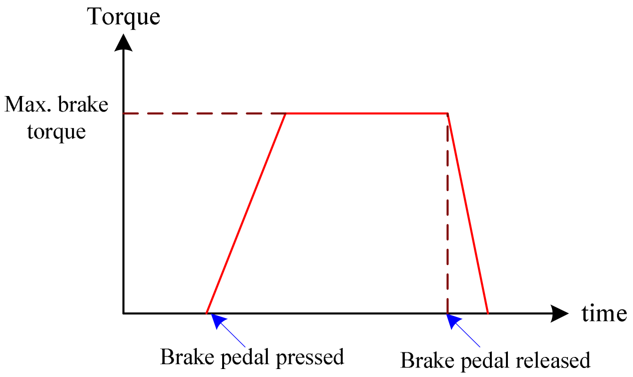

Figure 7.3 Brake torque demand of VISTA EV (TMETC, 2011)

Figure 7.4 shows the reference torque and regenerative torque of the VISTA M/G captured using CANlog 4 hardware (see section 6.3.3) while the VISTA was driven on the road. It can be seen that the reference torque was not constant after the rise time of 0.5s, unlike the reference torque in Figure 7.3. The fall time of the torque was observed to be similar with the rise time. When the brake pedal was steady, the magnitude of reference torque fluctuated around 26Nm. The torque on the front wheels was then 260Nm with a gear ratio of 10. The actual torque did not follow the reference torque at the beginning of braking. Their responses were close to each other after t = 3.6s. Using the vehicle speed of the VISTA in Figure 7.5, it was found that the M/G could not generate a retarding torque of 26Nm at speeds higher than 57.6km/h.

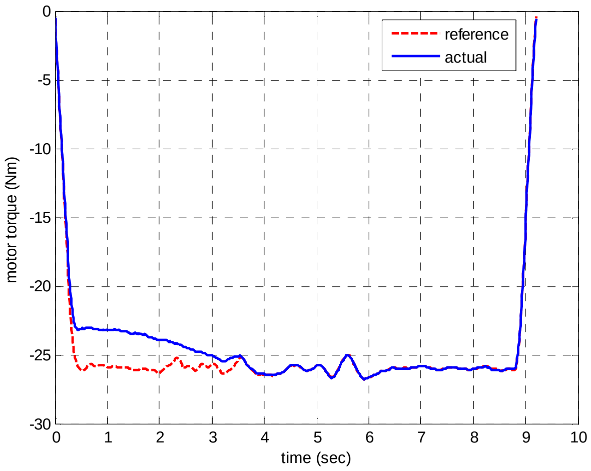

Figure 7.4 Reference and generated torques of VISTA M/G.

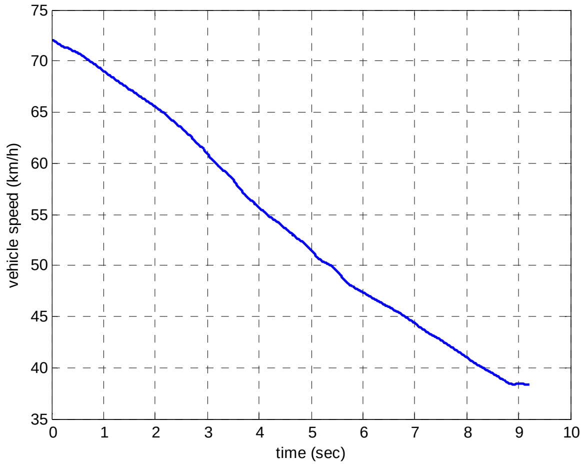

Figure 7.5 Vehicle road speed of VISTA during braking

The reference torque and motor speed of the VISTA were used as inputs to the regenerative braking system in Figure 5.24 to validate the simulation model. As shown in Figure 7.6, the control system could initially direct the induction M/G to follow the reference torque. But after t = 0.5s, the generated torque fluctuated around -20Nm and thus the torque error was 6Nm. Comparing this result with the actual torque of VISTA, neither was able to meet the demand at high vehicle speed. The parameters of direct torque control used in this simulation were constant and better performance would be achieved if adaptive parameters were applied.

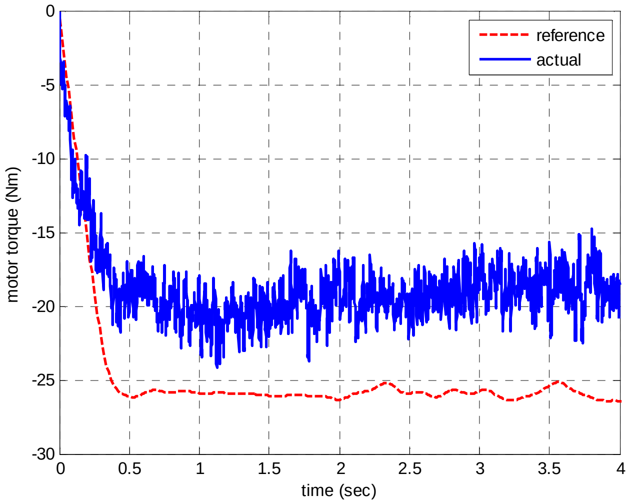

Figure 7.6 Reference and generated torques of simulation model

Experimental work was also carried out on the Toyota Auris Hybrid by Jaguar Land Rover who made the data available for this thesis, and it was used to investigate pressure control during brake blending. From the discussion in Chapter 2 Section 3, it was known that the brake controller generated pressure reference and the hydraulic control system must generate caliper pressure that closely follows this reference. Therefore, it was assumed that the caliper pressure acquired from the Toyota Auris Hybrid was a pressure reference generated by its brake controller. Hence, it could be used in this research to test the proposed pressure control system. The Auris data was not needed in this research since these were not used. The solenoid valves and brake caliper parameters had been setup and it was realised that these had not been optimised.

The Auris vehicle was fitted with sensors to measure brake pressures, pedal force, pedal travel, vehicle speed and wheel speeds. In a test where it was braked from 70km/h with braking time of 11s, the data presented in Figure 7.7 clearly shows that front wheel brake actuation pressure was modulated to meet brake demand in terms of brake pedal travel. After *t* = 4s, the pedal was held at about 16.5mm and returned to its initial position when *t* > 14s. Initially, the front brake actuation pressure increased with pedal travel and was maintained at about 6bar. But it was gradually reduced after *t* = 7s which indicates that the regenerative brake portion increased. At lower vehicle speeds, the front pressure was increased to 10barto stop the vehicle completely. This front pressure response was then used to validate the model of the hydraulic brake system proposed here as shown in Figure 7.8, the model presented in Figure 5.29 successfully follows the Auris front pressure despite the occurrence of pressure spikes in the output.

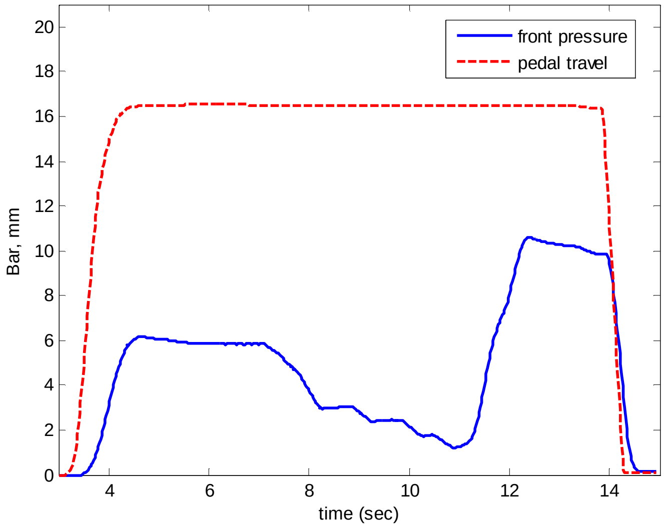

Figure 7.7 Pedal travel and front brake actuation pressure of the Auris braking system

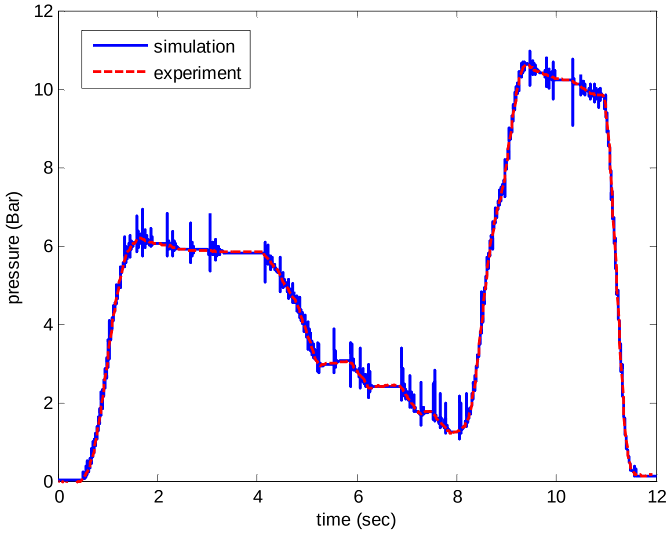

Figure 7.8 Comparison of the model output with experimental results

To explain why the simulation and experimental results were close, the pressure response to a step reference input was studied as shown in Figure 7.9. Here, the pressure reference was 30 bar and the caliper pressure was able to follow after 0.17 secs. The pressure control was achieved by controlling the opening of the inlet and outlet valves. The valve positions around t = 0.2 secs are shown in Figure 7.10. As can be seen, the inlet valve was opened to raise the caliper pressure up to 30 bar. When the caliper pressure was higher than 30 bar, the outlet valve was then opened. Subsequently, the controller directed both valves to close. The curve indicated that the valves could not be closed instantly due to their inertias.

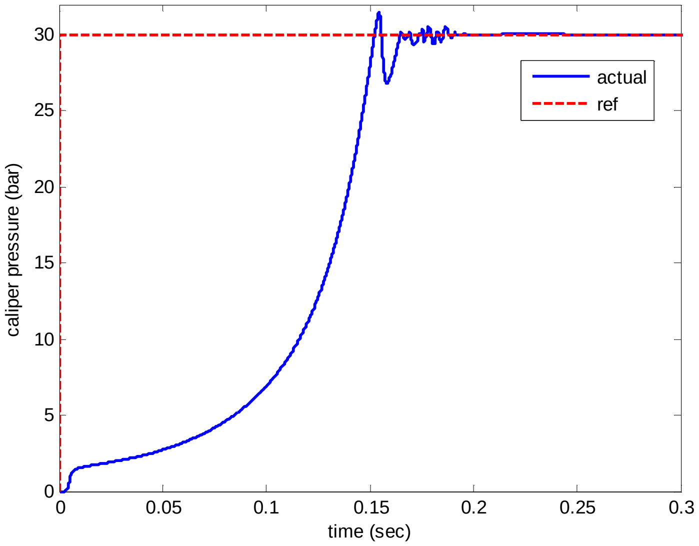

Figure 7.9 Reference and actual caliper pressures

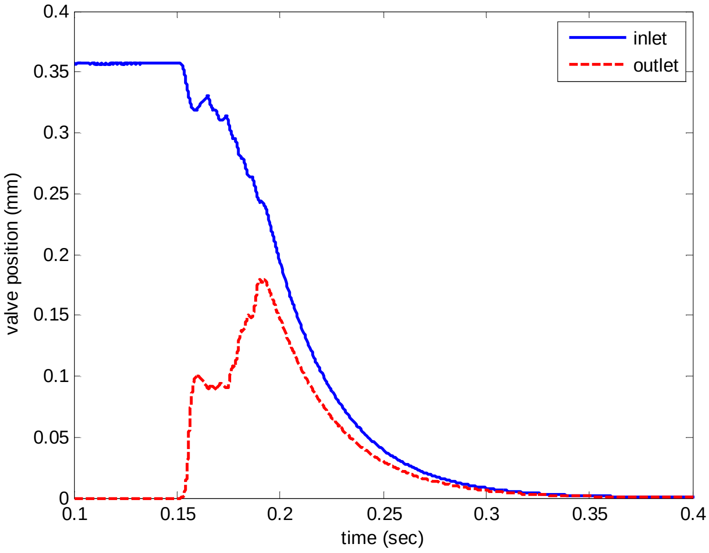

Figure 7.10 Inlet and outlet valve positions to follow reference pressure.

CHAPTER 8

SUMMARY, CONCLUSIONS AND RECOMMENDATIONS

8.1 Summary

There is up to 367.25kJ, 749.19kJ and 833.33kJ braking energy available in the FTP, US06 and EUDS drive cycles respectively. To recover as much of this energy as possible, an electric regenerative braking system with an extended control strategy which includes friction and regenerative braking during ABS operation has been investigated and applied in this research. Figure 2.1 illustrates the portion of braking energy that has been recovered and that which is wasted at friction brakes. There are two options to implement brake blending in an EV or HEV, i.e. a parallel braking system or a series braking system. Energy recuperation is higher in the series braking system. The main difference between these two braking systems is the way to modulate wheel brake pressure as indicated in Figure 2.2. The wheel brake hydraulic actuation pressure is directly adjusted by the driver in the parallel braking system. However the wheel pressure is controlled by the electronic unit in the series system and the master cylinder pressure is considered to represent the driver demand.

The result is that the hydraulic friction brake of a series system is only engaged at low speeds in the FTP drive cycle as shown in Figure 5.21. At higher speeds, the 15kW 1500rev/min M/G was able to meet the all brake demands. But when higher deceleration was needed at higher speeds such as in the US06 drive cycle, the friction brake was needed to be applied as shown in Figure 5.22.

The advantage of greater energy recuperation comes at the expense of system cost. Figure 5.29 indicates all the devices needed to implement modulation of the wheel brake actuation pressure. The series system must also include a stroke simulator to generate the required brake pedal feel for the driver.

To quantify the amount of recovered braking energy in the FTP drive cycle using a series braking system, simulations were completed as presented in section 5.3. In average, 56.17% of braking energy was stored in the battery, but this is only valid for the vehicle under consideration. In simulation including both braking and traction, stored braking energy up to 0.7% of the battery capacity could be theoretically used to accelerate the vehicle up to 18km/h. Figures 5.19 and 5.20 illustrated how deceleration profiles of two braking intervals with similar initial speeds and braking times can result from different operating points of the electric motor and charging current.

The main elements which define the design of any regenerative braking system are the M/G and battery. Various M/Gs have been applied by vehicle manufacturers in their EV's and HEV's as listed in Table 2.1. Two types of battery that are widely adopted in modern EV's and HEV's are NiMH and Li-Ion. Mass-produced HEV’s and EV’s such as the Toyota Prius and Nissan Leaf employ permanent magnet M/Gs due to their high torque density, power density and high efficiency characteristics. But Dorrell et al. (2010) showed using computer simulation that Induction M/Gs and switched-reluctance M/Gs are also promising for HEV applications The main benefits of the induction M/G are lower material and manufacturing costs, and higher durability.

One of the control methods for induction M/G application is DTC. As indicated in Figure 5.25, the torque reference in the FTP drive cycle was followed by a M/G with DTC. It was shown in Figure 5.26 that high frequency torque ripple generated did not affect motor speed. Validation of the torque control model with experimental data from the TATA VISTA showed that the model could follow the reference torque in transient periods but the steady state error was significant as shown in Figure 7.6.

Since the DC M/G is still employed in low power vehicles such as the 5.52 kW TATA ACE EV, its operation was simulated in section 5.5. The field current was increased as the speed decreased in order to generate adequate armature current as shown in Figures 5.35 and 5.37. By switching armature circuits, that armature current was allowed to flow to the battery as indicated in Figure 5.34.

On the other side, the wheel brake actuation pressure is controlled through the use of solenoid valves, an active vacuum booster or a motor actuated master cylinder. The prediction of wheel brake actuation pressure to apply solenoid valves to meet the brake demand in the FTP drive cycle was shown in Figure 5.31, and indicates that the controller allowed the wheel brake actuation pressure to fluctuate around the desired value. This simulation model has been validated against experimental data on a Toyota Auris Hybrid (data supplied by Jaguar Land Rover) as shown in Figure 7.8.

Threshold pressure control was adapted in that simulation, which is a straight forward control technique. Experimental work from Park et al. (2009) also demonstrated the limitations in its accuracy as indicated in Figure 2.7. A better but more complicated control method is to use sliding mode control as proposed by Aoki et al. (2007) and this performance was shown in Figure 2.6.

A simulation model to investigate integration of the regenerative braking system with the vehicle's ABS was presented in Figure 5.42. When the ABS was initiated, the regenerative torque of 380Nm on the front axle was reduced to zero in 6 milliseconds. Figure 5.44 indicated how the front wheels were prevented from being locked by the ABS while at same time the regenerative brake was disabled.

The first part of the experimental verification work for this research was conducted on a TATA ACE EV using an axle mounted chassis dynamometer. This small EV employed a parallel braking system without a vacuum booster fitted. It was found that the average regenerative ratio on the

ECE drive cycle was 9.7% but the maximum speed was set to 40km/h, so the vehicle could not meet the 50km/h specified in the ECE drive cycle.

The efficiency of the ACE EV powertrain was found using the acceleration intervals of the ECE drive cycle. Figure 6.11 showed the vehicle speed during acceleration and the corresponding battery and wheel power. It was found that the average efficiency for four acceleration intervals was 69%.

The ACE controller achieves higher acceleration performance by using the energy of braking to charge the batteries and maintain field current for a longer time. This feature was found by taking a closer look at the braking interval in Figure 6.9 and using the electric circuit of the ECE power system in Figure 6.10.

The second part of the experimental verification work used a TATA VISTA EV. Since this vehicle had adopted a CAN bus in its powertrain architecture, data logging in real driving was possible. The VISTA was driven in Coventry over a drive cycle of duration 16.6 minutes in which an average of 49% of braking energy was recovered. From the collected data, the regenerative power was only known up to the battery terminal. To predict stored braking energy, a battery model from ADVISOR was used. On average, 3% of energy was lost during charging the battery with regenerative current.

Regenerative braking torque was generated even when the accelerator pedal was slightly depressed. In this case the vehicle was retarded by regenerative braking force and rolling resistance. From power calculation under such conditions, the rolling resistance was found to contribute 4 kW to decelerate the VISTA and the resulting deceleration was 2.2%*g* for an initial vehicle speed of 45km/h.

Beside normal driving with moderate braking, the VISTA was subjected to hard braking to initiate ABS intervention. Surprisingly, 10 kW of regenerative power was still generated for 0.5s. The regenerative brake was then disabled when the instantaneous deceleration was greater than 1*g*.

8.2 Conclusions

In the research presented here the main aim was to advance the knowledge and understanding of blended braking (i.e. friction and regenerative) on road vehicles, in particular the modeling, simulation and control of such systems, to make a contribution to extending the driving range of EV’s and to increase fuel efficiency in HEV’s by designing and optimizing improved mixed-mode braking to achieve safe braking under all conditions of vehicle usage while maximizing energy recovery and re-use, and hence fuel economy. This has been achieved by developing sophisticated computational simulation algorithms and models which could be implemented to achieve increased energy recuperation from regenerative braking on an EV or HEV.

Studying vehicle dynamics during braking has benefit in the calculation of the ideal instantaneous wheel brake torques for a given drive cycle. With the aim of quantifying the amount of recuperated and stored braking energy from a M/G fitted to drive/brake the front wheels, the more sophisticated and accurate methods proposed (than were currently used on the ‘low-cost’ passenger cars and light commercial vehicles investigated) here in this research have indicated how higher energy recuperation can be achieved as discussed in Chapter 7 section1.

Using modern computational modeling and simulation techniques, vehicle components related to the regenerative and friction brake systems can be modelled with a range of representation ranging from simple to highly detailed and sophisticated. For example, a M/G is usually represented by an efficiency curve with torque and speed as inputs in a simple model. In the research presented here a highly sophisticated model based on advanced electrical machine theory was developed to model the M/G in a highly detailed representation. Similarly, the solenoid valve in an hydraulic brake system was also modelled in a highly detailed representation. It can be concluded that this level of representation is essential for establishing the required detail in the algorithms necessary for the accurate control of a mixed-mode braking system for a road vehicle with regenerative braking, and has not specifically been published before.

The M/Gs of EV's and HEV's cannot meet the driver's brake demand under all braking conditions. Drive cycles which are characterised by substantial events containing higher decelerations such as the US06 cycle require the friction brake to be used in incorporation with e.g. a 15kW M/G whereas in the FTP drive cycle the friction brakes would not necessarily be required because the deceleration levels are lower. This emphasises the need for improved drive cycle designs for EV/HEV's with regenerative braking.

The control system methodology for an ideal blended braking system for a vehicle with friction braking and regenerative braking consists of two levels. First, the brake demand from the driver must be distributed into regenerative and friction portions using instantaneous knowledge of the vehicle speed and the battery SoC as detailed in Chapter 3 section 5. This research has confirmed that brake demand can be effectively quantified to achieve this by measuring master cylinder pressure or pedal travel. Secondly, the torque of the M/G and the actuation pressures for the friction brakes at each road wheel caliper must be accurately adjusted to match with the driver demand.

Simulation models to predict the operation of both regenerative and friction brake systems are applicable for EV's and HEV's, but the performance of the control systems needs to improve to achieve ideal braking under all conditions of use. Experimental validation work which was conducted as part of this research on 2 vehicles viz. the TATA Vista and the Toyota Auris Hybrid indicated that the torque control of the M/G exhibited a steady state error as shown in Figure 7.6 which would be reduced by the application of the research findings presented here. The experimental work also indicated that the actuation pressure fluctuation at the friction brake wheel calipers should be damped out by the application of the research findings as indicated in Figure 7.8.

The brake blending control systems used in the two EV's examined in this research, *viz*. the TATA ACE and VISTA which were equipped with parallel braking systems, was found to be unsophisticated and thus the regenerative braking was less than ideal from the point of view of recuperated energy. All the brake pressure generated by the driver was directly applied to the friction brake hydraulic wheel actuators and the regenerative braking was preset by the vehicle management system. The contribution of the M/G to regenerative braking could not be varied in the standard setup but could be adjusted from the vehicle management system using proprietary softwares. From this it can be concluded that advanced technology is available in modern EV/HEV's, but the control strategy, and algorithms such as those presented in this thesis have a great deal to offer in terms of the implementation of blended braking for improved energy recuperation.

Experimental data from an HEV equipped with a series braking system was supplied by another company and was not generated first hand in this research, however it was sufficient to validate the simulation model. As with the TATA VISTA, the regenerative braking system was not immediately de-activated when the ABS intervened; the regenerative braking still operated as long as the vehicle deceleration was less than 1g as shown in Figure 6.32. Using the models developed in this research to create detailed computer simulations, three scenarios of integrating regenerative braking with the ABS were investigated, viz. immediately disabled, enabled and reduced as explained in Chapter 5 section 6. One solution to prevent wheel lock while maintaining energy recovery via the RB was concluded to be by reducing the regenerative braking torque but not to zero. An approximate reduction by 20% was suggested from the simulation and although this was not investigated further, it can be concluded that if incorporated into the blended braking control strategy, maintaining regenerative braking action with a controlled bias to the friction braking under ABS operation could be an effective control strategy for blended braking.

The recuperation energy measured and predicted in the VISTA EV was much higher than in the ACE EV. This was expected since the M/G size of the VISTA was bigger than that of the ACE, but another important aspect was that the M/G was mounted at the front axle of the VISTA but at the rear axle in the ACE. The adhesion utilisation (wheel lockup force)of a 4-wheeled rigid road vehicle is higher on the front axle because of weight distribution and weight transfer during braking. For front wheel drive designs (i.e. where the M/G drives the vehicle’s front wheels) the amount of energy that can be recuperated is potentially therefore much higher than in a rear wheel drive design. In an electrical energy storage system the open-circuit battery voltage has a nonlinear relationship to the battery SoC, e.g. this research has shown that a larger voltage drop was observed when the battery was initially discharged. It can therefore be concluded that where the energy storage system will see a wide range of battery SoC with the high energy recuperation potential with a front-wheel drive design, sophisticated control of the M/G is needed to ensure good brake blending since the battery voltage will vary significantly.

A form of Direct Torque Control (DTC) has been applied in this research to control the regenerative torque of an induction M/G. Research found in the published literature has revealed that DTC is also used in PMBL M/Gs and shows an improvement in their performance. Validation work presented in section 7.2 showed that the torque control in the VISTA EV is a more advanced DTC, for instance, torque ripple was not apparent. It can be concluded that advanced DTC is important in future designs of EV and HEV, and will open up new possibilities for blended braking which can be investigated using the new modelling and simulation methods presented in this thesis.

8.3 Recommendations

In this research, various aspects of braking in HEV’s and EV’s have been investigated through simulation models and experimental work. For example, a new more accurate Simulink model of an hydraulic braking system has been developed which can be used to study the braking system of, for example, the Toyota Prius. But it was found in the literature that the Nissan Leaf employs a significantly different system as shown in Figure 2.5. Therefore further work would involve modelling such newly developed systems for validation purposes.

In the simulation, it was found that the regenerative torque level could be reduced by 20% to avoid the ABS preventing the front wheels from being locked during ABS operation in mixed-mode braking. Further work is needed to justify how, why and if this type of condition is applicable in practice.

Direct Torque Control (DTC) is used to control the regenerative torque of an induction M/G and is also used in PMBL M/G’s showing an improvement in their performance. Further work to analyse more advanced control systems based on advanced DTC should be carried out.

The ECB developed by Toyota which was shown in Figure 2.16 illustrates how complex a series regenerative braking system is. The brake demand is measured by a stroke sensor and subsequently the ECU performs calculations of required regenerative and friction torques. In this research, the delay time between the driver depressing the pedal to the vehicle deceleration being noticed by the driver was not considered. Further work is therefore recommended to integrate all the models developed here, including the vehicle model, controller models, electric drive model and hydraulic brake model. By running these models under conditions that mimic real application, the delay time can be predicted.

Finally, the experimental work on series braking systems should be extended to the next steps as future work. Both vehicles, i.e. the ACE EV and the VISTA EV investigated in this research were fitted with a parallel braking system. Though the VISTA EV adopts an advanced electric drive, its friction brake system is still conventional. More advanced designs, such as the Toyota Prius, Nissan Leaf and Chevrolet Volt are candidates for further research in blended braking research.

References

AHN, J. K., JUNG, K. H., KIM, D. H., JIN, H. B., KIM, H. S. & HWANG, S. H. (2009) Analysis of a Regenerative Braking System for Hybrid Electric Vehicles Using an Electro-Mechanical Brake. *International Journal of Automotive Technology, Vol. 10*, 229−234.

AIDA, S., AKITOMO, K. & MIKI, I. (2008) Basic Characteristics of Electric Vehicle Using 40kW Switched Reluctance Motor. *IEEE International Conference on Electrical Machines and* Systems, 3358-3361.

ALBRICHSFELD, C. V. & KARNER, J. (2009) Brake system for hybrid and electric vehicles. *SAE International* , 2009-01-1217.

AOKI, K., KURODA, S., KAJIWARA, S., SATO, H. & YAMAMOTO, Y. (2000) Development of Integrated Motor Assist Hybrid System: Development of the 'Insight', a Personal Hybrid Coupe. *SAE International*, 2000-01-2216.

AOKI, Y., SUZUKI, K., NAKANO, H., AKAMINE, K. (2007) Development of hydraulic servo brake system for cooperative control with regenerative brake. *SAE International*, 2007-01-0868.

BAISDEN, A. C. & EMADI, A. (2004) ADVISOR-Based Model of a Battery andan Ultra-Capacitor Energy Source for Hybrid Electric vehicle.*IEEE Transactions on Vehicular Technology, Vol. 53*, 199-205.

BENGER, R., WENZL, H., BECK, H. P., JIANG, M., OHMS, D. & SCHAEDLICH, G. (2009) Electrochemical and Thermal Modeling of Lithium-Ion Cells for Use in HEV or EV Application. *World Electric Vehicle Journal Vol. 3*. 1-10.

BUJA, G. S. & KAZMIERKOWSKI, M. P. (2004) Direct Torque Control of PWM Inverter-Fef AC Motors - a Survey. *IEEE Transactions on Industrial Electronics*, Vol. 51, 744 – 757.

BURKE, A.F. (2007) Batteries and Ultracapacitors for Electric, Hybrid, and Fuel Cell Vehicles. *Proceeding of the IEEE,*Vol 95, 806-820.

CHAU, K. T. & WONG, Y. S. (2002) Overview of Power Management in Hybrid Electric Vehicles, *Journal of Energy Conversion and Management Vol 43*, 1953–1968.

CHAU, K. T., CHAN, C. C. & LIU, C. (2008) Overview of Permanent-Magnet Brushless Drives for Electric And Hybrid Electric Vehicles. *IEEE Transactions on Industrial Electronics*Vol 55, 2246-2257.

CHOA, M. H., KIMB, S. J., KIMC, D. & JANGA, H. (2005) Effects of Ingredients on Tribological Characteristics of a Brake Lining: an Experimental Case Study. *Journal of Wear, Vol 258*, 1682–1687.

CHOI, S., LEE, J. & HWANG, I. (2003) New Generation ABS Using Linear Flow Control and Motor Speed Control. *SAE International*. 2003-01-0254

DAY, A. J. (2008) The dynamics of braking. *Braking of Road Vehicles 2008*, 57-64

DORRELL, D.G., KNIGHT, A.M., POPESCU, M., EVANS, L. & STATON, D.A. (2010) Comparison of Different Motor Design Drives for Hybrid Electric Vehicles. *Energy Conversion Congress and Exposition*, 3352 – 3359.

DUOBA, M., NG, H. & LARSEN, R. (2001) Characterization and Comparison of Two Hybrid Electric Vehicles (HEVs) – Honda Insight and Toyota Prius. *SAE International*, 2001-01-1335.

DURISEK, N. J. & GRANAT, K. J. (2008) Industry Implementation of Automotive Electronic Stability Control (ESC) Systems. *SAE International*, 2008-01-0593.

Emadi, A. (2005) *Handbook of Automotive Power Elelctronics and Motor Drives*. CRC Press

FU, H., TIAN, G., CHEN, Y. & CHEN, Q. (2009) Sliding Mode-based DTC-SVM Control of Permanent Magnet Synchronous Motors for Plug-in Hybrid Electric Vehicles. IEEE ???, 500-505.

FU, T. J. & XIE, W. F. (2006) Torque Control of Induction Motors for Hybrid Electric Vehicles. *Proceedings of the 2006 American Control Conference, Minnesota*, 5911-5915.

GAO, H., GAO, Y. & EHSANI, M. (2001) Design Issues of the Switched Reluctance Motor Drive for Propulsion and Regenerative Braking in EV and HEV. *SAE International*, 2001-01-2526.

GAO, Y. & EHSANI, M. (2001) Electronic Braking System of EV And HEV Integration of Regenerative Braking,Automatic Braking Force Control And ABS. *SAE International*, 2001-01-2478.

GAO, Y. & EHSANI, M. (2010)Design and Control Methodology of Plug-in Hybrid Electric Vehicles. *IEEE Transactions on Industrial Electronics, Vol. 57*, 633-640.

HANCOCK, M. J., WILLIAMS, R. A., GORDON, T. J. & BEST, M. C. (2005) A Comparison of Braking and Differential Control of Road Vehicle Yaw–Sideslip Dynamics. *Proceedings of the Institution of Mechanical Engineers, Part D Journal of Automobile Engineering, Vol 219*, 309-327.

HEISLER, H. (2002) *Advanced Vehicle Technology*. Butterworth-Heinemann, Oxford.

HO, H. P. (2009) *The influence of braking system component design parameters on pedal force and displacement characteristics*, University of Bradford.

HUSAIN, I. & ISLAM, M. S. (1999) Design, Modeling and Simulation of an Electric Vehicle System. *SAE International*, 1999-01-1149.

JAZAR, R. N. (2008) *Vehicle Dynamics: Theory and Applications*, Springer.

JING, H., LIU, Z. & CHEN, H. (2011) A Switched Control Strategy for Antilock Braking System With On/Off Valves. *IEEE Transactions On Vehicular Technology, Vol. 60*, 1470-1484.

KARDEN, E., PLOUMEN, S., FRICKE, B., MILLER, T. & SNYDER, K. (2007) Energy Storage Devices for Future Hybrid Electric Vehicles, *Journal of Power Sources Vol. 168*, 2-11.

KAWAMURA, H., ITO, K., KARIKOMI, T. & KUME, T. (2011) Highly-Responsive Acceleration Control for the Nissan LEAF Electric Vehicle. *SAE International*, 2011-01-0397.

KHALIGH, A. & LI, Z. (2010) Battery, Ultracapacitor, Fuel Cell, and Hybrid Energy Storage Systems for Electric, Hybrid Electric, Fuel Cell, and Plug-In Hybrid Electric Vehicles: State of the Art. *IEEE Transactions on Vehicular Technology, Vol. 59*, 2806-2814.

KHOUCHA, F., MAROUANI, K., HADDOUN, A., KHELOUI, A. & BENBOUZID, M. E. H. (2007) An Improved Sensorless DTC Scheme for EV Induction Motors. *IEEE Electric Machines & Drives Conference*, 1159-1164.

KIM, D. & KIM, H. (2006) Vehicle stability control with regenerative braking and electronic brake force distribution for a four-wheel drive hybrid electric vehicle. *Proceedings of the Institution of Mechanical Engineers, Part D Journal of Automobile Engineering, Vol 220,* 683-693.

LI, B. & YU, F. (2009) Design of a Vehicle Lateral Stability Control System Via a Fuzzy Logic Control Approach. *Proceedings of the Institution of Mechanical Engineers, Part D Journal of Automobile Engineering, Vol 224,* 313-326.

LIU, J., PENG, H. & FILIPI, Z. (2005) Modeling and Analysis of the Toyota Hybrid System. *International Conference on Advanced Intelligent Mechatronics, California*, 134-139.

LU, S., CORZINE, K. A. & FERDOWSI, M. (2007) A New Battery/Ultracapacitor Energy Storage System Design and Its Motor Drive Integration for Hybrid Electric Vehicles. *IEEE Transactions On Vehicular Technology, Vol. 56,* 1516-1523.

LYSHEVSKI, S. E. (1999) Transient Dynamics and Motion Control of Induction Motors. *IEEE lnternatianal Conference on Control Applications*, 950-955.

LYSHEVSKI, S. E. (2008) *Electromechanical Systems and Devices*, CRC Press.

MARKEL, T., BROOKER, A., HENDRICKS, T., JOHNSON, V., KELLY, K., KRAMER, B., O'KEEFE, M., SPRIK, S. & WIPKE, K. (2002) ADVISOR: a Systems Analysis Tool for Advanced Vehicle Modelling. *Journal of Power Sources Vol. 110*, 255–266.

MEYER, M., GROTE, T. & BÖCKER, J. (2007) Direct Torque Control for Interior Permanent Magnet Synchronous Motors with Respect to Optimal Efficiency., *European Conference on Power Electronics and Applications*, 1-7.

MILLER, J. M. (2004) *Propulsion Systems for Hybrid Vehicles*, IET Power and energy series 45.

MILLER, J. M., MCCLEER, P. J. & EVERETT, M. (2005) Comparative Assessment of Ultra-capacitors and Advanced Battery Energy Storage Systems in PowerSplit Electronic-CVT Vehicle PowerTrains. *IEEE International Conference on Electric Machines and Drives*, 1513-1520

NAKAMURA, E., SOGA, M., SAKAI, A., OTOMO, A. & KOBAYASHI, T. (2002) Development of electronically controlled brake system for hybrid vehicle. *SAE International*, 2002-01-0300.

OHTANI, Y., INNAMI, T., OBATA, T., YAMAGUCHI, T., KIMURA, T. & OSHIMA, T. (2011) Development of an Electrically-Driven Intelligent Brake Unit. *SAE International*, 2011-01-0572.

OMEKANDA, A. M. (2003) A New Technique for Multidimensional Performance Optimization of Switched Reluctance Motors for Vehicle Propulsion. *IEEE Transactions on Industry Applications, Vol. 39*, 672-676.

PACEJKA, H. (2012) Tire and Vehicle Dynamics, 3rd Edition, Butterworth-

Heinemann, ISBN 9780080970165.

PANAGIOTIDIS, M., DELAGRAMMATIKAS, G. & ASSANIS, D. (2000) Development and Use of a Regenerative Braking Model for a Parallel Hybrid Electric Vehicle. *SAE International*, 2000-01-0995.

PARK, M., KIM, S., YANG, L. & KIM, K. (2009) Development of the control logic of electronically controlled hydraulic brake system for hybrid vehicle. *SAE International*, 2009-01-1215.

PENG, D, ZHANG, Y., YIN. C. L. & ZHANG, J. W. (2008) Combined Control of a Regenerative Braking and Antilock Braking System for Hybrid Electric Vehicles. *International Journal of Automotive Technology, Vol. 9*, 749−757.

QI, X., SONG, J., WANG, H. (2005) Influence of hydraulic ABS parameters on solenoid valve dynamic response and braking effect. *SAE International*, 2005-01-1590.

RAHMAN, K. M. & SCHULZ, S. E. (2002) Design of High-Efficiency and High-Torque-Density Switched Reluctance Motor for Vehicle Propulsion. *IEEE Transactions On Industry Applications, Vol. 38*, 1500-1507.

RAHMAN, K. M., FAHIMI, B., SURESH, G., RAJARATHNAM, A. V. & EHSANI, M. (1998) Advantages of Switched Reluctance Motor Applications to EV and HEV: Design and Control Issues. *IEEE Industry Applications Conference*, 327-334.

RAJAMANI, R. (2006) *Vehicle Dynamics and Control*, Springer, ISBN 9780387288239

REUTER, D. F., LLOYD, E. W., ZEHNDER, J. W. & ELLIOTT, J. A. (2003) Hydraulic Design Considerations for EHB Systems. *SAE International*, 2003-01-0324.

SASAKI, S. (1998) Toyota's Newly Developed Hybrid Powertrain. *Proceedings of International Symposium on Power Semiconductor Devices & ICs, Kyoto*.

SATO, Y., ISHIKAWA, S., OKUBO, T., ABE, M. & TAMAI, K. (2011) Development of High Response Motor and Inverter System for the Nissan LEAF Electric Vehicle. *SAE International*, 2011-01-0350.

SONG, J., KIM, H. & BOO, K. (2007) A study on an anti-lock braking system controller and rear-wheel controller to enhance vehicle lateral stability. *Proceedings of the Institution of Mechanical Engineers, Part D Journal of Automobile Engineering, Vol 221,* 777-787.

TAKAHASHI, I. & NOGUCHI, T. (1986) A New Quick-Response and High-Efficiency Control Strategy of an Induction Motor. *IEEE Transaction of Industrial Application, Vol. 22*, 820–827.

TATE, E., HARPSTER, M., & SAVAGIAN, P. (2008) The Electrification of the Automobile: From Conventional Hybrid, to Plug-in Hybrids, to Extended-Range Electric Vehicles. *SAE International*, 2008-01-0458.

TAYLOR, A. M. K. P. (2008) Science Review of Internal Combustion Engines. *Journal of Energy Policy, Vol 36*, 4657–4667.

TMETC (2011) Private Communication.

TREMBLAY, O. & DESSAINT, L. A. (2009) Experimental Validation of a Battery Dynamic Model for EV Applications. *World Electric Vehicle Journal Vol. 3*, 1-10.

VLACIC, L., PARENT, M. & HARASHIMA, F. (2001) *Intelligent Vehicle Technologies : Theory and Applications*, Butterworth-Heinemann, Oxford.

VYNCKE, T. J., BOEL R. K., MELKEBEEK, J. A. A. (2006) Direct Torque Control of Permanent Magnet Synchronous Motors – An Overview. *3rd IEEE Benelux Young Researchers Symposium in Electrical Power Engineering*, *Belgium*, 1-5.

WANG, F. & ZHUO, B. (2008) Regenerative Braking Strategy for Hybrid Electric Vehicles Based on Regenerative Torque Optimization Control. *Proceedings of the Institution of Mechanical Engineers, Part D Journal of Automobile Engineering, Vol 222,* 499-513.

WANG, J. P., XU, L., GUO, J. G. & DING, L. (2009) Modelling of a Battery Pack for Electric Vehicles Using a Stochastic Fuzzy Neural Network. *Proceedings of the Institution of Mechanical Engineers, Part D Journal of Automobile Engineering, Vol 223,* 27-35.

WILLIAMSON, S. S., LUKIC, S. M. & EMADI, A. (2006) Comprehensive Drive Train Efficiency Analysis of Hybrid Electric and Fuel Cell Vehicles Based on Motor-Controller Efficiency Modeling. *IEEE Transactions on Power Electronics, Vol. 21*, 730-740.

www.avl.com

www. davebarton.com

www.epa.com

www.mathworks.com

www.tm4.com

XIAO, W. Y., WANG, F. & ZHUO, B. (2008) Regenerative Braking Algorithm for an ISG HEV Based on Regenerative Torque Optimization. *Journal of Shanghai JiaotongUniv, Vol 13*, 193–200.

YE, M., BAI, Z. F. & CAO, B. G. (2008) Energy Recovery for Battery Electric Vehicles. *Proceedings of the Institution of Mechanical Engineers, Part D Journal of Automobile Engineering, Vol 222.* 1827-1839.

YEO, H. & KIM, H. (2002) Hardware-In-The-Loop Simulation of Regenerative Braking for a Hybrid Electric Vehicle. *Proceedings of the Institution of Mechanical Engineers, Part D Journal of Automobile Engineering, Vol 216.* 855-864.

YEO, H., HWANG, S., & KIM, H. (2006) Regenerative Braking Algorithm for a Hybrid Electric. *Proceedings of the Institution of Mechanical Engineers, Part D Journal of Automobile Engineering, Vol 220*, 1589-1600.

ZEHNDER, J. W., KANETKAR, S. S. & OSTERDAY, C. A. (1999) Variable Rate Pedal Feel Emulator Designs for a Brake-By-Wire System. *SAE International*, 1999-01-0481

ZHU, Z.Q. & HOWE, D. (2007) Electrical Machines and Drives for Electric, Hybrid, and Fuel Cell Vehicles. *Proceeding of the IEEE, Vol. 95*, 746-765.

APPENDICES

Appendix A : Control Techniques for ABS

To understand how an ABS works, the time response of vehicle speed, wheel speed, wheel acceleration and brake torque, and slip-torque are needed. From the upper left of Figure A.1, braking torque T is applied in the opposite direction of rotation and the road exerts a braking frictional force B to the tyre in same direction as the rotation. As the braking torque increases, frictional force also increases but depends on the slip ratio. When point 1 is reached, the braking torque is T1 and since RrxB is less than T1, the wheel is decelerated and the slip ratio moves toward the right. Further increase in braking torque to point 2 as shown in the lower right curve, the wheel deceleration reaches the predicted threshold that initiates the ABS to reduce braking torque. Even if T1 is reduced, its value is still larger than RrxB, which causes the wheel to continue to decelerate up to point 3. Now, RrxB is larger than T1 and therefore the wheel starts to accelerate. This initiates the ABS to hold braking torque up to the time when maximum acceleration is reached and is indicated as point 4 in the graph. Next, the ABS starts to increase the braking torque to prevent the wheel accelerating further.

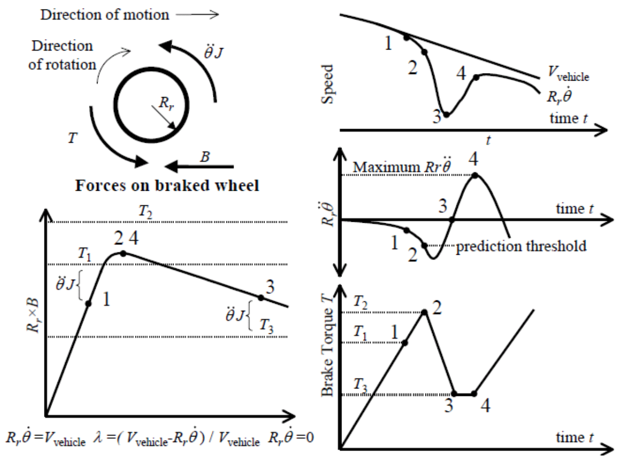
Direction of motion
Direction of rotation
$\ddot{\theta} J$
R_r
T
B
Forces on braked wheel
T_2
T_1
2 4
$\ddot{\theta} J$
1
3
$\ddot{\theta} J$
T_3
$R_r \times B$
$R_r \dot{\theta} = V_{\text{vehicle}}$
$\lambda = (V_{\text{vehicle}} - R_r \dot{\theta}) / V_{\text{vehicle}}$
$R_r \dot{\theta} = 0$
Speed
1
2
3
4
V_{vehicle}
$R_r \dot{\theta}$
time t
t
$R_r \ddot{\theta}$
Maximum $Rr\ddot{\theta}$
4
3
time t
1
2
prediction threshold
Brake Torque T
T_2
T_1
T_3
1
2
3
4
time t

Figure A.1 ABS mechanics (Kienhöfer et al., 2004)

Appendix B : Basic Circuits of Inverter and Buck-boost converter

An inverter is an electronic switch used to convert DC voltage into AC voltage at a specified amplitude and frequency. The DC voltage comes from either the battery or the output of rectifier. To stabilise voltage at the input terminal of the inverter, a large capacitor is added in parallel with the DC source. The switching operation results in square-wave AC voltage at the output terminal of the inverter.

The inverter in figure B.1 consists of four switching devices and four freewheeling diodes. The semiconductor switch is a power transistor, and a gate turn-off (GTO) thyristor or silicon-controlled rectifier (SCR) with its commutation circuit. To generate square wave voltage as shown in figure B.2, switches S_1 and S_4 are turned on for the positive half-cycle and switches S_2 and S_3 are turned on for the negative half-cycle. The current waveform is rectangular when the load is resistive. When the load contains an inductive component, the diode provides a return path to the current after the switches are turned off. Figure B.3 illustrates the output voltage, load current and the currents flowing at each switch employing the SCR and diode. It can be seen that diodes D_1 and D_4 conduct after switches SCR_2 and SCR_3 are turned off, also diodes D_2 and D_3 conduct after switches SCR_1 and SCR_4 are turned off. The current rises and decays exponentially whereas the time constant equals the ratio of inductance and resistance.

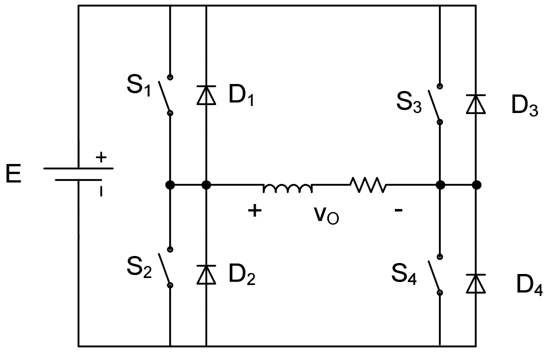
S1
D1
S3
D3
E
+
+
vO
-
S2
D2
S4
D4

Figure B.1 Full-bridge single-phase inverter

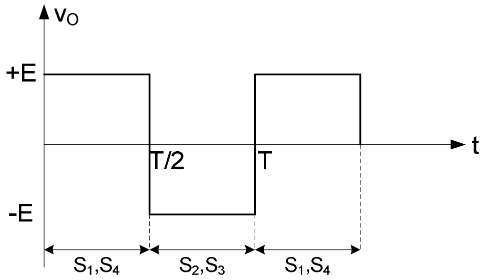

Figure B.2 Switching sequence and output voltage waveform

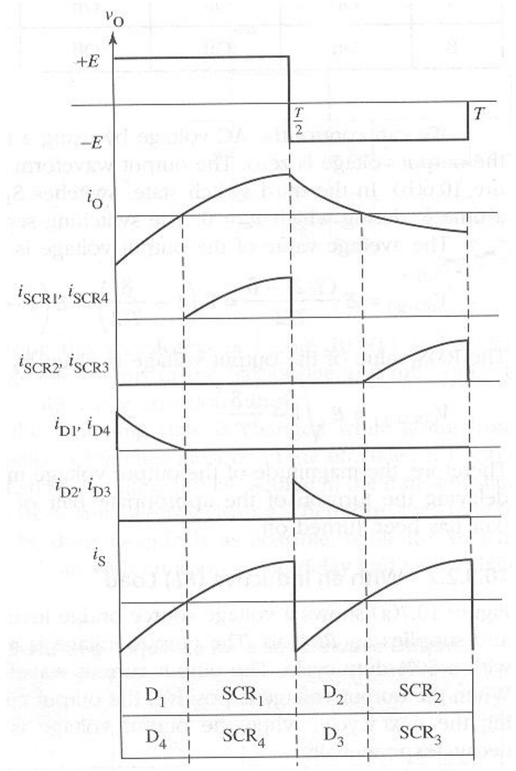

Figure B.3 Voltage and current waveforms (Ahmed, 1999)

For DC drive application, the power electronic device needed is DC-DC converter. During traction of EV, the battery voltage is switched to control the current and thus the traction torque. While during regenerative braking, the motor current is pumped to battery by combining electronic switch with inductor. The DC-DC converter to produce lower average output voltage than DC input voltage is called buck (step-down) converter. For greater output voltage, the circuit is called boost (step-up) converter. As shown in Figure B.4, both ordinary converters employ electronic switch, inductor, capacitor and diode.

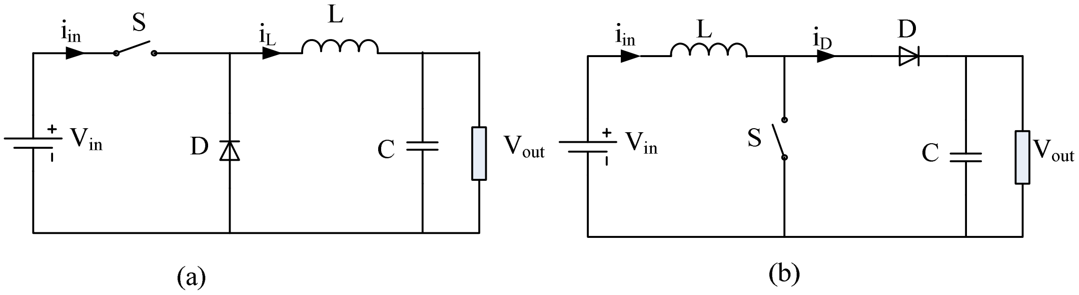

Figure B.4 DC-DC converter (a) buck converter (b) boost converter

(Luo and Ye, 2010)

The output voltage is buck converter is:

$$V_{out} = kV_{in} \tag{B.1}$$

For $kT<t<T$, the switch S is opened, T is switching period and k is a number between 0 and 1. This tells that the output voltage of buck converter is always less than the input voltage. The output voltage of boost converter is:

$$V_{out} = \frac{V_{in}}{1-k} \tag{B.2}$$

Theoretically, as the duty cycle *k* increases the output voltage also increases. But due to circuit parasitic element, the k value is limited below 0.9 for proper operation of boost converter (Luo and Ye, 2010).

During the operation of power electronic devices, there are conduction and switching losses in each component. The source of conduction losses arenon-ideal behavior of on-state voltage drop and switching losses are caused due to the efforts to to clear any stored charge and to recover forward voltage blocking capability (Emadi, 2005). Conduction loss of transistor is axpproximated by:

$$P_{loss,cond} = V_{on} I_{on} \tag{B.3}$$

Where V_{on} is voltage drop in the transistor, usually less than 1 V and I_{on} is current flowing in ON state. Figure B.5 illustrates the losses incur when the device is either turned- on or turned-off. 't_{rise}' is defined as time the current needs to change from its minimum to maximum values. 't_{fall}' is defined as time the current needs to change from its maximum to minimum values. Switching frequency f_{sw} is important factor in power electronic applications since it ranges up to Megahertz and contributes to the power losses significantly.

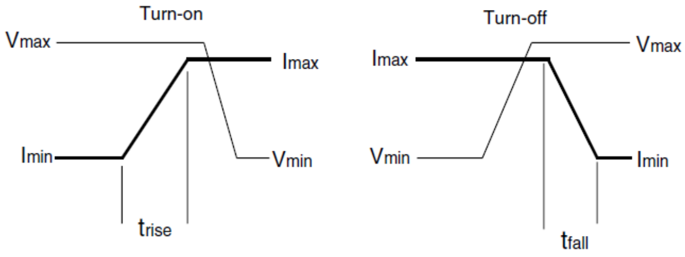
Turn-on
Vmax
Imax
Imin
Vmin
trise
Turn-off
Imax
Vmax
Vmin
Imin
tfall

$$P_{sw\_rise} = \frac{f_{sw} V_{max} I_{max} t_{rise}}{2}$$

$$P_{sw\_fall} = \frac{f_{sw} V_{max} I_{max} t_{fall}}{2}$$

Figure B.3 Approximate switching losses in MOSFETs and IGBTs

(Emadi, 2005)

The power electronic device used in in the simulation was IGBT and its physical model is available in the Simulink software that incluces efficiency in term of switching resistance.

Appendix C.1: Matlab program to calculate braking characteristic of drive cycle

```
clc
%load CYC_UDDS.mat
%load CYC_US06.mat
load CYC_EUDC.mat
mass=1500;
mph=cyc_mph;
[n,m]=size(mph);
dcc(1)=0;
sec=mph(:,1);
speed=1.609344*mph(:,2);
j=0;k=1;
for i=2:n
  dcc(i)=(speed(i)-speed(i-1))*10/36;
  if dcc(i) >= 0
    dcc(i)=0;
  end
end
for i=1:n-1
 if dcc(i)== 0 & dcc(i+1) < 0
   j=j+1;
   brake1(j,1)=i-1;
   V1(j)=speed(i-1);
 end
 if dcc(i) < 0 & dcc(i+1) == 0
    brake2(j,1)=i-1;
    V2(j)=speed(i-1);
 end
end
nBrake=j;
for i=1:nBrake
  dt=brake2(i)-brake1(i);
  dV=V1(i)-V2(i);
  tBrake(i)=dt;
  z(i)=(10/36/9.8)*dV/dt;
  Ek(i)=1e-3*0.5*mass*(10/36)^2*(V1(i)^2-V2(i)^2);
end
```

Appendix C.2: Simulation parameters for braking dynamic model

Parameter	Description	Value
m	Vehicle mass (kg)	1500
a	Distance of front axle from the vertical projection point of vehicle CG onto the axle-ground plane (m)	1.008
b	Distance of rear axle from the vertical projection point of vehicle CG onto the axle-ground plane (m)	1.542
h	Height of vehicle CG above the ground (m)	0.569
C_{d}	Aerodynamic drag coefficient ($Ns^2m^{-1}kg^{-1}$)	0.346
A	Effective frontal vehicle cross-sectional area (m^2)	1.746
R_e	Effective rolling radius (m)	0.279
I_{w}	Wheel-tyre assembly inertia ($kg.m^2$)	0.5
A_{cf}	Area of front wheel cylinder (m^2)	$2*10^{-3}$
A_{cr}	Area of rear wheel cylinder (m^2)	$0.7*10^{-3}$
R_{disk}	Disc mean radius, $(R_o + R_i)/2$ (m)	0.105
μ_{pad}	Friction coefficient of brake pad	0.4

Appendix C.3: Matlab program to calculate regenerative ratio of serial braking system

```
clc
j=0;k=1;
fori=2:n
dcc(i)=(speed(i)-speed(i-1))*10/36;
if dcc(i) >= 0
dcc(i)=0;
end
end
fori=1:n-1
if dcc(i)== 0 & dcc(i+1) < 0
   j=j+1;
brake1(j)=i-1;
end
if dcc(i) < 0 & dcc(i+1) == 0
brake2(j)=i-1;
end
end
[n1,n2]=size(brake1);
i=1;
for j=1:n2
  n1=brake1(j);
  m=brake2(j);
  SoC=0.5;
```

```
Ebat=0;
for k=n1:m
     v1=speed(k)*10/36;
wf=v1/Reff;
Fd=0.5*Cd*rho*Af*v1^2;
FzF=Nf-hg*(mass*dcc(k)+Fd)/Lb;
FzR=Nr+hg*(mass*dcc(k)-Fd)/Lb;
FxF=(mass*dcc(k)+Fd)/(1+0.333*FzR/FzF);
Tf(k)=abs(Reff*FxF+Iw*dcc(k)/Reff);
% regenerative torque at front wheels
ifwf>wbase/gear
Treg=Pmax/wf;
else
Treg=Tmax*gear;
end
% weight due to vehicle speed
if speed(k) >= vb
       w1=1;
elseif speed(k) <vb& speed(k) >va
        w1=(speed(k)-va)/(vb-va);
else
        w1=0;
end
% weight due to SoC
if SoC <= 0.8
```

```
       w2=1;
elseifSoC< 0.9 & SoC > 0.8
       w2=0.9-SoC;
else
       w2=0;
end
Treg=Treg*w1*w2;
% torque distribution
ifTreg>Tf(k)
Tmot(k)=Tf(k);
else
Tmot(k)=Treg;
end
% M/G output
Tgen=-Tmot(k)/gear;
Wgen=wf*gear;
effG=interp2(torque,rad_s,eff,Tgen,Wgen);
Pgen(k)=Tgen*Wgen*effG;
% battery SoC update
     R1=module*interp1(soc_bat,r_chg,SoC);
     V1=module*interp1(soc_bat,voc_bat,SoC);
if k==n1
      amp1=(-V1+sqrt(V1^2-4*Pgen(k)*R1))/(2*R1);
      Pbat1=V1*amp1;
else
```

```
       amp2=(-V1+sqrt(V1^2-4*Pgen(k)*R1))/(2*R1);

       Pbat2=V1*amp2;

       Ah1=0.5*(amp1+amp2)*(sec(k)-sec(k-1))/3600;

Ebat=Ebat+0.5*(Pbat1+Pbat2)*(sec(k)-sec(k-1));

       SoC=SoC+Ah1/Ah;

       amp1=amp2;

       Pbat1=Pbat2;

end

soc1(k)=SoC;

Ibat(k)=amp1;

end

  v1=speed(n1)*10/36;

  v2=speed(m)*10/36;

Ek=0.5*mass*(v1^2-v2^2);

ifEk> 0

reg_ratio(i)=100*Ebat/Ek;

speedA(i)=speed(n1);

speedB(i)=speed(m);

t1(i)=n1;

t2(i)=m;

i=i+1;

end

end
```

Appendix C.4: M/G and battery data for calculating regenerative braking ratio

```
% Data source:

% NREL's testing of PRIUS_JPN 30 kW motor at Unique Mobility 4/1999

% (N*m), torque range of the motor

mc_map_trq=[-305 -275 -245 -215 -185 -155 -125 -95 -65 -35 -5 0 5     35     65     95     125     155     185     215     245     275
          305];

mc_map_spd=[0 500 1000 1500 2000 2500 3000 3500 4000 4500  6000]*(2*pi)/60;

% LOSSES AND EFFICIENCIES

% multiplied by 0.95 because data was for motor only, .95 accounts for inverter/controller efficiencies

mc_eff_map=0.95*[...

.905.905.905.905.905.905.905 .905 .905 .905 .905.905.905 .905 .905.905 .905 .905 .905 .905 .905 .905 .905

0.56    0.59    0.62    0.65    0.68    0.72    0.76    0.8     0.85    0.9     0.87    .905    0.87    0.9     0.85    0.8     0.76    0.72    0.68
        0.65    0.62    0.59    0.56

0.72    0.74    0.76    0.78    0.81    0.83    0.86    0.89    0.91    0.94    0.85    .905    0.85    0.94    0.91    0.89    0.86    0.83    0.81
        0.78    0.76    0.74    0.72

0.72    0.74    0.76    0.78    0.86    0.88    0.9     0.92    0.93    0.94    0.83    .905    0.83    0.94    0.93    0.92    0.9     0.88    0.86
        0.78    0.76    0.74    0.72

0.72    0.74    0.76    0.78    0.86    0.88    0.92    0.93    0.95    0.95    0.82    .905    0.82    0.95    0.95    0.93    0.92    0.88    0.86
        0.78    0.76    0.74    0.72

0.72    0.74    0.76    0.78    0.86    0.88    0.92    0.94    0.95    0.95    0.81    .905    0.81    0.95    0.95    0.94    0.92    0.88    0.86
        0.78    0.76    0.74    0.72
0.72   0.74   0.76   0.78   0.86   0.88   0.92   0.95   0.96   0.95   0.81   .905   0.81   0.95   0.96   0.95   0.92   0.88   0.86
       0.78   0.76   0.74   0.72

0.72   0.74   0.76   0.78   0.86   0.88   0.92   0.95   0.96   0.95   0.8    .905   0.8    0.95   0.96   0.95   0.92   0.88   0.86
       0.78   0.76   0.74   0.72

0.72   0.74   0.76   0.78   0.86   0.88   0.92   0.95   0.95   0.95   0.8    .905   0.8    0.95   0.95   0.95   0.92   0.88   0.86
       0.78   0.76   0.74   0.72

0.72   0.74   0.76   0.78   0.86   0.88   0.92   0.95   0.95   0.95   0.79   .905   0.79   0.95   0.95   0.95   0.92   0.88   0.86
       0.78   0.76   0.74   0.72

0.72   0.74   0.76   0.78   0.86   0.88   0.92   0.95   0.95   0.95   0.79   .905   0.79   0.95   0.95   0.95   0.92   0.88   0.86
       0.78   0.76   0.74   0.72];
```

Appendix C.5: Simulation parameters for regenerative braking system using IM drive

a. Induction motor

Nominal power : 30 kW

Voltage : 500 V

Frequency : 50 Hz

Stator resistance : 0.2147 Ohm

Stator Inductance : 0.991 mH

Rotor resistance : 0.2205 Ohm

Rotor Inductance : 0.991 mH

Mutual inductance : 64.19 mH

Pole pair : 4

b. DTC controller

Torque hysteresis bandwidth : 10 Nm

Flux hysteresis bandwidth : 0.2 Wb

Initial machine Flux : 0.4 Wb

Maximum switching frequency : 20 kHz

DTC sampling time : 20 usec

c. Inverter

Number of bridge arms : 3

Snubber resistance : 10 kOhm

Snuber capacitance : inf F

Power electronic device : IGBT/Diodes

R on : 1 mOhm

Forward IGBT voltage : 1.4 V

Forward diode voltage : 1.4 V

Fall time of IGBT : 1 usec

Tail time of IGBT : 1 usec

d. Battery

Battery type : Lithium-Ion

Nominal voltage : 400 V

Rated Capacity : 120 Ah

Initial state-of-charge : 50 %

Maximum capacity : 120 Ah

Fully charged Voltage : 465.5949 V

Nominal discharge current : 52.1739 A

Internal resistance : 33.3 mOhm

Capacity at nominal voltage : 108.5217 Ah

Voltage at exponential zone : 432.1543 V

Capacity at exponential zone : 5.895652 Ah

Appendix C.6: Data of Hydraulic braking system

1	**Gas-charged accumulator**	Values
	Capacity (l)	2
	Preload pressure (Bar)	2
	Specific heat ratio	1.4
	Initial valume (l)	0
2	**Pressure relief valve**	
	Maximum passage area (cm^2)	0.1
	Valve pressure setting (Bar)	60
	Valve regulation range (Bar)	2
	Flow discharge coefficient	0.7
	Critical Reynolds number	2000
	Leakage are (cm^2)	1.0E-08
3	**2-way directional valve**	
	Valve passage maximum area (cm^2)	15
	Valve maximum opening (mm)	5
	Flow discharge coefficient	0.7
	Critical Reynolds number	2000
	Leakage area (cm^2)	1.0E-10
4	**Single-acting hydraulic cylinder**	
	Piston area (cm^2)	3.14
	Piston stroke (mm)	5
	Initial distance between piston and cap	0
	Dead volume (cm^3)	1.0E-02

Chamber initial pressure (Bar)	
Specific heat ratio	1.4
Contact stiffness (N/m)	1.0E+06
Contact damping (N/m/s)	150
Cylinder orientation	Act in positive direction

5 Mechanical load

Mass (kg)	0.25
Damping coefficient (N/(m/s)	150
Spring rate (N/m)	200

Appendix C.7: Simulation parameters for regenerative braking system using DC drive

No	Parameter	Unit	Value
1	Armature resistance	Ohm	0.8
2	Armature inductance	H	0.05
3	Field resistance	Ohm	1.3
4	Field inductance	H	0.5
5	Field-armature mutual inductance	H	0.05
6	Total inertia	kg.m^2	0.25
7	DC voltage source	V	80
8	Hysteresis band	A	1
9	Carrier frequency	Hz	1080
10	Sample time	sec	5.00E-06
11	Modulation index	-	0.7
12	Frequency of output voltage	Hz	60
13	Phase of output voltage	degree	0
14	Resistance Ron	Ohm	0.05
15	Inductance Lon	H	0
16	Forward voltage Vf	V	1
17	Current 10% fall time Tf	sec	1.00E-06
18	Current tail time Tt	sec	1.00E-06
19	Snubber resistance Rs	Ohm	1.00E+05
20	Snubber capacitance Cs	F	inf
21	vehicle mass	kg	1150
22	Rolling constant	-	0.014

23	Frontal area	m^2	2.40
24	Aero drag coefficient		0.4
25	Air density	kg/m^3	1.202
26	Effective wheel radius	m	0.2825
27	gear ratio	-	4

Appendix D: Description of Simulink blocks used in the research

1. Pressure source

   The source is “ideal” where its pressure isn’t affected by the flow rate of the fluid. Inlet and outlet ports are denoted by T and P letters in the block. The control signal representing source pressure is connected to control port S.

2. Hydraulic fluid

   Hydraulic properties such as density, kinematic viscosity and bulk modulus are determined in this block and kept constant in the simulation. The density is specific to the type of fluid used, but the kinematic viscosity is affected by the working temperature. For pure liquid, the bulk modulus is fixed for the type of fluid used and the temperature. Its value changes if there is air trapped in the fluid and becomes:

$$E = E_l \frac{1+\alpha\left(\frac{p_a}{p+p_a}\right)^{1/n}}{1+\alpha\frac{p_a^{1/n}}{n\left(p+p_a\right)^{1+1/n}}E_l}$$

Where:

E_l : Pure liquid bulk modulus

p_a : Atmospheric pressure

α : Relative gas content at atmospheric pressure, $\alpha = V_G/V_L$

V_G : Gas volume at atmospheric pressure

V_L : Volume of liquid

n : Gas-specific heat ratio

At higher actuation pressure, $p$is much higher than p_a, so the aircontent doesn′t affect the bulk modulus at high pressure but of course the piston travel to compress the trapped air and this may exceed the allowable travel so high pressure cannot be generated.

3. Accumulator

Precharged gas and fluid chambers in the form of an accumulator are fitted withpistons or bladdersto separate them. The function of an accumulator is to store hydraulic energy. Fluid enters when the fluid pressure is higher than the precharge pressure and flows back into the fluid system when the inlet pressure is lower than the precharge pressure. An Inlet valve isolates the gas chamber if system pressure is lower than prechargepressure. Flow rate and fluid volume are given by:

$$q = \frac{dV_F}{dt}$$

$$V_F = \begin{cases} 0, p_{in} \le p_{pr} \\ V_A\left(1 - \left(\frac{p_{pr}}{p}\right)^{1/k}\right), p_{in} > p_{pr} \end{cases}$$

Where:

V_F :Fluid volume

VA :Accumulator capacity

p :Inlet gauge pressure

p_{pr} :Precharge pressure

k :Specific heat ratio

q :Volumetric flow rate

t :Time

4. Check Valve

This valve in the simulation is used to allow the fluid to flow only from the source to the rest of the hydraulic system, not in the reverse direction. The relationship between the pressure differential across the valve and the valve passage area is shown in Figure 1. Minimum pressure p_{crack} is the point where the valve starts to move and then the passage area changes linearly with the pressure differential until maximum passage area A_{max} reached. Further pressure increase doesn't affect the passage area.

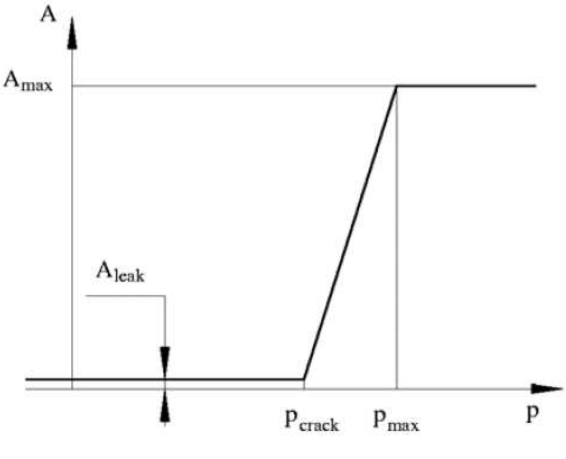

Figure D.1 Check valve characteristic (Mathworks, 2011)

5. Relief Valve

This valve is located between the hydraulic loop and the reservoir to maintain the system pressure. If the preset pressure p_{set} is reached, the valve is opened and thus the pressurised fluid flows out the hydraulic loop. When this causes the system pressure to drop below p_{set}, the valve is then closed.

6. Pipeline

   The cross section of the hydraulic pipelines can be either circular or noncircular. The model considers both friction loss and fluid compressibility, and not fluid inertia. The friction loss is represented inthe model and the constant volume chamber accounts for the fluid compressibility.

7. Valve

   The poppet valve as shown in Figure D.2 was used in this simulation. It has a cylindricalsharp-edged stem and a conical seat. This model is valid for both laminar and turbulent flow by calculating Reynoldsnumber (*Re*) and comparing it with thecritical Reynolds number(*Rec_{cr}*).

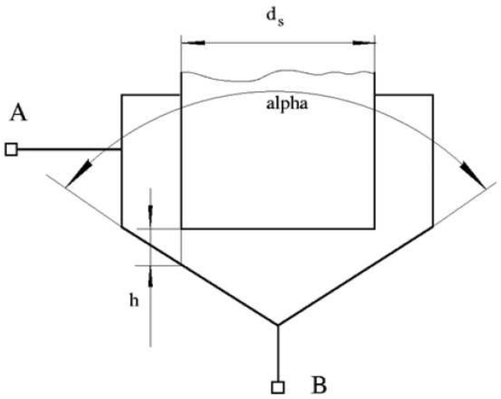

Figure D.2 Cross section of poppet valve (Mathworks, 2011)

Flow rate from port A to port B is given by:

$$q = \begin{cases} C_D A \sqrt{\frac{2}{\rho}|p|}sign(p), Re \geq Re_{cr} \\ 2C_{DL} A \frac{D_H}{v\rho} p, Re < Re_{cr} \end{cases}$$

$$A(h) = \begin{cases} A_{leak}, h \leq 0 \\ (d_s + h\cos\alpha\sin\alpha)h\sin\alpha + A_{leak}, 0 \leq h \leq h_{\max} \\ A_{\max} + A_{leak}, h \geq h_{\max} \end{cases}$$

$$h = x_0 + x$$

$$p = p_A - p_B$$

$$Re = \frac{qD_H}{A(h)v}$$

$$C_{DL} = \sqrt{\frac{4A(h)}{\pi}}$$

$$A_{\max} = \frac{\pi d_s^2}{4}$$

8. Hydraulic cylinder

This device generates translational motion from the pressurised fluid in the cylinder chamber. Since force and motion are in one direction, an external device such as a spring is used to move the rod in the opposite direction. The model accounts for fluid compressibility, energy conversion and a translational hard stop.